ISSN 1811-1165 (Print)
ISSN 2413-2179 (Online)

EURASIAN PHYSICAL TECHNICAL JOURNAL

VOLUME 21, NO. 3(49), 2024

phtj.buketov.edu.kz

EURASIAN PHYSICAL TECHNICAL JOURNAL

p - ISSN 1811-1165
e - ISSN 2413-2179

Volume 21, No. 3(49), 2024

1st issue – June, 2004

Journal Founder:

NLC "KARAGANDY UNIVERSITY OF THE NAME OF ACADEMICIAN E.A. BUKETOV

https://phtj.buketov.edu.kz
www.facebook.com/groups/1103109540750967

Registration Certificate No.4382-Zh, November 7, 2003.
Re-registration Certificate No.KZ50VPY00027647, October 6, 2020 issued by Information Committee of the Ministry of Information and Public Development of the Republic of Kazakhstan

Contact information:

Editorial board of EAPhTJ (Build. 2, room 216)
Karaganda Buketov University
Universitetskaya Str.28, Karaganda,
Kazakhstan, 100024
Subscription index: 75240

Tel: +7(7212) 77-04-03
Fax: +7(7212) 35-63-98
E-mail: ephtj@mail.ru, ephtj2021@gmail.com

Signed to print **30.09.2024**
Format 60x84 1/8. Offset paper.
Volume **18.5 p.sh.** Circulation 300 copies.
Order No. 105.

Printed in the Publishing House of
Karagandy University of the name
of academician E.A.Buketov

Tel. (7212) 35-63-16.
E-mail: izd_kargu@mail.ru

Eurasian Physical Technical Journal, 2024, Vol. 21, No. 3(49)

CONTENTS

.

Dear authors and readers!
Dear colleagues!

In the preface, we traditionally inform authors and readers about the most important achievements of the Eurasian Physical Technical Journal at the moment.

In this aspect, it can be noted that Eurasian Physical Technical Journal is included in List 1 of the updated List of scientific publications recommended by the Committee for Quality Assurance in Science and Higher Education of the Ministry of Science and Higher Education of the Republic of Kazakhstan for publishing the main results of scientific work in 4 scientific areas: physical sciences (physics and astronomy), materials science, energy, engineering (technical sciences), Order No. 603 dated July 12, 2024. This fact attracted the attention of many scientists and doctoral students, and number of people wishing to publish has increased. We hope that this will lead to an increase in the number of readers and, accordingly, will have a positive effect on the growth of citations. Moreover, the articles published in the journal are prepared based on the results of the most modern research on current problems of technical physics.

This issue presents 15 papers to the readers' attention, 12 works are devoted to solving problems of traditional Journal sections, and 3 papers are offered as a Special Issu. These 3 articles have been prepared as extended versions of papers recommended by the organizing committee of the 7th International Conference on Engineering Sciences and Technology on April 6-18, 2024 in Luxor, Egypt.

The chairman of the organizing committee, Professor Dr. Gamal Abouelmagd (Minia University, Egypt) noted that the aim of the conference is to bring together leading academic scientists and researchers to exchange information, experience and research results on all aspects of specialized and interdisciplinary fields. The scientific program of ICEST2024 focuses on current achievements in the field of research, production and use of engineering sciences with a special emphasis on their role in maintaining the academic level in the field of engineering and applied sciences, as well as their impact on expanding the frontiers of science. In total, more than 300 participants took part in the conference.

The Guest Editors of the special issue are Professor A.L. Kozlovsky (Institute of Nuclear Physics, National Nuclear Center of the Republic of Kazakhstan, Almaty) and Professor, Dr. Nouby M. Ghazaly**,** General Conference Secretary **(**Head of the International Foundation for Sciences and Development (IFSDL) and El Minya High Institute for Engineering and Technology, Egypt.

Let's move on to a brief description of the issue's contents.

The Materials Science section presents new original results on the study of the properties of various materials. The article by scientists from Orenburg (Russia) shows unique results of a study of "conformational changes in generally neutral polyampholytic and uniformly charged macrochains, polypeptides adsorbed on the surface of a longitudinally polarized gold nanorod in the form of a cylinder with spherical ends." Authors from Tashkent (Uzbekistan) and Baku (Azerbaijan) proposed the results of complex modeling of recombination processes in symmetric and asymmetric p-n junctions under various conditions. The results of joint studies by Kazakh and Ukrainian scientists on the corrosion behavior of NZ30K magnesium alloys showed that "NZ30K alloy doped with 0.1 wt.% silver can be used as a structural material for the manufacture of biodegradable implants."

In the "Energy" section, readers are offered two articles that examine various nuclear energy issues, the solution of which is of great practical importance both for energy and for maintaining a safe environmental situation. The article by scientists from the Institute of Nuclear Physics of Uzbekistan Academy of Sciences devoted to identifying the service life of the VVR-SM research reactor, determined "the electrical conductivity and thermal conductivity of low-ash medium-grain graphite in the masonry of the thermal column in the range of measurement temperatures corresponding to the conditions of normal operation of the reactor." The article by Kazakh scientists examined "the thermal state of the active zone of the IVG.1M research reactor under various operating modes. "The relevance of these studies is associated with the determination of the thermal characteristics of the active zone of the IVG.1M research reactor with low-enriched uranium fuel under nominal and design operating modes."

The Engineering section offers solutions to current problems of automation of modern technologies and control and monitoring systems. In the article by authors from Tomsk (Russia) during the processes of synthesis of hydroxyapatite under the influence of ultraviolet radiation and ultrasound, established a decrease in the size of solar particles of hydroxyapatite to 4 microns. In general, "the use of ultraviolet transition at the development stage led to an increase in the content of hydroxyapatite in products."

As a result of modeling the "plastic-deformation state of the contact surface during friction," the authors from Zaporizhzhia (Ukraine) developed and proposed a method for calculating the surface strength and deployment of tribo-units, which "links the quality parameters of the state of the point (friction coefficient, shape factor) with the thermomechanical parameters of the process."

The authors of the article from Almaty "dedicated to the analysis of experimentally obtained fluctuations caused by a laser beam in the sight in a photodiode (signal receiver) due to its impact not only at the atomic level, but also on the scale of clusters of nanoparticle molecules." The authors received unique and practically important results that "the gas concentration is measured in the fluctuation-dissipative direction.

The article by Ukrainian and Kazakh researchers provides an assessment of the "resistance of heat-resistant yttrium-containing sealing coatings to mechanical destruction during turning of cutting paths." Based on the results of tribotechnical tests, "changes in the nature of the dynamic coefficient of friction during the testing period and the value of the energy intensity of material wear" were established.

The article by authors from Astana scientific centers presents "a scientific and technical justification for the parameters of a radar device that allows detecting and visualizing prohibited items using microwave electromagnetic radiation." A model of a multi-static scheme for measuring waves reflected from an object based on a holographic method has been developed. The work by Karaganda authors investigated "properties of lanthanum ferrite perovskite synthesized by the hydrothermal method". Lanthanum ferrite was chosen as the object of study due to its high activity under the influence of visible light. It is shown that "increasing the annealing time leads to an improvement in the crystal structure, an increase in the size of crystallites and a higher level of oxygen saturation."

The articles in the Special Issue section are devoted to solving topical problems in various engineering technologies. The article by authors from Iraq and Egypt examines the influence of environmental pollution on the behavior of drive tribology, in particular, the influence of humidity and quartz sand on the friction coefficient of a wind turbine braking system. The second article in this section is also devoted to solving the problem of the presence of surface defects, which can be the reason for their potential to serve as stress concentrators. Based on modeling, the important role of "non-stationary temperature fields in balancing the mechanical and physical aspects of the finishing process" is shown. The aim of the finite element study by the authors of the last article in the issue "is to study the influence of the radius of the unloading groove and taper with a gradual change in shaft diameter on the stress concentration factors. It is shown that a decrease in the taper angle has a significant effect on reducing the values of the stress concentration factors."

There is no doubt that the presented research results will be of interest to scientists, teachers, researchers, doctoral students and undergraduates.

I would especially like to express my deep gratitude to our reviewers for their objective and qualified examination of the materials, which contributed to ensuring the quality of the articles.

We will be glad to see you among our readers and authors of the next issues.

Best regards,
Editor-in-chief, professor Sakipova Saule E.
September, 2024

EURASIAN PHYSICAL TECHNICAL JOURNAL

2024, Volume 21, No.3 (49)

https://doi.org/10.31489/2024No3/6-20

Received: 03/04/2024 Revised: 26/06/2024 Accepted: 06/09/2024 Published online: 30/09/2024

Research Article

UDC 539.199, 544.723.2

CONFORMATIONAL STRUCTURE OF POLYAMPHOLYTES AND POLYELECTROLYTES ON THE SURFACE OF A LONGITUDINALLY POLARIZED GOLD SPHEROCYLINDER

Kucherenko M.G., Kruchinin N.Yu.*, Neyasov P.P.

Center of Laser and Informational Biophysics, Orenburg State University, Orenburg, Russia

*Corresponding author: *kruchinin_56@mail.ru

Abstract. *Conformational changes in generally neutral polyampholytic, as well as uniformly charged macrochains, polypeptides adsorbed on the surface of a longitudinally polarized gold spherocylinder—a cylindrical nanorod with spherical ends—were studied. An analytical model of the equilibrium structure of adsorbed macrochains on the surface of a polarized spherocylinder is presented, highlighting the entropy and field factors of the radial-angular distribution of link density. In the course of molecular dynamics simulation, the radial distributions of the density of polypeptide atoms in the central cylindrical part of the nanorod, as well as on its terminal hemispheres, were calculated. In addition, the distributions of the linear density of polypeptide atoms along the axis of the nanorod were calculated. A dumbbell-shaped polyampholyte edge was formed on the surface of the polarized nanorod, dense in the extended central cylindrical part and loose at the ends of the nanorod. There was also a shift of the macromolecular edge from the units of a uniformly charged polypeptide to the oppositely charged end of the nanorod, on which this polyelectrolyte edge swelled.*

Keywords: gold nanorod, polarized nanoparticle, polyampholyte, polyelectrolyte, conformational structure, molecular dynamics

1. Introduction

Currently, gold nanorods or nanospheroids that form conjugates with biopolymers are widely used in the creation of functional elements of various chemical sensors based on the effects of Förster energy transfer between nanoobjects connected by a macrochain and giant Raman scattering, as well as in the creation of nanostructured materials with embedded gold nanoparticles [1-13]. Of great interest in this case is the control of the characteristics of such nanosystems by changing the conformational structure of the adsorbed macrochain under the influence of an external electric field. In this case, it is necessary to use polyelectrolyte macromolecules that contain charged units, or polyampholytes, with electric dipole moments of monomers or unit fragments in their structure as such macrochains.

Previously, the authors in a number of works [14–22] studied electrically induced changes in the conformational structure of generally neutral polyampholytes or uniformly charged polyelectrolyte macrochains on the surface of a cylindrical gold nanowire transversely polarized in an external electric field, as well as an elongated or oblate gold nanospheroid polarized along the major axis. However, when creating such hybrid nanosystems, rather short cylindrical gold nanorods, the ends of which are spherical or spheroidal surfaces, are often used [1-13]. Such nanorods in some cases can be approximately considered as elongated nanospheroids with the length of the major axis equal to the length of the nanorod and the length

of the minor semi-axes equal to the radius of the nanorod. However, in the case of longitudinal polarization of such a nanorod in an external electric field, the distribution of induced charges on its surface will differ significantly from the distribution of induced charges on the surface of an elongated metal nanospheroid polarized along the major axis. On the surface of the cylindrical part of a metal nanorod, if it is longitudinally polarized, the surface density of induced electric charges will be zero, and all induced charges will be concentrated only at its ends. In particular, if the ends of the nanorod have a spherical surface shape, then the charges induced by the external electric field will be distributed according to the cosine law between the direction of the electric field and the normal to the surface [23]. This distribution of surface charges will have a significant impact on the conformational structure of polyelectrolytes adsorbed on the surface, which will vary significantly depending on the strength of the external polarizing electric field.

On the other hand, as was shown in [22], the formed conformational structure of the edge will also be influenced by the curvature of the adsorbing surface of the nanoparticle through the entropy factor. The radial distribution of the density of uncharged chain links on the cylindrical section of the particle has a different character than the similar distribution at the surface of the nanosphere.

Thus, the goal of this work is to study the conformational structure of generally neutral polyampholyte and uniformly charged polyelectrolyte macrochains on the surface of a longitudinally polarized cylindrical gold nanorod with spherical ends.

2. Mathematical model of the conformational structure of polyampholyte and polyelectrolyte chains on the surface of a spherocylinder polarized in an electric field

In [19, 22], the formation of an openwork structure of a polyampholyte macrochain (edge) adsorbed on the surface of nanoparticles of various shapes (spheres, spheroids, cylinders) was considered on the basis of a generalized model of an ideal Gaussian chain interacting with an adsorbent particle through two potential fields: van- der Waals $V(\mathbf{r})$ and electric, arising in addition to $V(\mathbf{r})$ as a result of polarization of the nanoparticle by an external field of intensity $\mathbf{E_0}$.

The configuration function $\psi(\mathbf{r})$ of an ideal Gaussian macrochain (i.e. a chain without bulk inter-link interactions) in the potential van der Waals field $V(\mathbf{r})$ of the adsorbent surface satisfies an equation that is isomorphic to the stationary Schrödinger equation [24]:

$$\frac{a_0^2 kT}{6}\nabla^2\psi(\mathbf{r}) = [V(\mathbf{r}) - \varepsilon]\psi(\mathbf{r}) \cdot \tag{1}$$

Here, in (1) a_0 is the length of the chain link, kT is the thermal energy at temperature T of the system, and ε is a constant with the dimension of energy (eigenvalue of the Grosberg-Khokhlov operator). Surfaces of constant density of monomer units of a polymer reflect the geometry of the adsorbing boundary, therefore, to write equation (1) in the case of a spherocylinder, cylindrical and spherical coordinate systems were used simultaneously, with each section of the composite particle having its own. The conformational function $\psi(\mathbf{r})$, depending on the radius vector $\mathbf{r}$ of the unit, found by solving equation (1), makes it possible to take into account the entropy aspects of the formation of various conformations of the adsorbed macrochain. Thus, the spatial distribution of the local density of chain links $n(\mathbf{r})$ is determined by the square of the conformational function corresponding to the minimum eigenvalue ε_0: $n_0(\mathbf{r}) = \psi_0^2(\mathbf{r})$ [24]. In the case of a quasi-stationary electric field of strength $E(t)$, one can consider quasi-equilibrium conformations of a macromolecule adsorbed on a nanoparticle, as was done, for example, in [20].

The energy of the additional (in addition to $V(\mathbf{r})$) interaction of the electric field of a nanoparticle with a separate link, or a group of polyampholyte links with a characteristic electric dipole moment $\mathbf{p}$ of a separate selected segment (a single link or a group of links) can be written in the form

$$V_{\mathbf{p}}^{(e)}(\mathbf{r}) = -\mathbf{p}\nabla\varphi^{(e)}(\mathbf{r}) \cdot \tag{2}$$

For a polyelectrolyte carrying a charge q on an individual chain link, the additional interaction energy

$$V_q^{(e)}(\mathbf{r}) = q \cdot \varphi^{(e)}(\mathbf{r}) \cdot \tag{2'}$$

The resulting equilibrium spatial distribution of the density $n(\mathbf{r})$ of macrochain units of a polyampholyte or polyelectrolyte adsorbed by a polarized nanoparticle in the approximation of the independent action of entropy and force factors [22] can be represented by the Boltzmann exponent:

$$n(\mathbf{r}) = \psi_0^2(\mathbf{r}) \exp\left[-\frac{V_{\mathbf{p}(q)}^{(e)}(\mathbf{r})}{kT} \right]. \tag{3}$$

The entropy factor $\psi_0^2(\mathbf{r})$ in (3) contains information about the linear memory of the polymer, as well as the features of the curvature of the surface of the adsorbing nanoparticle and its Van de Waals potential $V(\mathbf{r})$. The second, Boltzmann factor for the potential field $V_{\mathbf{p}(q)}^{(e)}(\mathbf{r})$, reflects the result of the action of the quasi-static field (2) or (2') within the framework of the independent links model. The role of this factor in the formation of macrochain conformations during its adsorption on a polarized elongated spheroidal nanoparticle in an external field was studied by us earlier in [19].

To determine the entropy factor $\psi_0^2(\mathbf{r})$ for a spherocylinder in (3), as in the case of a compressed spheroid [22], the solution to equation (3) can be represented by a simple analytical expression obtained for a composite figure of a circular cylinder with two hemispheres ("stubs" of radius $R=b=c$, where b and c are the minor semi-axes of the prolate spheroid).

Previously, in [14, 16], the radial dependences of the concentration of units were determined for cylindrical and spherical nanoparticles with δ-functional well simulating the attraction of units of a polymer molecule to the surface of the nanoparticle.

Then, for the cylindrical part of a composite model nanoparticle with radius $R=b=c$, i.e. in the region $-L/2 \le z \le L/2$ (L - length of the cylindrical part) the solution of equation (1) with a potential in the form of a delta-functional well and a solid wall

$$V(r) = \begin{cases} -\alpha\delta(r - r_0), & r > R \\ V_\infty(r) = \infty, & r = R \end{cases} \tag{4}$$

can be written in the form

$$\begin{cases} \psi_I = A\left(I_0(qr) - K_0(qr)\dfrac{I_0(qR)}{K_0(qR)} \right), & R < r < r_0 \\ \psi_{II} = AK_0(qr)\left(\dfrac{I_0(qr_0)}{K_0(qr_0)} - \dfrac{I_0(qR)}{K_0(qR)} \right) & r_0 < r < \infty \end{cases}, \tag{5}$$

where I_0 and K_0 are the Bessel functions of the imaginary argument of the zero order of the first and second kind, respectively, A is a constant, and the parameter q is found from the solution of the transcendental equation:

$$K_0(qr_0)I_0(qr_0) = \frac{a_0^2 kT}{6\alpha r_0} + K_0^2(qr_0)\frac{I_0(qR)}{K_0(qR)}. \tag{6}$$

The solution to Grosberg-Khokhlov equation (1) [24] with the delta-functional potential (4) of attraction at radius r_0 and the repulsive wall $V_1(r) = V_\infty(R) - \alpha\delta(r - r_0)$, where α - depth of well, on the surface of the nanoparticle for a spherical nanoparticle of radius R has the form ($A=const$)

$$\begin{cases} \psi_I(r) = A\left[\dfrac{I_{1/2}(qr)}{\sqrt{r}} - \dfrac{I_{1/2}(qR)}{K_{1/2}(qR)}\dfrac{K_{1/2}(qr)}{\sqrt{r}} \right], & R < r < r_0 \\ \psi_{II}(r) = A\left[\dfrac{I_{1/2}(qr_0)}{K_{1/2}(qr_0)} - \dfrac{I_{1/2}(qR)}{K_{1/2}(qR)} \right]\dfrac{K_{1/2}(qr)}{\sqrt{r}}, & r_0 < r < \infty \end{cases}, \tag{7}$$

where the parameter q is the root of the equation

$$\frac{a_0^2 kT}{6\alpha r_0} = I_{1/2}(qr_0)K_{1/2}(qr_0) - K_{1/2}^2(qr_0)\frac{I_{1/2}(qR)}{K_{1/2}(qR)}. \quad (8)$$

Spherically symmetric functions (7) are represented through the Bessel functions $I_{1/2}(qr)$ and $K_{1/2}(qr)$ the imaginary argument with index 1/2. Using (7), it is easy to represent the conformational functions on the surfaces of two stub hemispheres $L/2 \le z \le L/2 + R$ and $-L/2 - R \le z \le -L/2$, similar to how it was done for a compressed spheroid in [22].

Then the spatial distribution (3) of the density $n(\mathbf{r})$ of macrochain units adsorbed by a polarized nanoparticle takes the form

$$n(\mathbf{r}) = \left\{ \begin{matrix} \psi_I^2(r,z), & R < r < r_0 \\ \psi_{II}^2(r,z), & r_0 < r < \infty \end{matrix} \right\} \exp\left[-\frac{V_{\mathbf{p}(q)}^{(e)}(\mathbf{r})}{kT} \right]. \quad (3')$$

The entropy factor $\psi_{I,II}^2(\mathbf{r})$ in the form of the square of conformational functions (5) or (7) is used to describe the density of units in different sections of the spherocylinder: two hemispheres or a central cylindrical insert.

Approximation of the electric field of a spherocylinder by a prolate spheroid

The characteristics of the electric field of a spherocylinder can be described with acceptable accuracy by replacing a cylinder with two spherical ends of a radius $R=b=c$ with an elongated spheroid with similar geometric parameters (Fig. 1). Then the semimajor axis of the spheroid automatically determines the length L of the cylindrical part of the figure: $a=R+L/2>b$. The potential of the resulting field outside a conducting spheroid polarized in an alternating external uniform field parallel to its major axis a with the vector $\mathbf{E}_0$ oriented along the x axis can be written in the following form [23]:

$$\varphi^{(e)} = -E_0 x \times$$
$$\times \left\{ 1 - \frac{[\varepsilon(\omega) - \varepsilon^{(e)}]}{\left\{ \varepsilon^{(e)} + [\varepsilon(\omega) - \varepsilon^{(e)}] n^{(x)} \right\}} \frac{(1-e^2)}{2e^3} \left[\ln \frac{\sqrt{1+\xi_1/a^2} + e}{\sqrt{1+\xi_1/a^2} - e} - \frac{2e}{\sqrt{1+\xi_1/a^2}} \right] \right\}. \quad (9)$$

$$\varphi_0 = -E_0 x = -E_0 \xi\eta \frac{d^2}{4\sqrt{a^2-b^2}} = -E_0 \eta \frac{d}{2} \frac{\sqrt{(\xi_1 + a^2)}}{\sqrt{a^2-b^2}}. \quad (10)$$

Here, to describe the field of charged and polarized axisymmetric ellipsoidal bodies (ellipsoids of revolution, for which semi-axes $b=c$) ellipsoidal coordinates are used $\xi_1 = (r_1 + r_2)^2/4 - a^2$, $\eta_1 = (r_1 - r_2)^2/4 - a^2$, φ, where are the focal radii and the eccentricity of the prolate spheroid $e = \sqrt{1 - b^2/a^2}$. For points on the surface of a spheroid $\xi_1=0$.

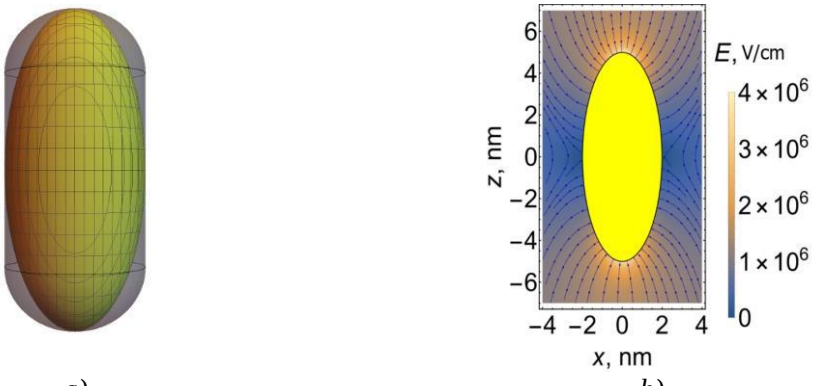

a) *b)*

Fig.1. Spherocylinder and its approximation by an elongated spheroid (a), distribution of electric field strength outside the spheroid (b).

In an alternating electric field that varies harmoniously with frequency ω, the metal nanoparticle is characterized by a dielectric constant $\varepsilon(\omega)$. In (9), the frequency dispersion of the dielectric constant $\varepsilon(\omega)$ of a metal in the form of a Drude-Lorentz is taken into account [23]. The dielectric constant of the external medium $\varepsilon^{(e)}$ is assumed to be constant.

In the model presented above, as in [19, 22], the adsorption van der Waals potential $V(\mathbf{r})$ of the surface of an uncharged spheroidal nanoparticle can be specified by a combination (4) of the simplest model potentials "solid wall – delta functional well".

3. Simulation results

Based on expressions (2 – 10), calculations were made of the field characteristics in the vicinity of a gold spherocylinder (total length 10 nm, radius of the cylindrical part and two hemispheres 2 nm) and the density of units of a macrochain of a polyelectrolyte or polyampholyte type adsorbed on it. The magnitude of the charge of the link or its dipole moment, the strength of the polarizing field, as well as the depth and position of the van der Waals well were varied, along with the temperature, the dimensions of the links and the lengths of the semi-axes of the spherocylinder.

Figure 1a shows the approximation of a spherocylinder by an elongated spheroid. And Figure 1b shows a picture of the field strength of an elongated polarized spheroid. It is more convenient to calculate the field characteristics by imagining the nanoparticle in the form of an elongated spheroid, so formulas (9) and (10) were used for this.

In Fig. 2 shows the concentration distributions of polyelectrolyte units near the surface of an uncharged polarized nanorod with hemispherical ends for different values and signs of charge q of the chain link: -0.1|*e*| (Fig. 2a and 2d), 0 (Fig. 2b and 2e), 0.1|e| (Figure 2c and 2f) taking into account the entropy factor $\psi_0^2(\mathbf{r})$ and Boltzmann factor factors $W(\mathbf{r}) = \exp\left[-V^{(e)}_{\mathbf{p}(q)}(\mathbf{r}) / kT\right]$ based on formula (3'). Simulation parameters: a =5nm, b=c=2nm (radius of the cylinder and hemispheres), α=5·10^{-3} eV·nm (potential well depth), a_0=0.5 nm (link length), temperature T=300 K, E_0=106 V/cm. The figure shows that for a macrochain with neutral links (Figs. 2b and 2e), monomers on the surface of a spherocylinder polarized in an external electric field are distributed uniformly throughout, since the macromolecule is not sensitive to the effect of an electric field.

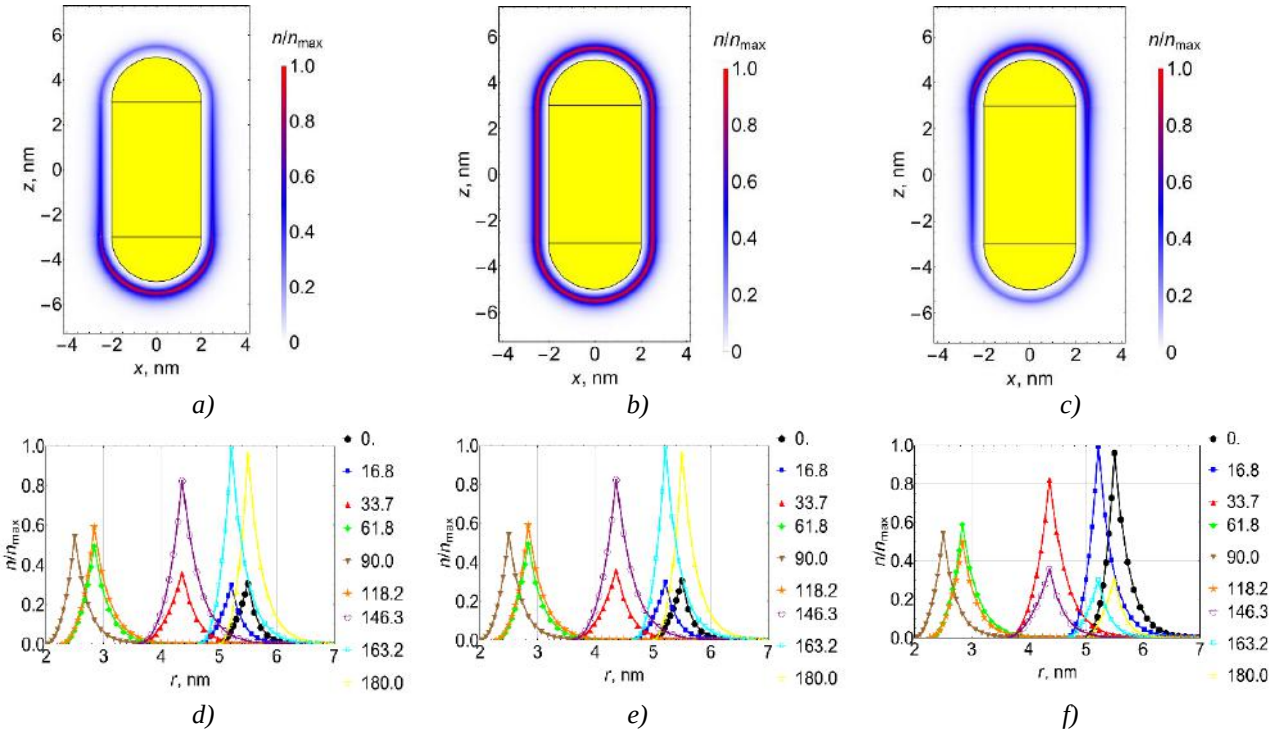

Fig.2. Distribution of the concentration of polyelectrolyte units near the surface of a polarized nanorod for different values and signs of the unit charge: -0.1|e| (a, d), 0 (b, e), 0.1|e| (c, f). Figures d, e, f show the angular distributions of unit concentrations from the center of the nanoparticle (angle 0 degrees is the direction along the external electric field strength vector, and angle 180 degrees is in the opposite direction).

And when the sign of the polyelectrolyte link charge changes, a mirror image of displaced monomers is observed on the surface of the spherocylinder (Figs. 2a and 2c), as well as the corresponding curves of the distributed concentration of the units in different directions (Figs. 2d and 2f).

When the localization radius r_0—the position of the delta-functional van der Waals well—changed from r_0=2.3 nm to r_0=2.7 nm, the radial-angular density distributions (3) changed noticeably both at the end sections of the nanoparticle and in the region of the cylindrical section.

Thus, the contribution of the van der Waals interaction, represented by the delta function, is felt when the radius of its action zone changes. The parameter α, which determines the effective depth of the van der Waals well, manifests itself in a similar way. Temperature T and the length of the macrochain link a_0 are included in (1) in the form of a product, therefore the influence of these parameters on the distribution picture should be considered together. Analysis of the calculated curves showed that an increase in the parameter a_0T levels out the difference in the amplitudes of the radial distributions at different ends of the spherocylinder

Figure 3 shows the pattern of changes in polyelectrolyte links on the surface of a spherocylinder at different values of the external electric field. It is evident that with an increase in the electric field strength from E_0=10^5 V/cm (Fig. 3a) to E_0=3 10^6 V/cm (Fig. 3c), a significant shift of the macrochain monomers to the oppositely charged end of the nanoparticle is observed. This is clearly seen in the graphs of the angular distributions of the link concentration (Fig. 3, d-f). At the lowest value of the external electric field strength (Fig. 3d) in any direction from the center of the nanoparticle, the peaks of the monomer concentration distributions are at the same level. And as the external electric field strength increases (Fig. 3, e and f), the peaks of the link concentration become lower and lower, the larger the angle.

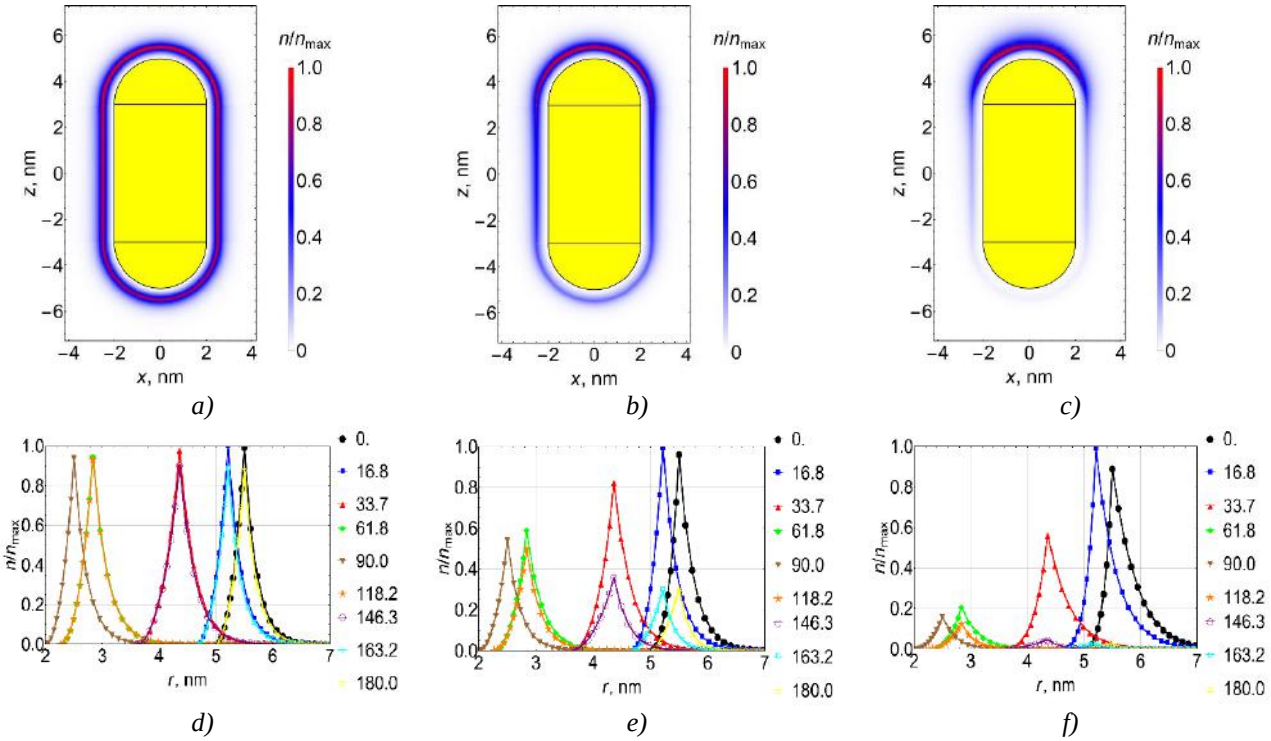

Fig.3. Distribution of the concentration of polyelectrolyte units (unit charge q=0.1|e|) at different values of the polarizing field strength E_0: 10^5 V/cm (a, d), 10^6 V/cm (b, e), 3 10^6 V/cm (c, f). Figures d, e, and f show the angular distributions of unit concentrations from the center of the nanoparticle.

The degree of elongation of the nanoparticle (Fig. 4) also significantly affects the distribution of monomer density: it, as expected, has the least pronounced angular dependence for a sphere, and a more pronounced one for a nanoparticle with a relatively large cylindrical part. With a proportional change in the radii of the cylinder and hemispheres, the angular dependences appear more noticeable for nanoparticles with a large radius. In Figure 4d, corresponding to the sphere (Fig. 4a), the smallest difference between the curves of the monomer concentration distributions in opposite directions is observed. With increasing elongation of the spherocylinder (Fig. 4, b and e) and even stronger elongation (Fig. 4, c and f), an increasingly greater

difference is observed between the curves of the angular distributions of the monomer concentration in the lower half of the spherocylinder (angles from 90 to 180 degrees) and the upper (angles from 0 to 90 degrees).

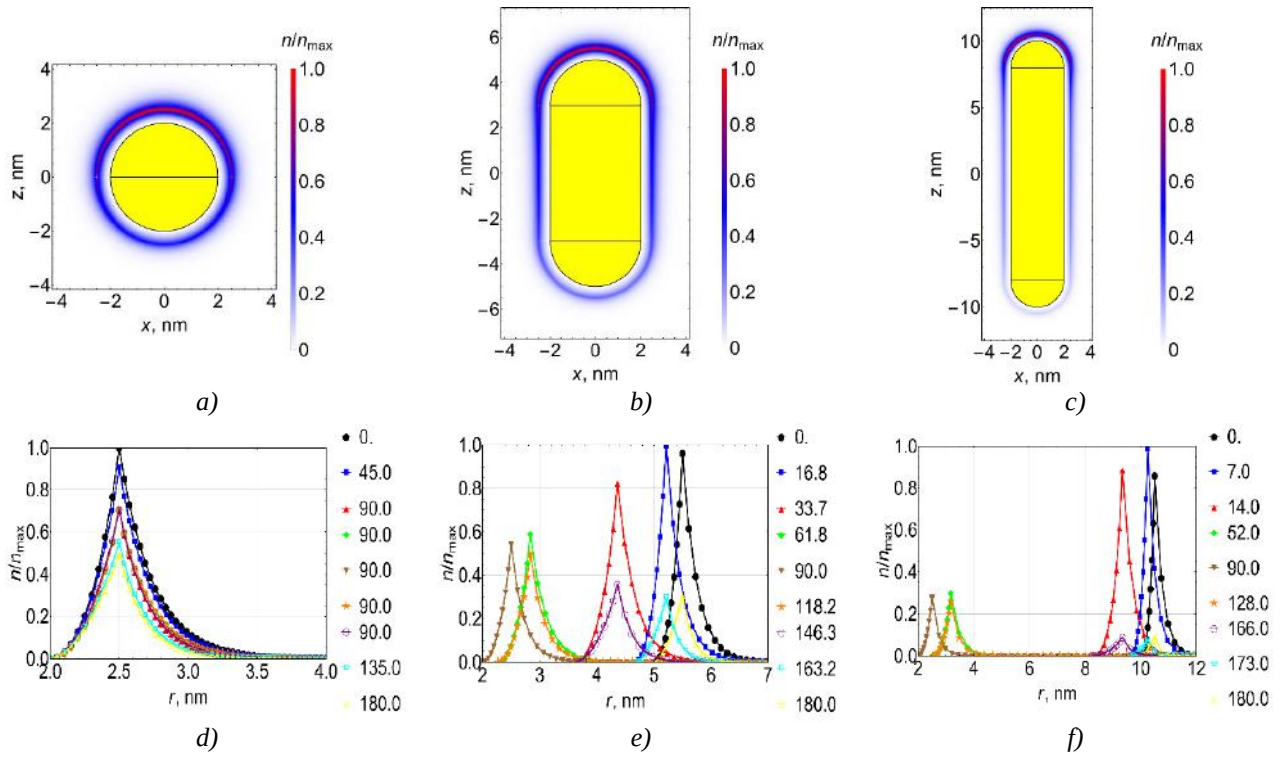

Fig.4. Distribution of the concentration of polyelectrolyte units (unit charge q=0.1|e|) for different lengths of the cylindrical part of the nanorod b=c=2 nm: a=2 nm (a, d), a=5 nm (b, e), a=10 nm (c, f). Figures d, e, and f show the angular distributions of unit concentrations from the center of the nanoparticle.

In Fig. 5 shows the distribution of the concentration of polyampholyte units in a longitudinal electric field of different strengths E_0, taking into account entropy and field factors together in the presence of a dipole moment at link $\boldsymbol{p}$ of the macrochain. Both factors (entropy and Boltzmann) are taken into account together in expression (3'), the reference point is at the center of the nanoparticle, on its axis. Values of modeling parameters used in the calculation, E_0=10^5-3 10^6 V/cm, a=5 nm, b=c=2 nm, α=$5\cdot10^{-3}$ eV·nm, r_0=R+0.5 nm, R=b=c (radius of the cylinder and both hemispheres), a_0=0.5 nm (link length), T=300 K. Significant differences are observed in the angular dependences of the distribution of polyampholyte units from the case of polyelectrolyte. Firstly, there is a symmetry of the angular density distribution associated with the free reorientation of the dipole p of the chain link in the field. Secondly, the lowest density of units is formed in the middle section passing through the origin at the center of the nanoparticle. The shift in the van der Waals well localization zone is not as noticeable as in the case of a polyelectrolyte. The same applies to the parameter of the effective depth of the van der Waals well. An increase in the a_0T (1) parameter leads to a leveling of the amplitudes of the radial distributions for different angles – as in the case of a polyelectrolyte. In a weak electric field, the anisotropy of the distribution is not pronounced, and the radial dependence of the density is entirely formed by the van der Waals field. However, in a field of E_0 = 3 10^6 V/cm, a strong shift in the density of the chain monomers to both ends of the nanoparticle is observed. Stretching the spherocylinder, that is, lengthening its cylindrical part, leads to an increase in the degree of anisotropy in the distribution.

A change in the radius r_0 of the delta-functional well localization from r_0=2.3 nm to r_0=2.7 nm leads to a noticeable change in the radial-angular distributions of the polyampholyte density (3) both at the end sections, i.e. in the region of hemispheres and in the region of the cylindrical section. The contribution of the van der Waals interaction to the pattern of link distribution should be recognized as significant, because it is transformed when the parameter α, which determines the effective depth of the van der Waals well, changes. The product of temperature and the length of the macrochain link a_0T affects the difference in the amplitudes of the radial distributions in the cylindrical part and at the ends of the spherocylinder.

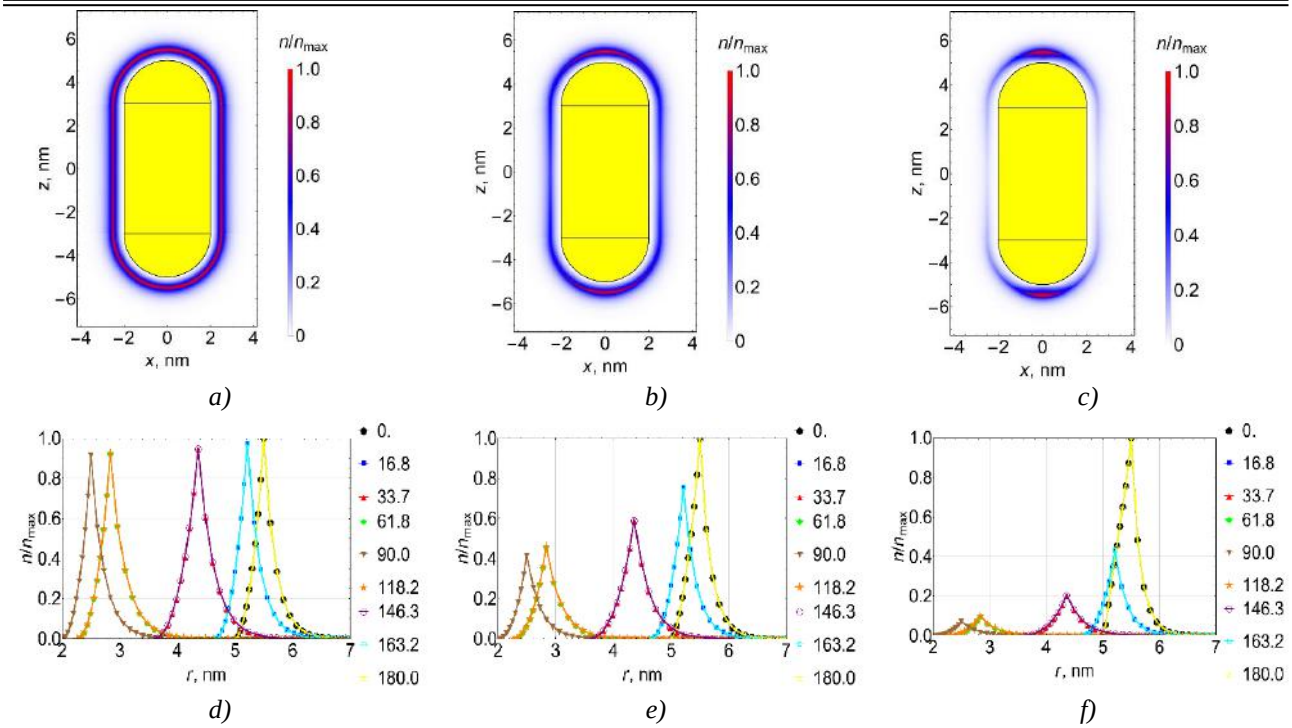

Fig.5. Concentration distribution of polyampholyte units (unit dipole moment 5 D) in a longitudinal electric field of strength E_0: 10^5 V/cm (a, d), 10^6 V/cm (b, e) 3 10^6 V/cm (c, f). Figures c, d show the angular distributions of unit concentrations from the center of the nanoparticle.

A relative increase in the length of the cylindrical part of the spherocylinder (Fig. 6) leads to the effect of depletion of the density of links in the central zone and enrichment of the density at the ends. A proportional change in the radii and length of the central part of the sphero-cylinder does not lead to the same noticeable effect of redistribution of monomer density, but gives a smoother differentiation.

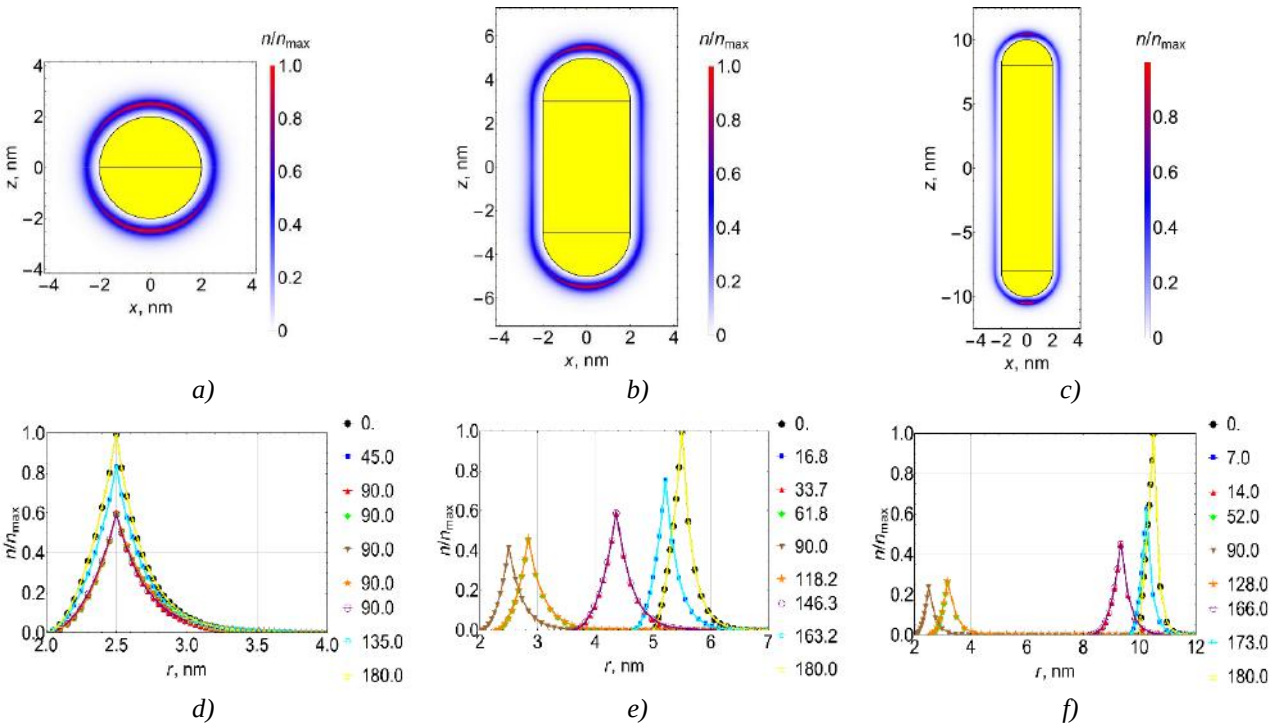

Fig.6. Distribution of the concentration of polyampholyte units (unit dipole moment 5 D) for different lengths of the cylindrical part of the nanorod b=c=2 nm: a=2 nm (a, d), a=5 nm (b, e) a=10 nm (c, f). Figures d, e and f show the angular distributions of unit concentrations from the center of the nanoparticle.

4. Initial data for molecular dynamics simulation, features of its implementation and processing

Molecular dynamics (MD) simulation of polypeptides on the surface of a gold nanorod was carried out using the NAMD 2.14 software package [25]. A model of a gold nanorod was obtained by cutting out a gold crystal: the central part of a cylindrical nanorod with a length of about 6 nm and a radius of 1.5 nm, and two hemispheres with a radius of 1.5 nm were located at the ends. During the MD simulation, the atoms of the nanorod remained fixed.

Three generally neutral polyampholytic polypeptides were considered:

1) polypeptide **P1**, consisting of 600 amino acid residues with 480 Ala (A) units with evenly distributed 60 Asp units (D, charge -1*e*) and 60 Arg units (R, charge +1*e*) – $(A_2DA_4RA_2)_{60}$;

2) polypeptide **P2**, consisting of 980 amino acid residues with 784 Ala units with evenly distributed 49 pairs of Asp units and 49 pairs of Arg units– $(A_4R_2A_8D_2A_4)_{49}$;

3) polypeptide **P3**, consisting of 988 amino acid residues with 880 Ala units with evenly distributed 27 pairs of Asp units and 27 pairs of Arg units– $A_8(A_8D_2A_{16}R_2A_8)_{27}A_8$.

Three uniformly negatively charged polypeptides consisting of 800 amino acid residues were also considered:

4) polypeptide **P4** (total macrochain charge -40*e*), consisting of 760 Ala units with 40 Asp units evenly distributed– $(A_{10}DA_9)_{40}$;

5) polypeptide **P5** (total macrochain charge -80*e*), consisting of 720 Ala units with 80 Asp units evenly distributed– $(A_5DA_4)_{80}$;

6) polypeptide **P6** (total macrochain charge -160*e*), consisting of 640 Ala units with 160 Asp units evenly distributed– $(A_2DA_2)_{160}$.

For polypeptides, the CHARMM36 force field was used [26-27]. Noncovalent interactions with a gold nanospheroid were described by the Lennard-Jones potential parameterized in [28], which is widely used in studying the adsorption of molecules on the surface of a gold nanoparticle [29–33]. The van der Waals potential was cut off at 1.2 nm using a smoothing function between 1.0 and 1.2 nm. Electrostatic interactions were calculated directly at a distance of 1.2 nm, and at a larger distance the particle-mesh Ewald method (PME) [34] was used with a grid step of 0.11 nm. The entire nanosystem was placed in a cube with 24 nm edges filled with TIP3P water molecules [35]. To control the obtaining of equilibrium conformations, the change in the root mean square distance between polypeptide atoms in different conformations (RMSD) was monitored. MD simulation was carried out at a constant temperature at 900 K with a subsequent decrease to 300 K. The length of the time trajectory reached 20 ns.

To obtain starting conformations, MD simulation of generally neutral polyampholytic polypeptides (P1-P3) was performed on the neutral surface of a gold nanorod, and to obtain starting conformations of negatively charged polypeptides (numbered P4-P5), MD simulation was performed on the positively charged surface of gold nanorod, in which each surface atom had a partial charge equal to +0.1*e*. In all cases, conformational structures were obtained in which the macrochain completely enveloped the nanorod. Three starting conformations were obtained for each polypeptide considered, which were used as starting ones in modeling on the surface of a longitudinally polarized nanorod.

In the case of longitudinal polarization, the cylindrical part of the metal nanorod remains neutral. Therefore, the local electric field was set through a change in the charges of atoms on the surface of spherical hemispheres located at the ends of the nanorod, where the induced charges were distributed according to the cosine law between the normal to the surface and the direction of the electric field, codirectional with the axis of the nanorod [23]. The following values of the induced dipole moment of the longitudinally polarized nanorod were obtained: $p_{0.25} \approx 11.5$, $p_{0.5} \approx 23$, and $p_{1.0} \approx 46$ kDa. At these values of the dipole moment of the nanorod, the atoms at the pole of its positively charged hemisphere had partial charges: +0.25*e*, +0.5*e* and +1*e*, respectively.

Based on the results of MD simulation for all obtained conformations, the radial distributions of the average density of polypeptide atoms on the surface of the terminal hemispheres of the nanorod and in the middle of the central cylindrical part in a layer 2 nm wide relative to the nanorod axis, as well as the distributions of the linear density of polypeptide atoms along the nanorod axis, were calculated.

5. Results of MD simulation

5.1 Conformational structure of polyampholytic polypeptides on the surface of a longitudinally polarized spherocylinder

Figure 7a shows the conformational structure of polyampholytic polypeptide P2 obtained from MD simulations on the surface of an unpolarized gold nanorod. It can be seen that the macromolecular chain completely envelops the gold nanorod. Similar conformations have been obtained for other polyampholytic polypeptides. Figure 8 (curves 1) shows the radial distributions of the density of polypeptide atoms at the end of the simulation on the surface of a non-polarized neutral nanoparticle. Both in the terminal spherical part (Fig. 8a) of the nanorod and in its central cylindrical part (Fig. 2b), a characteristic distribution of the density of polypeptide atoms with a peak near the surface is formed.

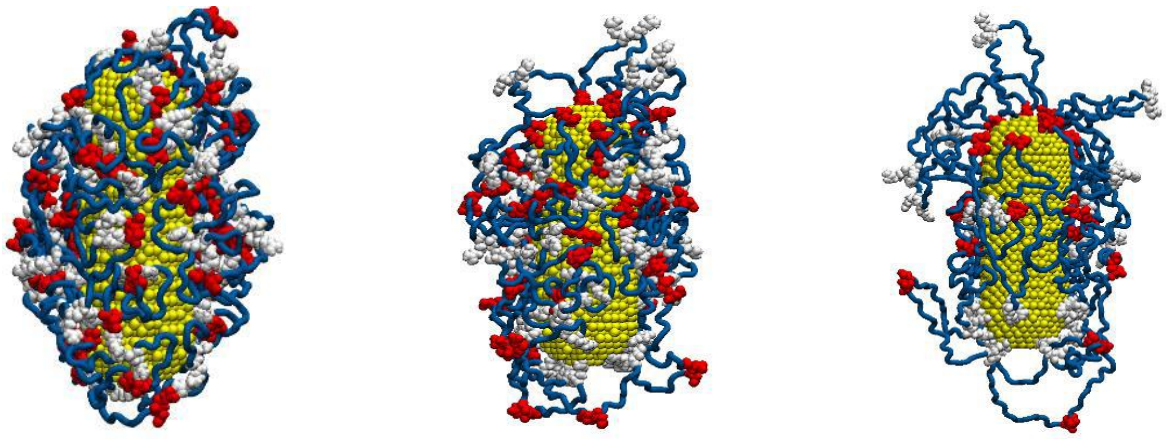

a) *b)* *c)*

Fig.7. Conformational structure of polypeptide P2 after MD simulation on an unpolarized (a) and polarized (b) gold nanorod with a dipole moment of $p_{0.5}$, as well as the conformation of polypeptide P3 (c) on a nanorod polarized with a dipole moment of $p_{1.0}$ (the dipole moment is directed from below - up, the blue tube is the Ala links, the Asp links are shown in red, and the Arg links are white).

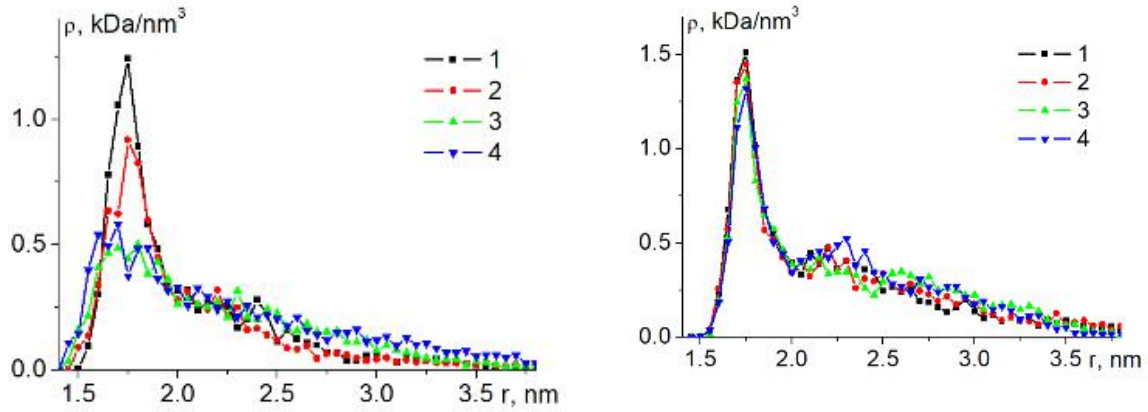

a) b)

Fig.8. Radial distributions of the atomic density of polypeptides P2 (a) and P3 (c) in the region of the upper (Fig. 7) terminal hemisphere (a) of the gold nanorod, as well as in the central region of the cylindrical part of the nanorod (b) at the end of MD simulation at different values of the dipole moment of the nanorod: 1 – 0, 2 - $p_{0.25}$, 3- $p_{0.5}$, 4 - $p_{1.0}$.

As the dipole moment of the longitudinally polarized nanorod increased, the conformational structure of the adsorbed polyampholyte macromolecules changed significantly (Figs. 7b and 7c). At the ends of the gold nanorod, due to the induced electric charges, repulsion of similarly charged units occurred in relation to the surface charge of the terminal hemispheres from the nanorod. This led to elongation of the loops of the polyampholyte macrochain and swelling of the polyampholyte edge at the ends of the nanorod. The radial

distributions of the atomic density of polyampholytic polypeptides obtained at the end of the MD simulation on the surface of a longitudinally polarized nanorod (Fig. 8a) show that as the dipole moment of the nanorod increases, there is a significant decrease in the radial distribution curves of the polypeptide atoms in the terminal spherical region of the nanorod. This decrease in the density of macrochain atoms indicates that the macromolecular edge at the ends of the nanorod swells significantly.

In addition, despite the fact that the central cylindrical part of the nanorod remained neutral, some of the charged units are displaced from it to the charged terminal hemispheres due to the rearrangement of the conformational structure of the polyampholyte at the ends of the longitudinally polarized nanorod. Therefore, in the central cylindrical part of the nanorod, a slight decrease in the radial distribution curves of the atomic density of polyampholytic polypeptides is observed as the dipole moment of the nanorod increases (Fig. 8b).

5.2 Conformational structure of uniformly charged polypeptides on the surface of a longitudinally polarized spherocylinder

In the case of MD simulation of uniformly charged polypeptides, as the dipole moment of the gold nanorod increased, the macrochain units gradually shifted towards the oppositely charged end of the nanorod. Figure 9a shows that when the dipole moment of the nanorod is equal to $p_{0.25}$, the lower negatively charged end of the nanorod is partially exposed, which in the starting conformation was completely enveloped by the P5 polypeptide. With a further increase in the dipole moment to $p_{0.5}$, the lower terminal hemisphere of the nanorod turned out to be completely exposed (Fig. 9b), and at $p_{1.0}$ the macrochain shifted even higher towards the positively charged end of the nanorod (Fig. 9c). Moreover, due to the fact that the central cylindrical part of the nanorod is neutral, the displacement of the charged macrochain after exposure of the lower terminal hemisphere is very weak. Most of the cylindrical part turns out to be covered with macrochain links, in contrast to the case of a polarized elongated gold nanospheroid [19, 21]. This displacement is caused by the displacement of the charged links of the macrochain to the oppositely charged terminal hemisphere, and this is prevented by the van der Waals forces of attraction to the cylindrical part and forces of an entropic nature [24].

This can be seen in the distributions of the linear density of atoms of the P5 polypeptide (Fig. 10a) along the axis of the nanorod depending on the value of its dipole moment. It can be seen that the greater the value of the dipole moment of the gold nanorod, the stronger the shift of the profile in the positive direction of the *z* axis, which coincides with the direction of the dipole moment of the nanorod.

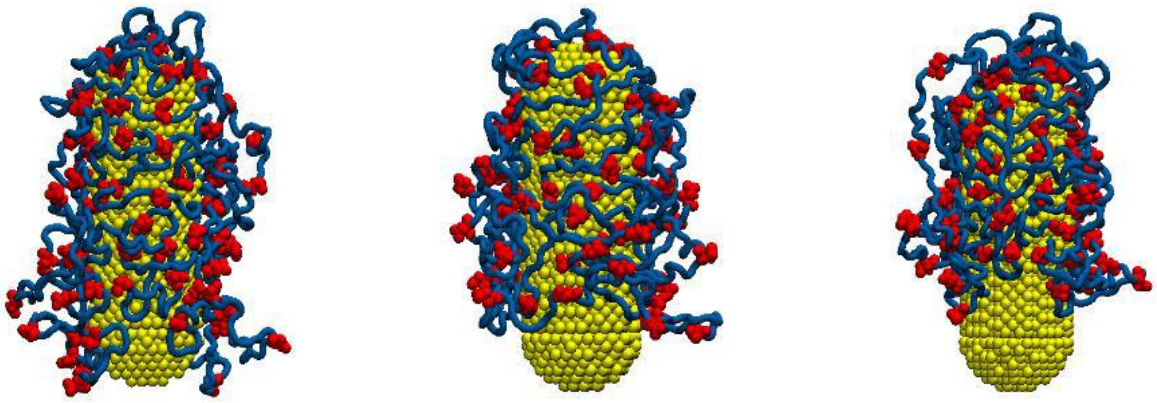

a) *b)* *c)*

Fig.9. Conformations of polypeptide P5 at the end of MD simulation on the surface of a longitudinally polarized gold nanorod (the dipole moment is directed upward) at different values of the dipole moment of the nanorod: $p_{0.25}$ (a), $p_{0.5}$ (b), $p_{.1.0}$ (c) (blue tube - Ala links, Asp links are shown in red).

In addition, in the upper (Fig. 9) positively charged spherical part of the nanorod, as its dipole moment increases, the macromolecular edge of the negatively charged macromolecule swells. This can be seen in the graphs of the radial distributions of the density of atoms of the P5 polypeptide (Fig. 10b) depending on the value of the dipole moment of the nanorod. As the dipole moment of the nanorod increases, a decrease in the radial density distribution curves of a uniformly charged polypeptide is observed (Fig. 10).

This swelling of the edge is due to the fact that as the dipole moment of the nanorod increases, an increasingly greater electrical charge is induced at its positive end, which leads to a displacement of the negative amino acid residues of the polypeptide there.

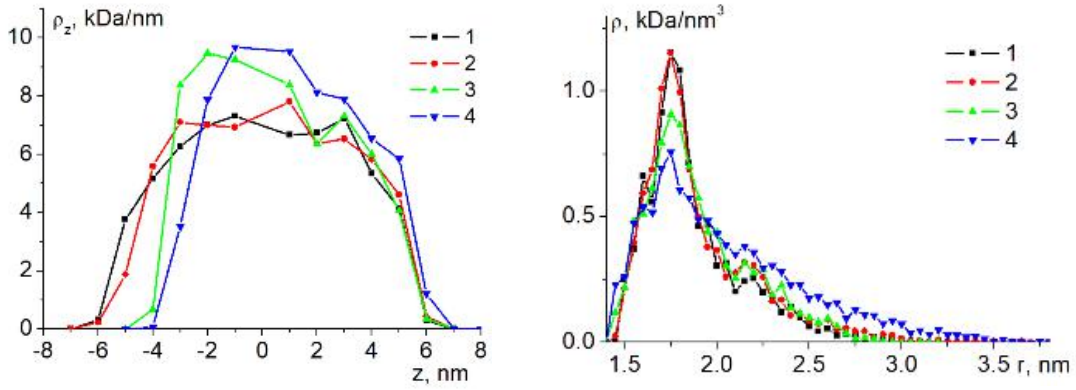

a) *b)*

Fig.10. Distributions of the linear density of atoms of polypeptide P5 (a) along the axis of the nanorod, as well as radial distributions of the density of atoms of polypeptide P5 (b) in the region of the upper (Fig. 9) terminal hemisphere at the end of MD simulation at different values of the dipole moment of the nanorod: 1 – 0, 2 - $p_{0.25}$, 3- $p_{0.5}$, 4 - $p_{1.0}$.

Negative charged amino acid residues Asp gradually fills most of the surface of the terminal positively charged hemisphere, displacing the neutral amino acid residues Ala located between them in the macrochain. And this leads to the formation of macrochain loops, which are formed only by fragments of neutral units, in contrast to the loops of polyampholytic polypeptides (Fig. 7b and 7c).

6. Conclusion

Thus, the work presents an analytical version of the mathematical model of the conformational structure of a polyampholyte and polyelectrolyte macromolecule formed on an elongated nanospheroid in a longitudinal electric field with approximation of the spherocylinder by an elongated spheroid when calculating the characteristics of the resulting field. This model, which takes into account the separated Boltzmann and entropy factors in the density distribution of units, makes it possible to describe the conformational changes of a polymer chain adsorbed on the surface of a cylindrical nanorod with spherical ends in an external electric field without a significant loss of accuracy using simpler expressions than those previously obtained in [18-19] for an elongated nanospheroid. Calculations of radial-angular distributions of unit density based on the proposed model showed significant differences in the response of the distributions to the action of an external electric field polarizing the spherocylinder for polyelectrolytes and polyampholytes. The independent molecular dynamics simulation carried out in the work, in turn, showed that on the surface of a longitudinally polarized gold nanorod, consisting of a central cylindrical part and terminal hemispherical parts, significant conformational changes occur in both generally neutral polyampholyte and uniformly charged macrochains.

Upon adsorption of polyampholyte macromolecules, a dumbbell-shaped macromolecular edge is formed, loose at the ends of the longitudinally polarized nanorod and dense in its central cylindrical part, which is generally similar to the polyampholyte edge on the surface of an elongated spheroidal gold nanoparticle polarized along the major axis. But at the same time, the dumbbell-shaped polyampholyte edge on the surface of a longitudinally polarized nanorod has clearer shapes associated with a clear division into a neutral uncharged cylindrical region and charged terminal hemispheres, in contrast to an elongated polarized gold nanospheroid [21], where the surface density of induced charges was equal to zero only at the equator.

In the case of uniformly negatively charged polypeptides adsorbed on the surface of a longitudinally polarized nanorod, the macromolecular edge gradually shifted to the positively charged hemisphere of the nanorod, swelling there due to the high concentration of charged units on the surface. But in contrast to an elongated spheroidal gold nanoparticle [19, 21], polarized along the major axis, most of the macrochain links remained on the extended neutral cylindrical part of the longitudinally polarized nanorod.

Thus, such control of the shape of the macromolecular edge of polyelectrolyte macromolecules on the surface of a gold nanorod polarized in the longitudinal direction under the influence of an external electric

field can find application in creating and improving the characteristics of sensitive elements of measuring nanoelectronics and nanomaterials, as well as in creating nanoprobes with controlled characteristics for biomedical applications.

Conflict of interest statement

The authors declare that they have no conflict of interest in relation to this research, whether financial, personal, authorship or otherwise, that could affect the research and its results presented in this paper.

CRediT author statement:

Kucherenko M.G.: Conceptualization, Methodology, Investigation, Writing - Original Draft; Kruchinin N.Yu.: Conceptualization, Methodology, Software, Investigation, Writing - Original Draft; Neyasov P.P.: Methodology, Software, Investigation, Writing - Original Draft.

The final manuscript was read and approved by all authors.

Acknowledgments

This work was supported by the Ministry of Science and Higher Education of the Russian Federation within the framework of project no. FSGU-2023-0003.

References

1 Lenjani S.V., Mayer M., Wang R., Dong Y., Fery A., Sommer J., Rossner C. (2022) Importance of electrostatic forces in supracolloidal self-assembly of polymer-functionalized gold nanorods. *J. Phys. Chem. C.*, 126, 14017 – 14025. DOI: 10.1021/acs.jpcc.2c04930.

2 Vedhanayagam M., Andra S., Muthalagu M., Sreeram K.J. (2022) Influence of functionalized gold nanorods on the structure of cytochrome –c: an effective bio-nanoconjugate for biomedical applications. *Inorganic Chemistry Communications*, 146, 110182. DOI: 10.1016/j.inoche.2022.110182.

3 Chakraborty K., Biswas A., Mishra S., Mallick A.M., Tripathi A., Jan S., Roy R.S. (2023) Harnessing peptide-functionalized multivalent gold nanorods for promoting enhanced gene silencing and managing breast cancer metastasis. *ACS Appl. Bio Mater.*, 6, 458–472. DOI: 10.1021/acsabm.2c00726.

4 Dong X., Yu P., Zhao J., Wu Y., Ali M., El-Sayed M.A., Wang J. (2023) Structural Dynamics of (RGD)4PGC peptides in solvated and au nanorod surface-bound forms examined by ultrafast 2d IR Spectroscopy. *J. Phys. Chem. C*, 127, 3532–3541. DOI: 10.1021/acs.jpcc.2c07830.

5 Wei W., Bai F., Fan H. (2019) Oriented gold nanorod arrays: self-assembly and optoelectronic applications. *Angewandte Chemie International Edition*, 58, 11956–11966. DOI: 10.1002/anie.201902620.

6 Halder K., Sengupta P., Chaki S., Saha R., Dasgupta S. (2023) Understanding conformational changes in human serum albumin and its interactions with gold nanorods: do flexible regions play a role in corona formation? *Langmuir*, 39, 1651–1664. DOI: 10.1021/acs.langmuir.2c03145.

7 Trofymchuk K., Kołątaj K., Glembockyte V., Zhu F., Acuna G.P., Liedl T., Tinnefeld P. (2023) Gold Nanorod DNA Origami Antennas for 3 Orders of Magnitude Fluorescence Enhancement in NIR. *ACS Nano*, 17, 1327–1334. DOI: 10.1021/acsnano.2c09577.

8 Han S., Wang J.T., Yavuz E., Zam A., Rouatbi N., Utami R.N., Liam-Or R., Griffiths A., Dickson W., Sosabowski J., Al-Jamal K.T. (2023) Spatiotemporal tracking of gold nanorods after intranasal administration for brain targeting. *Journal of Controlled Release*, 357, 606-619. DOI: 10.1016/j.jconrel.2023.04.022.

9 Pal S., Koneru J.K., Andreou C., Rakshit T., Rajasekhar V.K., Wlodarczyk M., Healey J.H., Kircher M.F., Mondal J. (2022) DNA-Functionalized Gold Nanorods for Perioperative Optical Imaging and Photothermal Therapy of Triple-Negative Breast Cancer. *ACS Appl. Nano Mater*., 5, 9159–9169. DOI: 10.1021/acsanm.2c01502.

10 Hosseinniya S., Rezayan A.H., Ghasemi F., Malekmohamadi M., Taheri R.A., Hosseini M., Alvandi H. (2023) Fabrication and evaluation of optical nanobiosensor based on localized surface plasmon resonance (LSPR) of gold nanorod for detection of CRP. *Analytica Chimica Acta*, 1237, 340580. DOI: 10.1016/j.aca.2022.340580.

11 Chang Y., Wang Q., Xu W., Huang X., Xu X., HanF.Y., Qiao R., Ediriweera G.R., Peng H., Fu C., Liu K., Whittaker A.K. (2022) Low-fouling gold nanorod theranostic agents enabled by a sulfoxide polymer coating. *Biomacromolecules*, 23, 3866–3874. DOI: 10.1021/acs.biomac.2c00696.

12 Zhao H., Jiang T., Yi L., Tang L. (2021) DNA sequences-mediated fine-tuning of nanostructures and their plasmonic properties over gold nanorods. *Optik*, 228, 166137. DOI: 10.1016/j.ijleo.2020.166137.

13 Li M., Lu D., You R., Shen H., Zhu L., Lin Q., Lu Y. (2022) Surface-enhanced Raman scattering biosensor based on self-assembled gold nanorod arrays for rapid and sensitive detection of tyrosinase. *J. Phys. Chem. C*, 126, 12651–12659. DOI: 10.1021/acs.jpcc.2c03408.

14 Kruchinin N.Yu., Kucherenko M.G. (2020) Molecular-Dynamics Simulation of Rearrangements in the Conformational Structure of Polyampholytic Macromolecules on the Surface of a Polarized Metal Nanoparticle. *Colloid Journal*, 82, 136-143. DOI: 10.1134/S1061933X20020088.

15 Kruchinin N.Yu., Kucherenko M.G. (2021) Rearrangements in the conformational structure of polyampholytic polypeptides on the surface of a uniformly charged and polarized nanowire: Molecular dynamics simulation. *Surfaces and Interfaces*, 27, 101517. DOI: 10.1016/j.surfin.2021.101517.

16 Kucherenko M.G., Kruchinin N.Yu., Neyasov P.P. (2022) Modeling of conformational changes of polyelectrolytes on the surface of a transversely polarized metal nanowire in an external electric field. *Eurasian Physical Technical Journal*, 19, 19-29. DOI: 10.31489/2022No2/19-29.

17 Kruchinin N.Yu., Kucherenko M.G. (2021) Molecular dynamics simulation of conformational rearrangements in polyelectrolyte macromolecules on the surface of a charged or polarized prolate spheroidal metal nanoparticle. *Colloid Journal*, 83, 591-604. DOI:10.1134/S1061933X21050070.

18 Kruchinin N.Yu., Kucherenko M.G. (2021) Modeling the conformational rearrangement of polyampholytes on the surface of a prolate spheroidal metal nanoparticle in alternating electric field. *High Energy Chemistry,* 55, 442-453. DOI:10.1134/S0018143921060084.

19 Kruchinin N.Yu., Kucherenko M.G. (2022) Molecular dynamics simulation of the conformational structure of uniform polypeptides on the surface of a polarized metal prolate nanospheroid with varying pH. *Russian Journal of Physical Chemistry A*, 96, 624-632. DOI:10.1134/S0036024422030141.

20 Kruchinin N.Y., Kucherenko M.G. (2022) Conformational changes of polyelectrolyte macromolecules on the surface of charged prolate metal nanospheroid in alternating electric field. *Polymer Science Series A*, 64, 240–254. DOI:10.1134/S0965545X2203004X.

21 Kruchinin N.Yu., Kucherenko M.G. (2022) Modeling of electrical induced conformational changes of macromolecules on the surface of metallic nanospheroids. *Materials Today: Proceedings*, 71, Part 1, 18-30. DOI:10.1016/j.matpr.2022.07.139.

22 Kruchinin N.Y., Kucherenko M.G. (2023) Rearrangements in the Conformational Structure of Polyelectrolytes on the Surface of a Flattened Metal Nanospheroid in an Alternating Electric Field. *Colloid Journal*, 85, 44-58. DOI:10.1134/S1061933X22600440.

23 Landau L.D., Pitaevskii L.P., Lifshitz E.M. (1984), *Electrodynamics of Continuous Media*, 2nd Edition, Elsevier Ltd., 460.

24 Grosberg A.Y., Khokhlov A.R. (1994) *Statistical Physics of Macromolecules*. AIP Press, New York. 347.

25 Phillips J.C., Braun R., Wang W., Gumbart J., Tajkhorshid E., Villa E., Chipot C., Skeel R.D., Kale L, Schulten K. (2005) Scalable molecular dynamics with NAMD. *J Comput Chem*., 26, 1781-1802. DOI:10.1002/jcc.20289.

26 MacKerell A.D. Jr., Bashford D., Bellott M., Dunbrack Jr. R.L., Evanseck J.D., Field M.J., Fischer S., Gao J., Guo H., Ha S., Joseph-McCarthy D., Kuchnir L., Kuczera K., Lau F.T.K., Mattos C., Michnick S., Ngo T., Nguyen D.T., Prodhom B., Reiher III W.E., Roux B., Schlenkrich M., Smith J.C., Stote R., Straub J., Watanabe M., Wiorkiewicz-Kuczera J., Yin D., Karplus M. (1998) All-atom empirical potential for molecular modeling and dynamics studies of proteins *J. Phys. Chem. B.*,102, 3586-3616. DOI:10.1021/jp973084f.

27 Huang, J., Rauscher, S., Nawrocki, G., Ran T., Feig M., de Groot B.L., Grubmüller H., MacKerell Jr. A.D. (2016) CHARMM36m: an improved force field for folded and intrinsically disordered proteins. *Nature Methods*, 14. 71-73. DOI: 10.1038/nmeth.4067.

28 Heinz H., Vaia R.A., Farmer B.L., Naik R.R. (2008) Accurate simulation of surfaces and interfaces of face-centered cubic metals using 12−6 and 9−6 Lennard-Jones potentials. *J. Phys. Chem. C.*, 112, 17281-17290. DOI: 10.1021/jp801931d.

29 Cappabianca R., De Angelis P., Cardellini A., Zhuang Y., Hernandez R. (2022) Assembling biocompatible polymers on gold nanoparticles: toward a rational design of particle shape by molecular dynamics. *ACS Omega*, 7, 42292-42303. DOI: 10.1021/acsomega.2c05218.

30 Wei X., Harazinska E., Zhao Y., Zhuang Y., Hernandez R. (2022) Thermal transport through polymer-linked gold nanoparticles. *The Journal of Physical Chemistry C*., 126, 18511-18519. DOI: 10.1021/acs.jpcc.2c05816.

31 Chew A.K., Pedersen J.A., Van Lehn R.C. (2022) Predicting the physicochemical properties and biological activities of monolayer-protected gold nanoparticles using simulation-derived descriptors. *ACS Nano*, 16, 6282-6292. DOI: 10.1021/acsnano.2c00301.

32 Jia H., Zhang Y., Zhang C., Ouyang M., Du S. (2023) Ligand–ligand-interaction-dominated self-assembly of gold nanoparticles at the oil/water interface: an atomic-scale simulation. *The Journal of Physical Chemistry B*, 127, 2258-2266. DOI:10.1021/acs.jpcb.2c07937.

33 Wang X., Ham S., Zhou W., Qiao R. (2023) Adsorption of rhodamine 6G and choline on gold electrodes: a molecular dynamics study. *Nanotechnology*, 34, 025501. DOI: 10.1088/1361-6528/ac973b.

34 Darden T., York D., Pedersen L. (1993) Particle mesh Ewald: An N·log(N) method for Ewald sums in large systems *J. Chem. Phys*., 98, 10089-10092. DOI: 10.1063/1.464397.

35 Jorgensen W.L., Chandrasekhar J., Madura J.D., Impey R.W., Klein M.L. (1983) Comparison of simple potential functions for simulating liquid water. *J. Chem. Phys*., 79, 926-935. DOI:10.1063/1.445869.

AUTHORS' INFORMATION

Kucherenko, Michael Gennadievich - Doctor of phys.-math. sciences, Professor, Director of the Center for Laser and Informational Biophysics, Orenburg State University, Orenburg, Russia; Scopus Author ID: 7003581468; ORCID iD: 0000-0001-8821 -2427, clibph@yandex.ru

Kruchinin, Nikita Yurevich - Doctor of phys.-math. sciences, Associate Professor, Department of radiophysics and electronics, Orenburg State University, Orenburg, Russia; Scopus Author ID: 35170029600; ORCID iD: 0000-0002-7960-3482; kruchinin_56@mail.ru

Neyasov, Petr P. – Master (Sci.), Head of the Laboratory of Nanostructure Synthesis, Orenburg State University, Orenburg, Russia; Scopus Author ID: 57222337052; ORCID iD: 0000-0002-7133-8741; nejapetr@yandex.ru

EURASIAN PHYSICAL TECHNICAL JOURNAL

2024, Volume 21, No. 3 (49)

https://doi.org/10.31489/2024No3/21-28

Received: 13/04/2024 Revised: 17/07/2024 Accepted: 17/09/2024 Published online: 30/09/2024
Research Article

UDC 537.534

OPTIMIZING THE INFLUENCE OF DOPING AND TEMPERATURE ON THE ELECTROPHYSICAL FEATURES OF P-N AND P-I-N JUNCTION STRUCTURES

Abdullayev J.SH.[1,2], Sapaev I.B.[1,3]

[1] National Research University "TIIAME", Tashkent, Uzbekistan
[2] Tashkent International University, Tashkent, Uzbekistan
[3] Western Caspian University, Scientific researcher, Baku, Azerbaijan
*Corresponding authors: j.sh.abdullayev6@gmail.com

Abstract. *In this paper, we investigate the effects of doping and temperature (at 300 K and 400 K) on the characteristics of Silicon (Si) and Gallium Arsenide (GaAs) p-n and p-i-n homojunction structures, utilizing doping concentrations of* $p^+ = n^+ = 2 \cdot 10^{17}$ *and* $p = n = 10^{16}$ cm^{-3} *through numerical calculation and modeling. Furthermore, we have analyzed three different cases: A) p-n, B)* p^+*-n, and C) p-*n^+*, to examine their influence on the distributions of space charge, potential, electric field, minority charge carriers, and the I-U curve at 300 K. It can be seen from the results that in case A, the recombination process is not observed at a lower voltage in the symmetrical p-n junction compared to than case B and C asymmetrical p-n junction. The voltage-temperature characteristics of the prepared samples were then measured at a temperature of 300K. I-U curve at 300 K. Calibration of the Si p-n homojunction structures is performed using experimental data to validate the proposed model. With the help of this constructed complex model, the influence of various geometrical changes, such as the radial p-n transition, on electrophysical properties will be examined in our next work.*

Keywords: Space charge density, doping concentration, modeling, calibration, optimization.

1. Introduction

In today's world, there is a growing demand for electronic devices that are integral to our daily lives. This surge in demand underscores the necessity for semiconductor electronic devices, prompting extensive scientific exploration in this field. Despite this demand, the outcomes of both theoretical and practical scientific investigations often fall short of meeting expectations.

Over five decades ago, scientific research delved into the initial p-n junction structures [1], yet several issues remain unresolved. Subsequent studies have theoretically examined the charge distribution within these junctions [2], though temperature variations have not been fully explored. Recombination mechanisms have been inferred solely from volt-ampere characteristics, neglecting by coordinate distribution of recombination rates [3]. Various devices, including solar cells [4], thermos sensors [5], diodes [6], and transistors [7], utilize p-n junction structures, while p-i-n junctions prove more effective for photodiodes and LEDs.

The characteristics and performance of p-i-n and p-n junction diodes are intricately tied to carrier behavior within the junction formed at the interface between p-type and n-type materials. These junctions serve as fundamental building blocks for various devices, with analysis techniques applicable to broader electronic problems. The kinetic processes of electrons and holes at p-n and p-i-n junctions are elucidated through two mechanisms: drift-diffusion and recombination-generation. The ideality factor, theoretically

ranging from 1 to 2, distinguishes between these mechanisms [8]. However, experimental data often indicate ideality factors exceeding 2 [9]. This study aims to explore the relationship between forward voltage and the ideality factor across different thicknesses of the i-layer. By modeling and analyzing the electrophysical properties of these junctions, semiconductor electronic devices can operate optimally with minimal energy consumption. Furthermore, such modeling enables understanding of quantum effects as semiconductor devices scale down from micro to nanoscale, facilitating analysis of external influences on optimal operational modes. Utilizing software platforms such as Synopsys Centaurus Device [10], Keysight ADS [11], SPICE [12], COMSOL Multiphysics [13], MATLAB [14], SCAPS1D [15], Numerical [16], and others addresses this need, facilitating comprehensive modeling of semiconductor electronic devices.

In this work, we study and simulate semiconductor p-n and p-i-n junctions based on GaAs and Si. Our research aims to understand the mechanisms that control current transport and the physical distribution of electrons within these junctions. Building upon these considerations, this work model p-n and p-i-n junction structures based on Si and GaAs under different forward voltages, doping concentrations, and temperatures. Section 2 discusses material and geometrical parameters, along with methodologies employed. Section 3 presents our model's results, and Section 4 summarizes our findings

2. Experimental measurements vs. device simulations

2.1 Theory and material parameters

The current mechanism in p-n or p-i-n junction semiconductor structures often involves the use of five fundamental expressions. These expressions play a decisive role in determining the distribution of the electric field and potential, which are derived from the Poisson equation (1). To perform this analysis, it is important to establish the charge distribution, usually represented by the concentration distribution.

$$\frac{dE(x)}{dx} = -\frac{d^2\varphi(x)}{dx^2} = \frac{q}{\varepsilon\varepsilon_0}(p - n + N_D - N_A) \tag{1}$$

From this expression, by substituting the electric field and potential distributions found when solving the differential equation into expressions (2) and (3), we derive expression (4) for the relationship between current and voltage for an ideal diode.

$$\frac{\partial n}{\partial t} = G_{net,n} - R_{net,n} + \frac{1}{q}\cdot\Delta J_n \tag{2a}$$

$$\frac{\partial p}{\partial t} = G_{net,p} - R_{net,p} - \frac{1}{q}\cdot\Delta J_p \tag{2b}$$

Equations (2a) and (2b), which detail the behavior of excess carriers within a semiconductor volume for electrons and holes, respectively, arising from phenomena such as generation, recombination, drift, and diffusion, are referred to as continuity equations.

$$J_n = J_{n,drift} + J_{n,diff} = q(n\mu_n E + D_n\frac{dn}{dx}) \tag{3a}$$

$$J_p = J_{p,drift} + J_{p,diff} = q(p\mu_p E - D_p\frac{dp}{dx}) \tag{3b}$$

The transport equations for electrons and holes in semiconductors can be formulated to include both diffusion and drift terms, represented as equations (3a) and (3b) respectively.

$$J = J_0(\exp(\frac{qU_{p-n}}{mkT}) - 1) \tag{4}$$

Where J_0 represents the saturation current, m denotes the ideality factor. m=1 corresponds to the drift-diffusion current loading mechanism at the source, while m=2 signifies the generation-recombination current carrier mechanism. (4) We can observe the expression values in figures 4 and 5.

To find the electric field, we integrate the expression (1) and obtain the electric field expression under the following conditions. (5a) and (5d) represent the quasi-neutral (QNR) fields in p-type and n-type regions, respectively, where the field is zero. (5b) and (5c) denote the depleted fields in p-type and n-type regions, respectively, where the electric field behaves like a linear function of distance. The four fields are depicted in Figs. 2 a), b), c), and d), respectively, with varying values

$$E(-\infty < x \le x_p) = 0 \quad (5a)$$

$$E(x_p < x < 0) = \frac{qN_A}{\varepsilon\varepsilon_0}(x + x_p) \quad (5b)$$

$$E(0 < x < x_n) = -\frac{qN_D}{\varepsilon\varepsilon_0}(x - x_n) \quad (5c)$$

$$E(x_n \le x < \infty) = 0 \quad (5d)$$

Where is ε permittivity dielectric constant, which is ε=11.9 for Si, ε=13 for GaAs, the electric field helps in separating the majority carriers injected into the opposite semiconductor regions due to diffusion or drift. Electrons move towards the positively charged region (p-type) and holes move towards the negatively charged region (n-type). The magnitude and distribution of the electric field affect the rate of carrier recombination and hence the current flow across the junction. Understanding the electric field helps in analyzing the current-voltage characteristics and overall performance of semiconductor devices like diodes and transistors. In optoelectronic devices like photodiodes and solar cells, the electric field assists in the separation of photo-generated electron-hole pairs, contributing to the device's efficiency. Electro field distribution together with the injection process is also important.

Injection of majority carriers (electrons from the n-type region and holes from the p-type region) across the junction occurs when the p-n junction is under forward bias. Injection affects the behavior of the p-n junction diode. Under forward bias, injection leads to a reduction in the width of the depletion region, facilitating the movement of majority carriers and allowing current to flow easily. In contrast, under reverse bias, injection is suppressed, and the depletion region widens, preventing significant current flow. Injection in a p-n junction is essential for controlling current flow, determining device characteristics, influencing carrier recombination, and enabling the operation of various semiconductor devices, particularly diodes and optoelectronic devices. The change in concentration of electrons on the p-side and holes on the n-side the quasi-neutral (QNR) fields expressed as:

$$\Delta n_p(x) = n_p(x) - n_{p0} = n_{p0}[\exp(\frac{qU_{p-n}}{kT}) - 1]\exp(\frac{x_p + x}{L_n}) \quad x < -x_p \quad (6a)$$

$$\Delta p_n(x) = p_n(x) - p_{n0} = p_{n0}[\exp(\frac{qU_{p-n}}{kT}) - 1]\exp(\frac{x_n - x}{L_p}) \quad x_n > x \quad (6b)$$

Where L_n, L_p are diffusion length electron and holes respectively, To calculate the various junction parameters it is important to define some concentration terms. On the p-side, let N_A be the concentration of the acceptors. If n_i is the carrier concentration, then the electron and hole concentrations on the p side are defined as $p_{p0}(-x_p < x < 0) = N_A$, $n_{p0}(-x_p < x < 0) = \frac{n_i^2}{N_A}$. Similarly, on the n-side, with donor concentration of N_D, the electron and hole concentration are as we move across the device is shown in Figure 3.

$$n_{n0}(0 < x < x_n) = N_D, \; p_{n0}(0 < x < x_n) = \frac{n_i^2}{N_D}.$$

$$\Delta n_p(x) = n_p(x) - n_{p0} = N_D[\exp(\frac{qU_{p-n}}{kT}) - 1] \quad x = -x_p \quad (7a)$$

$$\Delta p_n(x) = p_n(x) - p_{n0} = N_A[\exp(\frac{qU_{p-n}}{kT}) - 1] \quad x_n = x \quad (7b)$$

2.2 Device simulations

For the chosen model, geometric dimensions of a=10 μm, b=8 μm, and c=6 μm were selected. The following distinctions are made within the electrophysical models: the gap width varies with temperature [17], and the mobility of electrons and holes changes with temperature and concentration [18]. Additionally, Shockley-Read-Hall (SRH) recombination also varies with temperature and doping concentration [19].

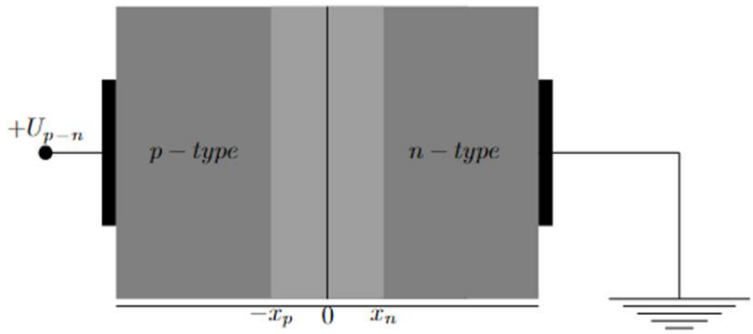

Fig. 1. This schematic depicts a 2D cross-section of our model planar p-n junction. The light grey area signifies the depletion region, while the dark grey area represents the quasi-neutral (QNR) fields in the p-type and n-type regions, respectively, based on both Si and GaAs materials.

The electric field distribution in this chosen model is illustrated in Figure 2, while the minority charge carriers are depicted in Figure 3. Additionally, the I-U characteristics are presented in Figures 4 and 5. The current-voltage *I-U* characteristic was studied at a voltage of +1 V for Si and +1.5 V for GaAs when the selected model was appropriately connected. The voltage supplied from the external source equals the p-n junction voltage. In this model, doping concentration is selected in three cases as follows: A) p-n, B) p^+-n, and C) p-n^+. After establishing the mathematical framework to describe a physical or engineering problem, such as through calculation geometry, the next step involves discretizing the problem domain into smaller elements using a finite-element grid. These elements break down the area of interest into manageable parts, often referred to as finite elements, with specific properties and behaviors. Each finite element grid node represents a point within the problem domain where the solution to the problem is evaluated or approximated. The solution typically involves determining scalar or vector fields, which represent physical quantities or properties of interest, at these nodes. Interpolation methods play a crucial role in finite-element analysis, allowing the estimation of values not only at the grid nodes but also at any point within the computational domain. This means that the behavior of the investigated function can be approximated or extrapolated at arbitrary locations, providing a comprehensive understanding of the system's behavior beyond the discrete grid points.

2.3 Experimental measurements

To calibrate and verify the theoretical and modeling analytical data presented above, an experimental sample was taken. In this case, an epitaxial layer of n-type silicon doped with Boron with a thickness of 30 μm and a concentration of $5 \cdot 10^{15}$ cm^{-3} is placed on a p-type silicon substrate doped with Phosphorus with a thickness of 280 μm and a concentration of $3 \cdot 10^{16}$ cm^{-3} grown and prepared based on the resulting silicon p-n structure. The experimental sample was prepared by depositing an aluminum layer on the contacts using the thermal sputtering method under vacuum conditions. The voltage-temperature characteristics of the prepared samples were then measured at a temperature of 300K. I-U curve at 300 K. Calibration of the Si p-n homojunction structures is performed using experimental data to validate the proposed model. The current-voltage characteristics of the sample were measured using current sources Б5-46М and Б5-47М, with a voltage step of 0.05 V during the experiment. Voltage was measured with a universal voltmeter Щ301-1, and current with a universal electronic device Щ300. The results of the experiment and the model are depicted in Fig. 4, where the I-U curve was concurrently measured for the GaAs material in this model.

3. Results and discussion

3.1 Distributions by distance

The electric field is a crucial parameter in various applications. Studying the dependence of field distribution on external parameters is essential because the field and potential distributions play significant roles in thermal sensors and photosensors. It can be observed from the second picture that the electric field is zero in both the p-type and n-type quasi-neutral regions (QNRs), as indicated by equations (5a) and (5d) respectively. In three cases as follows: A) p-n, B) p^+-n, and C) p-n^+, According to expressions (5a) and (5d), the depleted fields in p-type and n-type regions behave as linear functions of the electric field distance.

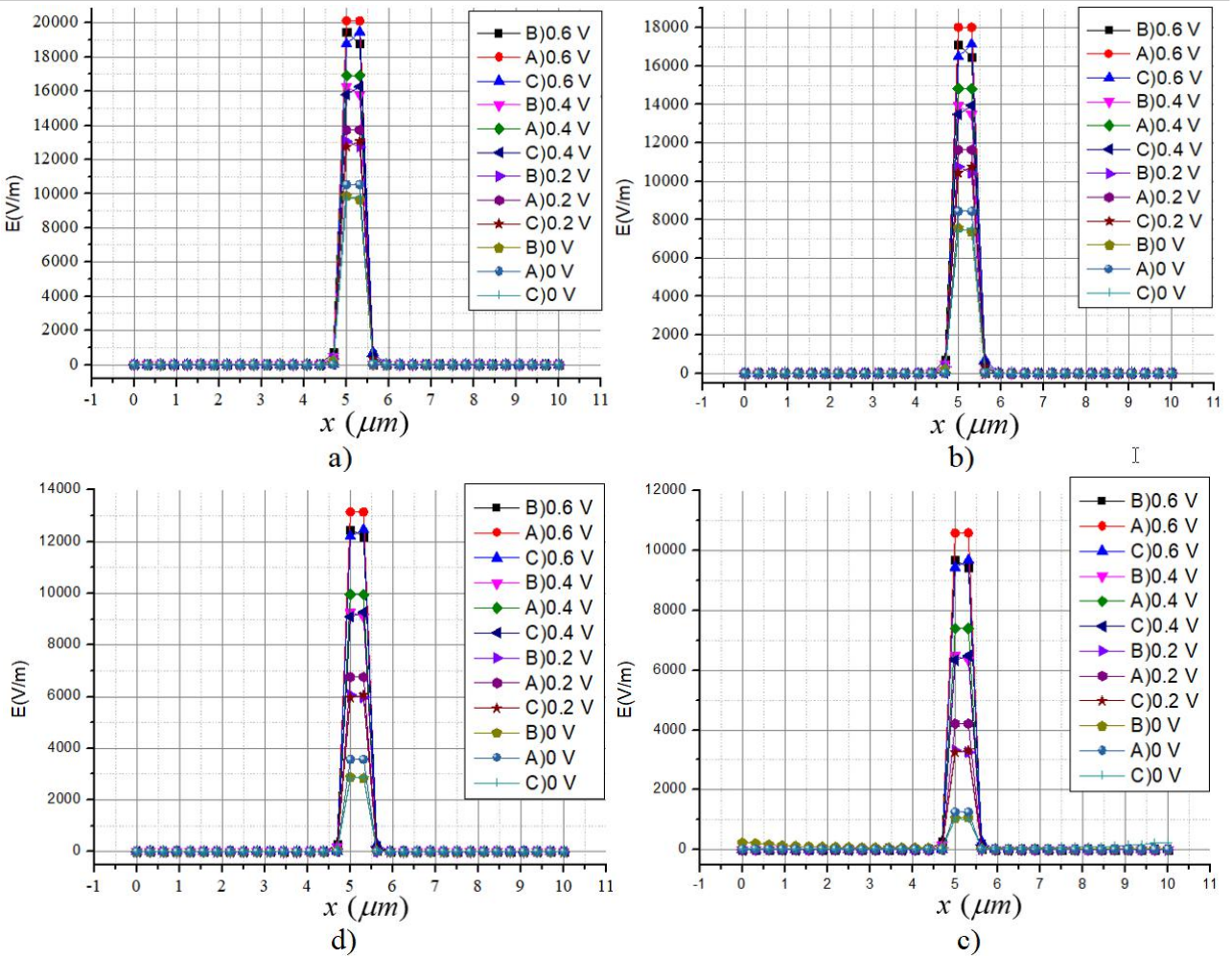

Fig.2. Electric field E(x) across a p-n junction a) 300 K b) 400 K based on GaAs, d)300 K c) 400 K based on Si.

The diffusion of minority charge carriers is called the injection process, and this injection depends on various external factors. Figure 3 shows the distance distribution of injected minor charge carriers. Adjusting the values of these fields alters the configurations shown in Figures 2 and 3. Moreover, at elevated temperatures, the field diminishes, reflecting characteristics specific to Si and GaAs. In Figure 3, it is evident that there is a close correspondence between the theoretical (7a), 7b) predictions and the outcomes generated by our model. This alignment highlights the robustness and accuracy of our model in capturing the underlying principles elucidated by the theoretical framework. It is assumed to be derived using the same process for electron density in p-QNR. Minority holes density in n-QNR, Minority electron density in p-QNR. Minority charge density dependent on voltage both Si and GaAs. The potential barrier is 0.82V for Si and 1.27V for GaAs.

3.2 Current-voltage characteristics

In this section, we delve into the classification and VAX results yielded by our innovative new model. Figure 4 shows a) the experiment and our new model in one graph for calibration, and b) VAX when our new model is used on GaAs material. Results can be seen to match with high accuracy.

The analysis of Figure 5 reveals qualitative homogeneity but quantitative disparities in the current transfer mechanism between cases A) and C), while case B) displays noticeable deviations in both qualitative and quantitative traits. Specifically, in case B), the drift-diffusion mechanism remains consistent up to the specified direct switching voltage for both Si and GaAs materials.

Figure 4 illustrates the semi-log current-voltage (I-V) characteristics for a p-n junction based on GaAs (a) and Si (b) materials, showcasing different forward voltage scenarios: A) p-n, B) p^+-n, and C) p-n^+.

In Figure 5a, it's evident that for cases A) and B), recombination predominates from a voltage delay of 0.2 V to 0.9 V in GaAs. Subsequently, from 0.9 V to 1.2 V, the drift-diffusion mechanism takes precedence.

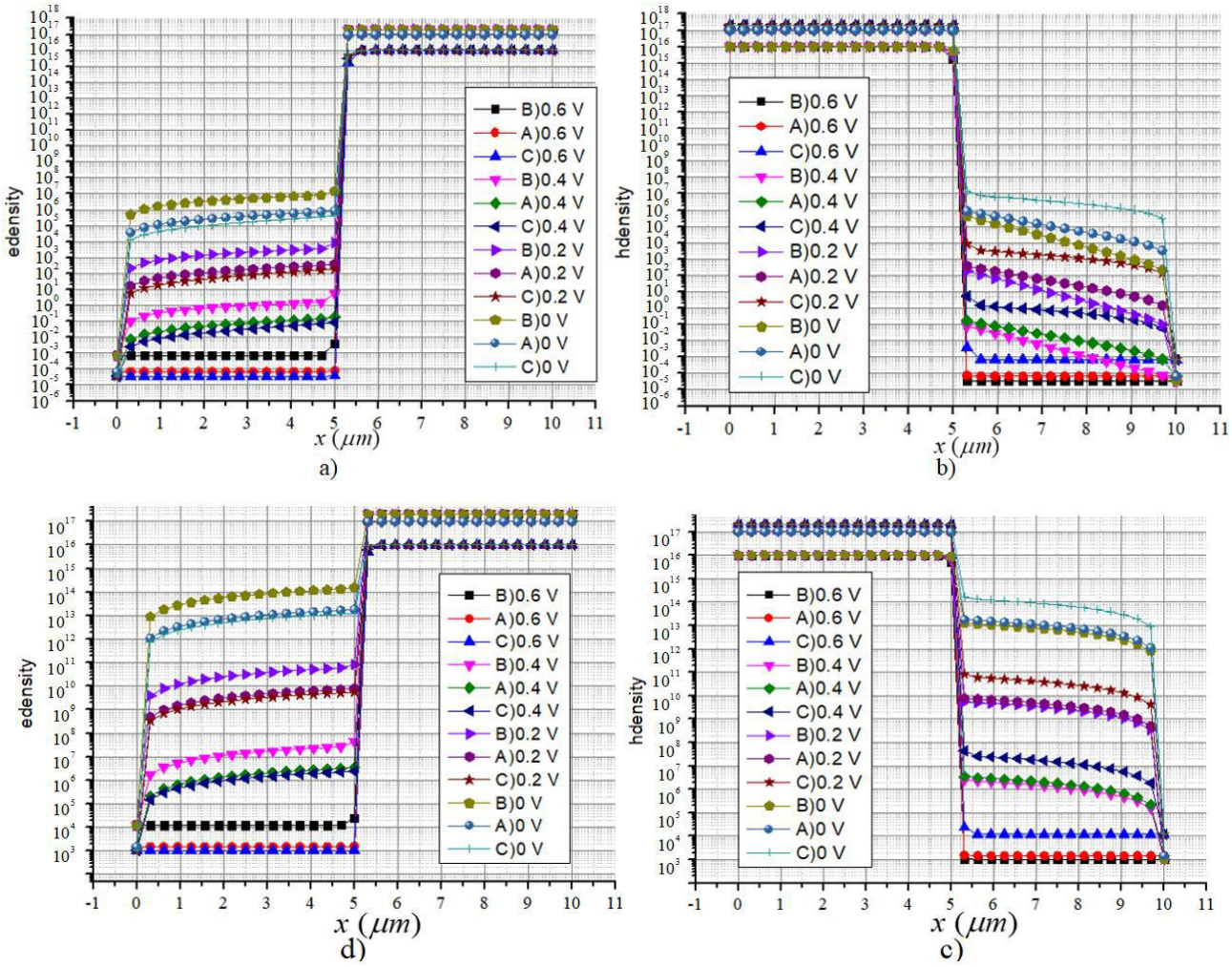

Fig.3. a) minority electrons density in n-QNR, b) minority holes density in p-QNR based on GaAs, a) minority holes density in n-QNR, b) minority electron density in p-QNR based on Si at 300 K at different voltage.

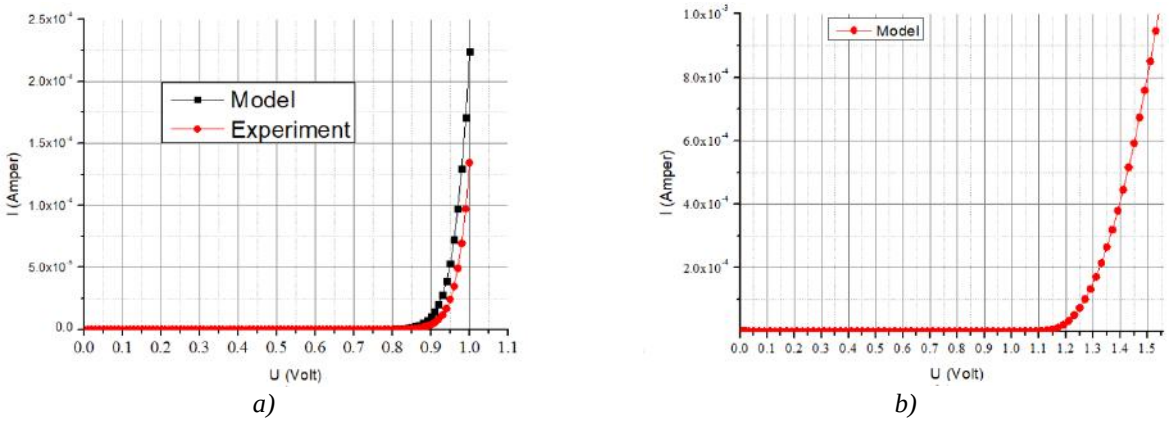

Fig. 4. Current-voltage characteristics for a p-n junction based on a) GaAs, b) Si forward voltage (Volts).

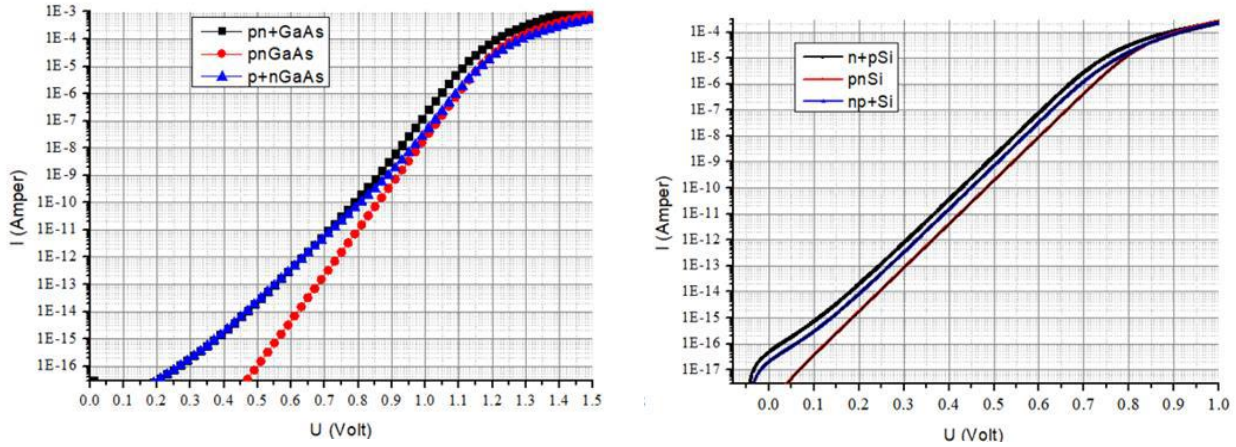

a) *b)*

Fig. 5. Semi-logarithmic current-voltage characteristics for a p-n junction based on a) GaAs, b) Si forward voltage (Volts).

Beyond 1.2 V, series resistance values and high injection processes are observable, explained by recombination, where minority charge carriers migrate from the emitter to the base region. Furthermore, Figure 5 illustrates that GaAs exhibit higher series resistance and demonstrate more pronounced injection phenomena at higher voltages compared to Si material. At low voltages, the slope often reflects the recombination mechanism. This is because, at lower forward biases, recombination within the depletion region or through defect states may dominate the current. At high voltages, the slope typically represents the drift-diffusion mechanism. Here, the current is mainly driven by the drift and diffusion of carriers across the junction, and the exponential behavior of the I-V curve is more apparent. In Figures 5a) and b), if the slopes at low and high voltages differ, it suggests a transition from one dominant mechanism to another as the applied voltage increases. This transition can be key in understanding the behavior of the junction under different electrical conditions.

4. Conclusion

In summary, the electric field in a p-n junction plays a fundamental role in its operation, influencing carrier transport, device characteristics, and overall device performance. Our new model has been successfully calibrated with experimental results, revealing that the electric field value is inversely proportional to temperature in both Si and GaAs materials. in this paper demonstrates a strong alignment between the theory and our model. In figure 3 demonstrates a strong alignment between the theory and our model by minority charge density. When analyzing the I-U curve in these three cases A) p-n, B) p^+-n, and C) p-n^+, it was shown that in cases A) the correct connection from the recombination mechanism to the drift-diffusion mechanism prevails in Si and GaAs, respectively, at the values of 0-1 Volt and 0-1.5 Volt.

Conflict of interest statement

The authors declare that they have no conflict of interest in relation to this research, whether financial, personal, authorship or otherwise, that could affect the research and its results presented in this paper.

CRediT author statement: Abdullayev J.Sh.: Conceptualization, Data Curation, Writing Original Draft, Methodology, Investigation: Sapaev I.B.: Writing Review & Editing, Supervision.
The final manuscript was read and approved by all authors.

References

1 Shockley W. (1949) The Theory of p-n Junctions in Semiconductors and p-n Junction Transistors. *Bell System Technical Journal*, 28(3), 435–489. DOI: 10.1002/j.1538-7305.1949.tb03645.x.

2 Takeuchi D., Makino T., Kato H., Okushi H., Yamasaki S. (2011) Electron emission from diamond p-i-n junction diode with heavily P-doped n+ top layer. *Physica Status Solidi* (a), 208(9), 2073–2078. DOI:10.1002/pssa.201100140.

3 Pohl P., Renner F.H., Eckardt M., Schwanhäußer A., Friedrich A., Yüksekdag Ö., Gossard A. C. (2003) Enhanced recombination tunneling in GaAs pn junctions containing low-temperature-grown-GaAs and ErAs layers. *Applied Physics Letters*, 83(19), 4035-4037. DOI: 10.1063/1.1625108.

4 Goktas N.I., Wilson P., Ghukasyan A., Wagner D., McNamee S., LaPierre R.R. (2018) Nanowires for energy: A review. *Appl. Phys. Rev.*, 5 (4), 041305. DOI: 10.1063/1.5054842.

5 Qiang Zeng, Na Meng, Yulong Ma, Han Gu, Jing Zhang, Qingzhu Wei, Yawei Kuang, Xifeng Yang, Yushen Liu (2018) Two-Dimensional Modeling of Silicon Nanowires Radial Core-Shell Solar Cells. *Advances in Condensed Matter Physics*, 2018, 7203493. DOI: 10.1155/2018/7203493.

6 Shin J.C., Chanda D., Chern W., Yu K.J., Rogers J.A., Li X. (2012) Experimental Study of Design Parameters in Silicon Micropillar Array Solar Cells Produced by Soft Lithography and Metal-Assisted Chemical Etching. *IEEE Journal of Photovoltaics*, 2(2), 129–133. DOI: 10.1109/JPHOTOV.2011.2180894.

7 Pylypova O.V., Evtukh A.A., Parfenyuk P.V., Ivanov I.I., Korobchuk I.M., Havryliuk O.O., Semchuk O.Y. (2019) Electrical and optical properties of nanowires-based solar cell with radial p-n junction. *Opto-Electronics Review*, 27(2), 143–148. DOI: 10.1016/j.opelre.2019.05.003.

8 Jung J.-Y., Guo Z., Jee S.-W., Um H.-D., Park K.-T., Hyun M.S., Lee J.-H. (2010) A waferscale Si wire solar cell using radial and bulk p–n junctions. *Nanotechnology*, 21(44), 445303. DOI:10.1088/0957-4484/21/44/445303.

9 Prabhat B.N., Balamurugan K. (2021) Characteristics and Modeling of PN Junction Diode in Verilog-A Including Reverse Recovery. *Proceding of the IEEE 6th International Conference on Computing, Communication and Automation (ICCCA)*, Arad, Romania, 509 – 516. DOI: 10.1109/ICCCA52192.2021.9666261.

10 Khalid M., Raza W., Riaz S., Naseem S. (2015). Simulation and Analysis of Static and Dynamic Performance of Normally-off TIVJFET Using Sentaurus TCAD. *Materials Today: Proceedings*, 2(10), 5720–5725. DOI:10.1016/j.matpr.2015.11.117.

11 Kurbanov U., Zhumabaeva G., Dzhumanov S. (2024) New metal/superconductor-insulator transitions and their effect on high-T_C superconductivity in underdoped and optimally doped cuprates. *Eurasian Physical Technical Journal*, 21, 1(47), 21–27. DOI: 10.31489/2024No1/21-27.

12 Arefinia Z., Asgari A. (2015) Optical and electrical modeling of solar cells based on graphene/Si nanowires with radial p–i–n junctions. *Solar Energy Materials and Solar Cells*, 137, 146 – 153. DOI: 10.1016/j.solmat. 2015.01.032.

13 Ferreira, Gabriel M., Vítor Silva, Graça Minas, Susana O. Catarino (2022) Simulation Study of Vertical p–n Junction Photodiodes' Optical Performance According to CMOS Technology. *Applied Sciences*, 12, 5: 2580. DOI:10.3390/app12052580.

14 Abdullayev J.S., Sapaev, I. B. (2024) Optimization of The Influence of Temperature on The Electrical Distribution of Structures with Radial p-n Junction Structures. *East European Journal of Physics*, (3), 344-349. DOI:10.26565/2312-4334-2024-3-39.

15 Muhammed O.A., Danladi E., Boduku P.H., Tasiu J., Ahmad M.S., Usman N. (2021) Modeling and simulation of lead-free perovskite solar cell using SCAPS-1D. *East European Journal of Physics*, 2, 146-154.

16 Ali N.M., Allam N.K., Abdel Haleem A.M., Rafat N.H. (2014) Analytical modeling of the radial pn junction nanowire solar cells. *Journal of Applied Physics*, 116(2), 024308. DOI:10.1063/1.4886596.

17 Bal S.S., Basak A., Singh U.P. (2022) Numerical modeling and performance analysis of Sb-based tandem solar cell structure using SCAPS–1D. *Optical Materials*, 127, 112282.

18 Kelzenberg M.D., Boettcher S.W., Petykiewicz J.A., Turner-Evans D.B., Putnam M.C., Warren E.L., Atwater H.A. (2010). Erratum: Enhanced absorption and carrier collection in Si wire arrays for photovoltaic applications. *Nature Materials*, 9(4), 368–368. DOI:10.1038/nmat2727.

19 Shura M.W., Wagener V., Botha J.R., Wagener M C. (2012). Photoconduction spectroscopy of p-type GaSb films. *Physica B: Condensed Matter*., 407(10), 1656 – 1659. DOI: 10.1016/j.physb.2011.09.110.

AUTHORS' INFORMATION

Abdullayev, Jo`shqin Shakirovich – PhD, Senior Research, Senior Lecture, National Research University TIIAME, Tashkent, Uzbekistan; Scopus Author ID: 58258727900; ORCID iD:0000-0001-6110-6616; j.sh.abdullayev6@gmail.com

Sapaev, Ibrokhim Bayramdurdievich – PhD (Phys.), Associate professor, Head of the department «Physics and chemistry». National Research University TIIAME, Tashkent, Uzbekistan; Western Caspian University, Scientific researcher, Baku, Azerbaijan; Scopus Author ID: 56102062900; ORCID iD: 0000-0003-2365-1554; sapaevibrokhim@gmail.com

EURASIAN PHYSICAL TECHNICAL JOURNAL

2024, Volume 21, No. 3 (49)

https://doi.org/10.31489/2024No3/29-36

Received: 11/06/2024 Revised: 27/08/2024 Accepted: 13/09/2024 Published online: 30/09/2024

Research Article

UDC: 537.622.3:620.193.4:699.15

CORROSION BEHAVIOUR OF MAGNESIUM ALLOYS NZ30K AND NZ30K ALLOYED WITH SILVER IN THE MODEL SOLUTION OF THE OSTEOSYNTHESIS PROCESS

Greshta V.[1], Narivskyi O.[1,2], Dzhus A.[1], Vynar V.[3], Yar-Mukhamedova G.[4], Mukashev K.[5], Beissen N.[4], Mussabek G.[4], Imanbayeva A.[4,6*], Zelele D.[4], Atchibayev R.[4], Kemelzhanova A.[4]

[1] National University "Zaporizhzhya Polytechnic", Ukraine
[2] Ukrspetsmash LLC, Berdiansk, Ukraine
[3] Karpenko Institute of Physics and Mechanics of the National Academy of Sciences of Ukraine, Lviv, Ukraine
[4] Al-Farabi Kazakh National University, Almaty, Kazakhstan
[5] Energo University, Almaty, Kazakhstan
[6] Research Centre "KazAlfaTech LTD", Almaty, Kazakhstan
*Corresponding author: akmaral@physics.kz

Abstract. *The corrosion behaviour of magnesium alloys NZ30K and NZ30K alloyed with 0.1 wt.% silver in Ringer's Locke solution has been studied, since their components are not toxic to the human body and do not cause clinical complications in the treatment of bone fractures, and silver has antibacterial properties inherent in antibiotics. It has been found that the E_{cor} potential of the silver-alloyed NZ30K sample was -1.57V during the first 100 seconds of testing, but then it intensively shifted to the positive side to -1.54V within 512 seconds at a rate of 0.051 mV/s, which decreased to 0.014 mV/s after the next 1000 seconds, and a stationary value of the potential E_{cor} on the sample has been recorded. The sample to uniform general corrosion has been subjected, and the improvement of its potential E_{cor} during its corrosion study was due to the most intense selective dissolution of magnesium, which has the most negative value of the standard potential among the alloy components, and the enrichment of its surface with Zn, Nd, Zr, Ag, which have a positive value of the standard potential. This trend contributed to a decrease in the rate of general corrosion and made it impossible to develop local corrosion. The NZ30K alloy alloyed with 0.1 wt.% silver is recommended for further potentiodynamic and volumetric corrosion studies to justify its selection as a structural material for the production of biodegradable implants in osteosynthesis.*

Keywords: bioimplant, magnesium alloy NZ30K alloyed with silver, local corrosion, osteosynthesis

1. Introduction

The controlled corrosion behaviour of magnesium alloys supports the development of advanced biodegradable implants for surgical treatment in traumatology [1]. Magnesium is a very reactive metal and corrodes rapidly in body fluids because it is unable to form self-protective oxide films [2]. Magnesium alloys in the state of supply have low mechanical characteristics, which makes it impossible to produce biodegradable implants for surgery. Currently, two approaches are used to improve the mechanical, physical, chemical, and biological properties of magnesium implants, including various methods of magnesium alloying [3-5] and grinding the microstructure to ultrafine or nanoscale grain [6-8].

Al, Ca, Cu, Fe, Li, Mn, Ni, Sr, Y, Zn, Zr are most commonly used to alloy Mg, and rare earth elements are used to modify its structure [9,10]. Aluminium-containing alloys are most commonly used in the production of biodegradable implants because they have excellent casting properties, high strength, and good relative elongation [11]. However, the corrosion products of this alloy contain AlO_{23} oxide, which can contribute to Alzheimer's disease, muscle breakdown, and reduced osteosynthesis [12]. The magnesium alloy NZ30K, unlike Al-containing alloys based on Al-Ca, Al-Zn, and Al-Li [13], does not have such disadvantages. In addition, the mechanical properties of NZ30K magnesium alloy have high performance for the production of biodegradable implants, since their yield strength (140 MPa) [14] is higher than that of tubular bones (120 MPa) [15]. At the same time, the alloying of NZ30K alloy with silver in the amount of 0.1 wt. % increased its temporary tensile strength (σ_B) by 8.6 and relative elongation by 63.9% [16]. In addition, it has antibacterial properties characteristic of antibiotics [17], but long-term (6 weeks) corrosion tests of samples in a solution of helofusin (an artificial blood substitute) contributed to its reduction by 22.9% [16]. At the same time, after prolonged corrosion tests of the alloy, this figure was 205 MPa [16], which is significantly higher than the strength of tubular bones [15], and the presence of silver in the alloy gives it antibacterial properties [17]. If the corrosion test results of silver-alloyed NZ30K alloy are satisfactory, it can be recommended for the manufacture of biodegradable implants and clinical testing. Therefore, we studied the corrosion behaviour of this alloy in Ringer-Locke solution.

2. Research materials and methods

We studied samples of magnesium alloys NZ30K and NZ30K alloyed with silver in the amount of 0.1 wt.% smelted in an induction crucible furnace and subjected to aging [16]. The diameter of the samples was 12 and the length was 30 mm. Their chemical composition by the X-ray spectral method at the installation INKA ENERGY 350 has been determined (Table 1).

Table 1. Chemical composition of the studied samples.

Alloy	Content of chemical elements, wt. %				
	Mg	Zn	Zr	Nd	Ag
NZ30K	95.67	0.67	0.89	2.77	-
NZ30K + Ag	95.57	0.69	0.86	2.79	0.09

Corrosion tests of the samples in a Ringer-Locke solution (an aqueous solution of bi-distilled water with the following chemicals, in mg/l: NaCl – 9; $NaHCO_3$; $CaCl_2$; KCl по 0,2; $C_6H_{12}O_6$ – 1) at a temperature of 20±1°C has been carried out. The establishment of a stationary value of the corrosion potential E_{cor} on the tested samples on the PN-2MK-10A potentiostat in automatic mode has been recorded. The surface of corrosion damage on the samples after their testing in Ringer Locke's solution using an optical microscope MMR-2P has been examined.

3. Research results and discussion

According to the results of the corrosion test of the NZ30K alloy sample (Table 1) in a Ringer-Locke solution at 20°C, it has been found that its corrosion potential E_{cor} slowly shifted to the positive side from -1.579 to -1.576V during 1400 seconds of testing (Fig. 1, curve 1). Thus, the rate of this process was 0.0021 mV/s. Most likely, this trend is due to the formation of a magnesium hydroxide precipitate coating on the alloy surface. After 1400 seconds of exposure of the sample to the test solution, a shift of the potential E_{cor} in the negative direction by about 2 mV within 100 seconds and a shift of its value in the opposite direction with the same intensity have been observed. After that, during 200 seconds of testing, the steady-state value of this potential at -1.575 V has been recorded (Fig. 1, curve 1). The characteristic small fluctuation of the potential E_{cor} during the establishment of its steady-state value is most likely due to the delamination of the magnesium hydroxide precipitate coating on the surface of the sample in the vicinity of corrosion ulcers and other corrosion damage formed near intermetallic compounds, which were identified in [16]. This is consistent with the data from [18-20] on the nucleation and growth of pitting in the vicinity of inclusions in passivated steels and alloys.

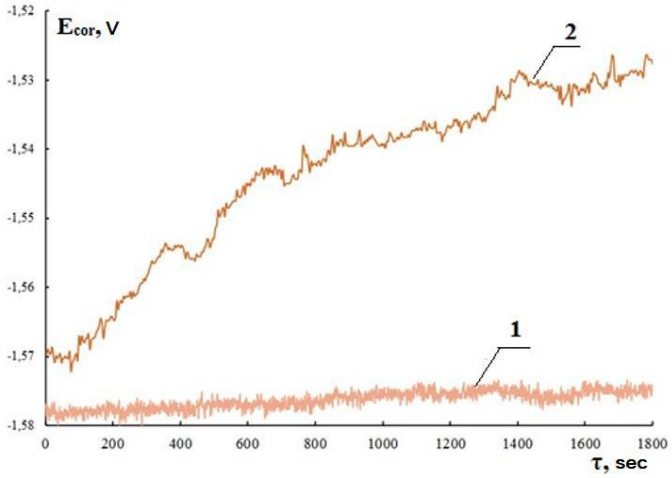

Fig.1. Dependence between the corrosion potential E_{cor} of NZ30K alloy (1) and NZ30K alloy alloyed with 0.1 wt. % silver (2) on the time of corrosion tests (τ) of the sample in Ringer-Locke solution at a temperature of 20° C.

It has been found that the sample subjected the greatest corrosion damage in the peripheral areas, i.e., in the places of the greatest plastic deformation of the alloy and the number of microdefects on its surface associated with the casting technology (Fig. 2, a).

a) *b)*

Fig.2. Corrosion damage on the end surface of NZ30K alloy (a) and silver alloyed NZ30K (b) samples after corrosion tests in Ringer-Locke solution.

These places are most often the focus of the origin and growth of local corrosion damage in chloride-containing media, such as Ringer-Locke solution. In particular, it has been found that the area of local corrosion damage on the end surface of the cylindrical specimen was 8.78 mm^2, which is 17.5% of the area of the end surface of the cylindrical specimen (Table 2).

Table 2. Area of corrosion damage on the end surfaces of the tested samples

No.	Sample	Corrosion damage area, mm^2	% of the end surface area of the sample
1	NZ30K alloy	8.78	17.5
2	NZ30K alloy additionally alloyed with Ag	8.12	16.24

Note: total end surface area of the sample is 50.24 mm^2.

About 90% of the local corrosion damage at the intersection of the cylindrical and flat surfaces of the sample has been recorded. In general, its cylindrical surface to intense local corrosion in the form of pitting and deep corrosion ulcers has been subjected (Fig. 3, a). This type of corrosion damage is typical for passivated steels and alloys in chloride-containing media [20]. Zirconium and zinc contribute to the formation of a dense oxide film on the surface of the magnesium alloy NZ30K, which can be locally damaged by chloride ions in the vicinity of intermetallic inclusions found in the alloy [16]. Such areas on the surface of steels and alloys are the most likely centres of pitting nucleation and growth observed on the surface of the NZ30K alloy sample (Fig. 3, a). Summarizing the above, it can be noted that NZ30K alloy under intensive pitting in a Ringer-Locke solution with active hydrogen release, so it cannot be used for the production of biodegradable implants without improving its resistance to local corrosion. Alloying NZ30K alloy with silver in the amount of 0.1 wt.% significantly changed its corrosion behaviour.

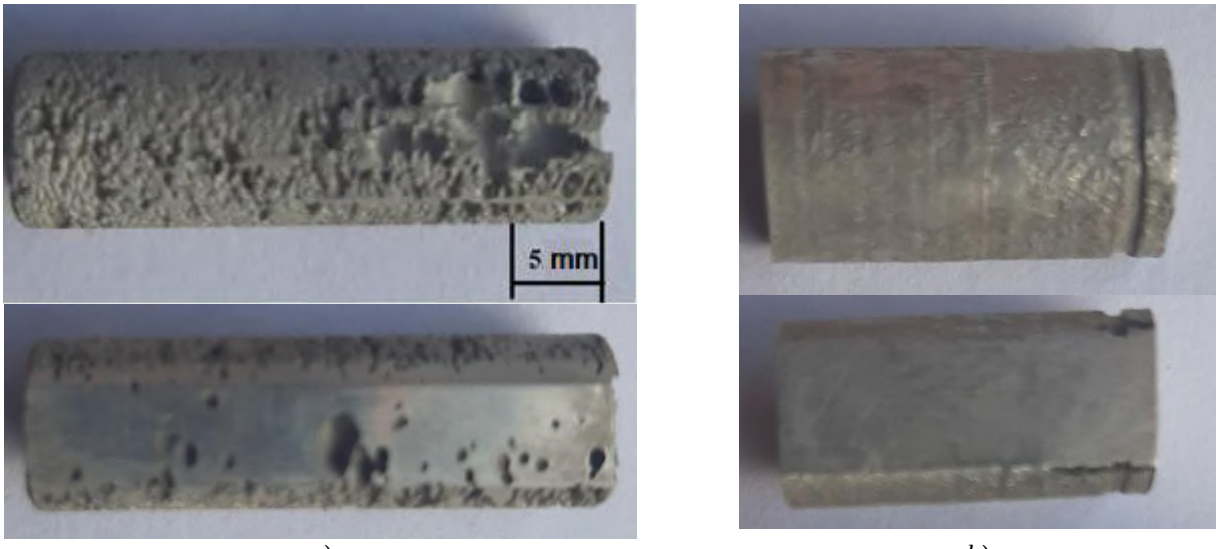

a) *b)*

Fig.3. Corrosion damage on the cylindrical surface of NZ30K alloy (a) and silver-alloyed NZ30K (b) samples after corrosion tests in Ringer-Locke solution.

In particular, according to the results of a corrosion study of a sample made of NZ30K alloy alloyed with Ag in Ringer-Locke solution, it has been found that its corrosion potential E_{cor} after immersion in the solution was ~ -1.57 V (Fig. 1, curve 2) and remained practically unchanged for 100 seconds (points 1-4 of Table 3).

However, in the interval from 100 to 612 seconds of testing, it shifted intensively to the positive side to -1.54432 V (point 20 of Table 3). Thus, it turns out that the rate of shift of the potential E_{cor} in the positive direction was 0.051 mV/s. Then, in the interval from 612 to 1620 seconds, it decreased to 0.014 mV/s, and from 1620 to 1800 seconds of testing, the sample recorded a stationary value of the potential E_{cor} ~ -1.52 V. It turns out that the steady-state value of the potential E_{cor} of the NZ30K alloy alloyed with Ag was set from -1.5696 (point 1) to -1.52716 V (point 40 of Table 3) within 1800 seconds.

The characteristic features of establishing the stationary value of the potential E_{cor} of the NZ30K alloy alloyed with Ag in Ringer-Locke solution are due to the different intensity of dissolution of its components, which formed the microrelief of the sample surface after its corrosion test (Fig. 2, b). In (Fig. 2, b), we observed etched areas of metal in the form of irregularly shaped black spots up to 500 μm in size, which is characteristic of corrosion destruction of micro volumes of metal in the vicinity of inclusions at the intersection with alloy grain boundaries [20, 21] and multidirectional curved lines, which is inherent in the local selective dissolution of metals by grain boundaries in alloys and steels. It should be noted that the area of corrosion damage on the end surfaces of the silver-alloyed NZ30K sample is 7.8% smaller than that of the MZ30K sample (Table 2). It is obvious that secondary phases, grain size, and structure affect the corrosion rate [22, 23]. In particular, works [24, 25] found that the larger the mean austenite grain diameter of the studied steels and alloys, the less likely they are to intersect with inclusions in the vicinity of which pitting occurs and develops, which under certain conditions can turn into corrosion ulcers.

Table 3. Corrosion potentials E_{cor} of NZ30K alloy alloyed with Ag depending on the sample holding time (τ) in Ringer-Locke solution

No. of points	τ, s	E_{cor} , V	No. of points	τ, s	E_{cor} , V
1	4	-1.5696	21	852	-1.53792
2	36	-1.57024	22	884	-1.53952
3	68	-1.57024	23	948	-1.5392
4	100	-1.56704	24	980	-1.53888
5	132	-1.56896	25	1012	-1.53888
6	164	-1.56448	26	1044	-1.53824
7	196	-1.56416	27	1108	-1.53696
8	228	-1.56224	28	1140	-1.53664
9	260	-1.56064	29	1204	-1.53664
10	292	-1.55872	30	1236	-1.53664
11	324	-1.55648	31	1300	-1.53536
12	356	-1.5536	32	1332	-1.5344
13	388	-1.55424	33	1364	-1.5328
14	420	-1.55488	34	1492	-1.53088
15	452	-1.55552	35	1556	-1.53184
16	484	-1.55328	36	1588	-1.5312
17	516	-1.54976	37	1620	-1.53024
18	548	-1.54816	38	1716	-1.52928
19	580	-1.54688	39	1748	-1.52864
20	612	-1.54432	40	1800	-1.52768

Secondary phases, inclusions, and grain size of Ag alloy NZ30K alloy alloyed with Ag are primarily caused by magnesium alloying with zinc, zirconium, neodymium, and silver (Table 1). Due to their low solubility in Mg, the metastable supersaturated solid solution can decompose naturally, forming fine inclusions in magnesium grains. They can block the increase in grain size [26]. In particular, work [16] found that alloying NZ30K alloy with silver in the amount of 0.1 wt.% contributed to a 4-fold reduction in the mean grain diameter. This may contribute to reduce the rate of general corrosion, but increase the likelihood of pitting in chloride-containing media [27]. It is also known [28], that alloying elements of magnesium alloys can create a micro-galvanic effect between the Mg matrix and various inclusions and secondary phases. They play the role of cathodes, in the vicinity of which a solid magnesium solution selectively dissolves [29]. In particular, the formation of pitting in the vicinity of the secondary phases AlMg, AlMgFe, Mg_{17} Al_{12} or Mg_2 Cu in [30] has been observed. This is consistent with the data of [18-20, 24, 25, 31] for chromium-nickel steels and alloys.

It should be noted that the sample from the NZ30K alloy of alloyed Ag 612 s after its immersion in the test solution had a potential E_{cor} =-1.544V (point 20 of Table 3), which corresponds to a change in the intensity of selective dissolution of metals from the sample surface and its enrichment with silver (the place of a rapid change in the potential E_{cor} Fig. 1, curve 2). This may be one of the reasons for the rapid, almost 5-fold decrease in the rate of shift of its potential E_{cor} to the positive side. After 1620 s of studying the alloy in the Ringer-Locke solution, the sample reached a stationary value of the potential E_{cor} =-1.53 V (point 37 of Table 3), which most likely corresponds to the process of maximum saturation of the sample surface with silver and the formation of a stable double electric layer on it.

Summarizing the above, it can be noted that the NZ30K alloy alloyed with silver in the amount of 0.1 wt.% was subjected mainly to general corrosion (Fig. 3, b), because no local corrosion damage was found on the sample cylindrical surface, which is typical for the NZ30K alloy sample (Fig. 3, a). Therefore, it is promising for the production of biodegradable implants, provided that the results of electrochemical, volumetric, and clinical studies are positive.

4. Conclusions

According to the results of corrosion studies, it has been found that the steady-state value of the corrosion potential E_{cor} of the NZ30K alloy sample has been formed from 1.579 to -1.575V during 1800 seconds of testing in the Ringer-Locke solution, and its surface to intense pitting and ulcer corrosion has been subjected with intense hydrogen release at the cathodic areas of the sample. The most intense hydrogen emission on the surface of the sample after its immersion in the test solution at the most negative value of E_{cor} has been visually recorded. It has been found that E_{cor} of the sample made of NZ30K alloy alloyed with 0.1 wt.% silver during the first 100 seconds in the solution was ~ 1.57V, then during 500 seconds of testing it shifted to the positive side at a rate of 0.051 mV/s, but in the test interval from 612 to 1620 seconds it decreased to 0.014 mV/s, and after 1800 seconds a stationary value of this potential at ~ -1.53V has been established. The sample was mainly subjected to uniform general corrosion with varying intensity until the steady-state value of E_{cor} has been established, and its ennoblement was most likely due to the most intense selective dissolution of Mg from the sample surface and its enrichment with silver, zirconium, and neodymium. This alloy is recommended for further research as a structural material for the production of biodegradable implants.

Conflict of interest statement

The authors declare that they have no conflict of interest in relation to this research, whether financial, personal, authorship or otherwise, that could affect the research and its results presented in this paper.

CRediT author statement:

Greshta V., Narivskyi O., Dzhus A, and Vynar V.: Conceptualization, Validation, and Formal analysis; Yar-Mukhamedova G., Mukashev K., Mussabek G., Zelele D., and Atchibayev R.: Validation and Investigation; Beissen N., Imanbayeva A., and Kemelzhanova A.: Verification.

The final manuscript was read and approved by all authors.

Acknowledgements

This research has been funded by the Science Committee of Kazakhstan's Ministry of Science and Higher Education (AP23484310).

References

1 Li H., Zheng Y., Qin L. (2014) Progress of biodegradable metals. *Progress in Natural Science: Materials International*, 24 (5), 414 – 422. DOI: 10.1016/j.pnsc.2014.08.014.

2 Samal S. (2016) High-Temperature Oxidation of Metals. In book: High Temperature Corrosion. 156. DOI:10.5772/63000.

3 Zeng R.-C., Sun L., Zheng Y.F., Cui H.-Z., Han E.-H. (2014) Corrosion and characterization of dual phase Mg–Li–Ca alloy in Hank's solution: The influence of microstructural features. *Corrosion Science*, 79, 69 – 82. DOI:10.1016/j.corsci.2013.10.028.

4 Cui L.Y., Li X.-T., Zeng R., Ii S., Han E.-H., Song L. (2017) In vitro corrosion of Mg–Ca alloy — The influence of glucose content. *Frontiers of Materials Science***,** 11, 284-295. DOI: 10.1007/s11706-017-0391-y.

5 Zheng Y.F., Cu X.N., Witte F. (2014) Biodegradable metals. *Materials Science and Engineering: R: Reports*, 77, 1-34. DOI: 10.1016/j.mser.2014.03.001.

6 Lowe T.C., Valiev R.Z. (2014) Frontiers for bulk nanostructured metals in biomedical applications. *Advanced Biomaterials and Biodevices*, 1 - 52. Wiley Blackwell. DOI: 10.1002/9781118774052.ch1.

7 Xu W., Birbilis N., Sha G., Wang Y., Daniels J.E., Xiao Y., Ferry M. (2015). A high-specific-strength and corrosion-resistant magnesium alloy. *Nature Materials*, 14, 1229–1235. DOI: 10.1038/nmat4435.

8 Rad H.R.B., Idris M.H., Kadir M.R. A., Farahany S. (2012) Microstructure analysis and corrosion behavior of biodegradable Mg–Ca implant alloys. *Materials & Design*, 33, 88-97. DOI: 10.1016/j.matdes.2011.06.057.

9 Müller W.D., Nascimento M.L., Zeddies M., Córsico M., Gassa L.M., Mele M.A.F.L.D. (2007). Magnesium and its alloys as degradable biomaterials: Corrosion studies using potentiodynamic and EIS electrochemical techniques. *Materials Research*, 10, 5-10. DOI: 10.1590/S1516-14392007000100003.

10 Witte F., Ulrich H., Rudert M., Willbold E. (2007) Biodegradable magnesium scaffolds: Part 1: Appropriate inflammatory response. *Journal of Biomedical Materials Research Part A*, 81, 748–756. DOI: 10.1002/jbm.a.31170.

11 Witte F., Hort N., Vogt C., Cohen S., Kainer K.U., Willumeit R., Feyerabend F. (2008) Degradable biomaterials based on magnesium corrosion. *Current Opinion in Solid State and Materials Science*, 12, 63–72. DOI:10.1016/j.cossms.2009.04.001.

12 Ferreira P.C., Piai K.D.A., Takayanagui A.M.M., Segura-Muñoz S.I. (2008) Aluminum as a risk factor for Alzheimer's disease. *Revista Latino-Americana de Enfermagem*, 16, 151-157. DOI: 10.1590/S0104-11692008000100023.

13 Bach F.W., Schaper M., Jaschik C. (2003) Influence of lithium on hcp magnesium alloys. *Materials Science Forum*, 419-422, 1037-1042. DOI: 10.4028/www.scientific.net/MSF.419-422.1037.

14 Avedesian M., Baker H. (1999) *ASM specialty handbook: Magnesium and magnesium alloys*. Materials Park, OH: ASM Intern., 327. https://s2.iran-mavad.com/book/en/asm-specialty-handbook-magnesium-and-magnesium-alloys.pdf.

15 An Y., Draughn R.A., Bonucci E. (1999) *Mechanical testing of bone and the bone-implant interface*. CRC Press, 648. DOI: 10.1201/9781420073560.

16 Greshta V., Shalomeev V., Dzhus A., Mityaev O. (2023) Study of the influence of silver alloying on the microstructure and properties of magnesium alloy NZ30K for implants in osteosynthesis. *New Materials and Technologies in Metallurgy and Mechanical Engineering*, 2, 14-19. DOI: 10.15588/1607-6885-2023-2-2. [in Ukrainian]

17 Kulyk M.F., Zasukha T.V., Lutsyuk M.B. (2012) *Saponite and aerosil in animal husbandry and medicine*. Textbook Vinnytsia, Ukraine: FOP Rogalska I.O., 362. [in Ukrainian].

18 Narivs'kyi O.E. (2005) Corrosion Fracture of Platelike Heat Exchangers. *Mater Sci*., 41, 122–128. DOI:10.1007/s11003-005-0140-8.

19 Narivs'kyi O.E. (2007) The influence of heterogeneity steel AISI321 on its pitting resistance in chloride-containing media. *Materials Science*, 2(43), 256-264. DOI: 10.1007/s11003-007-0029-9.

20 Narivs'kyi O.E. (2007) Micromechanism of corrosion fracture of the plates of heat exchangers. *Mater Sci*., 43, 124–132. DOI: 10.1007/s11003-007-0014-3.

21 Wang H., Estrin Y., Zúberová Z. (2008) Biocorrosion of a magnesium alloy with different processing histories. *Materials Letters*, 62(16), 2476-2479. DOI: 10.1016/j.matlet.2007.12.052.

22 Salahshoor M., Guo Y. (2012) Biodegradable orthopedic magnesium-calcium (MgCa) alloys, processing, and corrosion performance. *Materials (Basel)*, 5(1), 135–155. DOI: 10.3390/ma5010135.

23 Pu Z., Song G.-L., & Yang, S. (2012). Grain refined and basal textured surface produced by burnishing for improved corrosion performance of AZ31B Mg alloy. *Corrosion Science*, 57, 192-201. DOI:10.1016/j.corsci.2011.12.018.

24 Narivs'kyi O., Atchibayev R., Kemelzhanova A., Yar-Mukhamedova G., Snizhnoi G., Subbotin S., Beisebayeva A. (2022) Mathematical modeling of the corrosion behavior of austenitic steels in chloride-containing media during the operation of plate-like heat exchangers. *Eurasian Chemico-Technological Journal*, 24(4), 295-302. DOI:10.18321/ectj1473.

25 Narivskyi O.E., Subbotin S.A., Pulina T.V., Khoma M.S. (2022) Assessment and prediction of the pitting resistance of plate-like heat exchangers made of AISI304 steel and operating in circulating waters. *Materials Science*, 58, 41–46. DOI: 10.1007/s11003-022-00628-4.

26 Wang H., Estrin Y., Fu H. F. (2007) The effect of pre-processing and grain structure on the biocorrosion and fatigue resistance of magnesium alloy AZ31. *Advanced Engineering Materials*, 9(11), 967-972. DOI:10.1002/adem.200700200.

27 Südholz A.D., Kirkland N.T., Buchheit R.G., Birbilis N. (2010) Electrochemical properties of intermetallic phases and common impurity elements in magnesium alloys. *Electrochemical and Solid-State Letters*, 14(2), C5. DOI:10.1149/1.3523229.

28 Zeng R.-C., Zhang J., Huang W.-J., Dietzel W., Kainer K.U., Blawert C., Wei K.E. (2006) Review of studies on corrosion of magnesium alloys. *Transactions of Nonferrous Metals Society of China*, 16(2), 763-771. DOI:10.1016/S1003-6326(06)60297-5.

29 Kozlovskiy A. (2024) Study of the influence of the accumulated dose of damage in the near-surface layer on resistance to external influences associated with corrosion processes during high-temperature annealing. *Eurasian Physical Technical Journal*, 21(1(47)), 14–20. DOI: 10.31489/2024No1/14-20.

30 Ghali E. (2010) Properties, use, and performance of magnesium and its alloys in *Corrosion resistance of aluminum and magnesium alloys: Understanding, performance, and testing.* Wiley. Parts 3. 319 – 347. DOI:10.1002/9780470531778.ch9.

31 Narivskyi O.E., Belikov S.B., Subbotin S.A., Pulina T.V. (2021) Influence of chloride-containing media on the pitting resistance of AISI321 steel. *Materials Science*, 57(2), 291-297. DOI:10.1007/s11003-021-00544-z.

AUTHORS' INFORMATION

Greshta, Victor Leonidovich – Candidate of Technical Science, Professor, National University «Zaporizhzhia Polytechnic»: Zaporizhzhia, Ukraine; Scopus Author ID: 55944039900; ORCID ID: 0000-0002-4589-6811; greshtaviktor@gmail.com

Narivskyi, Oleksii Eduardovich – Doctor of Technical Sciences, Professor, National University "Zaporizhzhya Polytechnic", Ukraine; Ukrspetsmash LLC, Berdiansk, Ukraine; Scopus Author ID: 22035375800; ORCID ID: 0000-0003-2934-183X; amz309@ukr.net
Dzhus, Anna Vyacheslavivna – PhD Student, Senior Lecturer, National University "Zaporizhzhya Polytechnic", Ukraine; Scopus Author ID: 58722586900; ORCID ID: 0000-0002-6474-0732; anna-92@ukr.net
Vynar, Vasyl Andriyovich - Doctor of Technical Science, Senior Researcher, Karpenko Institute of Physics and Mechanics of the National Academy of Sciences of Ukraine, Lviv, Ukraine; Scopus Author ID: 8630747800; ORCID ID: 0000-0002-5314-7052; vynar.va@gmail.com
Yar-Mukhamedova, Gulmira Sharipovna – Doctor of Phys. and Math. Sciences, Professor, Al-Farabi Kazakh National University, Almaty, Kazakhstan; Scopus Author ID: 6505954975; ORCID ID: 0000-0001-5642-3481; gulmira-alma-ata@mail.ru
Mukashev, Kanat – Doctor of Phys. and Math. Sciences, Professor, Energo University, Almaty, Kazakhstan; Scopus Author ID: 10640069200; ORCID ID: 0000-0002-3568-7143; mukashev.kms@gmail.com
Beissen, Nurzada Abdibekovna – Candidate of Phys. and Math. Sciences, Associate Professor, Al-Farabi Kazakh National University, Almaty, Kazakhstan; Scopus Author ID: 26530753300; ORCID ID: 0000-0002-1957-2768; nurabd@mail.ru
Mussabek, Gauhar Kalizhanovna – PhD (Sci.), Associate Professor, Al-Farabi Kazakh National University, Almaty, Kazakhstan; Scopus Author ID: 37028867500; ORCID ID: 0000-0002-1177-1244; gauhar-mussabek@mail.ru
Imanbayeva, Akmaral Karimovna – Candidate of Phys. and Math. Sciences, Researcher, Al-Farabi Kazakh National University; KazAlfaTech LTD", Almaty, Kazakhstan; Scopus Author ID: 15054326000; ORCID ID: https://orcid.org/0000-0001-9900-9782; akmaral@physics.kz
Zelele, Daniel – PhD student, Al-Farabi Kazakh National University, Almaty, Kazakhstan**;** ORCID ID: 0009-0003-1085-5264; danielmekonnenz@gmail.com
Atchibayev, Rustem Alibekovich – PhD, Al-Farabi Kazakh National University, Almaty, Kazakhstan; Scopus Author ID: 57202802182; ORCID ID: 0000-0002-1959-7199; rustematch@gmail.com
Kemelzhanova, Aiman Esteuovna – Master (Eng.), Al-Farabi Kazakh National University, Almaty, Kazakhstan; Scopus Author ID: 57216317480; ORCID ID: 0000-0002-3406-9714; aiman_90.08@mail.ru

EURASIAN PHYSICAL TECHNICAL JOURNAL

2024, Volume 21, No.3 (49)

https://doi.org/10.31489/2024No3/37-44

Received: 12/02/2024 Revised: 17/04/2024 Accepted: 14/08/2024 Published online: 30/09/2024

Original Research Article

UDC 537.9

DETERMINATION OF THE ELEMENTAL COMPOSITION AND CHANGES IN THERMAL AND ELECTRICAL CONDUCTIVITY OF "HANFORD" AND LOW-ASH MEDIUM-GRAINED GRAPHITE'S GRADE GRAPHITES DEPENDING ON THE FAST NEUTRONS FLUENCE

Baytelesov S.A., Tojiboev D.D., Sadikov I.I., Kungurov F.R., Alikulov Sh.A.

Institute of Nuclear Physics of Uzbekistan Academy of Sciences, Tashkent, Uzbekistan
*Corresponding author: baytel@inp.uz

Abstract. *Studying the properties of graphite recovered from operating nuclear reactors is vital for predicting the properties and integrity of graphite as part of assessing the continued operation and life extension of nuclear reactors. The purpose of the study is to determine the electrical conductivity and thermal conductivity of low-ash medium-grained graphite's grade graphite in the thermal column masonry of the VVR-SM research reactor in the measurement temperature range corresponding to the conditions of normal operation of the reactor to determine the service life. In this work, the change in thermal conductivity and electrical conductivity of GMZ graphite was studied, as well as for comparison of Hanford grade graphite depending on the fluence of fast neutrons and the measurement temperature. The dependence of electrical conductivity and thermal conductivity on dose and temperature has been established. It has been shown that the greater the neutron fluence, the more both the thermal conductivity and electrical conductivity of the material decreases. The service life of the thermal column has been determined.*

Keywords: thermal conductivity, electrical conductivity, low-ash medium-grained graphite's, "Hanford" grade graphite, fast neutrons, fluence, dose.

1. Introduction

The development of nuclear technology is moving in the direction of increasing energy and heat intensity, the intensity of radiation exposure on individual structural elements of nuclear reactors, which puts forward increased demands on the materials used. Especially for high-temperature gas-cooled reactors (HTGR) and thermonuclear reactors (TNR). Among others, carbon-graphite materials are increasingly used in nuclear technology, not only as a masonry material, but also for structural elements. For example, for claddings and matrices of spherical fuel elements, coatings of microfuel elements in HTGR, screens in nuclear reactors, etc. Naturally, depending on the operating conditions (neutron fluence, irradiation intensity and temperature), the requirements for materials for these installations differ significantly from the usual requirements for nuclear graphite [1].

The works [2-7] investigated the properties of graphite materials for a high-temperature gas-cooled reactor, such as the electronic structure and properties of composites based on the carbon isotope, the durability of reactor graphites, and the thermal conductivity of graphite. Natural carbon has two stable isotopes - ^{12}C (98.892%) and ^{13}C (1.108%). There are also four radioactive isotopes (^{10}C, ^{11}C, ^{14}C and ^{15}C), of which only the ^{14}C isotope is long-lived with a half-life of 5730 years. The neutron absorption cross sections in the reaction with carbon nuclei are less than 4.5 microbarns for high-purity graphite [8]. Most of the collisions of neutrons with carbon nuclei in this case occur via the elastic scattering mechanism. The latter circumstance determined

the effective use of graphite as a moderator. In particular, for a nuclear reactor operating on enriched uranium, graphite, as a moderator, is second in efficiency to beryllium and heavy water. In this case, high-purity graphite is used, where the total impurity content does not exceed 1×10^{-3}%.

Graphite serves as a key material for heat dissipation in electronic devices and nuclear engineering due to its remarkable thermal properties [1]. Thermal expansion and conductivity of graphite have always been the main scientific parameters in the field of carbon materials. Therefore, great attention is paid to theoretical and experimental research in this area. It is known that neutron irradiation noticeably reduces the electrical and thermal conductivity of graphite materials [9]. When nuclear graphite is annealed, Wigner energy is released [10]. The thermal conductivity values of individual grades of graphite vary greatly from each other, this is the result of different production processes leading to differences in the microstructure of the final product [11].

Studying the properties of graphite recovered from operating nuclear reactors is vital for predicting the properties and integrity of graphite as part of assessing continued operation and life extension of a nuclear plant [12]. Reactors have limited space available for monitoring structural materials, so size-constrained samples require reliable and efficient measurement methods.

2. Materials and experimental methods

Graphite samples taken from the "residual" graphite stockpile from the construction of the B reactor in the 1940s (the first graphite reactor at the Hanford site) were prepared and represent first-generation nuclear reactor graphite. Samples of "Hanford" grade graphite, representing a cylinder with a diameter d=Ø12 mm and a height h=19 mm, weighing 4.79 g, from which samples for irradiation with a diameter d=Ø12 mm and a height h=3.4 mm, weighing 0.6 g were prepared.

Samples of GMZ (low-ash medium-grained graphite's) grade graphite with a diameter d=Ø16 mm and a height h=3.64 mm, weighing 1.3 g, as well as a prism type, a=8.18 mm, b=7.95 mm, L=59.1 mm, m=6.3 g were prepared. GMZ grade graphite is characterized by high density (>1.8 kg/m^3) and electrical conductivity, low porosity (7%) and gas permeability. It is heat- and wear-resistant, chemically inert. Graphite hardness – 52 Shore, ash content <0.1%, grain size <10 microns.

The samples were placed in the vertical channels of the VVR-SM research reactor of the Institute of Nuclear Physics of Academy of Sciences, Republic of Uzbekistan (INP AS RU) with a modified loading scheme at 10 MW power for irradiation with fast neutrons. Vertical channels 1-5 and 1-3 were used in the reactor core, where the fast neutron flux density (E_n>0.8 MeV) in the channels was 1.19×10^{13} n/(cm$^2\times$s) and 9.72×10^{12} n/(cm$^2\times$s), respectively.

The temperature in the channel was maintained at about 318 K. The heat released due to radiation heating was removed by circulating primary circuit water at a volumetric rate of 1250 m^3/hour. Measurements of the thermal conductivity coefficient in the original samples and those irradiated with various doses were carried out using the dynamic calorimeter method on an IT-λ-400 installation in the temperature range from 290 K to 490 K.

The value of the thermal conductivity coefficient was calculated from the results of measuring the thickness, cross-sectional area of disk samples and the temperature difference in the sample and the heat meter, using the relationship [13,14]:

$$\lambda = K_T \cdot \frac{n_t}{n_0} \cdot \frac{h}{S(1+\sigma_C)} \quad , \tag{1}$$

where n_t and n_0 are, respectively, the temperature differential in the heat-meter rod and the sample, respectively; h and S are, respectively, the height and area of the transverse cross section of the sample; K_T is the thermal conductivity of the heat-meter rod; and σ_C is the correction for the specific heat of the sample.

A chemically pure copper sample was used as a thermal conductivity standard when determining the thermal conductivity of the heat meter K_T. The above formula did not take into account the influence of the specific contact thermal resistance P_k, the relative contribution of which to the total thermal resistance of the sample and the heat meter rod is negligibly small. The thermal conductivity coefficient was determined with an error of no more than 10%.

The electrical resistance of graphite samples was measured using a four-probe compensation method at a current of 1 mA [15,16] in the temperature range from 290 K to 490 K. Electrical resistivity ρ was determined from the relation:

$$\rho = \frac{U \cdot S \cdot R_{et}}{L \cdot U_{et}} \tag{2}$$

where U and U_{et} are the voltage drop across the measured and reference samples, R_{et} is the resistance of the reference coil, equal to 0.01 Ohm, S and L are the cross section and length of the sample, respectively. Electrical conductivity coefficients were determined with an error of no more than 10%.

3. Results of experiments and calculations

Solid (piece) and powder of the GMZ grade graphite were prepared to determine the impurity composition of the sample. Figure 1 shows an electronic image of the GMZ grade graphite surface and its elemental composition using an EVO MA10 scanning electron microscope.

Table 1 shows the percentage of impurities of GMZ grade graphite obtained using an EVO MA10 scanning electron microscope.

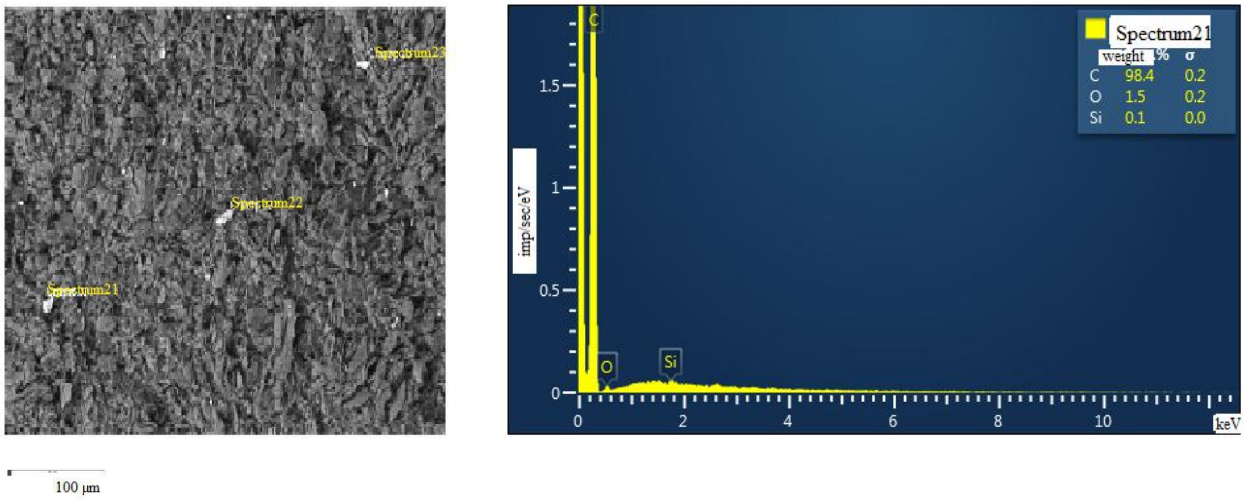

a) graphite surface image b) elemental composition of GMZ grade graphite

Fig. 1. Electronic image of the GMZ grade graphite surface and elemental composition.

Table 1. Content of impurities of GMZ grade graphite

Element	Type of line	Conditional concentration	Weight, %	Accuracy Weight, %	Standard name
C	K series	2.41	98.39	0.25	C Vit
O	K series	0.02	1.51	0.24	SiO_2
Si	K series	0.00	0.11	0.05	SiO_2
Sum:			100.00		

Figure 1 shows areas with different contrasts, which indicate the presence of impurity elements such as oxygen and silicon and others in the graphite matrix. To test the assumption, the content of impurity elements in the samples was determined using the technique of instrumental neutron activation analysis of elements. The content of impurity elements in the samples was determined.

To measure the samples, a gamma spectrometer with a GC-1820 semiconductor detector and an InSpector-2000 multichannel analyzer with Genie-2000 software (CANBERRA USA) was used. To calculate the concentration of impurity elements, IAEA standards with certified contents of elements in soil and bottom sediments were used. Table 2 shows the results of determining the content of impurity elements in the GMZ grade of graphite, obtained by instrumental neutron activation analysis.

Table 2. Content of impurity elements in GMZ grade graphite.

Element	Concentration, C ± ΔC, ppm (μg/g)	Concentration, C ± ΔC, ppm (μg/g))	Element	Concentration, C ± ΔC, ppm (μg/g)	Concentration, C ± ΔC, ppm (μg/g)
	Graphite piece	Graphite powder		Graphite piece	Graphite powder
As	(2.96 ± 0.09) E-02	(1.24 ± 0.07) E-01	Nd	(7.52 ± 0.83) E-01	(1.26 ± 0.23)
Ba	(7.48 ± 0.60)	(1.50 ± 0.27) E+01	Ni	(8.60 ± 1.03) E-01	(2.73 ± 0.63)
Br	(4.16 ± 0.40) E-02	(3.65 ± 0.13) E-01	Rb	(5.33 ± 0.69) E-02	(3.88 ± 0.39) E-01
Ce	(1.59 ± 0.13)	(2.33 ± 0.19)	Sb	(8.90 ± 0.71) E-03	(1.02 ± 0.09) E-01
Co	(1.79 ± 0.20) E-02	(1.69 ± 0.19) E-01	Sc	(2.83 ± 0.11) E-01	(4.12 ± 0.16) E-01
Cr	(8.28 ± 0.75) E-02	(5.40 ± 0.38)	Se	(3.96 ± 0.59) E-03	(2.10 ± 0.76) E-02
Cs	(8.25 ± 1.32) E-03	(2.25 ± 0.36) E-02	Sm	(7.53 ± 0.45) E-02	(1.48 ± 0.10) E-01
Eu	(1.42 ± 0.12) E-02	(2.01 ± 0.17) E-02	Sr	(3.10 ± 0.43)	(5.10 ± 0.72)
Fe	(5.30 ± 0.27) E-04	(4.51 ± 0.17) E-02	Ta	(2.14 ± 0.30) E-03	(5.76 ± 0.98) E-03
Hf	(8.23 ± 1.25) E-03	(2.35 ± 0.53) E-02	Tb	(2.60 ± 0.26) E-02	(4.03 ± 0.13) E-02
K	(9.69 ± 1.98)	(6.51 ± 1.33) E+01	Th	(2.92 ± 0.23) E-02	(5.55 ± 0.78) E-02
La	(7.79 ± 0.62) E-01	(1.23 ± 0.10)	U	(5.71 ± 0.79) E-02	(1.22 ± 0.11) E-01
Lu	(1.31 ± 0.09) E-02	(2.36 ± 0.33) E-02	W	(3.60 ± 0.40) E-02	(9.17 ± 0.73) E-01
Mn	(1.66 ± 0.22) E-01	(5.14 ± 0.41)	Yb	(7.92 ± 0.46) E-03	(1.78 ± 0.24) E-02
Mo	(1.56 ± 0.14) E-01	(4.18 ± 0.67) E-01	Zn	(5.79 ± 0.87) E-01	(1.02 ± 0.15) E+01
Na	(2.39 ± 0.25)	(3.19 ± 0.21) E+01			

Figure 2 shows electron images of the “Hanford” grade graphite surface and its elemental composition using an EVO MA10 scanning electron microscope.

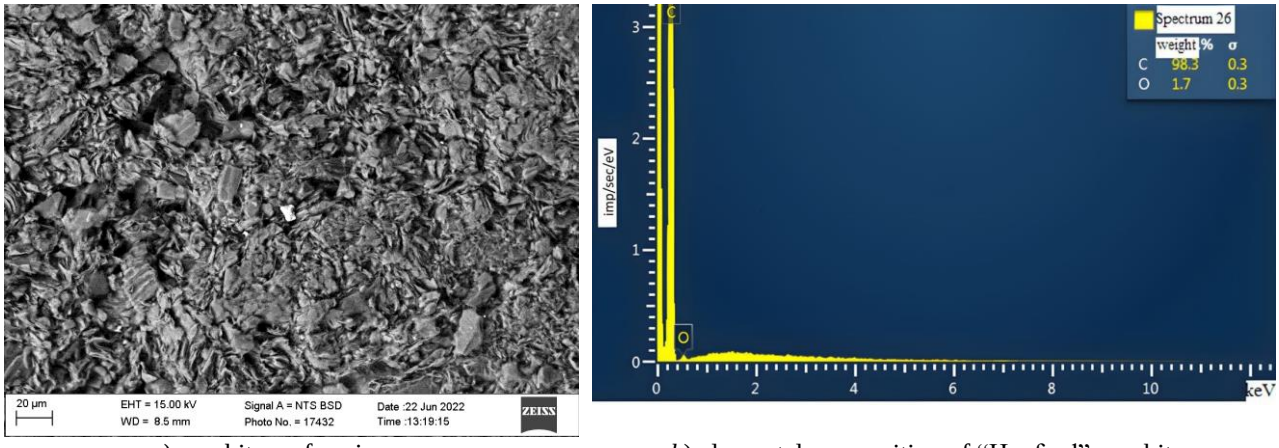

a) graphite surface image

b) elemental composition of “Hanford” graphite

Fig. 2. Electron image of the “Hanford” grade graphite surface and its elemental composition.

Table 3 shows the percentages of impurities in “Hanford” grade graphite obtained using an EVO MA10 scanning electron microscope.

Table 3. Impurity content in "Hanford" grade graphite.

Element	Type of line	Conditional concentration	Weight, %	Accuracy Weight, %	Standard name
C	K series	3.75	98.32	0.29	C Vit
O	K series	0.03	1.68	0.29	SiO_2
Sum:			100.00		

The content of impurity elements in the samples was determined using the technique of instrumental neutron activation analysis of elements. We used a CANBERRA semiconductor gamma spectrometer with Genie-2000 software, an AB204-S/FACT Mettler Toledo analytical balance, and a VM5101 VESTA laboratory balance to measure the samples. IAEA standards with certified contents of elements in soil and bottom sediments were also used. Table 4 shows the results of determining the content of impurity elements in the "Hanford" grade graphite.

Table 4. Content of impurity elements in the "Hanford" grade graphite (1 ppm = 1 μg/g)

"Hanford" grade graphite (KSO/CSO)		
Element	Concentration, ppm	
	Minimal	Maximal
Al	0.3	0.5
B	2.8	3
Ba	2.6	2.6
Ca	135	210
Cr	0.3	1.1
Cu	0.2	0.6
Fe	2.8	5.6
Li	0.2	0.3
Ni	0.3	2.5
S	31	33
Si	1.3	6
Sr	3.1	4
Ti	7.5	8.2
V	11	12
Zn	5.4	160

Table 5 shows the results of the electrical conductivity measurements of GMZ grade graphite, non-irradiated and irradiated with a neutron fluence of 1.59×10^{19} n/cm^2, depending on temperature.

Table 5. Electrical conductivity of GMZ grade graphite, non-irradiated and irradiated with a neutron fluence of 1.59×10^{19} n/cm^2, depending on temperature.

K	Non-irradiated ρ, Ohm×m	Irradiated ρ, Ohm×m
298	$11.4\cdot10^{-6}$	$31.7\cdot10^{-6}$
323	$11.2\cdot10^{-6}$	$31.5\cdot10^{-6}$
348	$11\cdot10^{-6}$	$31.3\cdot10^{-6}$
373	$10.8\cdot10^{-6}$	$31\cdot10^{-6}$
398	$10.7\cdot10^{-6}$	$30.6\cdot10^{-6}$
423	$10.5\cdot10^{-6}$	$30.1\cdot10^{-6}$
448	$10.3\cdot10^{-6}$	$29.7\cdot10^{-6}$

Figures 3 and 4 show the results of the thermal conductivity measurements of GMZ and "Hanford" grade graphite's irradiated with a fluence of 3.17×10^{19} n/cm^2, depending on the sample temperature. The temperature

dependence of the graphite thermal conductivity should be determined by the dependence of carrier mobility on temperature. The periodicity of the crystal lattice potential in the samples, disrupted by thermal vibrations, is additionally disrupted by randomly distributed impurity atoms. This leads to additional scattering of charge carriers and a decrease in their mobility. As a result, the thermal conductivity of graphite, depending on the neutron fluence, decreases. As can be seen from Figure 3, at a temperature of 298 K, the thermal conductivity of GMZ grade graphite with a 3.17×10^{19} n/cm^2 neutron fluence decreases by about 22% relative to the non-irradiated sample.

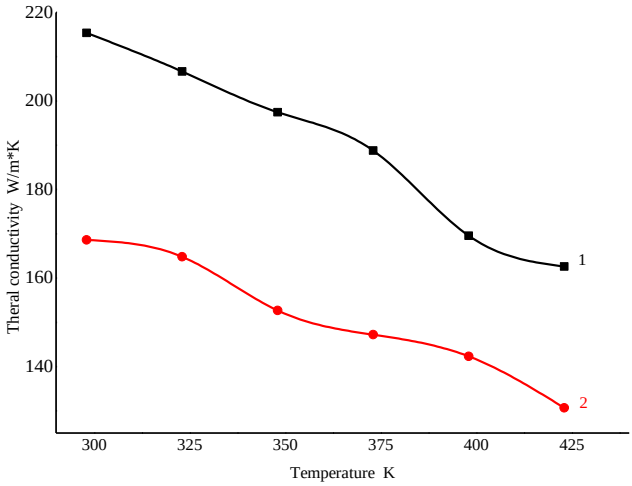

Fig.3. Thermal conductivity λ(T) of GMZ grade graphite samples before and after irradiation with 3.17×10^{19} n/cm^2 neutrons fluence, depending on the sample temperature. 1 – non-irradiated sample; 2 - irradiated sample.

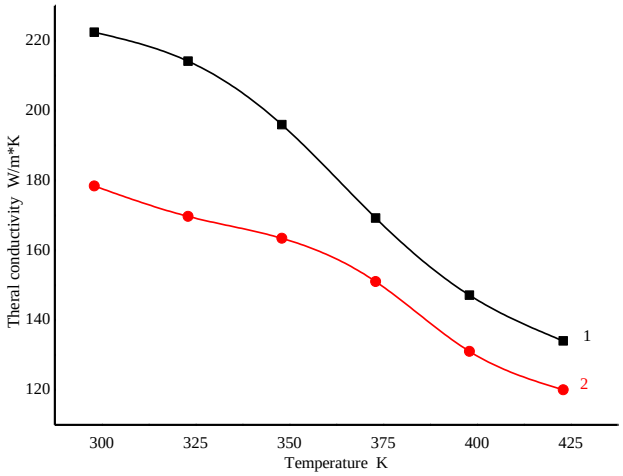

Fig. 4. Dependence of thermal conductivity λ(T) of "Hanford" grade graphite samples before and after irradiation with 3.19×10^{19} n/cm^2 neutrons fluence, depending on the sample temperature. 1 – Non-irradiated sample; 2 - irradiated sample.

Figure 4 shows that the thermal conductivity of "Hanford" grade graphite at a temperature of 298 K with a 3.17×10^{19} n/cm^2 neutron fluence decreases by about 20%, relative to the non-irradiated sample. In this case, a decrease in thermal conductivity was observed depending on the temperature of the sample in the range from 298 K to 423 K. The resistivity value of GMZ grade graphite at room temperature before irradiation was 1.14×10^{-7} Ohm×m. The resistivity value of GMZ grade graphite as a result of irradiation increased by 2.78 times and amounted to 3.17×10^{-7} Ohm×m. The increase in resistivity is due to the formation of defects as a result of irradiation of samples with fast neutrons in the VVR-SM reactor core.

In this case, a decrease in resistivity was observed depending on the increase in sample temperature in the range from 298 K to 423 K. This is due to an increase in the mobility of charge carriers with increasing

temperature. An increase in resistivity, as well as a decrease in thermal conductivity of G347A graphite at high fluence, was also noted in the work [17].

4. Conclusion

Thus, the analysis of the obtained experimental results made it possible to establish that the electrical and thermal conductivity of graphite varies with both temperature and irradiation dose. In this case, with increasing neutron fluence, the deviation from the linear dependence and, accordingly, the rate of decrease in the electrical and thermal conductivity of graphite decreases with temperature. It is known that at low fluences ($<10^{18}$ n/cm^2), the electrical and thermal conductivity of graphite increases due to radiation annealing. At high doses of radiation, the accumulation of radiation defects, vacancies and their small complexes occurs, due to this the electrical and thermal conductivity of graphite decreases. Fluence $>10^{22}$ n/cm^2 is the critical fluence of neutrons, which begins to graphite swelling, thermal conductivity decreases tens of times.

Conflict of interest statement
The authors declare that they have no conflict of interest in relation to this research, whether financial, personal, authorship or otherwise, that could affect the research and its results presented in this paper.

Credit author statement
Baytelesov S.A.: Writing - Original Draft; Tojiboev D.D.: Development of Facility and Measurements; Sadikov I.I.: Review & Editing; Kungurov F.R.: Conceptualization, Data Curation; Alikulov Sh.A.: Methodology, Investigation.
The final manuscript was read and approved by all authors.

References

1 Zhao Lu, Tang Jiang, Zhou Min, Shen Ke. (2022) A review of the coefficient of thermal expansion and thermal conductivity of graphite. *New Carbon Mater*, 37(3), 544–555. DOI: 10.1016/S1872-5805(22)60603-6.

2 Virgiliev Yu.S., Kalyagina I.P., Zemlyanikin V.F., Klimenko A.A. (2007) Graphite for the high-temperature gas-cooled reactor GT-MGR. *Atomic Energy*, 103 (4), 235 – 237. https://elib.biblioatom.ru/text/atomnaya-energiya_t103-4_2007/p235/ [in Russian].

3 Zhmurikov E.I., Romanenko A.I., Bulusheva L.G., Anikeeva O.B., Lavskaya Yu.V., Okotrub A.V., Abrosimov O.G., Tsybulya S.V., Logachev P.V., Tecchiol L. (2007) Studies of the electronic structure and properties of composites based on the ^{13}C carbon isotope. *Surface. X-ray, synchrotron and neutron studies*, 11, 29 – 35. https://elibrary.ru/item.asp?id=9554577&ysclid=lxvqu4h420350625560 [in Russian].

4 Zhmurikov E.I., Bolkhovityanov D.Yu., Blinov M.F., Ishchenko A.V., Kot N.Kh., Titov A.T., Tsybulya S.V., Tecchio L. (2010) On the issue of the durability of reactor graphites. *Surface. X-ray, synchrotron and neutron studies*, 5, 89 - 99. https://elibrary.ru/item.asp?id=15108600 [in Russian].

5 Zhang H., Lee G., Fonseca A.F., Bolders T.L., Cho K. (2010) Isotope effect on the thermal conductivity of graphene. *Journal of Nanomaterials*, Article ID 537657, 1 - 6. DOI: 10.48550/arXiv.1007.1496.

6 Belan E.P., Pokrovskiy A.S., Kharkov D.V. (2017) The effect of thermal annealing on thermal conductivity of graphite GR-280 irradiated up to high neutron fluence. *Physical and mathematical sciences*, I (1), 82 - 91. DOI:10.21685/2072-3040-2017-1-8. [in Russian].

7 Stankus S.V., Savchenko I.V., Agazhanov A.Sh., Yatsuk, O.S.; Zhmurikov, E.I. (2013) Thermophysical properties of MPG-6 graphite. *Thermophysics of High Temperatures*, 51(2), 205–209. https://www.mathnet.ru/php/archive.phtml?wshow =paper&jrnid=tvt&paperid=75&option_lang=eng [in Russian].

8 Vlasova K.P. (1964). *Graphite as a high-temperature material*. Collection of articles. 420. http://elcat.lib.misis.ru/vmsua5379ghkip/index.php?url=/notices/index/IdNotice:987677977/ Source:default# [in Russian].

9 Tadashi M., Masaaki H. (1992) Neutron irradiation effect on the thermal conductivity and dimensional change of graphite materials. *Journal of Nuclear Materials*, 195(1–2), 44-50. DOI: 10.1016/0022-3115(92) 90362-O.

10 Yumeng Zh., Yuhao J., Shasha L., Jie Gao., Zhou Zhou., Toyohiko Yano., Zhengcao Li. (2022) The Wigner energy and defects evolution of graphite in neutron-irradiation and annealing. *Radiation Physics and Chemistry*, 201, 110401. DOI: 10.1016/j.radphyschem.2022.110401.

11 Pavlov T.R., Lestak M., Wenman M.R., Vlahovic L., Robba D., Cambriani A., Staicu D., Dahms E., Ernstberger M., Brown M., Bradford M.R., Konings R.J.M., Grimes R.W. (2020) Examining the thermal properties of unirradiated nuclear grade graphite between 750 and 2500 K. *Journal of Nuclear Materials*, 538, 152176. DOI:10.1016/j.jnucmat.2020.152176.

12 Matthew S.L. Jordan., Paul R., Karen E. V., Tjark O. van Staveren., Matthew Brown., Bruce Davies., Nassia Tzelepi., Martin Metcalfe. (2018) Determining the electrical and thermal resistivities of radiolytically-oxidized nuclear

graphite by small sample characterization. *Journal of Nuclear Materials*, 507, 68 - 77. DOI:10.1016/j.jnucmat.2018.04.022.

13 Denisova E.I., Shaq A.V. (2005) *Measuring thermal conductivity using the IT-λ-400 meter*. Ekaterinburg, 35. https://study.urfu.ru/Aid/Publication/279/1/Denisova_Shak2.pdf [in Russian].

14 Abdukadyrova I.Kh., Alikulov Sh.A., Akhmedjanov F.R., Baytelesov S.A., Boltabaev A.F., Salikhbaev U.S. (2014) High-Temperature Thermal Conductivity of SAV-1 the Aluminum Alloys. *Atomic Energy*, 116 (2), 100 - 104. https://link.springer.com/content/pdf/10.1007/ s10512-014-9825-0.pdf

15 Instruction manual model 3207 digital micro-ohm meter. USA (2011), 35 https://www.instrumentation2000.com/pub/media/pdf/ballantine-3207-manual.pdf

16 Kuntse H.I. (1989) *Methods of physical measurements*. Moscow, 216. https://lib-bkm.ru/12583 [in Russian].

17 Anne A.C., Yutai K., Snead M.A., Takizawa K. (2016) Property changes of G347A graphite due to neutron irradiation. *Carbon*, 109, 860 - 873. DOI:10.1016/j.carbon.2016.08.042.

AUTHORS' INFORMATION

Baytelesov, Sapar Akimovich – Doctor (Sci.), Professor, Head of laboratory, Institute of Nuclear Physics, Uzbekistan Academy of Sciences, Ulugbek, Tashkent, Uzbekistan; SCOPUS Author iD: 9740002000; ORCID iD: 0000-0003-3926-9579; baytel@inp.uz

Tojiboev, Davronbek Davlatalievich – PhD student, Institute of Nuclear Physics, Academy of Sciences of Uzbekistan, Ulugbek, Tashkent, Uzbekistan; ORCID iD 0009-0006-0405-696X; tojiboyev_davron89@mail.ru

Sadikov, Ilkhom Ismailovich – Doctor (Sci.), Academician, Professor, Director, Institute of Nuclear Physics, Uzbekistan Academy of Sciences, Ulugbek, Tashkent, Uzbekistan; ORCID iD: 0000-0002-9779-370X, ilkham@inp.uz

Kungurov, Fakhrulla Rakhmatullayevich – Doctor (Sci.), Senior researcher, Deputy Director; Institute of Nuclear Physics, Uzbekistan Academy of Sciences, Ulugbek, Tashkent, Uzbekistan; ORCID iD: 0000-0003-4359-3523; fkungurov@inp.uz, +99871-2893758

Alikulov, Sherali Abdusalomovich – PhD, Senior researcher, Institute of Nuclear Physics, Uzbekistan Academy of Sciences, Ulugbek, Tashkent, Uzbekistan; ORCID iD: 0000-0003-4028-6501; alikulov@inp.uz; +99871-2893508

EURASIAN PHYSICAL TECHNICAL JOURNAL

2024, Volume 21, No.3 (49)

https://doi.org/10.31489/2024No3/45-53

Received: 04/04/2024 Revised: 29/06/2024 Accepted: 17/09/2024 Published online: 30/09/2024

Original Research Article

UDC 536.7

THERMAL TECHNOLOGICAL CONDITION OF IVG.1M RESEARCH REACTOR CORE UNDER VARIOUS OPERATING MODES

Skakov M.K.[1], Martynenko Ye.A.*[2,3], Yerdybayeva N.K.[3], Akayev A.S.[2], Bekmuldin M.K.[2], Prozorova I.V.[2]

[1] National Nuclear Center of the Republic of Kazakhstan, Kurchatov, Kazakhstan
[2] Institute of Atomic Energy Branch of RSE NNC RK, Kurchatov, Kazakhstan,
[3] D.Serikbayev East Kazakhstan Technical University, Ust-Kamenogorsk, Kazakhstan
*Corresponding author: Kirichek@nnc.kz

Abstract. *The relevance of the study is related to the determination of the thermal characteristics of the IVG.1M research reactor core with the low enriched uranium fuel under the nominal and design operating modes. The thermal technological condition of the IVG.1M research reactor during the start-up are determined by the readings of the temperature, pressure and coolant flow sensors of the information and measuring system. The indirect methods including the computer simulating ones are used to determine the temperature of the core structural materials and the distribution of the coolant temperature by the height of the fuel assembly. The research has been carried out using the method of the finite element analysis using the ANSYS Fluent software package. The study goal was to verify the adequacy of the calculation methodology and obtain the calculated data on the temperature distribution in the fuel assembly in the reactor power range from the nominal to design one. The article presents a description of the IVG.1M reactor, the research methodology, computer model, simulation results and the comparison of the calculated data with the experimental ones. The study scientific novelty consists in determining the temperature conditions of the fuel rods during the reactor operation at various levels of the design capacity with a conservative approach to the cooling conditions. The significance of the research results lies in the fact that a computer model can be used to determine the characteristics of the IVG.1M reactor core under the reactor various operating modes and to analyze the thermohydraulic processes in the fuel assembly.*

Keywords: IVG.1M RR, fuel rod, temperature field, computer simulation, fuel assembly, thermophysical calculation.

1. Introduction

The IVG.1M research reactor (RR) is a heterogeneous thermal neutron nuclear reactor with a light-water coolant. It is possible to conduct the scientific research on the safety of the peaceful atomic energy use at the reactor, including: studying on the radiation material science, testing the structural materials of the nuclear technology, practicing the operating modes of the fuel assemblies (FA), studying the emergency situations. In 2023 the reactor core was transferred from the highly enriched uranium fuel (HEU) to the low enriched uranium fuel (LEU) in order to reduce the risks of the proliferation of the fissile materials [1]. During the conversion, the neutronics and thermal characteristics of the reactor were improved, which was confirmed in a series of the power starts-up. To date, scientific research has been resumed.

The IVG.1M research reactor core is a set of water-cooled technological channels (WCTC) with the fuel assemblies (FA). The maximum design capacity of the reactor core consisting of 30 WCTC is estimated at 60 MW, while at the moment the research starts-up are carried out at a capacity of no more than 10 MW. The limitations on the realized capacity are related to the configuration of the cooling system, which has restrictions

on the coolant specified flow rate. The reactor cooling system upgrading is a relevant task and requires the comprehensive study.

Throughout the entire life cycle of the IVG.1M research reactor the engineering and technical staff collects, processes, systematizes and analyzes the operational information. The calculation and methodological base created on the basis of many-year experience, which is a complex of methods, procedures and software, allows ensuring the safe operation and research at the reactor. New computational and experimental techniques are being developed on an ongoing basis to control the parameters of the nuclear reactor and conduct the research at a high technological level. The reactor is equipped with the information and measurement system, which records, displays and archives the sensor readings during the start-up. The reactor thermal parameters are recorded with a frequency of 10 Hz by the resistance thermometers, pressure, level and flow sensors [2]. The coolant parameters are recorded at the inlet and outlet to the reactor core, therefore, the determination of the temperature distribution of the water and structural materials in the core is carried out by the indirect methods, including the computer simulation. The computer simulating methods have also been successfully applied to analyze the safety of conducting the reactor experiments at the IVG.1M reactor [3], determining the core neutronics and thermophysical characteristics [4-7], analyzing the hydraulic and thermophysical processes in the reactor FA [8-10]. When simulating the neutronics and thermohydraulic processes of the reactor core, each model had its drawbacks and assumptions.

The goal of the study presented in the article was to verify the adequacy of the chosen calculation method and obtain the calculated data on the temperature distribution in the fuel assembly of the IVG.1M research reactor when it operates at nominal and design levels of the realized power. The research was carried out using the method of the finite element analysis using a three-dimensional computer simulation. The advantage of the computer simulation used for the study, compared with previously used ones [8-10], is the fact that the twisted structure of the fuel rod was taken into account when developing the model. The scientific novelty of the research consists in determining by calculation the temperature modes of the fuel rods operation in the range of the reactor design power from 10 to 60 MW with a conservative approach to the cooling conditions.

2. Materials and methods

The IVG.1M RR core is equipped with a set of 30 WCTCs, which are located radially along three circles with the different radii. There are 12 WCTC with the FA height of 800 mm in the first and second rows, along the diameter of the radius 126 and 163.5 mm. There are 18 WCTCs with a 600 mm height of the fuel part in the third row along a circumference with a radius of 239 mm. The reflector surrounding the core is made of beryllium. Ten control drums (CD) with absorbing elements control the reactor and protect it. Each CD is equipped with a stepper motor that allows turning the drum from 0° to 180°. There is an experimental channel designed for the installation of the irradiated devices in the core central part. The experimental channel is surrounded by 12 beryllium reactivity compensation rods. Figure 1 shows the reactor diagram [5].

The fuel part of each of the 30 WCTC contains 468 fuel rods in a tight package. Twelve fillers with a diameter of 1.6 mm, 24 fillers with a diameter of 2.2 mm and an axial insert with a diameter of 7.4 mm are used to distance the fuel rods in the fuel assemblies. The fillers and the axial insert are made of E110 alloy. The fuel rods are in the form of spiral rods made using innovative technology [11]. The fuel rod is a metallurgically bonded cladding and core. The fuel core of the fuel rod is a matrix made of E110 alloy with strands of metallic uranium located along the axis. The number of uranium strands is 133, the diameter of the strand is ~40 μm. The fuel rod cladding is made of E110 zirconium alloy.

Figure 2 shows the diagram of the fuel element with the dimensions [8]. The reactor is cooled using a single-circuit coolant pumping pattern from a storage tank with a volume of 1,500 m^3. Three 4MSK-10 pumps are used to provide the sufficient coolant flow during the power start-up. The core is cooled as follows. The water is supplied through four paths to cool the reactor cover, the loop channel, the side reflector and the interchannel space in the reactor nominal operation mode. In the inter-channel space, the coolant moves upwards, cooling the outer surfaces of the walls. In the collection chamber under the reactor cover, the water is collected from the cover cooling paths, the side reflector and the interchannel space and enters the WCTC for cooling the FA, after which it is drained into a storage tank.

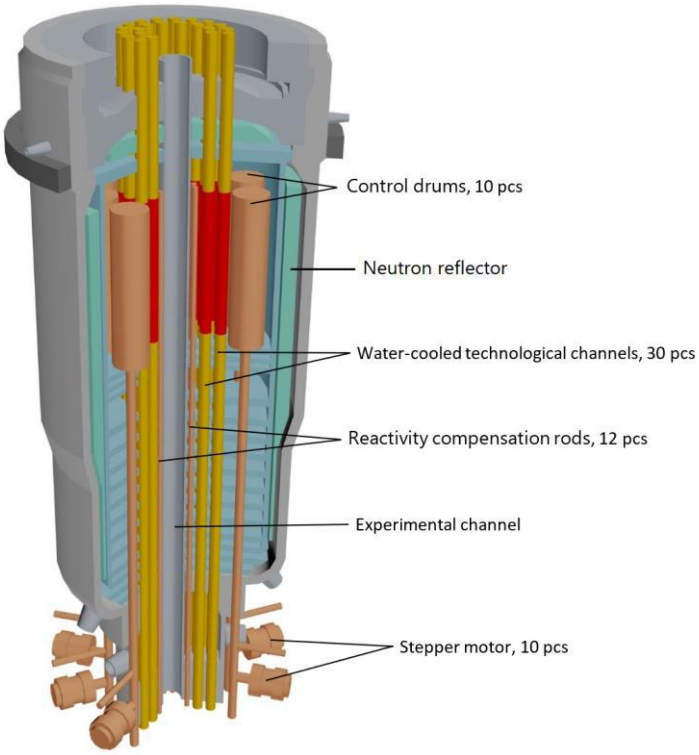

Fig.1. IVG.1M reactor diagram.

A three-dimensional model of the IVG.1M reactor FA was constructed in the ANSYS Fluent release 2021R2 software package to conduct the study [12]. The ANSYS Fluent is a universal software analysis system that implements the finite element method (FEM), which allows solving the stationary and non-stationary physical problems, including the simulation of the liquid and gas flows, heat transfer and heat exchange processes [13].

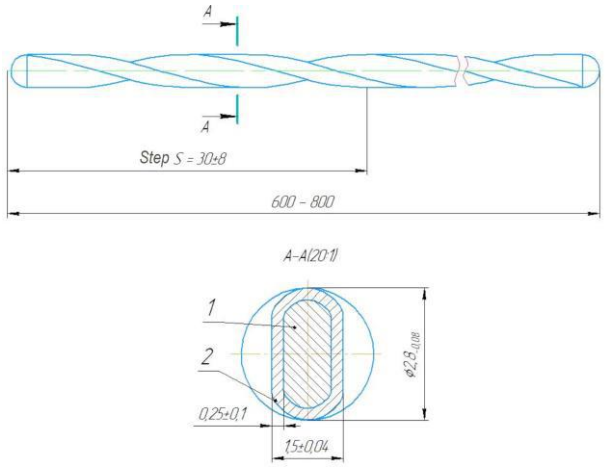

Fig.2. Fuel rod diagram: 1-core, 2-cladding.

Solving the problem using the numerical methods in the ANSYS Fluent software package includes the implementation of the basic sequential actions:

- defining the geometry of a computational model;
- splitting the model into a finite number of simple elements;
- setting the material properties required for the calculation;
- setting the initial and boundary conditions of the problem;
- selecting and configuring the solver, performing the calculation;
- analyzing and interpreting the results, performing additional calculations if necessary.

Figure 3 shows the computer simulation used to conduct the study with a superimposed finite element grid. The geometry of the computational model was chosen in the following way. The computational model is the FA elementary cell. The fuel rod fully corresponds to the actual geometric dimensions, taking into account the twist step of 30 mm. The model height corresponds to the height of the fuel part of the WCTC of 1st and 2nd rows in the and is 800 mm. During the construction of the model, it was assumed that the cross-sectional area for the coolant in the model is 1/468 of the cross-sectional area for the coolant in the WCTC since the fuel assembly contains 468 fuel rods.

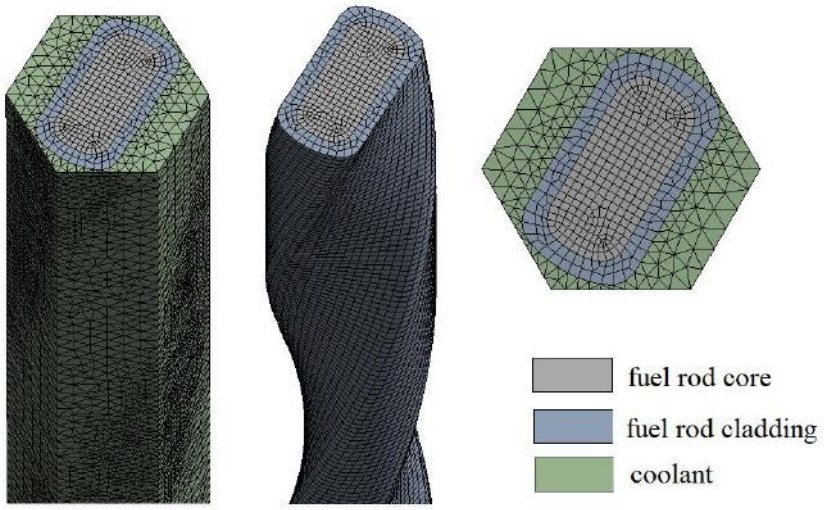

Fig.3. Calculation model of the IVG.1M reactor FA.

The flow section area for the coolant in the WCTC was determined by the formula (1):

$$S = 0.25 \cdot \pi \cdot d_0^2 - 468 \cdot S_{tv} - 0.25 \cdot \pi(n_1 \cdot d_1^2 + n_2 \cdot d_2^2 + d_c^2) \quad (1)$$

where:

d_0 is inner diameter of the FA shell, d_0=66.4 mm;

S_{tv} is cross-sectional area of the fuel rod, according to the technical documentation, S_{tv}=3.967 mm^2;

n_1 is number of type 1 fillers, n_1 = 12;

n_2 is number of type 2 fillers, n_2 = 24;

d_1 is diameter of type 1 fillers, d_1 = 1.6 mm;

d_2 is diameter of type 2 fillers, d_2 = 2.2 mm;

d_c is diameter of the axial insert, d_c = 7.4 mm.

The boundary conditions set for obtaining the temperature distribution in the FA model are given below:

- the symmetry condition is set on the side faces of the computational model;
- the coolant flow is determined by the conditions of mass flow inlet into the path and the outflow;
- the initial pressure in the path is assumed to be 1 MPa;
- the energy release profiling by the FA height is set using a text file.

The calculations have been carried out using the average values for the WCTC of 1st and 2nd rows, since the greatest energy release occurs in these channels, and consequently, the coolant and fuel rods reach the highest temperature values. The obtained data on the energy release as a result of the neutronics calculations are used to conduct the study. The energy release for the calculation is set with the assumption that all fuel rods in the assembly have the same energy release. Figure 4 show the relative energy release profile for the FAs of the WCTC of 1st and 2nd rows per 1 MW of the reactor power [14]. During the calculation, the thermophysical properties of the materials of the computer model [15, 16] are set depending on the temperature in the form of a piecewise linear function, while the properties of the fuel rod core are homogenized.

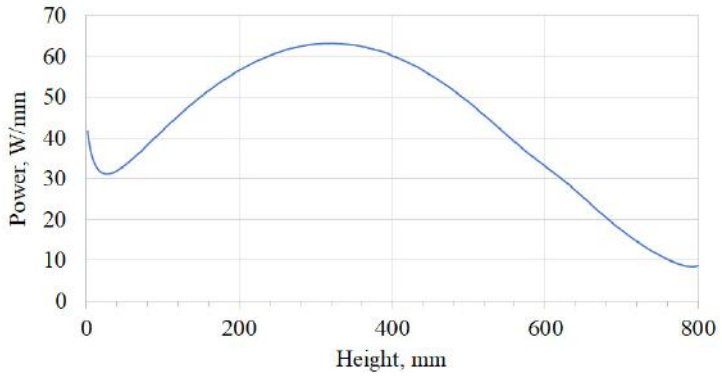

Fig.4. Profile of relative energy release of the WCTC of 1st and 2nd rows.

A k-ϵ Realizable flow model has been chosen to simulate the coolant turbulent flow. The finite element grid of the model consists of 3,353,802 units and 7,503,831 elements, the solution convergence is achieved by an iterative process. The temperature at the WCTC outlet is also determined by the energy balance equation [17] for substantiating the correctness of the calculation model and the selected solver settings (2):

$$\int_0^{800} Q = G \cdot Cp \cdot (T_{out} - T_{in}) \quad (2)$$

where:

Q – distribution of the energy release in the fuel rod by the assembly height, W;
G – coolant flow, kg/s;
Cp – water heat capacity at an average temperature in the path, J/(kg × °C);
Tout, Tin – coolant temperature at the FA outlet and inlet, respectively, °C.

3. Results and discussion

As a result of the study, the temperature field distributions for the stationary reactor operation modes have been obtained. The information on the technological parameters of the IVG.1M reactor, obtained from the results of power starts-up, was used as initial data for the thermophysical calculations. The problem boundary conditions were determined in accordance with the water temperature values at the core inlet and the water flow through the WCTC. The energy release by the FA height was set according to the reactor thermal power realized in the experiments. Table 1 shows the experimental values of the water flow through the WCTC, the water temperature at the WCTC inlet and outlet for 10 levels of the stationary reactor power.

Table 1. Comparison of the experimental data with calculated ones.

Parameter	Reactor power level[1], MW					
	1.00	**1.97**	**2.91**	**6.07**	**9.08**	**10.21**
Water flow for the WCTC of 1st and 2nd rows[1], kg/s	2.08	2.08	2.13	2.14	2.13	2.11
Water temperature at the WCTC inlet[1], °C	24.8	17.4	22.9	26.2	29.6	28.2
Water temperature at the WCTC outlet[1], °C	28.9	25.1	34.3	49.5	64.0	67.3
Water temperature at the FA outlet[2], °C	28.7	25.2	33.9	49.3	64.4	67.7
Water temperature at the FA outlet[3], °C	28.7	25.2	34.1	49.3	64.3	67.6
Maximum temperature of the outer surface of the fuel rod cladding[2], °C	29.3	26.3	35.6	52.8	69.6	73.5
Maximum temperature of the fuel core[2], °C	29.6	26.9	36.5	54.7	72.5	76.8

[1]experimental values; [2]calculated values by computer modeling; [3]calculated values by the energy balance equation.

The table also shows the water temperature values at the WCTC outlet obtained by computer modeling and the values of the maximum calculated temperatures of the fuel core and the fuel rod surface for the given stationary power levels. For the comparison, the table shows the values of the calculated temperature at the FA outlet, calculated using the energy balance formula (2).

According to the analysis of the data given in Table 1, the value of the standard deviation of the experimental and calculated (according to the energy balance formula) water temperature at the FA outlet is ~0.31. The value of the standard deviation of the experimental and calculated (by the computer modeling method) water temperature at the FA outlet is ~0.23. Good consistency of the calculated results with experimental data allows estimating the adequacy of the calculated model and the chosen calculation method.

Figure 5 shows, as an example, the volumetric distribution of the temperature field obtained as a result of the calculation with the reactor thermal power at a stationary level of 10.21 MW. Figure 6 shows the temperature field and the velocity vector field of the model cross-section (10.21 MW) at the height with the maximum energy release (0.309 m).

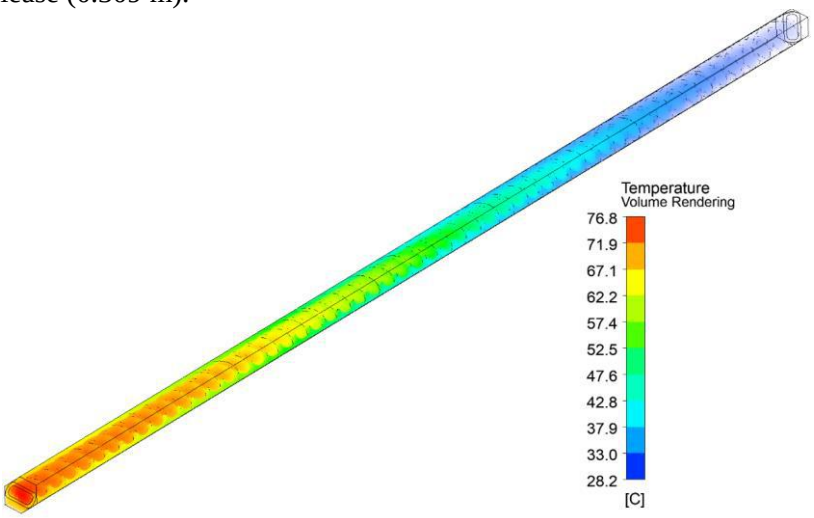

Fig.5. Volumetric distribution of the temperature field of the model.

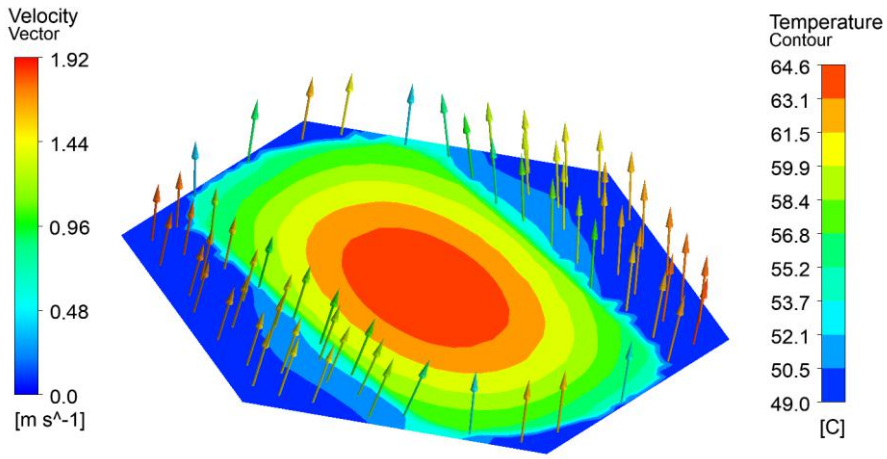

Fig.6. Temperature field of the FA model cross-section.

The operational documentation of a WCTC with low enriched fuel contains the information on the limits of the permissible values of the thermal technical parameters during the operation, however, the cooling modes of the core for ensuring the safe operation at a power level from 10 to 60 MW are not regulated. At present, the restrictions on the realized capacity of the IVG.1M research reactor are associated with the complete set of the cooling system, which can provide a water flow rate of no more than 2.5 kg/s, while the limit of the WCTC normal operation for a set flow rate is 12 kg/s.

A series of calculations has been carried out to assess the temperature modes of the fuel rods during the reactor operation at a design capacity of 10 to 60 MW. When setting the boundary conditions, the conservative cooling conditions were chosen. The water temperature at the FA inlet was assumed to be 55 °C, which is the limit value of the WCTC normal operation. The water flow for cooling was chosen according to the energy

balance equation (2) in such a way that the water temperature at the FA outlet was of maximum permissible value of the WCTC normal operation, equal to 95 °C.

Figure 7 shows the dependence of the calculated values of the water temperature at the FA outlet, the maximum temperatures of the fuel core and the fuel rod cladding at the reactor operating power at the level from 10 to 60 MW at the specified coolant flow rates through the WCTC.

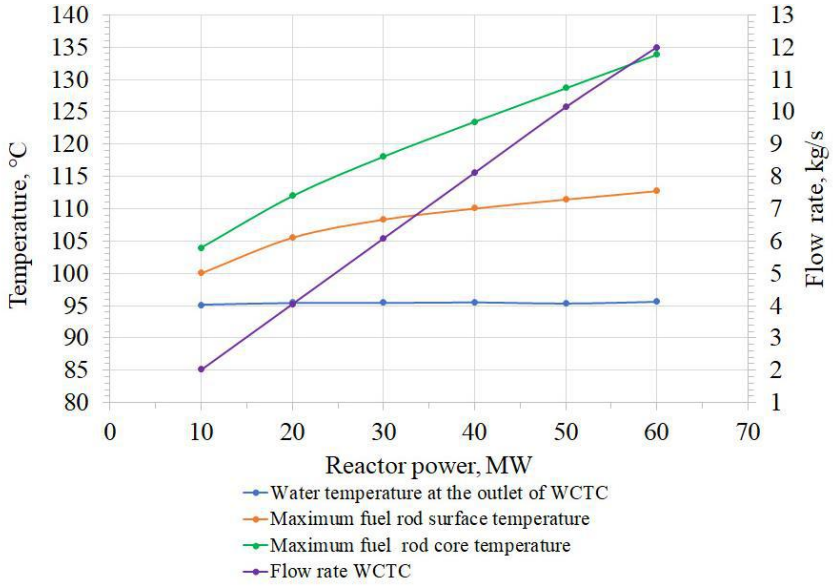

Fig.7. Dependence of the fuel rod temperature on the reactor operation power at a set water flow rate.

As Figure 7 shows, the maximum calculated temperature of the fuel core under the specified cooling conditions does not exceed the limit of the WCTC normal operation equal to 146 °C. The temperature limit of the WCTC normal operation for the surface of the fuel rod is 110 °C. The maximum calculated surface temperature of the fuel rod slightly (2 °C) exceeds the limit value of the WCTC normal operation only if the reactor is operating at a power level of 60 MW and the WCTC water rate is 12 kg/s.

To analyze the calculated results, it is necessary to take into account that the emergency protection settings of the reactor are set by the personnel according to the appropriate start-up program for each experiment and under the standard conditions of conducting the experiments at a power level of up to 10 MW for the coolant temperature values and are 50 °C at the reactor inlet and 95 °C at the outlet.

4. Conclusions

As a result of the computational studies using the three-dimensional computer model of the FA of the IVG.1M reactor, the temperature distribution of fuel rods and coolant has been determined under the stationary reactor operating modes at various power levels from 1 to 10 MW. The good consistency of the calculated results with experimental data has confirmed the adequacy of the calculation model and the chosen calculation method.

In a series of the calculations, the temperature modes of the operation of the fuel rods have been determined in the range of the design capacity from 10 to 60 MW with the minimum values of the coolant flow, providing the coolant temperature within the values of the WCTC normal operation. The calculation results show that under the set cooling conditions, the temperature modes of the operation of the fuel rods correspond to the values of the WCTC normal operation.

The computer model can be used for determining the characteristics of the IVG.1M reactor core under various operating modes, as well as for analyzing the thermohydraulic processes in the FA. The disadvantage of the model is that the model geometry does not allow determining the radial temperature distribution of the fuel rods in the FA, and also does not take into account the heat transfer from the WCTC outer surface into the coolant.

Conflict of interest statement

The authors declare that they have no conflict of interest in relation to this research, whether financial, personal, authorship or otherwise, that could affect the research and its results presented in this paper.

CRediT author statement

Skakov, M.K.: Supervision, Project administration; Martynenko, Ye.A.: Writing-Original Draft, Investigation, Methodology; Yerdybayeva N.K.: Writing-Review and Editing; Akayev A.S.: Conceptualization; Bekmuldin M.K: Data Curation, Visualization; Prozorova I.V.: Resources. The final manuscript was read and approved by all authors.

Funding

This work was funded by the Ministry of Science and Higher Education of the Republic of Kazakhstan (Program-Target Financing Project BR21882185 "Research in Support of the Creation and Safe Operation of a Nuclear Power Plant in the Republic of Kazakhstan").

References

1 Sabitova R., Popov Y., Irkimbekov R., Prozorova I., Derbyshev I., Nurzhanov E., Surayev A., Gnyrya V., Azimkhanov A. (2023) Results of Experiments under the Physical Start-Up Program of the IVG.1M Reactor. *Energies*, 16, 6263. DOI: 10.3390/en16176263.

2 Korovikov A.G., Ilyinych S.A., Yermakov V.A., Serikbayev B.S. (2018) Third phase of information and measuring system modernization of IVG.1M research reactor. *NNC RK Bulletin*, 3, 33 – 39. DOI:10.52676/1729-7885-2018-3-33-39. [in Russian]

3 Surayev A.S., Irkimbekov R.A., Ponkratov Yu.V. (2020) Calculation of the thermal state of the experimental device for tests in the IVG.1M reactor. *NNC RK Bulletin*, 2, 144 – 153. Available at: https://journals.nnc.kz/jour/article/view/253?locale=en_US [in Russian]

4 Sabitova R.R., Prozorova I.V., Irkimbekov R.A., Popov Yu.A., Bedenko S.V., Prozorov A.A., Mukhamediyev A.K. (2022) Methods to Study Power Density Distribution in the IVG.1M Research Reactor After Conversion. *Applied Radiation and Isotopes*, 185, 110259. DOI:10.1016/j.apradiso.2022.110259.

5 Prozorova I.V., Martynenko Y.A., Irkimbekov R.A., Popov Y.A., Suraev A.S., Gnyrya V.S., Sabitova R.R., Medetbekov B.S. (2023) Definition of Thermophysical Parameters of the IVG.1M reactor core with LEU fuel. *Neutron Spectroscopy. Nuclear structure. Related topics*. Russia, Dubna, 59 – 66. Available at: http://isinn.jinr.ru/proceedings/isinn-29/pdf/Prozorova.pdf

6 Irkimbekov R., Vurim A., Vityuk G., Zhanbolatov O., Kozhabayev Z., Surayev A. (2023) Modeling of Dynamic Operation Modes of IVG.1M Reactor. *Energies*, 16, 932. DOI:10.3390/en16020932.

7 Irkimbekov R.A., Zhagiparova L.K., Kotov V.M., Vurim A.D., Gnyrya V.S. (2019) Neutronics Model of the IVG.1M Reactor: Development and Critical-State Verification. *Atomic Energy*, 127, 69–76. DOI:10.1007/s10512-019-00587-1.

8 Martynenko E.A., Erdybayeva N.K., Akaev A.S., Bekmuldin M.K., Turkach A.A. (2023) Kompyuternoe modelirovanie raspredeleniya temperaturyi TVS reaktora IVG.1M. *Bulletin of Toraigyrov University*. *Energetics series*, 3, 197 – 209. DOI: 10.48081/YBCY7199. [in Russian]

9 Khazhidinov A.S., Akayev A.S., Ganovichev D.A. (2019) Computation of a temperature field of the IVG.1M WCTC-LEU in optimized and advanced models. *NNC RK Bulletin*, 3, 76-80. DOI:10.52676/1729-7885-2019-3-76-80. [In Russian]

10 Khazhidinov A.S., Ganovichev D.A., Akaev A.S., Martynenko Ye.A., Khazhidinova A.R. (2018) Validation of the thermophysical model of IVG.1M reactor WCTC-LEU. *NNC RK Bulletin*, 3, 45-49. DOI:10.52676/1729-7885-2018-3-45-49. [In Russian]

11 Zaytsev D.A., Repnikov V.M., Soldatkin D.M., Solntsev V.A. (2017) Studies of behavior of the fuel compound based on the U-Zr micro-heterogeneous quasialloy during cyclic thermal tests. *Journal of Physics: Conference Series*, 891(1). DOI:10.1088/1742-6596/891/1/012181.

12 ANSYS Fluent Workbench Tutorial Guide Release 2021 R2. (2021), ANSYS Inc., Southpointe. Available at: https://dl.cfdexperts.net/cfd_resources/Ansys_Documentation/Fluent/Ansys_Fluent_Workbench_Tutorial_Guide_2021_R2.pdf

13 Bruyaka A., Fokin V.G., Soldusova E.A., Glazunova N.A., Adeyanov I.E. (2010) *Inzhenernyj analiz v ANSYS Workbench*, Samar.gos.tekhn.un-t, Samara, 217 p. [In Russian] Available at: https://studizba.com/show/1041590-2-bruyaka-va-inzhenernyy-analiz-v-ansys.html

14 Sabitova R.R., Popov Yu.A., Irkimbekov R.A., Prozorova I.V., Bedenko S.V. (2023) Calculated and experimental data on energy release profile in the fuel assembly of the IVG.1M reactor after fuel enrichment reduction. *NNC RK Bulletin*, 83-87. DOI:10.52676/1729-7885-2023-1-83-87. [In Russian]

15 Bobkov V.P., Fokin L.R., Petrov E.E., Popov V.V. Rumiantsev V.N., Savvatimsky A.I. (2008) *Thermo-physical Properties of Materials for Nuclear Engineering: A Tutorial and Collection of Data*, International Atomic Energy Agency, Vienna, 2000 p. Available at: https://www-pub.iaea.org/MTCD/Publications/PDF/IAEA-THPH_web.pdf

16 Rivkin S.L., Aleksandrov A.A. (1984) *Termodinamicheskie svojstva vody i vodyanogo para*. Energoatomizdat, Moskow, 84 p. [In Russian] Available at: https://studizba.com/show/850980-14-.html

17 Miheev M.A., Miheeva I.M. (1977) *Osnovy teploperedachi*, Energiya, Moscow, 344 p. [In Russian] Available at: https://studizba.com/show/1013624-1-osnovy-teploperedachi-miheev-ma.html

AUTHORS' INFORMATION

Skakov, Mazhyn Kanapinovich - Doctor of phys.-math. sciences, Professor, Chief Researcher, National Nuclear Center of the Republic of Kazakhstan, Kurchatov, Kazakhstan; Scopus Author ID: 6506859122; ORCID iD: 0000-0003-3716-8846; skakov@nnc.kz

Martynenko, Yekaterina Alexandrovna - PhD Student, Chief of Group, Institute of Atomic Energy Branch of RSE NNC RK, Kurchatov, Kazakhstan; D. Serikbayev East Kazakhstan Technical University, Ust-Kamenogorsk, Kazakhstan; Scopus Author ID: 57854824300; ORCID iD: 0000-0002-1423-4524; Kirichek@nnc.kz

Yerdybayeva, Nazgul Kadyrbekovna - Doctor of phys.-math. sciences, Professor, D.Serikbayev East Kazakhstan Technical University, Ust-Kamenogorsk, Kazakhstan; Scopus Author ID: 36633438100; ORCID iD: 0000-0003-0314-0503; nyerdybayeva@mail.ru

Akayev, Asan Sabyrovich. - Head of Department, Institute of Atomic Energy Branch of RSE NNC RK, Kurchatov, Kazakhstan; Scopus Author ID: 57321455500; ORCID iD: 0000-0003-4792-6161; akaev@nnc.kz

Bekmuldin, Maksat Kuatbekovich - PhD Student, Chief of Laboratory, Institute of Atomic Energy Branch of RSE NNC RK, Kurchatov, Kazakhstan; Scopus Author ID: 57321072600; ORCID iD: 0000-0002-6895-536X; bekmuldin@nnc.kz

Prozorova, Irina Valentinovna - Head of Laboratory, Institute of Atomic Energy Branch of RSE NNC RK, Kurchatov, Kazakhstan; Scopus Author ID: 57220986470; ORCID iD: 0000-0001-8701-9756; prozorova@nnc.kz

EURASIAN PHYSICAL TECHNICAL JOURNAL

2024, Volume 21, No.3 (49)

https://doi.org/10.31489/2024No3/54-62

Received: 22/03/2024 Revised: 03/07/2024 Accepted: 20/09/2024 Published online: 30/09/2024

Original Research Article

UDC 53.043, 546.05

SYNTHESIS AND CHARACTERIZATION OF HYDROXYAPATITE UNDER INFLUENCE OF ULTRAVIOLET RADIATION AND ULTRASONIC EXPOSURE

Mostovshchikov A.V.[1, 2], Grebnev M.E.[2], Rudmin M.A.[1], Nazarenko O.B.[1*], Derina K.V.[1], Galtseva O.V.[1, 2]

[1]Tomsk Polytechnic University, Tomsk, Russia
[2] Tomsk State University of Control Systems and Radioelectronics, Tomsk, Russia
*Corresponding author: olganaz@tpu.ru

Abstract. *Hydroxyapatite has a wide range of possible applications in biomedicine, optics and electronics, sensors, catalysis and in environmental decontamination. The present study focused on the synthesis of hydroxyapatite by the wet precipitation method. The influence of drying time on the properties of synthesized material was investigated. The particle size increases from 80 to 200 μm by increasing the drying time from 24 hours to 96 hours. The morphology and properties of hydroxyapatite powders obtained under the action of the ultraviolet radiation and ultrasonic exposure acting together and individually was studied. The obtained samples were analyzed using X-ray diffraction, Fourier transform infrared spectroscopy, scanning electron microscope, Brunauer–Emmett–Teller methods. The results showed that the properties of the obtained hydroxyapatite powders were highly dependent on the synthesis conditions. Ultrasonic treatment at the synthesis stage led to a decrease in the size of the resulting hydroxyapatite particles to 4 μm. The use of ultraviolet radiation at the stabilization stage led to an increase in the content of hydroxyapatite in the reaction products.*

Keywords: hydroxyapatite, wet precipitation, ultrasound, ultraviolet radiation.

1. Introduction

Hydroxyapatite (HAp) is a calcium phosphate mineral of composition $Ca_{10}(PO_4)_6(OH)_2$, it is widely known as a biomaterial and used for bone repair and bone regeneration [1–3]. HAP has excellent biocompatibility and exhibits dielectric and piezoelectric properties [4]. Theoretically, the band gap of HAP can reach 7.4–7.9 eV, although the values of 3.8–4.5 were observed in the experiments [5,6]. Such values of the band gap make it possible to use HAp as a dielectric in metal-insulator-semiconductor (MIS) structures, which presents new opportunities for sensorics and microelectronics. Based on the fact that HAp has a piezoelectric effect, it is possible to convert some physical influences, such as sound vibrations, touch, temperature, into an electrical signal. This effect is already being used in such devices as sensors, actuator devices, transducers, micro power generators in electronics, civil infrastructure systems, biomedical and automotive applications [7,8]. A number of studies are devoted to the use of HAp in catalytic process: for catalytic oxidation of organic pollutants and CO [9,10], catalytic reduction of CO_2 and N_2O [11,12], for environmental remediation [13].

There are a large number of different methods for the synthesis of HAp. Depending on the composition of the initial substances and the synthesis conditions, the following main methods for obtaining hydroxyapatite can be distinguished: solid state reactions [14], chemical precipitation [15], hydrothermal synthesis and sol-

gel process [16]. In addition, microwave irradiation accelerates the synthesis of HAp and produces a high-purity powder with a small and narrow particle size distribution [17, 18].

Various methods of obtaining hydroxyapatite have their advantages and disadvantages due to the multifactorial nature of the synthesis process, the need to coordinate such parameters as reaction temperature, pH, molar ratio of chemicals, etc. to obtain a product with the required properties [19]. Therefore, researchers are studying the possibility of influencing the reaction mixture to various factors, including ultraviolet (UV) radiation and ultrasonic (US) exposure, in order to synthesize HAp with desired characteristics. UV irradiation of the source materials made it possible to carry out the solid-phase synthesis of HAp without the use of heat treatment [20-21]. It was found that ultrasonic treatment of the initial suspension of calcium hydroxide during chemical precipitation increases the rate of formation of the hydroxyapatite nanocrystalline phase [22, 23].

The aim of the present work is to study the effect of drying time, ultraviolet radiation and ultrasonic exposure on the synthesis of hydroxyapatite by the wet precipitation method and the properties of synthesized material.

2. Materials and methods

The starting materials for the synthesis of HAp were calcium hydroxide $Ca(OH)_2$, distilled water, orthophosphoric acid H_3PO_4. Figure 1 shows the scheme for obtaining hydroxyapatite, according to which the process consists of the following stages: preparation of initial solutions – synthesis – stabilization – filtration and washing – drying. In this synthesis method, by controlling the feed rate of the phosphoric acid solution and its concentration, it is possible to ensure complete interaction of the initial reagents, which will exclude the formation of side phosphates or minimize this probability, leading the entire synthesis to the desired result – calcium hydroxyapatite of stoichiometric composition.

8% solution of orthophosphoric acid and 20% suspension of calcium hydroxide were prepared at the first stage. The calcium hydroxide suspension was loaded into the reactor at the second stage. A solution of orthophosphoric acid was added and reacts with calcium hydroxide according to the following reaction with continuous stirring [24, 25]:

$10\ Ca(OH)_2 + 6H_3PO_4 \rightarrow Ca_{10}(PO_4)_6(OH)_2 + 18H_2O$.

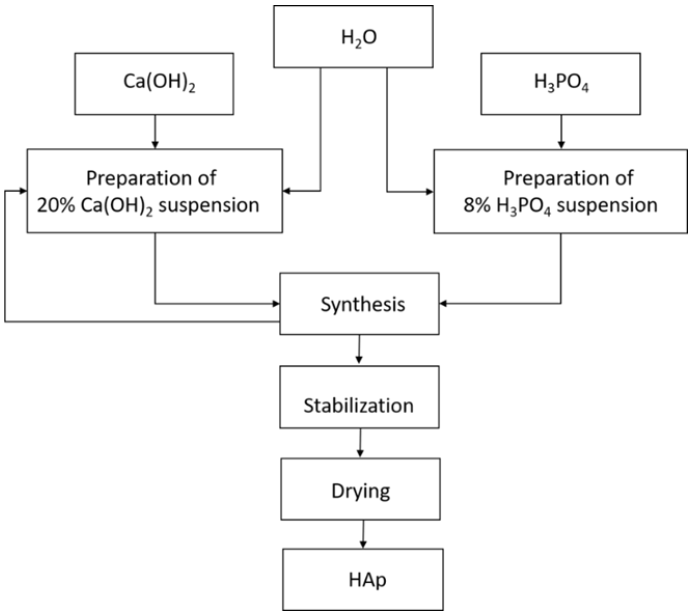

Fig.1. Scheme for synthesis of hydroxyapatite.

Synthesis time varied depending on the quantity of reagents used. It took 65 minutes to produce 20 grams of hydroxyapatite. In order for all reagents to completely react with each other, a stage of stabilization of the hydroxyapatite solution was introduced. This process was carried out at room temperature. Stabilization should be carried out in a sealed container to avoid impurities. The solution was infused for a day from the moment of stopping stirring. As a result, HAp was at the bottom of the vessel, and the liquid phase was at the top. After

the stabilization stage, the obtained sample was washed with distilled water until a neutral medium was obtained, which was controlled by a litmus indicator. Then, the resultant suspension was filtered through the "blue ribbon" filter, as a result of which HAp was separated from the liquid phase. At the stage of drying, HAp was dried at room temperature until the liquid is completely removed. To study the effect of drying time on the structure of the material, drying was carried out for 24 hours and 96 hours. To obtain the final product in the form of a powder, the synthesized material was ground using an agate mortar and pestle.

To study the influence of external factors on the change in the properties of the HAp obtained during the synthesis, ultrasonic (US) exposure, ultraviolet (UV) irradiation separately at various stages of production, as well as their combination, were used. The mixture of reagents in the reactor at the stage of synthesis was exposed to ultrasound at a frequency of 20 kHz for 20 min. At the stabilization stage, the synthesized sample was irradiated with ultraviolet. The wavelength of ultraviolet radiation was 180 nm. The following combinations of the experimental conditions have been investigated:

1) wet precipitation without the stabilization stage (standard conditions according to the methodology);
2) US (20 minutes, synthesis stage) and UV (120 minutes, stabilization stage);
3) US (20 minutes, synthesis stage);
4) UV (120 minutes, stabilization stage);
5) wet precipitation including the stabilization stage.

The phase composition of the obtained samples was analyzed by the X-ray diffraction (XRD) method using a Difray 401 diffractometer (JSC Scientific Instruments, St. Petersburg, Russia). The XRD peaks were recorded in 2Θ range of 30–110°, CuKα, λ = 1.5405 Å. Identification of crystalline phases was achieved by comparing the recorded diffraction patterns with ICDD PDF2 database; numbers of patterns from database, that was 11008 and 30747.

The functional groups of the obtained samples were identified by the method of Fourier transform infrared spectroscopy (FTIR) using a Shimadzu IRPrestige-21 FTIR spectrophotometer (Shimadzu, Kyoto, Japan). The analysis was performed in the absorption mode in the wavelength range from 400 cm^{-1} to 4000 cm^{-1} with a resolution of 4 cm^{-1}. The surface morphology and microstructure of the obtained samples was studied using a scanning electron microscope (SEM) TESCAN VEGA 3 SBU (Brno, Czech Republic) with an OXFORD X-Max 50 energy-dispersive adapter (High Wycombe, UK), operated at 10–20 kV accelerating voltage, specimen current of 3–12 nA, and a spot diameter of ~2 μm.

The surface area study was carried out using the BET adsorption method with the calculation of pore diameter using the BJH method [26]. Measurements were performed using a 3P Sync 420A specific surface area and porosity adsorption analyzer (3P Instruments, Germany). Nitrogen was used as an adsorptive. The results were processed using built-in software. All samples were pre-dried to remove gases for 10 hours at 200 °C. Based on the results of the analysis, adsorption isotherms were obtained.

3. Research results

3.1 Effect of drying time

Using scanning electron microscopy, the morphology of the samples for drying time of 24 and 96 hours was analyzed. The SEM images with different magnification are shown in Figure 2. All synthesized particles are characterized by the form of aggregates and porous structure. With a drying time of 24 hours, the particles have a size of more than 80 μm. With an increase in drying time to 96 hours, the particle size becomes larger than 200 μm, and the faceting becomes more noticeable. Based on the XRD-results shown in Figure 3, it was revealed that both samples correspond to the crystalline phase of calcium hydroxyapatite and do not contain additional reflections of other phases. On the XRD pattern of the Sample 1, there is a doubling high for reflections, which is associated with incomplete crystallization.

3.2 Influence of external factors

FTIR spectra of the samples obtained under the influence of external factors of ultrasonic and ultraviolet exposure and control samples are shown in Figure 4. Absorption bands related to the phosphate group PO_4^{3-} are observed at 470, 567, 603, 962 and 1039÷1080 cm^{-1} [27]. The absorption bands at 873 and 1421÷1465 cm^{-1} is attributed to CO_3^- groups [27, 28], the presence of which can be explained by the adsorption of atmospheric carbon dioxide during sample preparation. The broad absorption band at 3420 cm^{-1} and weak band at 1640 cm^{-1} are due to the presence of adsorbed water molecules [29].

The bands appearing at 3571 cm^{-1} corresponds to the hydroxyl bond stretch which is characteristic of stoichiometric HAp [27]. Comparing the spectra with each other, we can conclude that US exposure (Sample 3) and the combined action of US and UV (Sample 2) does not give particularly noticeable changes. At the same time, in the case of using only UV radiation (Sample 4), it can be seen that UV radiation has a weak effect on water, but actively destroys carbon compounds.

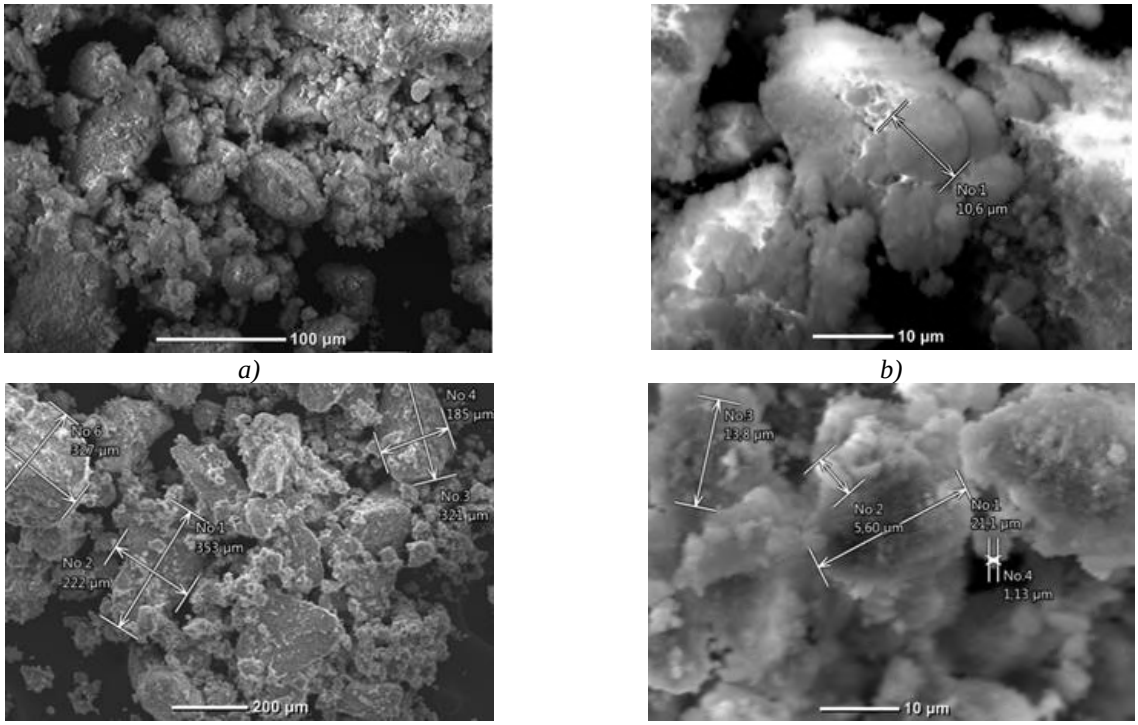

a) *b)*

c) *d)*

Fig.2. SEM images of the HAp samples obtained at different drying time: 24 h (a, b) and 96 h (c, d).

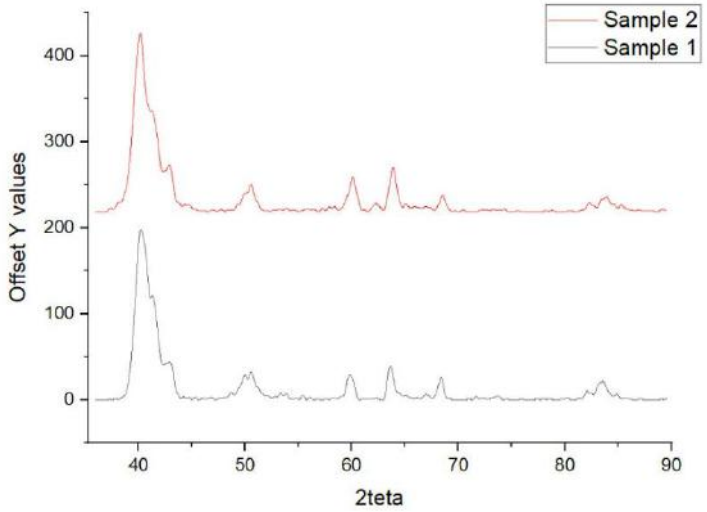

Fig.3. XRD patterns of the HAp samples obtained at different drying time: 24 h (Sample 1) and 96 h (Sample 2).

Figure 5 shows the XRD patterns of the HAp samples obtained under the influence of US exposure and UV radiation and of the control samples. According to the XRD data, the highest content of HAp is characteristic of the sample obtained by exposure to UV radiation only (Sample 4). The lowest content of hydroxyapatite is typical for the Sample 1, where the wet precipitation method without stabilization stage was used.

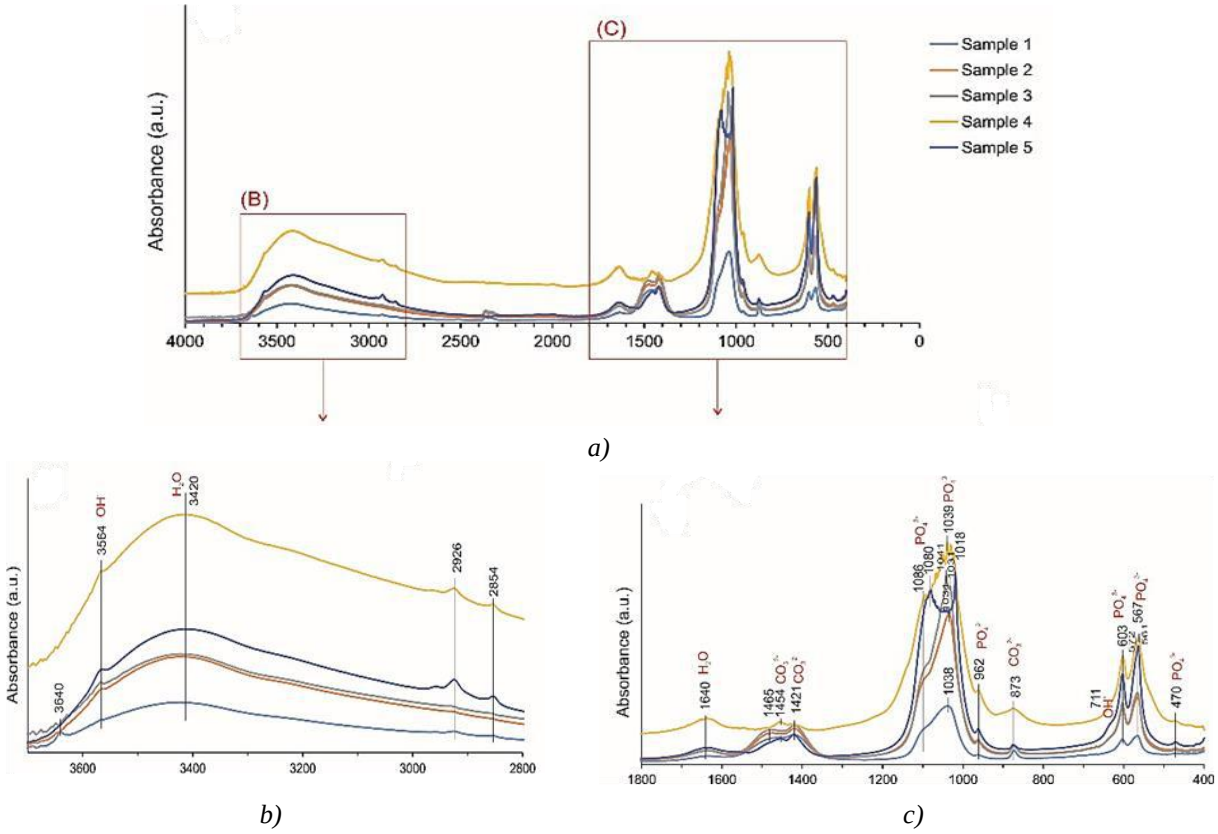

Fig.4. FTIR spectra of the HAp samples obtained under the influence of external factors.

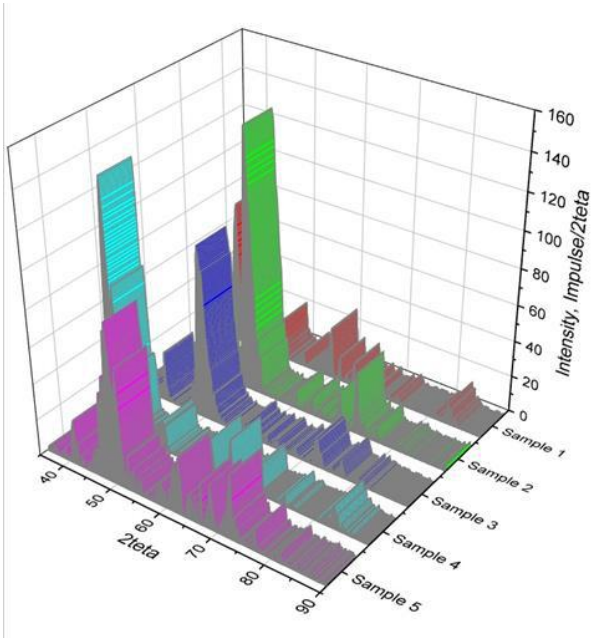

Fig.5. XRD patterns of the HAp samples obtained under the influence of external factors.

Figure 6 and 7 show the SEM images of the control samples synthesized under conditions without external influences and the samples under the action of US and UV. The Sample 1 is characterized by the presence of a greater number of agglomerates with a size of more than 100 μm, compared with Sample 5, for which the particle size is from 100 μm to 15 μm or less (Figure 6). Thus, introduction of the stabilization stage makes it possible to obtain the particles of smaller sizes without additional use of external factors. The Sample 2 (US+UV) and Sample 3 (US) are characterized by a rounded structure, which was formed as a result of a decrease in the crystallization rate due to US exposure (Figure 7).

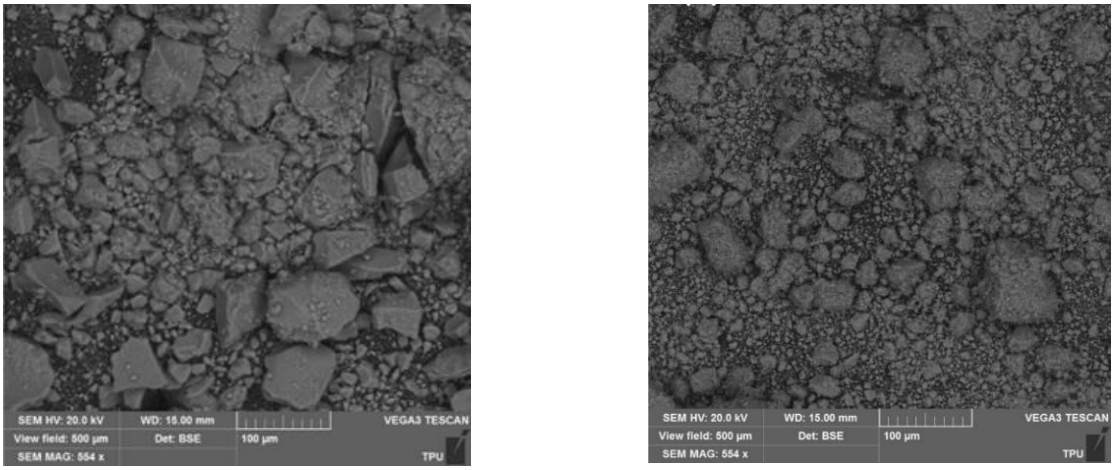

a) *b)*

Fig.6. SEM images of the HAp obtained at standard conditions of wet precipitation: Sample 1 (a), Sample 5 (b).

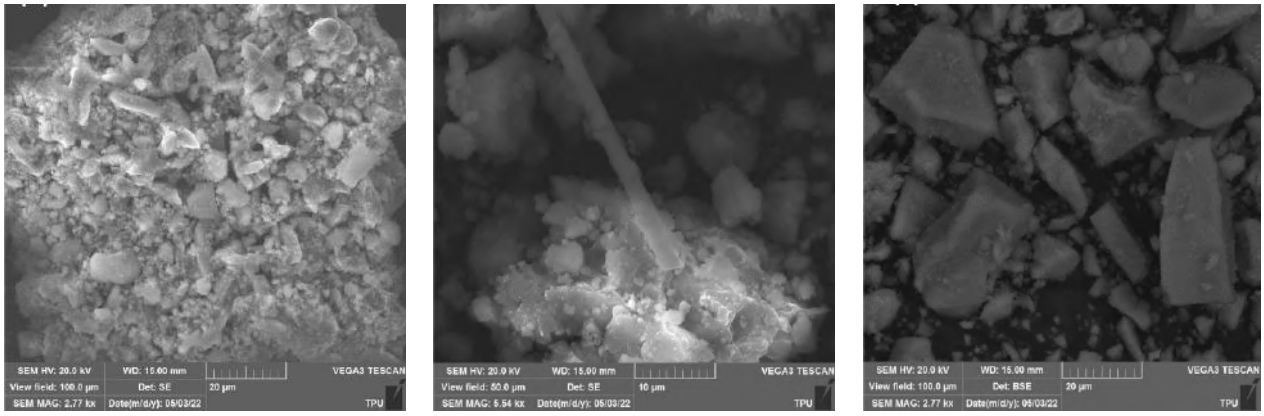

a) *b)* *c)*

Fig.7. SEM images of the HAp obtained under the influence of external factors: Sample 2 (a), Sample 3 (b), Sample 4 (c).

These samples are characterized by particle sizes from 4 μm to 1 μm or less. The Sample 4, obtained under exposure to UV only, is characterized by a faceted structure, which may be due to the fact that the crystallization processes were not interfered with by US. In this case, the particle sizes are in the range from 20 μm to 2 μm or less. The use of ultrasound at the stage of synthesis prevents the formation of bonds between particles and makes it possible to significantly reduce the size of the obtained particles with a spherical shape, in contrast to faceted crystallites in the case of ultraviolet irradiation.

Adsorption isotherms with sorption hysteresis were obtained, which are typical for systems with weak interaction of the adsorbate with the adsorbent, based on the results of the analysis of the specific surface area. The results are summarized in Table 1. It follows that the considered external influences on the synthesis of HAp increase the average pore diameter from the analysis of the data obtained, while a significant decrease in the specific surface area occurs, except for Sample 3. Thus, short-term exposure to ultrasound on a sample of hydroxyapatite during its synthesis leads to an increase in the specific surface area surface and the increase in average pore size.

Table 1. Specific surface area and pore size of the HAp samples obtained under the influence of external factors.

Parameters	Sample number				
	1	2	3	4	5
BET surface area (m^2/g)	138.280	118.239	157.628	110.235	117.492
Average pore diameter (nm)	9.450	12.076	13.445	15.367	10.390

4. Conclusion

In this study, hydroxyapatite was obtained by wet precipitation method. A stabilization stage was introduced into the technological scheme of synthesis, due to which the average particle size of the obtained hydroxyapatite was reduced to 15 μm. The drying time of the obtained hydroxyapatite affects the particle size of the material. An increase in the duration of drying of hydroxyapatite from 24 to 96 hours led to an increase in particle size up from 80 μm to 200 μm and to a more pronounced faceting. It was found that the use of ultraviolet irradiation at the stabilization stage makes it possible to increase the content of the main product – hydroxyapatite of stoichiometric composition. The ultrasonic treatment of reagents at the stage of HAp synthesis for 20 min led to a reduction in the size of the obtained HAp particles with a spherical shape from 15 μm to 4 μm. In addition, the production of hydroxyapatite under ultrasound exposure resulted in an increase in the specific surface area of particles by 14% and the average pore size by 42% compared to the wet precipitation method under standard conditions. The method of hydroxyapatite production considered in this work allows synthesizing a bulk material, unlike the CVD or PVD methods traditionally used to produce hydroxyapatite-based coatings [30]. Using the proposed method will allow to create bulk medical products filled with hydroxyapatite with the required properties.

Conflict of interest statement

The authors declare that they have no conflict of interest in relation to this research, whether financial, personal, authorship or otherwise, that could affect the research and its results presented in this paper.

CRediT author statement

Mostovshchikov A.V.: Writing – original draft, Methodology, Conceptualization; Grebnev M.E.: Investigation, Visualization; Rudmin M.A.: Formal analysis, Data curation; Nazarenko O.B.: Writing – review & editing, Validation, Supervision; Derina K.V.: Investigation; Galtseva O.V.: Formal analysis.

The final manuscript was read and approved by all authors.

Acknowledgments

This research was supported by the Tomsk Polytechnic University development program.

The equipment of the TPU's "Physical and chemical methods of analysis" has been applied.

References

1 LeGeros R.Z., LeGeros J.P. Hydroxyapatite. (2008) *Bioceramics and their Clinical Applications*. Woodhead Publishing. 367 – 394. DOI: 10.1533/9781845694227.2.367.

2 Rial R., González-Durruthy M., Liu Z., Ruso J.M. (2021) Advanced materials based on nanosized hydroxyapatite. *Molecules*, 26, 3190. DOI: 10.3390/molecules26113190.

3 Dorozhkin S.V. (2022) Calcium orthophosphate (CaPO4)-based bioceramics: preparation, properties, and applications. *Coating*, 12, 1380. DOI: 10.3390/coatings12101380.

4 Das A., Pamu D. (2019) A comprehensive review on electrical properties of hydroxyapatite based ceramic composites. *Materials Science and Engineering: C*, 101, 539–563. DOI: 10.1016/j.msec.2019.03.077.

5 Corno M., Busco C., Civalleri B., Ugliengo P. (2006) Periodic ab initio study of structural and vibrational features of hexagonal hydroxyapatite $Ca_{10}(PO_4)_6(OH)_2$. *Physical Chemistry Chemical Physics*, 8, 2464–2472. DOI:10.1039/B602419J.

6 Bystrov V., Paramonova E., Avakyan L., Coutinho J., Bulina N. (2021) Simulation and computer study of structures and physical properties of hydroxyapatite with various defects. *Nanomaterials*, 11, 2752. DOI:10.3390/nano11102752.

7 Yang Z., Zhou S., Zu J., Inman D. (2018) High-performance piezoelectric energy harvesters and their applications. *Joule*, 2(4), 642–697. DOI:10.1016/j.joule.2018.03.011.

8 Aabid A., Raheman M.A., Ibrahim Y.E., et al. (2021) A systematic review of piezoelectric materials and energy harvesters for industrial applications. *Sensors*, 21, 4145. DOI: 10.3390/s21124145.

9 Xu Z., Li C., Wang N., Ding Y., Yan Z., Li Q. (2024) Functional graphitic carbon nitride/hydroxyapatite heterojunction for robust formaldehyde removal at ambient temperature. *Journal of Environmental Chemical Engineering*, 12(1), 111679. DOI: 10.1016/j.jece.2023.111679.

10 Lan Y.-T., Yang X.-Y., Liu S.-X., Miao Y.-X., Zhao Z. (2022) Highly dispersed silver nanoparticles supported on a hydroxyapatite catalyst with different morphologies for CO oxidation. *New Journal of Chemistry*, 46, 6940–6945. DOI: 10.1039/D2NJ00464J.

11 Wang Y., Zhou X., Wei X., et al. (2021) Co/hydroxyapatite catalysts for N_2O catalytic decomposition: design of well-defined active sites with geometrical and spacing effects. *Molecular Catalysis*, 501, 111370. DOI:10.1016/j.mcat.2020.111370.

12 Guo J., Duchesne P.N., Wang L., et al. (2020) High-performance, scalable, and low-cost copper hydroxyapatite for photothermal CO_2 reduction. *ACS Catalysis*, 10, 13668–13681. DOI: 10.1021/acscatal.0c03806.

13 Yamada H., Tamura K., Watanabe Y., Iyi N., Morimoto K. (2011) Geomaterials: their application to environmental remediation. *Science and Technology of Advanced Materials*, 12, 064705. DOI: 10.1088/1468-6996/12/6/064705.

14 Javadinejad H.R., Ebrahimi-Kahrizsangi R. (2021) Thermal and kinetic study of hydroxyapatite formation by solid-state reaction. *International Journal of Chemical Kinetics*, 53, 583–595. DOI: 10.1002/kin.21467.

15 Mobasherpour I., Soulati Heshajin M., Kazemzadeh A., Zakeri M. (2007) Synthesis of nanocrystalline hydroxyapatite by using precipitation method. *Journal of Alloys and Compounds*, 430, 330–333. DOI:10.1016/j.jallcom.2006.05.018.

16 Bilton M., Milne S.J., Brown A.P. (2012) Comparison of hydrothermal and sol-gel synthesis of nano-particulate hydroxyapatite by characterization at the bulk and particle level. *Open Journal of Inorganic Non-metallic Materials*, 2, 1–10. DOI: 10.4236/ojinm.2012.21001.

17 Yang Y., Ong J.L., Tian J. (2002) Rapid sintering of hydroxyapatite by microwave processing. *Journal of Materials Science Letters*, 21, 67–69. DOI: 10.1023/A:1014250813564.

18 Shaban N.Z., Kenawy M.Y., Taha N.A., Abd El-Latif M.M., Ghareeb D.A. (2021) Synthesized nanorods hydroxyapatite by microwave-assisted technology for in vitro osteoporotic bone regeneration through Wnt/β-catenin pathway. *Materials*, 14, 5823. DOI: 10.3390/ma14195823.

19 Mohd Pu'ad N.A.S., Abdul Haq R.H., Mohd Noh H., Abdullah H.Z., Idris M.I., Lee T.C. (2020) Synthesis method of hydroxyapatite: a review. *Materials Today: Proceedings*, 29(1), 233–239. DOI:10.1016/j.matpr.2020.05.536.

20 Sultana S., Hossain M.S., Mahmud M., et al. (2021) UV-assisted synthesis of hydroxyapatite from eggshells at ambient temperature: cytotoxicity, drug delivery and bioactivity. *RSC Advances*, 11(6), 3686–3694. DOI:10.1039/D0RA09673C.

21 Leonov A., Usacheva T., Lyapunov D., Voronina N., Galtseva O., Rogachev A. (2021) Improving the heat resistance of polymer electrical insulation systems for the modernization of induction motors. *Eurasian Physical Technical Journal*, 18(1) (35), 34–42. DOI: 10.31489/2021No1/34-42.

22 Poinern G.E., Brundavanam R.K., Mondinos N., Jiang Z.T. (2009) Synthesis and characterisation of nanohydroxyapatite using an ultrasound assisted method. *Ultrasonics Sonochemistry*, 16(4), 469–474. DOI:10.1016/j.ultsonch.2009.01.007.

23 Rouhani P., Taghavinia N., Rouhani S. (2010) Rapid growth of hydroxyapatite nanoparticles using ultrasonic irradiation. *Ultrasonics Sonochemistry*, 17(5), 853–856. DOI:10.1016/j.ultsonch.2010.01.010.

24 Bouyer E., Gitzhofer F., Boulos M.I. (2000) Morphological study of hydroxyapatite nanocrystal suspension, *Journal of Materials Science: Materials in Medicine*, 11(8), 523–531. DOI: 10.1023/A:1008918110156.

25 Agbeboh N.I., Oladele I.O., Daramola O.O., Adediran A.A., Olasukanmi O.O., Tanimola M.O. (2020) Environmentally sustainable processes for the synthesis of hydroxyapatite. *Heliyon*, 6(4), e03765. DOI:10.1016/j.heliyon.2020.e03765.

26 Sing K.S.W. (1998) Adsorption methods for the characterization of porous materials. *Advances in Colloid and Interface Science*, 76–77, 3–11. DOI:10.1016/S0001-8686(98)00038-4.

27 Kannan S., Lemos A.F., Ferreira J.M.F. (2006) Synthesis and mechanical performance of biological-like hydroxyapatites. *Chemistry of Materials*, 18(8), 2181–2186. DOI:10.1021/cm052567q.

28 Szterner P., Biernat M. (2022) The synthesis of hydroxyapatite by hydrothermal process with calcium lactate pentahydrate: the effect of reagent concentrations, pH, temperature, and pressure. *Bioinorganic Chemistry and Applications*, 3481677. DOI: 10.1155/2022/3481677.

29 Wang Y.J., Chen J.D., Wei K., Zhang S.H., Wang X.D. (2006) Surfactant-assisted synthesis of hydroxyapatite particles. *Materials Letters*, 60(27), 3227–3231. DOI: 10.1016/j.matlet.2006.02.077.

30 Safavi M.S., Walsh F.C., Surmeneva M.A., Surmenev R.A., Khalil-Allafi J. (2021) Electrodeposited hydroxyapatite-based biocoatings: Recent progress and future challenges. *Coatings*, 11, 110. DOI:10.3390/coatings11010110.

AUTHORS' INFORMATION

Mostovshchikov, Andrei Vladimirovich – Doctor of Technical Sciences, Associate Professor, Professor, School of Earth Sciences and Engineering, Tomsk Polytechnic University; Professor, Department of Physical Electronics, Tomsk State University of Control Systems and Radioelectronics, Tomsk, Russia; Scopus Author ID: 15019762000; ORCID ID: 0000-0001-6401-9243; avmost@tpu.ru

Grebnev, Mark Ernestovich – Master's Student, School of Nuclear Science & Engineering, Tomsk State University of Control Systems and Radioelectronics, Tomsk, Russia; ORCID ID: 0009-0003-0937-5298; mark18091@gmail.com
Rudmin, Maxim Andreevich – Candidate of Geological and Mineralogical Sciences, Associate Professor, Division for Geology, School of Earth Sciences and Engineering, Tomsk polytechnic university, Tomsk, Russia; Scopus Author ID: 56350797200**;** ORCID ID: 0000-0002-9004-9929**;** rudminma@tpu.ru
Nazarenko, Olga Bronislavovna – Doctor of Technical Sciences, Professor, Division of Testing and Diagnostics, NDT School, Tomsk polytechnic university, Tomsk, Russia; Scopus Author ID: 57193908313; ORCID ID: 0000-0003-3245-3584; olganaz@tpu.ru
Derina, Ksenia Vladimirovna – Candidate of Technical Sciences, Associate Professor, Division of Chemical Engineering, School of Earth Sciences and Engineering, Tomsk Polytechnic University, Tomsk, Russia; Scopus Author ID: 57195258640; ORCID ID: 0000-0003-1663-4019; derinakv@tpu.ru
Galtseva, Olga Valerievna – Candidate of Technical Sciences, Associate Professor, Division of Testing and Diagnostics, NDT School, Tomsk Polytechnic University; Associate Professor, Department of Innovation Management, Tomsk State University of Control Systems and Radioelectronics, Tomsk, Russia; Scopus Author ID: 15049236900; ORCID ID: 0000-0001-6919-4833; tpuolga@tpu.ru

EURASIAN PHYSICAL TECHNICAL JOURNAL

2024, Volume 21, No.3 (49)

https://doi.org/10.31489/2024No3/63-70

Received: 29/06/2024 Revised: 27/08/2024 Accepted: 17/09/2024 Published online: 30/09/2024

Original Research Article

UDC 531.43; 621.8

MODELING THE PLASTIC DEFORMATION STATE OF THE CONTACT SURFACE DURING FRICTION

Tsyganov V.[1*], Sheyko S.[2], Hrechanyi O.[2], Vasilchenko T.[2]

[1] National University Zaporizhzhia Polytechnic, Zaporizhzhia, Ukraine
[2] Zaporizhzhia National University, Zaporizhzhia, Ukraine
*Corresponding author: tsyganov705@gmail.com

Abstract. *The mechanics of contact destruction of compounds during friction under conditions of complex thermodynamic loading was researched. The possibility of a mathematical description of complex damage to friction units and wear intensity is shown, taking into account the peculiarities of the surface layer formation during contact. A method for calculating the surface strength and durability of tribo-compounds is presented. This allows us to relate the parameters of the stressed state of a point (friction coefficient, shape factor) with the thermomechanical parameters of the process. By assessing changes in the friction coefficient and shape parameters, it becomes possible to determine the yield stress and establish structural transformations corresponding to a given stress state.*

Keywords: friction, load, plasticity theory, deformation, stress, tribocompounds.

1. Introduction

The main vector of modern mechanical engineering development is not only the creation of new materials, but also the study of their behavior during operation [1-2]. Currently, the results of research in the field of wear of materials under particularly severe conditions of mechanical and thermal loads, which are dynamic in nature, do not allow with a high degree of reliability to select (or develop) certain design and technological measures that are aimed at increasing the durability of products. This is caused, first of all, by the research conditions, which often do not correspond to the actual operating conditions of tribounits, since most of the parts of tribounits operate under conditions of complex dynamic loading associated with vibrations acting in different directions, which affects unstable synergetic processes [3].

The processes of friction and wear, as well as the destruction of surface layers of tribocompounds, are determined by the dynamic nature of the application of loads in contact, the amplitudes of mutual movements, creating specific conditions for contact interaction [4]. At the same time, most tribocompounds operate under conditions of complex three-dimensional dynamic loading: impact and slipping in two mutually perpendicular directions with exposure to both high and low temperatures. Such loading conditions cause a complex stress state of the surface layers of contacting pairs [5]. This explains the limited capabilities of the general provisions of the theory of friction, as well as most of the results of experimental studies.

2. Research methods

The solution of the contact problem of fracture mechanics of tribocompounds, which are operated under conditions of complex thermomechanical loading, is possible within the framework of assessing the

heterogeneity of the plastic deformation state, which is the main feature of metal products shaped by pressure processes. As a result, the metal of the product has different mechanical properties and fatigue resistance.

It is obvious that under contact loading conditions, the near-surface layers of the material are more damaged than the deep ones. Under repeated loading, fatigue microcracks appear on the surface even in the absence of contact loads and are located in active sliding planes, in which maximum shear stresses act [6]. Four successive stages of processes in the material can be distinguished in accordance with the characteristics of deformation and destruction of materials during fatigue: strengthening of the material due to an increase in the dislocation density in local volumes to a critical value; initiation and development of submicroscopic cracks; development of microcracks to the size of macrocracks; development and merging of macrocracks prior to spalling of surface elements.

The accumulation of defects, leading to the formation of microcracks, is determined by the characteristic features of the main structural elements of the material. Under the action of repeated impulse loads, the initial structure of the deformed material changes significantly. The subsurface zone (depth from several units to hundreds of micrometers) is a plastically deformed layer of material with a certain size and orientation of crystallites. The relationship between mechanical properties and structural parameters given in [7] shows that the resistance to brittle fracture depends not only on the grain size, but also on the size of the mosaic block. Moreover, the grain size does not uniquely determine the mechanical properties of the metal. The flow stress linearly depends on the size of the subgrains - the element of the substructure. A conclusion is made about the determining influence of the degree of misorientation on the resistance to destruction of the metal.

The need for an analytical solution to the spatial problem of plasticity theory is obvious. In general, the stressed and deformed state of the metal at each point of the deformation zone is different. This leads to heterogeneity of the physical and mechanical properties of the metal, ambiguity in determining the power parameters of the process, and energy consumption. Works have appeared showing the influence of plastic deformation on structural-phase transformations in metal. In this regard, determining the stress state at each point of the deformation zone is an urgent problem [8, 9].

3. Results and discussion

As shown by preliminary studies [9-12], complex three-dimensional loading (impact and sliding in two mutually perpendicular directions) creates conditions for the formation of fragments of the surface layer with relatively easy passage of dislocations through these crystallites to their boundaries. This helps to reduce the level of external stresses necessary for the mechanism of rotational plasticity to operate in the analyzed structures. The result is a surface layer with a more even texture, which is accompanied by increased wear. A change in the nature of the loading leads to a change in the state of the surface layer and, as a consequence, a change in the wear resistance of the tribocompounding.

Studies using an electron microscope made it possible to establish that as a result of plastic deformation, a developed cellular structure is formed in the surface layers, oriented along the direction of friction [13]. Fracture is initiated by cell edges perpendicular to the sliding direction, and the initial crack runs along these edges. Therefore, with relative sliding of surfaces, the initiation of differently oriented cracks is possible. Especially in the case of friction with sliding in two mutually perpendicular directions.

In the general case, the formation and growth of microcracks under cyclic loading significantly depends on both the structural state of the material and the number of loading cycles N. To describe the development of microstructurally short cracks, the equation presented in [14] is applicable:

$$\frac{db}{dN} = C(\Delta\gamma)^m (d - b), \tag{1}$$

where b – crack depth; $\Delta\gamma$ – shear strain range; d – characteristic size of a structure element; C and m – experimentally determined material constants.

From this equation it follows that as a crack grows to grain size, its speed decreases down to zero. At stresses above the endurance limit, the crack does not stop, but only slows down its growth or may stop for some time.

Moreover, the nature of the accumulation of deformations under the action of repeated impulsive and pulse loads is approximately the same [15]. Thus, under impact loading, the dependence of contact deformation on the number of cycles is nonlinear with three sections: in the first section, the hardening stage (approximately up to N = 20), contact deformation occurs; in the second section there is a slow accumulation of contact strain

at an approximately constant rate (up to N = 103 ... 104); in the third section, a significant increase in deformation and intensive destruction of the surface are observed.

It has been established [6] that wear under impact loading is a nonlinear function of the number of cycles and normal stress:

$$W = BN^n\sigma^m, \quad (2)$$

where *B, n, m* – coefficients.

In this case, the normal stress σ and the maximum contact pressure are determined by the impact force, which in turn depends on the speed, contact geometry and material properties.

Cyclic stresses lead to fatigue damage, both at the surface and at some depth. The phenomenon of surface fatigue is a consequence of normal collisions of micro-roughnesses, which lead to the occurrence of tangential stresses under the roughnesses, acting at a depth of the order of the heights of the protrusions (micrometers). The maximum shear stress under the protrusion is:

$$\tau'_m = \left(E'/\pi^2\right)\varphi, \quad (3)$$

where E' – modulus of elasticity; φ – protrusion angle coefficient.

It is obvious that microscopic (second kind) maximum shear stresses can indeed be the cause of the formation of initial cracks under the surface.

The general case of a diagram of vertical surface and horizontal subsurface cracks under friction with three-dimensional dynamic loading is shown in Fig.1.

The surface is loaded with normal alternating stress q(z) under impact loading and tangential stresses τx and τy during reciprocating sliding in two mutually perpendicular directions of the counter-specimen.

The analysis shows that if it is possible to mathematically describe the areas of transition from one zone of plastic flow of a metal to another, then it becomes possible to analytically solve problems in the theory of plasticity. In [16-20], an analytical solution to the plane problem of plasticity theory using harmonic functions was proposed. The spatial problem is solved in stresses [21]. The use of harmonic functions, as further analysis shows, allows us to analytically obtain a closed solution to the spatial problem, both taking into account the statistical and kinematic components.

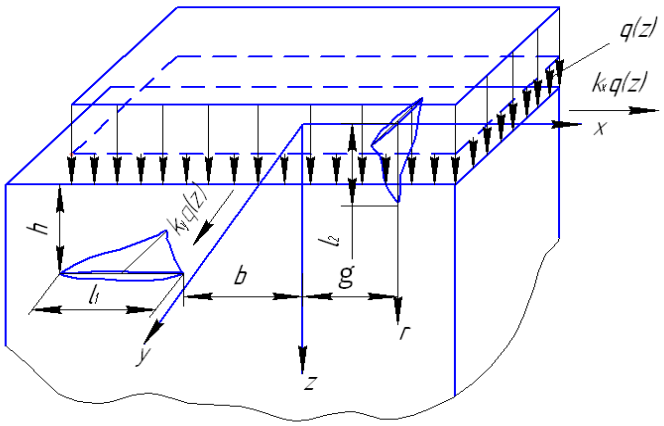

Fig.1. Scheme of horizontal and vertical cracks during friction with three-dimensional dynamic loading.

Takes the τ_{xy}=0. In many problems of metal forming, the influence of this component of the stress tensor is neglected [22, 23]. Hence, in the formulation part of the closed problem of plasticity theory, the system should contain 14 equations.

Problem formulation

1. Equilibrium equations:

$$\frac{\partial \sigma_x}{\partial x} + \frac{\partial \tau_{xz}}{\partial z} = 0,$$

$$\frac{\partial \tau_{yz}}{\partial z}+\frac{\partial \sigma_y}{\partial y}=0, \tag{4}$$
$$\frac{\partial \tau_{xz}}{\partial x}+\frac{\partial \tau_{yz}}{\partial y}+\frac{\partial \sigma_z}{\partial z}=0$$

4. Generalized equilibrium equations:

$$\frac{\partial^2 \tau_{xz}}{\partial x^2}-\frac{\partial^2 \tau_{xz}}{\partial z^2}=\frac{\partial^2}{\partial x \partial z}2k_1\sqrt{1-\left(\frac{\tau_{xz}}{k_1}\right)^2}, \tag{5}$$
$$\frac{\partial^2 \tau_{yz}}{\partial y^2}-\frac{\partial^2 \tau_{yz}}{\partial z^2}=\frac{\partial^2}{\partial y \partial z}2k_2\sqrt{1-\left(\frac{\tau_{yz}}{k_2}\right)^2}$$

3. Connection equations:

$$\frac{\sigma_x-\sigma_z}{2\tau_{xz}}=\frac{\xi_x-\xi_z}{\dot{\gamma}_{xz}}=\frac{2\xi_x+\xi_y}{\dot{\gamma}_{xz}}, \quad \frac{\sigma_y-\sigma_z}{2\tau_{yz}}=\frac{\xi_y-\xi_z}{\dot{\gamma}_{yz}}=\frac{2\xi_y+\xi_x}{\dot{\gamma}_{yz}} \tag{6}$$

4. Incompressible equation:

$$\xi_x+\xi_y+\xi_z=0 \tag{7}$$

5. Continuity equations for strain rates:

$$\frac{\partial^2 \xi_x}{\partial z^2}+\frac{\partial^2 \xi_z}{\partial x^2}=\frac{\partial^2 \dot{\gamma}_{zx}}{\partial z \partial x}, \quad \frac{\partial^2 \xi_y}{\partial z^2}+\frac{\partial^2 \xi_z}{\partial y^2}=\frac{\partial^2 \dot{\gamma}_{zy}}{\partial z \partial y} \tag{8}$$

6. Boundary conditions:

$$\tau_{n1}=k_1\cdot Sin(\mathrm{A}_1\Phi_1-2\alpha_1), \ \tau_{n2}=k_2\cdot Sin(\mathrm{A}_2\Phi_2-2\alpha_2), \tag{9}$$
$$\gamma_{n1}=2\cdot\beta_1\cdot Sin(\mathrm{B}_1\Phi_1-2\alpha_1), \ \gamma_{n2}=2\cdot\beta_2\cdot Sin(\mathrm{B}_2\Phi_2-2\alpha_2)$$

The use of generalized equilibrium equations (5) allows us to bring the obtained result into conformity with equations (8). Boundary conditions (9) mathematically describe the transition zones from one section of the plastic flow of a metal to another, both in stress and strain. The solution of plane problems in analytical form is presented in [16-20]. To satisfy boundary conditions of the form (9) it is necessary:

$$\tau_{xz}=k_1\cdot Sin\mathrm{A}_1\Phi_1, \quad \tau_{yz}=k_2\cdot Sin\mathrm{A}_2\Phi_2, \tag{10}$$

where A_1 and A_2 – constants that determine the parameters of the plastic medium; Φ_1 and Φ_2 – unknown coordinate functions determined by the solution of the problem; k_1, k_2 – resistance to plastic shear deformation along the X and Y axes, depending on the coordinates of the deformation zone.

A special feature of solving equations (5), in addition to trigonometric substitution, is the use of fundamental functions. They are used if the partial differential equation is linear [24–28]. Therefore:

$$k_1=C_{\sigma 1}\cdot\exp\theta_1', \quad k_2=C_{\sigma 2}\cdot\exp\theta_2', \tag{11}$$

where $C_{\sigma 1}$ and $C_{\sigma 2}$ – constants that determine the dimension of shear resistance in the directions of the X and Y axes; θ_1 and θ_2 – coordinate unknown functions determined by solving the problem along the same axes.

It must be borne in mind that $\tau_{xz}=f(x,z)$, $\tau_{yz}=f(y,z)$. Putting the introduced functions (10) and (11) into (5) we obtain:

$$\begin{aligned} &C_{\sigma 1}\left[\theta_{1xx}'+(\theta_{1x}'+\mathrm{A}_1\Phi_{1z})^2-\theta_{1zz}'-(\theta_{1z}'-\mathrm{A}_1\Phi_{1x})^2\right]\cdot Sin\mathrm{A}_1\Phi_1+ \\ &+C_{\sigma 1}\left[2\cdot(\mathrm{A}_1\Phi_{1x}-\theta_{1z}')\cdot(\theta_{1x}'+\mathrm{A}_1\Phi_{1z})+(\mathrm{A}_1\Phi_{1xx}-\mathrm{A}_1\Phi_{1zz})\right]\cdot Cos\mathrm{A}_1\Phi_1= \\ &=-2\cdot C_{\sigma 1}\cdot\mathrm{A}_1\Phi_{1xz}\cdot Sin\mathrm{A}_1\Phi_1+2\cdot C_{\sigma 1}\cdot\theta_{1xz}'\cdot Cos\mathrm{A}_1\Phi_1 \end{aligned} \tag{12}$$

Identical brackets $(\theta_{1x}'+\mathrm{A}_1\Phi_{1z})$ and $(\theta_{1z}'-\mathrm{A}_1\Phi_{1x})$ appear in operators of trigonometric functions (12). Taking them equal to zero, we get rid of nonlinearity and obtain the Cauchy–Riemann equations, which turn the equations into an identity. Let's show it. We have

$$\theta_{1x}^{'} = -\mathrm{A}_1\Phi_{1z}, \quad \theta_{1z}^{'} = \mathrm{A}_1\Phi_{1x} \tag{13}$$

$$\theta_{1xx}^{'} = -\mathrm{A}_1\Phi_{1zx}, \quad \theta_{1zz}^{'} = \mathrm{A}_1\Phi_{1xz}, \quad \theta_{1xz}^{'} = \mathrm{A}_1\Phi_{1zz} = -\mathrm{A}_1\Phi_{1xx} \tag{14}$$

From relations (13) and (14) the functions $\theta_1^{'}$ and $\mathrm{A}_1\Phi_1$ are determined. They are harmonic and satisfy the Laplace equation, i.e.:

$$\theta_{1xx}^{'} + \theta_{1zz}^{'} = 0, \quad \mathrm{A}_1\Phi_{1xx} + \mathrm{A}_1\Phi_{1zz} = 0 \tag{15}$$

Similar transformations take place for the second generalized equilibrium equation when substituting (10) and (11) into (5). We can write:

$$C_{\sigma 2}\left[\theta_{2yy}^{'} + (\theta_{2y}^{'} + \mathrm{A}_2\Phi_{2z})^2 - \theta_{2zz}^{'} - (\theta_{2z}^{'} - \mathrm{A}_2\Phi_{2y})^2\right] \cdot Sin\mathrm{A}_2\Phi_2 + \tag{16}$$

$$+ C_{\sigma 2}\left[2 \cdot (\mathrm{A}_2\Phi_{2y} - \theta_{2z}^{'}) \cdot (\theta_{2y}^{'} + \mathrm{A}_2\Phi_{2z}) + (\mathrm{A}_2\Phi_{2yy} - \mathrm{A}_2\Phi_{2zz})\right] \cdot Cos\mathrm{A}_2\Phi_2 =$$

$$= -2 \cdot C_{\sigma 2} \cdot \mathrm{A}_2\Phi_{2yz} \cdot Sin\mathrm{A}_2\Phi_2 + 2 \cdot C_{\sigma 2} \cdot \theta_{2yz}^{'} \cdot Cos\mathrm{A}_2\Phi_2$$

next:

$$\theta_{2y}^{'} = -\mathrm{A}_2\Phi_{2z}, \quad \theta_{2z}^{'} = \mathrm{A}_2\Phi_{2y}, \tag{17}$$

$$\theta_{1yy}^{'} = -\mathrm{A}_2\Phi_{2zy}, \quad \theta_{2zz}^{'} = \mathrm{A}_2\Phi_{2yz}, \quad \theta_{2yz}^{'} = \mathrm{A}_2\Phi_{2zz} = -\mathrm{A}_2\Phi_{2yy},$$

$$\theta_{2yy}^{'} + \theta_{2zz}^{'} = 0, \quad \mathrm{A}_2\Phi_{2yy} + \mathrm{A}_2\Phi_{2zz} = 0$$

Taking into account (16), (17), certainty appears for the functions $\theta_2^{'}$ and $\mathrm{A}_2\Phi_2$.

Substituting expressions for tangential stresses into equilibrium equations (4), integrating, we obtain analytical dependences for normal stresses. The components of the stress tensor have the form:

$$\sigma_x = C_{\sigma 1} \cdot \exp\theta_1^{'} \cdot Cos\mathrm{A}_1\Phi_1 + \sigma + f(y,z) + C_1, \tag{18}$$

$$\sigma_y = C_{\sigma 2} \cdot \exp\theta_2^{'} \cdot Cos\mathrm{A}_2\Phi_2 + \sigma + f(x,z) + C_2,$$

$$\sigma_z = -\left(C_{\sigma 1} \cdot \exp\theta_1^{'} \cdot Cos\mathrm{A}_1\Phi_1 + C_{\sigma 2} \cdot \exp\theta_2^{'} \cdot Cos\mathrm{A}_2\Phi_2\right) + \sigma + f(x,y) + C_3,$$

$$\tau_{xz} = C_{\sigma 1} \cdot \exp\theta_1^{'} \cdot Sin\mathrm{A}_1\Phi_1, \quad \tau_{yz} = C_{\sigma 2} \cdot \exp\theta_2^{'} \cdot Sin\mathrm{A}_2\Phi_2$$

at $\theta_{1x}^{'} = -\mathrm{A}_1\Phi_{1y}$, $\theta_{1y}^{'} = \mathrm{A}_1\Phi_{1x}$, $\theta_{1xx}^{'} + \theta_{1zz}^{'} = 0$, $\mathrm{A}_1\Phi_{1xx} + \mathrm{A}_1\Phi_{1zz} = 0$, $\theta_{2y}^{'} = -\mathrm{A}_2\Phi_{2z}$, $\theta_{2y}^{'} = \mathrm{A}_2\Phi_{2x}$, $\theta_{2yy}^{'} + \theta_{2zz}^{'} = 0$, $\mathrm{A}_2\Phi_{2yy} + \mathrm{A}_2\Phi_{2zz} = 0$.

The conditions for the existence of the introduced functions and the differential equations that determine their values are determined. Thus, solutions (18) satisfy the system of equations for the spatial problem in stresses. It becomes possible to connect the parameters of the stressed state of a point (friction coefficient, shape factor) with the thermomechanical parameters of the process (degree, rate, and temperature of deformation). In this case, production factors and loads are directly linked. By setting the parameters of the stress state, it is possible to determine, using different calculation methods, the thermomechanical parameters of the process. As an example, for the contact surface of samples of 10HFTBch two–phase steel type, is calculated the intensity of normal stresses σi from various friction coefficients and shape parameters (stress state) in the MathCAD program. The ratio of the length of the deformation zone to the height l/h = 1 and l/h = 6 is considered. By setting different friction coefficients (0.1; 0.2...0.5), the maximum values of the σi curves for a point on the contact are obtained (Table 1).

Table 1. Maximum values of normal stress intensity for various shape parameters and friction coefficients

l/h	Friction coefficient				
	0.1	0.2	0.3	0.4	0.5
1	1.155	1.31	1.442	1.532	1.564
6	1.286	1.574	1.828	1.997	2.058

Fig.2 shows the change in normal stress intensity values along the length of the deformation zone (along the X axis). Along the X and Y axes, the stresses σ_i are distributed along a convex curve, which is determined by the tangential contact stresses τ_{xz} and τ_{yz}. It has been established that the greater the σ_i, he higher the yield strength.

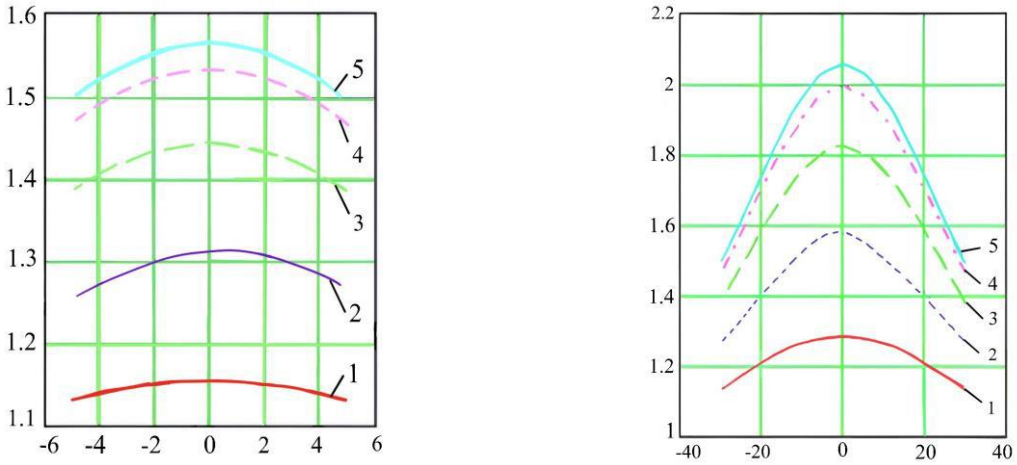

a) *b)*

Fig.2. Change in the intensity of normal stresses along the length of the deformation zone:
a) – l/h= 1; b) – l/h=6.
1 – f=0,1; 2 – f=0,2; 3 – f=0,3; 4 – f=0,4; 5 – f=0,5

Thus, σ_i depends on the friction coefficient and the shape parameter (stress state), that is, the ratio l/h and b/h. Analysis of the results of calculating the intensity of normal stresses from the parameters of shape and friction coefficient shows that it is possible to increase this parameter compared to unhardened metal. There is an increase in this indicator by 1.13...2.0 times. This means that, based on the Huber–Mises's hypothesis, the physical quantity, that is, the yield strength, also increases by 1.13...2.0 times. With an increase in the friction coefficient and shape parameters, we determine the yield stress, which in this case, through the temperature factor and recrystallization diagrams, makes it possible to establish structural transformations corresponding to a given stress state.

4. Conclusion

The presented models confirm the relevance of the mathematical description of complex damage to friction units. An assessment of the mechanics of contact fracture should be made on the basis of studying the behavior of surface layers of materials in connection with the peculiarities of thermomechanical loading of tribocompounds under real operating conditions. The use of harmonic functions allows one to analytically obtain a closed solution to a spatial problem, both taking into account the statistical and kinematic components. In turn, the development of methods for calculating surface strength assessment is a necessary prerequisite for the development of more wear–resistant tribounits.

Conflict of interest statement

The authors declare that they have no conflict of interest in relation to this research, whether financial, personal, authorship or otherwise, that could affect the research and its results presented in this paper.

CRediT author statement

Tsyganov V.: Conceptualization, Resources; Sheyko S.: Methodology, Supervision, Hrechanyi O.: Project administration, Writing – review & editing, Vasilchenko T.: Data Curation, Writing - Original Draft.
The final manuscript was read and approved by all authors.

References

1 Belokon Y., Hrechanyi O., Vasilchenko T., Krugliak D., Bondarenko Y. (2023) Development of new composite materials based on TiN-Ni cermets during thermochemical pressing. *Results in Engineering*, 16, 100724. DOI:10.1016/j.rineng.2022.100724.

2 Vagonova O.G., Metelenko N.G., Shapurov O.O., Chornobayev V.V. (2023) Efficiency and internationalization of mining and metallurgical groups of Ukraine. *Naukovyi Visnyk Natsionalnoho Hirnychoho Universytetu*, 2, 177–183. DOI: 10.33271/nvngu/2023-2/177.

3 Belodedenko S., Hanush V., Hrechanyi O. (2022) Fatigue lifetime model under a complex loading with application of the amalgamating safety indices rule. *Procedia Structural Integrity*, 36, 182–189. DOI:10.1016/j.prostr.2022.01.022.

4 Sereda B., Kruglyak I., Kovalenko A., Sereda D., Vasilchenko T. (2011) The deformation zone geometrical factors and its influence on deformation shift degree for the axial zone of rolled high bars. *Metallurgical and Mining Industry*, 3(7), 102–106. https://doi.org/metaljournal.com.ua/assets/Uploads/attachments/102Sereda.pdf

5 Belodedenko S., Grechany A., Yatsuba A. (2018) Prediction of operability of the plate rolling rolls based on the mixed fracture mechanism. *Eastern-European Journal of Enterprise Technologies*, 1, 7(91), 4–11. DOI:10.15587/1729-4061.2018.122818.

6 Morozov E.M., Zernin M.V. (1999) *Contact problems of fracture mechanics*. Mechanical engineering. 544 p. (in Russian). https://doi.org/read.in.ua/book253007.

7 Rakhadilov B.K. Satbaeva Z.A., Kozhanova R.S., Kowalewski P., Bayatanova L.B., Kalitova A.A. (2022) Effect of the structure formed after bulkand surface hardening on the hardnessand wear resistance of 20Cr2Ni4A steel. *Eurasian Physical Technical Journal*, 19, 1(39), 20–25. DOI: 10.31489/2022no1/20-25.

8 Sheyko S., Tsyganov V., Hrechanyi O., Vasilchenko T., Hrechana A.H. (2023) Determination of the optimal temperature regime of plastic deformation of micro alloyed automobile wheel steels. *Research on Engineering Structures and Materials*, 10, 1, 331-339. DOI: 10.17515/resm2023.49me0428tn.

9 Tsyganov V.V. (2023) Features of mechanics destruction tribounitsat difficult dynamic loading. *Eurasian Physical Technical Journal*, 20, 2 (44), 99–105. DOI: 10.31489/2023no2/99-105.

10 Byalik H., Ivschenko L., Mokhnach R., Sakhniuk N., Tsyganov V. (2019) Creation of Wearproof Eutecticum Composition Materials for the Details of the High Temperature Dynamic Systems. *Materials Science and Technology*, 1, 450-456. DOI: 10.7449/2019/mst_2019_450_456.

11 Tsyganov V.V., Sheyko S. (2022) Features of engineering the wear-resistant surface of parts with the multicomponent dynamic load. *Wear*, 494-495, 204255. DOI: 10.1016/j.wear.2022.204255.

12 Tsyganov V.V., Mokhnach R.E., Sheiko S.P. (2021) Increasing wear resistance of steel by optimizing structural state of surface layer. *Steel in Translation*, *51*(2), 144–147. DOI: 10.3103/s096709122102011x.

13 Eremin E.N., Guchenko S.A., Yurov V.M. (2020) Wear resistance and tribological properties of high entropy coatings CrNiTiZrCu. *Eurasian phys. tech. j.*, 17(1(33), 13–18. DOI: 10.31489/2020No1/13-18.

14 Miller K.J. (1987) The behaviour of short fatigue cracks and their initiation part. Part I.A review of two recent books. *Fatigue & Fracture of Engineering Materials and Structures*, 10(1), 75–91. DOI: 10.1111/j.1460-2695.1987.tb01150.x.

15 Kolesnikov Yu.V., Morozov E.M. (2007) *Mechanics of contact fracture.* Science. 224 p. (in Russian) https://doi.org/obuchalka.org/2018020398820.

16 Fernández J., Illescas S., Guilemany J.M. (2007) Effect of microalloying elements on the austenitic grain growth in a low carbon HSLA steel. *Materials Letters*, 61(11-12), 2389-2392. DOI: 10.1016/j.matlet.2006.09.021.

17 Mishchenko V.G., Sheyko S.P. (2014) Structural changes of multiphase low-carbon steel in deformation and heat treatment. *Steel in Translation*, 44 (12), 928-930. DOI: 10.3103/S0967091214120122.

18 Chen C., Sun M., Chen X., Wang B., Zhou J., Jiang Z. (2021) State of the Art in Control of Inclusions and Microalloying Elements in Tire Cord Steel and Saw Wire Steel. *Steel Res. Int.*, 93(4): 2100507. DOI:10.1002/srin.202100507.

19 Chigirinsky V., Naizabekov A., Lezhnev S., Kuzmin S., Naumenko O. (2022) Solving applied problems of elasticity theory in geomechanics using the method of argument functions of a complex variable. *Eastern-European Journal of Enterprise Technologies*, 5(7 (119)), 105–113. DOI: 10.15587/1729-4061.2022.265673.

20 Chigirinsky V.V. (1997) Some features of the theory of plasticity in relation to mechanical engineering processes. *Proceedings of the scientific and technical conference "Theory and technology of plastic deformation processes-96*". 568-572. https://doi.org/repository.kpi.kharkov.ua/server/api/core/bitstreams/24f7c8a5-52c4-4490-9c23-86c7c9a02861/content.

21 Chigirinsky V., Naumenko O. (2020) Invariant differential generalizations in problems of the elasticity theory as applied to polar coordinates. *Eastern-European Journal of Enterprise Technologies*, 5(7 (107)), 56–73. DOI:10.15587/1729-4061.2020.213476.

22 Hryhoriev S., Petryshchev A., Krupey K., Andreev A., Katschan A., Stepanov D., Manidina Y., Ryzhkov V., Berenda N., Matiukhin A. (2017) A study of environmentally safe obtaining of molybdenum-based alloying material by solid phase extraction. *Eastern-European Journal of Enterprise Technologies*, 6 (12-90), 35 - 40. DOI:10.15587/1729-4061.2017.119498.

23 Shejko S., Yechyn S., Demchenko N. (2016) The method for determination of the influence of the stress-strain state of metal on the structural transformations in the low-alloy steel. *Materials Science and Technology Conference and Exhibition, MS and T*, 1, 353-358. https://www.proceedings.com/32780.html.

24 Shalomeev V., Tabunshchyk G., Matiukhin A., Shyrobokov V., Shyrobokova N., Hornostai V., Kulabneva E. (2022) Refining of biosoluble alloy of mg-nd-zr system for manufacture of implants. *31st International Conference on Metallurgy and Materials, METAL 2022*, 622 - 627. DOI: 10.37904/metal.2022.4440.

25 Volokitina I.E., Volokitin A.V., Latypova M.A., Chigirinsky V.V., Kolesnikov A.S. (2023) Effect of Controlled Rolling on the Structural and Phase Transformations. *Progress in Physics of Metals*, 24, 1, 132–156. DOI:10.15407/ufm.24.01.132.

26 Shejko S., Shalomeev V., Mishchenko V. (2017) The effect of plastic deformation on the structure formation of low-alloy steel. *Materials Science and Technology Conference and Exhibition*, 1, 238-244. DOI:10.7449/2017/mst_2017_238_244.

27 Ivanov I., Matiukhin A., Ben A., Kryvykh Y., Kulabnieva O. (2023) Determination of the stressed metal state during hot rolling by the finite element method. *New Materials and Technologies in Metallurgy and Mechanical Engineering*, (4), 50–55. DOI: 10.15588/1607-6885-2023-4-7.

28 Pavlenko D.V., Belokon' Y.O., Tkach D.V. (2020) Resource-Saving technology of manufacturing of semifinished products from intermetallic γ-tial alloys intended for aviation engineering. *Materials Science*, *55*(6), 908–914. DOI: 10.1007/s11003-020-00386-1.

AUTHORS' INFORMATION

Tsyganov, Volodimir Vasilievich – Doctor of Techn. Sciences**,** Professor, National University Zaporizhzhia Polytechnic, Zaporizhzhia, Ukraine; Scopus Author ID: 56712109100; ORCID iD**:** 0000-0001-5682-7005**;** tsyganov705@gmail.com

Sheyko, **Sergey Petrovich –** Doctor of Techn. Sciences**,** Professor, Zaporizhzhia National University, Zaporizhzhia, Ukraine; Scopus Author ID: 23095863300; ORCID iD: 0000-0001-5761-4263; ss6309113@gmail.com

Hrechanyi, Oleksii – PhD, Associate Professor, Department of Metallurgical Equipment**,** Zaporizhzhia National University, Zaporizhzhia, Ukraine; Scopus Author ID: 57219488722; ORCID iD: 0000-0003-0524-4998; hrechanyi@znu.edu.ua

Vasilchenko, Tetiana – PhD, Associate Professor, Department of Metallurgical Equipment**,** Zaporizhzhia National University, Zaporizhzhia, Ukraine; Scopus Author ID: 54415072500; ORCID iD: 0000-0002-0340-3900; vasilchenko@znu.edu.ua

EURASIAN PHYSICAL TECHNICAL JOURNAL

2024, Volume 21, No.3 (49)

https://doi.org/10.31489/2024No3/71-80

Received: 13/05/2024 Revised: 22/08/2024 Accepted: 17/09/2024 Published online: 30/09/2024

Original Research Article

UDC 533.15, 681.586

SATURATION OF GAS CONCENTRATION SIGNAL OF THE LASER GAS SENSOR

Zhanabaev Z.Zh., Tileu A.O.*, Duisebayev T.S., Almen D.B.

Al-Farabi Kazakh National University, Almaty, Kazakhstan
*Corresponding author: tileuayan@gmail.com

Abstract. *Nowadays it is possible to determine the type of gas with sufficient accuracy when its concentration is less than* 10^{-6} *fractions using spectroscopic methods (optical, radio engineering, acoustic). Along with this, the value of permissible concentrations of explosive, toxic, harmful to technology and ecology gases is practically important. Known physical experimental studies indicate only a linear dependence of the response of a laser gas sensor at units* $\lesssim 10^3$. *The research methods for units* $\gtrsim 10^3$ *are based on the processes of combustion, micro-explosion, structural and phase transformations and are not always applicable in real practical conditions. The work is devoted to the analysis of experimentally obtained fluctuations caused by a laser beam in a gas in a photodiode (signal receiver) due to its influence not only at the atomic level, but also on the scale of clusters of nanoparticle molecules. The gas concentration is estimated by the fluctuation-dissipation ratio. It is shown that the signal correlator is saturated to a constant value when the quantum (laser photon energy) and thermal (nanoparticle temperature) factors are comparable with an increase in the concentration of the target gas. The critical values of the saturation concentration are determined by the equality of these two factors.*

Keywords: fluctuation-dissipation, correlator, photodiode, methane, carbon tetrachloride, ammonia.

1. Introduction

Determining the type of different gas and its concentration is an important task of production, medicine, safety, and environmental monitoring. Extensive studies have been carried out using sensors with different measurement principles [1-3]. Laser absorption spectroscopy systems have been developed, multi-pass sensors with lasers of various wavelengths have been developed to obtain spectral absorption lines and transmit information. The results of laser sensing are usually presented as a linear dependence of the response on the gas concentration. In practice, it becomes necessary to know the concentration of gas C_*, at which the saturation of the sensor response occurs. Thus, in [1] an experimental rule is indicated at $C_* \approx 10^4\ ppm$ (1%) for methane in a coal mine, sound and light alarms are triggered, and at $C_* \simeq 1{,}5$ % – production is turned off.

Saturation can also be observed in the signals of nanofilm sensors [4]. These facts indicate the need for a physical analysis of the concentration attenuation of the signal of a commonly used laser gas sensor.

When the laser beam interacts with gas particles, a sensitive element (photodiode), its intensity decreases. Due to the multiple factors of this process (absorption, reflection, polarization of the beam), the presence of technical noise of the devices, the output signal will fluctuate. Therefore, for the problem under consideration, one can choose a general method of statistical physics – the fluctuation-dissipation theorem (FDT). This method has been used to describe molecular, electromagnetic, and quantum phenomena.

Special experiments [5] have shown the bifurcation effect of thermal noise on microelectromechanical systems, the physical content of which is FDT. The possibility of using the fluctuation-dissipation ratio for modeling the spectrum of a condensed medium is considered in [6].

In recent decades, numerous articles have been published in leading physics journals devoted to expanding the formulation and possible applications of FDT from the point of view of nonequilibrium thermodynamics, the theory of nonlinear response away from equilibrium in shear fluids, bulk media, nanosystems, and glassy media. In a comprehensive list of modern research in this field, only the study [7] stands out, as its subject of analysis is distinct from the others discussed above.

The theoretical foundations of further applications of FDT to the optical phenomena of transmission, absorption, and reflection in media with microscopic structures of various geometries are discussed in [8]. The response of the medium to fluctuations in the external field is described by the Bose-Einstein distribution over the frequency ω and the field is described by the Greens function, which depends on the coordinates. The results of the technique of calculating the matrices of the electromagnetic field components are presented. The results of the fundamental nature of this work show the universal applicability of FDT to phenomena of a wide spatial and temporal spectral scale.

Following the preceding overview of various studies on laser gas sensors, the primary objective and novelty of this work are formulated. In well-known studies [1], at a low concentration of the target gas, its presence is determined with great accuracy by the characteristic atomic spectral absorption lines of the laser beam. However, as we indicated in the Abstract section, the study of physical phenomena occurring at high gas concentrations is of great practical importance.

With increasing gas concentration, the intensity of the transmitted radiation decreases over distance according to the Beer-Lambert law and at a fixed position of the sensor. At the same time, the proportion of absorption by molecular clots increases, and the power spectrum will be predominantly low-frequency. The intensity of the beam will be comparable to the thermal background. The mutual influence of these two factors is taken into account by the FDT formula. Therefore, it is possible to determine the effect of concentration on the change in the correlation function of fluctuations in the sensor output signal. The comparability of the energy of the average number of quanta of vibrational or rotational modes with the thermal energy of gas molecules will lead to saturation, the nonlinear nature of the change in the signal of the laser sensor.

The experiment will use a time-fluctuating signal of a laser beam transmitted through a layer of gas with different concentrations to a photodiode. At the same time, the conditions of partial coherence of the fluctuation signal are observed, which are necessary to obtain correlation and spectral characteristics.

2.Theoretical foundations of the experiment

The fluctuation-dissipation ratio (FDR) is written in various forms according to the types of characteristic variables. We will use the values of the time fluctuations of the output voltage from the photodiode $v(t_i) \equiv v_i$, the energy of the laser photon $\hbar\omega_0$, the thermal energy of the gas molecules kT (k is the Boltzmann constant). The generally accepted recording of FDT in statistical physics in spectral form by frequency ω [8]:

$$\langle v_i, v_j \rangle_\omega = \hbar\alpha''(\omega) cth\left(\frac{\hbar\omega}{2kT}\right) = 2\hbar\alpha''(\omega)\left\{\frac{1}{2} + \frac{1}{e^{\hbar\omega/kT}-1}\right\} \quad (1)$$

where $\alpha''(\omega)$ is the imaginary part of generalized susceptibility.

The curly bracket expresses the average energy of the oscillator in units of $\hbar\omega$ at temperature T. The left part (1) is equal to the Fourier spectrum of the correlation function (correlator) in frequency ω:

$$K_\omega\big(v(t)\big) = \left\{\frac{1}{N^2}\sum_{i=1}^{N}\sum_{j=1}^{N} v(t_i)v(t_j)\right\}_\omega \equiv \langle v_i, v_j \rangle_\omega \quad (2)$$

Let us take into account the conditions for completing our task. The concentration of gas C is usually determined in millionths (ppm) of the mass or volume of air. Therefore, the correlator of the mixture gas(g)+air(a) $K(v(t); g + a)$ must be attributed to its value for air:

$$K(v(t); g + a)/K(v(t); a) \quad (3)$$

Next, we establish the dependence of expression (3) only on concentration. Therefore, we are looking for the desired dependence relative to a fixed laser frequency ω_0 or a fixed modulation fundamental frequency

according to the experimental condition.Then, in the right part of formula (1), the constant value $\hbar\alpha''(\omega_0)$ we can include it in expression (3), which also clearly does not depend on concentration. Let's include a constant expression in the experimentally determined value of expression (3).

$$\hbar\alpha''(\omega_0;\ g+a)/\hbar\alpha''(\omega_0;\ a) \tag{4}$$

Thus, we have eliminated the frequency dependence and will proceed with using the original formula (2) without the frequency index ω. This is possible due to the equality of the integral characteristics in time and frequency of oscillations.

After that, in the left part of formula (1), we have a dimensionless expression (3) divided by a dimensionless constant (4). In the right part of formula (1), the number of absorbed coherent photons $cth\left(\frac{\hbar\omega_0}{2kT}\right)$ remains according to the accepted condition $\omega=\omega_0$. This hyperbolic function in formula (1) contains an exponent. The ratio of the close values in formula (3) in comparison with the exponent is calculated more accurately by the natural logarithm:

$$ln\{K(v(t);g+a)/K(v(t);a)\}/K_{max}=cth\left(\frac{\hbar\omega_0}{2kT}\right) \tag{5}$$

The logarithmic multiplier is calculated in a normalized form by dividing by its maximum value modulo K_{max}. This takes into account the negative sign in the balance of fluctuation (positive) and dissipation (negative) energies.

The concentration of gas C is clearly not taken into account in formula (5). The concentration value C_{*_0}, corresponding to saturation of the sensor signal is determined from the equality of fluctuation coherent quantum ($\hbar\omega_0/2$) and dissipation thermal (kT) factors:

$$C_{*_0}=\ 2kT/\hbar\omega_0 \tag{6}$$

C_{*_0} is determined experimentally at constant values of ω_0, T.

In cases of partial coherence, bifurcations of oscillations $C_*\ is$ the critical value of the onset of saturation differs from C_{*_0} (section 4). The hyperbolic function in (5) decreases at $C\to 2C_*$ and remains constant, close to one. To describe the increase in correlations of fluctuations in the right part of formula (5) at $C\lesssim 2C_*$, we use the inverse function $th(x)=cth^{-1}(x)$. Physically, this means that at $C\lesssim 2C_*$ the fluctuating energy of the laser photons is absorbed by the gas, at $C>2C_*$ it becomes dissipative, comparable to the thermal energy of molecules. Taking into account the influence of the gas concentration, we write formula (5) in a scale-invariant form relative to the maximum of the K_{max} correlator for the case $2C\le C_*$:

$$ln\{K(v(t,C);g+a)/K(v(t,C);a)\}/K_{max}=th\left(2C/C_{*_0}\right) \tag{7}$$

3. Experimental setup

The measurements were carried out using the instruments and devices shown in Figure 1. From the GAS BALLOON, through the pressure gauge and VALVE, the gas enters a 20 ml vessel, where an air + gas mixture is formed. The pressure gauge maintains the pressure of the incoming gas equal to atmospheric pressure. A semiconductor LASER with a wavelength of 532 nm is connected to a POWER SUPPLY source with voltage and current indicators. The laser beam passes through the gas+air mixture to the PHOTODIODE PIN. The output signal of the photodiode is fed through the TL081CP operational amplifier to the NIELVISII+ electronics engineering kit. Fluctuation signals from the measuring complex are processed by COMPUTER.

A Vishay BPW34 silicon P-i-N photodiode was used. The spectral sensitivity line does not coincide with the laser line. This is according to the statement of our task. We are not looking for atomic spectra, but for fluctuations from laser power. Among the available small laser sources, the green laser type SD 303 HUONIE has a higher power of 100 mW than the red laser type FLASH LUK5K 5 mW. In our experiment, the laser output power was controlled by the power supply; The supply current was 60 mA and the voltage was 1.8 V, which corresponds to a power (P=I*U) of 100 mW for a green laser.

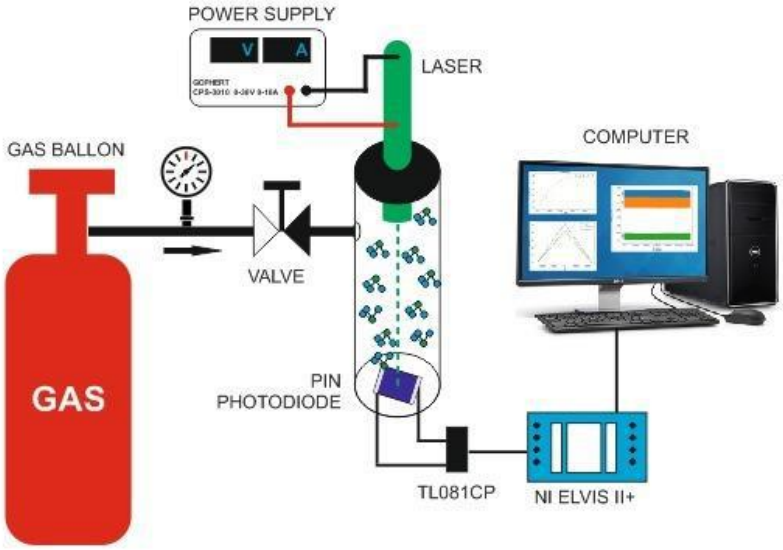

Fig.1. Nodes of the laser gas sensor.

4. Results of the experiment and discussion

Stable correlations of the fluctuation signal can be obtained at a degree of coherence of their intensity $\gamma \gtrsim 0{,}1$, which corresponds to the recommendations adopted in optics for choosing the contrast of partially coherent interference fringes. In the experiment, the required degree of coherence of fluctuations was achieved by the condition

$$\hbar\omega_0 \gtrsim U \tag{8}$$

where $\hbar\omega_0 = 2{,}3$ eV, it's the photon energy of a laser with a wavelength of 532 nm, $U \geq 1\ V$ is the stability region of the photodiode characteristic.

Figure 2 shows the time series of partially coherent fluctuations $v(t)$ obtained when a laser beam passes through air (a), through a mixture of air +ammonia at $C = 1200\ ppm$ (b). The degrees of coherence of the interference fringes were determined by the intensity of signal fluctuations

$$\gamma = \frac{[1-(v_{\min}/v_{\max})^2]}{[1+(v_{\min}/v_{\max})^2]} \tag{9}$$

where $v_{\min}$, $v_{\max}$ are minimum and maximum values of fluctuation voltage, $\gamma \gtrsim 0{,}2$. We use formula (9) to control the power of laser radiation, which provides a contrasting picture of correlations. For the modulation pattern, $v_{\min}/v_{\max}$ is used.

The correlation functions $K(v(t))$ of the voltage fluctuations of the sensor $v(t)$, are shown in Figure 3. The dashed approximation lines show the stability of the characteristic for 40 seconds with deviations of 1% (for clean air), 5% (for a mixture of air+gas). During processing, the data was divided into n=10 windows of 4 seconds each. Figure 3 allows us to estimate the total value of the noise intensity under the experimental conditions of fluctuations from air and technical instrument noise. The difference in maximum correlations (variances) is 4%, the standard deviation is 2%. This estimate is comparable to the thermal noise in the purely coherent mode (about 1%) determined by formula (12).

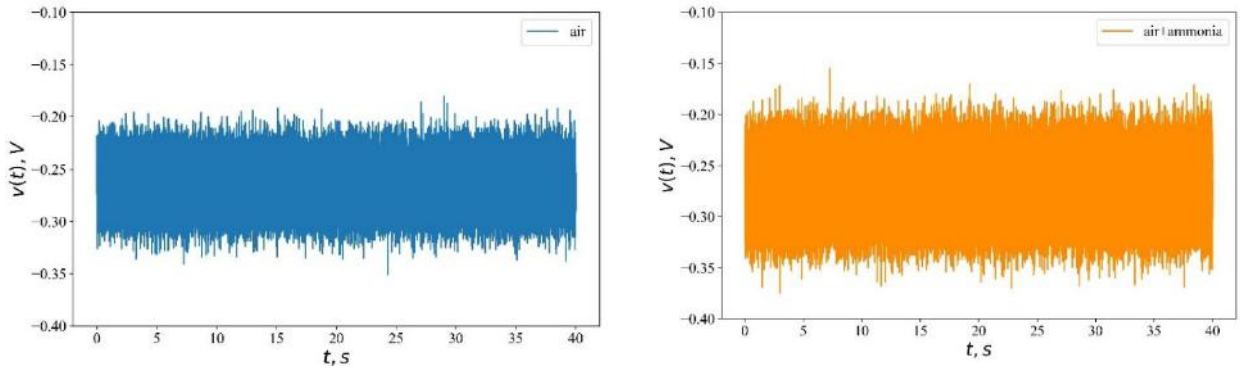

a) *b)*

Fig.2. Time series of partially coherent fluctuations $v(t)$:a) air, b) air+ammonia, $C = 1200\ ppm$.

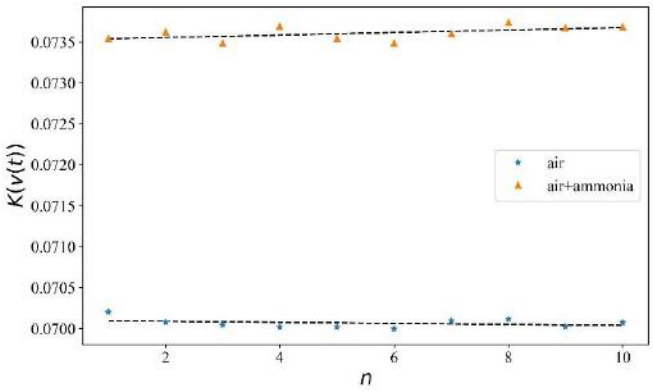

Fig.3. Correlation functions of sensor voltage fluctuations $v(t)$ from air (background noise) and from a mixture with gas, corresponding to the data in Figure 2.

The relative correlation functions calculated using the left side of formula (5) for gases will be smaller in magnitude than for air. Figure 4 shows the experimental dependences of the relative values of the K/K_{max} correlation functions on the concentration of $C(ppm)$ gases selected with varying degrees of symmetry of the structure of their molecules (methane CH_4, carbon tetrachloride CCl_4, ammonia NH_3) [9].

The ordinate axis shows the values

$$K/K_{max} = ln\{K(v(t); g + a)/K(v(t); a)\}/\ K_{max} \tag{10}$$

Experimental values of $K_{max} =$ 0,33 (CH_4); 0,11 (CCl_4); 0,058 (NH_3). The response of the laser sensor is saturated with an increase in the gas concentration $C \geq C_*$. Transient (bifurcation) modes $C = C_*$ occur near $K \approx K_{max}$. These points in the figures are connected by vertical lines that pass through $C_*(CH_4) = (1,2,4) * 10^4 ppm$, $C_*(CCl_4) = 3 * 10^3 ppm$, $C_*(NH_3) = 2{,}5 * 10^3 ppm$. Such a pronounced concentration saturation of the response of a laser gas sensor can be explained and described. The observed and theoretically described set of (1,2,4) values of C_* is explained separately below.

As the gas concentration increases, the absorption of the laser beam increases, and its intensity becomes comparable to the thermal energy of molecules. The energy of the average number of photons $\langle n \rangle$ according to the formula (1) is equal to

$$E(\langle n \rangle) = \hbar\omega \left(\langle n \rangle + \frac{1}{2} \right) \tag{11}$$

In the symmetric state $\langle n \rangle = 0$ and we have the energy of the coherent state of photons. The equality of the quantum factor at the concentration of photons C_{*_0} and the thermal factor is expressed as

$$\mathrm{C}_{*_0} \hbar\omega_0 = 2kT \tag{12}$$

Under the conditions of our experiment room temperature $T = 300°K$, multiplied by the Boltzmann constant $kT = 10^{-2}eV$, $\lambda_0 = 532$ nm, from $\omega_0 = \frac{2\pi}{\lambda_0} * c$, $\hbar = h/2\pi$ is Planck's constant, c is speed of light, $\hbar\omega_0/2 = 1{,}15\ eV$ have $C_{*_0} = 10^{-2}$, in units of ppm (part per million) $C_{*_0}(ppm) = 10^6 * 10^{-2} = 10^4\ ppm$. In methane (CH_4) with a symmetrical arrangement of molecules, saturation of the laser sensor signal occurs at the highest C_{*_0}. This value C_{*_0}, equal to 1% of the same order, at which in practice a warning alarm is given in mines [1].

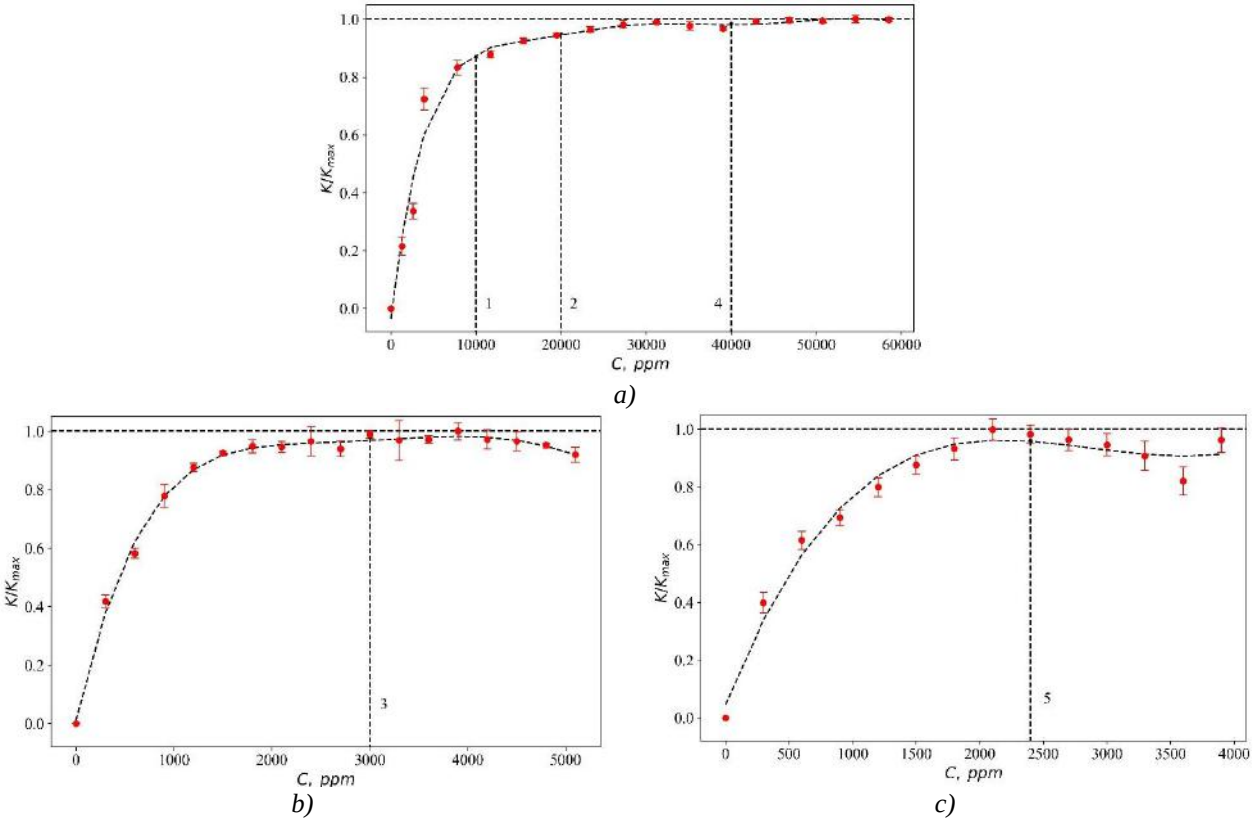

a) *b)* *c)*

Fig.4. Change in correlation functions from the concentration of a) methane b) carbon tetrachloride c) ammonia.

With asymmetry $(\langle n\rangle \neq 0)$ of the molecular structure, their vibrations will be partially coherent. Condition (12) will be fulfilled at lower values of C_*. This follows from formula (11) if the total energy of the photon is represented in terms of C_*, resulting in saturation of the signal. Denoting $\langle n\rangle = C_*$ and the corresponding number of coherent photons $C_*/2$, we have

$$E(C_*) = C_*\hbar\omega\left(1 + \frac{1}{2}\right) = \frac{3}{2}C_*\hbar\omega \tag{13}$$

From a comparison with $E(\langle n\rangle = 0) = C_{*_0}\hbar\omega/2$ it follows that $C_* = C_{*_0}/3$, indicating that C_* is three times less than for the symmetric case (methane). For example, for gas CCl_4 $C_* = C_{*_0}/3 = 3{,}3 * 10^3\ ppm$. The symmetry class NH_3 is lower than that of CH_4, CCl_4. This is due to the additional bonds between the molecules.

In general, the issue boils down to taking into account the correction of the anharmonicity of vibrations and rotations. Well-known publications [10] indicate the possibility of taking into account the $\frac{1}{2} < \alpha < \frac{3}{4}$ correction to formula (11) instead of $\frac{1}{2}$ based on the results of quantum mechanical calculations with various potential barriers for the electron.

We consider it possible to use the correction α of the fluctuation phenomena of the probabilistic information-entropy measure of self-similarity in the range $0{,}567 \leq \alpha \leq 0{,}806$, corresponding to the chaotic (to stochastic) regime of the phenomenon [11]. These criteria extend the «golden section» of the dynamic measure (the Fibonacci number is 0.618) to probabilistic phenomena.

Let us explain this statement. From the definition of information $I = -lnP$ through probability P its self-similar value (fixed point $P(I) = I$) is equal to

$$e^{-I_*} = I_*, I_* = 0.567 \quad (14)$$

The average value of information (information entropy $H(I)$) and its self-similar value $I_{*,H}$ are equal:

$$H(I) = -\int_I^\infty e^{-I} I dI = (I+1)e^{-I} \quad (15)$$

$$(I_{*,H}+1)e^{-I_{*,H}} = I_*,\ I_{*,H} = 0.806 \quad (16)$$

Formula (15) takes into account that the probability distribution functions, and its density are equal to e^{-I}, which follows from the probability normalization condition. The criteria I_*, $I_{*,H}$ are easily proved by nonlinear (Feigenbaum-type) maps of dynamic chaos. The Fibonacci criterion of 0.618 follows from (15) when taking into account the first term of the exponent expansion at $I < 1$, and at $I \ll 1$ the result (14) will be obtained. In formula (13), instead of 1/2 we substitute the correction $\alpha = 0{,}806$ (according to formula (16)), and to take into account the concentration we take $\hbar\omega_0 < n >= \hbar\omega_0 C$, $\langle n \rangle = 1$. Comparing $C(NH_3)(1 + 0{,}806) = C(CCl_4)\left(1 + \frac{1}{2}\right)$, we have $C(NH_3) = 0{,}83 * 3{,}3 * 10^3 = 2{,}5 * 10^3\ ppm$.

It follows from formula (7) that the graphs of Figure 4 can be constructed in scale-invariant form in the coordinates $th(2C/C_{*_0})$and C, ppm (Figure 5). Such a representation can be useful for establishing possible variations of the parameters ω_0, kT, C_*.

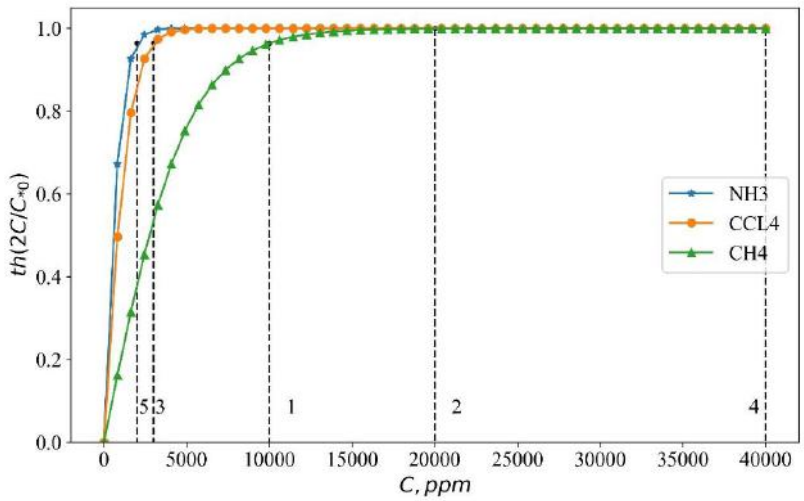

Fig 5. Experimental dependence of the dissipative factor in formula (7).
CH_4(1,2,4), CCL_4(3), NH_3(5), $C_{*_0} = 10^4 ppm$, values (5,3,1,2,4) according to Figure 4.

In this regard, we note that due to the fluctuation nature of the laser gas sensor signal under consideration, the measured correlation and dissipation characteristics through hyperbolic functions have harmonic saturation components. This is noticeable from Figures 4. Therefore, the minimum values of C_*, are selected, corresponding to the nonlinear behavior of the sensor response.

It's necessary to establish a connection between the minimum C_* and the experimental values of C_{0_α}, which differs from C_{*0} for the coherent state of laser photons. Due to the low volume density compared to the mass density, additional bifurcations with new values of $C_{*_B} > C_*$ are possible in gases. This case can significantly occur in the methane in the form $C_{*_B} > C_{*_0}$, because C_{*_0} was determined for the coherent States of photons with the symmetric arrangement of atoms. When taking into account anharmonism with the parameter α, we have $C_{*_\alpha} < C_{*_0}$.

The essence of the additional bifurcation is as follows. In the presence of a fluctuating effect, the amplitude of the oscillatory process in one period is lower from the equilibrium, in the next it is higher. After

a period, after 4 pulses modulo, a bifurcation occurs in the form of a burst. In the equilibrium process as a whole, energy is conserved. This phenomenon in the theory of dynamic chaos is called the period doubling bifurcation. This bifurcation is a universal phenomenon of nature, it is scale-invariant, described by a functional equation [12].

In our problem, due to the accepted condition, the saturation of the signal $\frac{C_*\hbar\omega_0}{2kT} = 1$, at constant ω_0 , T , $C_*{\sim}{\omega_0}^{-1}$. Next, instead of the frequency, it will use ${C_*}_0{}^{-1}$, ${C_*}_B{}^{-1}$. Scale invariance is manifested at multiple frequencies of ω_0, which is the fundamental frequency, subharmonics $\frac{\omega_0}{2}$, $\frac{\omega_0}{4}$, … . Certainly, in accordance with this in the experiment (Figure 4), the first harmonics can be specified as $C_{*_B} = 2C_{*_0}, C_{*_B} = 4C_{*_0}, C_{*_0} = 10^4$.

Thus, along with the set of values $C_{*,\alpha}$ according to the anharmonicity parameter (signal nonlinearity), there are also bifurcation values C_{*_B}, caused by fluctuations in gas volume. The sensor response – correlator responds to the joint effects $C_{*_\alpha} < C_{*_0}$,$C_{*_B} > C_{*_0}$. Therefore, in the vicinity of $C \approx C_{*_0}$ weaker deviations from linearity of the sensor response relative to its established maximum value are observed when $C_{*_B} > C_{*_0}$. This symptom of signal saturation is used in practice. As we have pointed out, the methane in mines prevention and appropriate measures are taken with $C_{*_0} = 10^4\ ppm$ (1%) and $C_{*_B} = 1.5 * C_{*_0}$.

Let us establish a relationship between K_{max} and the parameter, which takes into account anharmonicity. Taking into account the formula (13), we have

$$C_*(1+\alpha) = \frac{C_{*_0}}{2} \tag{17}$$

$$\frac{1}{2} < \alpha < \frac{3}{4} \text{ or } 0{,}567 < \alpha < 0{,}806$$

where C_{*_0} the saturation concentration of a purely coherent state. The relative correlation of fluctuations is proportional to the number of interacting pairs of particles $\left(K_{max} = \left(\frac{C_\alpha}{C_{*_0}}\right)^2\right)$. This ratio and formula (17) summarize experimental and theoretical results.

The above examples of experimental and theoretical estimates show the possibility of a fluctuation-dissipation approach to determining the saturation concentration of a laser gas signal. At the same time, the type of symmetry of gas molecules, fluctuation bifurcations and the condition of comparability of the energies of thermal and quantum perturbations were considered. It is possible to estimate the critical values of the gas concentration without using optical spectral complexes, that is, complex fundamental methods of molecular spectroscopy. Concentration-spectral analysis methods in this direction may be useful to replace specific plasma-photometric, chemiluminescent gas detection methods.

The complexity of the problems and the possibility of continuing in this direction will be indicated by the example of some modern research. The paper [13] presents the results of a theoretical and experimental study of the rotational and vibrational spectra of diamond nanocrystals from meteorites. More than 7000 purely rotational transitions and the first vibrational-rotational states have been detected. Using supercontinuum lasers, ammonia (NH_3) and methane (CH_4) can be detected in a photonic fiber at a telecommunication wavelength [14]. In [15], Raman scattering of a laser beam with a wavelength of 532 nm was used by a multi-pass ring resonator to detect gases with high sensitivity.

Our results were obtained by time correlation of fluctuations at a fixed point. Note that our new physical conclusions about the values of the saturation concentration of the sensor signal, taking into account the nonlinearity due to the anharmonicity of fluctuation bifurcations and the results of repeated measurements correspond within ± 5% of the RMS ratio.

5. Conclusion

In this paper, the possibility of determining the gas concentration values leading to saturation of the response of a laser gas sensor is shown. The correlation functions of fluctuations in the output voltage of a photodiode have been experimentally obtained. The fluctuation-dissipation ratio was used to theoretically describe the experimental results.

It is shown that the nonlinear response of saturation of the laser sensor signal with an increase in gas concentration occurs when the energy of absorbed photons in the gas and the thermal energy of molecules are comparable. The possibility of using universal functional relations of scale invariance to estimate the values of saturation concentrations of the sensor signal, taking into account the symmetry of the location and the appearance of bifurcations of the oscillation of gas molecules, is shown. This means that the methods of this work are applicable to determine both the gas concentration and the type of target gas.

Knowledge of the onset of the nonlinear sensor operation mode is a practical necessity to prevent disruption of the normal rhythms of life, production, and ecology. In this paper, we have indicated the possibilities of approaching this problem using simple physical methods without using spectral complexes or chemical methods. The experimental technique and measurement methods used by us with the addition of spectral modeling make it possible to create simpler small-sized sensors for the considered problem.

Conflict of interest statement

The authors declare that they have no conflict of interest in relation to this research, whether financial, personal, authorship or otherwise, that could affect the research and its results presented in this paper.

CRediT author statement

Zhanabaev Z.Zh.: Conceptualization, Methodology, Supervision; Tileu A.O.: Investigation, Writing – review & editing; Duisebayev T.S.: Investigation, Visualization, Writing – original draft; Almen D.B.: Data curation, Validation, Writing – original draft.

The final manuscript was read and approved by all authors.

Funding

This research was funded by the Committee of the Ministry of Science and Higher Education of the Republic of Kazakhstan, Grant IRN BR18574080.

Acknowledgments

We would like to express our sincerest gratitude to the Al-Farabi Kazakh National University for supporting this work by providing computing resources (Department of Physics and Technology).

References

1 Gong W., Hu J., Wang Z., Wei Y., Li Y., Zhang T., Zhang Q., Liu T., Ning Y., Zhang W., Grattan T. V. (2022) Recent advances in laser gas sensors for applications to safety monitoring in intelligent coal mines. *Frontiers in Physics*, 10, 1058475. DOI:10.3389/fphy.2022.1058475.

2 Shin W., Hong S., Jeong Y., Jung G., Park J., Kim D., Choi K., Shin H., Koo R.H., Kim J.J., Lee J.H. (2023) Low-frequency noise in gas sensors: A review. *Sensors and Actuators B:* Chemical, 383, 133551. DOI:10.1016/j.snb.2023.133551.

3 Liu K., Wang L., Tan T., Guishi W., Zhang W., Chen W., Gao X. (2015) Highly sensitive detection of methane by near-infrared laser absorption spectroscopy using a compact dense-pattern multipass cell. *Sensors and Actuators B: Chemical*, 220, 1000 – 1005. DOI: 10.1016/j.snb.2015.05.136.

4 Yu H.-L, Wang J., Zheng B, Zhang B.-W., Liu L.-Q., Zhou Y.-W., Zhang Ch., Xue, X.-L. (2020) Fabrication of single crystalline WO 3 nano-belts based photoelectric gas sensor for detection of high concentration ethanol gas at room temperature. *Sensors and Actuators A: Physical*, 303, 111865. DOI: 10.1016/j.sna.2020.111865.

5 Qiao Y., Arabi M., Xu W., Zhang H., Abdel-Rahman T.M. (2021) The impact of thermal-noise on bifurcation MEMS sensors. *Mechanical Systems and Signal Processing*, 161, DOI: 10.1016/j.ymssp.2021.107941.

6 Mehay T.P., Warmbier R., Quandt A. (2017) Investigation of density fluctuations in graphene using the fluctuation-dissipation relations. *Computational Condensed Matter*, 13, 1-5. DOI: 10.1016/j.cocom. 2017.08.008.

7 Hsiang J.T., Hu B.L., Lin S.Y., Yamamoto K. (2019) Fluctuation-dissipation and correlation-propagation relations in $(1+3)$D moving detector-quantum field systems. *Physics Letters B*, 795, 694-699, DOI:10.1016/j.physletb.2019.06.062.

8 Moskalensky A.E., Yurkin M.A. (2021) A point electric dipole: From basic optical properties to the fluctuation–dissipation theorem. *Reviews in Physics*, 6. DOI: 10.1016/j.revip.2020.100047.

9 Bunker P.R., Jensen P. (2005) Symmetry and Broken Symmetry in Molecules. *Encyclopedia of Life Support Systems (EOLSS), Eolss Publishers, Oxford* http://www.eolss.net/Sample-Chapters/C06/E6-12A-02-06.pdf]

10 Pippard A.B. (1989) The Physics of Vibration. *Cambridge University Press.* ISBN 10: 0521372003

11 Zhanabaev Z.Z., Grevtseva T.Y. (2014) Physical fractal phenomena in nanostructured semiconductors. *Reviews in Theoretical Science,* 2, 211 – 259. DOI: 10.1166/rits.2014.1023.

12 Schuster H.G. and Just W. (2005) Deterministic Chaos: An Introduction. *Wiley-VCH Verlag GmbH & Co.*4. https://doi.org/10.1002/3527604804

13 Chitarra O., Martin-Drumel M.A., Buchanan Z., Pirali O. (2021) Rotational and vibrational spectroscopy of 1-cyanoadamantane and 1-isocyanoadamantane. *Journal of Molecular Spectroscopy*, 378, 111468, DOI:10.1016/ j.jms.2021.111468.

14 Adamu A.I., Dasa M.K., Bang O., Markos C. (2020) Multispecies Continuous Gas Detection With Supercontinuum Laser at Telecommunication Wavelength. *IEEE Sensors Journal*, 20(18), 10591-10597, DOI:10.1109/JSEN.2020.2993549.

15 Wang K., Zhang Z., Wu Zh., Wang Sh., Guohua L., Shao J., Wu H., Tao M., Ye J. (2024) Diagnosis of multiple gases using a multi-pass ring cavity to enhance Raman scattering. *Optics Communications*, 559, 130438. doi:10.1016/j.optcom.2024.130438.

AUTHORS' INFORMATION

Zhanabaev, Zeinulla Zhanabaevich – Doctor of Phys. and Math. Sciences, Professor, al Farabi Kazakh National University, Almaty, Kazakhstan; Scopus Author ID: 15840905700; https://orcid.org/0000-0001-5959-2707; kenvp@kaznu.kz

Tileu, A.O. – PhD student, Department of Physics and Technology, Al-Farabi Kazakh National University, Almaty, Kazakhstan; Scopus Author ID: 57218680509; https://orcid.org/0000-0001-9965-6728; tileuayan@gmail.com

Duisebayev, T.S. – PhD student, Department of Physics and Technology, Al-Farabi Kazakh National University, Almaty, Kazakhstan; Scopus ID: 58071081400; https://orcid.org/0000-0002-4992-0495, tola.d@yandex.ru

Almen D.B. – PhD student, Department of Physics and Technology, Al-Farabi Kazakh National University, Almaty, Kazakhstan; https://orcid.org/0009-0000-8527-4921; dinara.almen@gmail.com

EURASIAN PHYSICAL TECHNICAL JOURNAL

2024, Volume 21, No.3 (49)

https://doi.org/10.31489/2024No3/81-92

Received: 23/04/2024 Revised: 05/07/2024 Accepted: 20/09/2024 Published online: 30/09/2024

Original Research Article

UDC 539.4:621.891; 621.793:620.22

RESISTANCE OF HEAT-RESISTANT YTTRIUM-CONTAINING SEALING COATINGS TO MECHANICAL FRACTURE WHEN FORMING CUTTING PATHS

Kubich V.[1], Fasol Ye.[1], Cherneta O.[2], Yershina A.K.[3], Sakipov N.Z.[4]

[1] National University Zaporizhzhia Polytechnic, Zaporizhzhia, Ukraine
[2] Dniprovsky State Technical University, Kamenske, Ukraine
[3] Kazakh National Women's Teacher Training University, Almaty, Kazakhstan
[4] Civil Aviation Academy, Almaty, Kazakhstan
*Corresponding author: schmirung@gmail.com

Abstract. *According to the results of tribotechnical tests of coatings made of KNA-82 alloy ligatures with the addition of yttrium of 0.1%, 0.3%, 0.5%, data were obtained that allowed us to establish the nature of changes in the dynamic coefficient of friction over the test period and numerous values of the energy intensity of material wear. The evaluation of coatings formed by the gas-flame and ion-plasma method was based on the following premise. The maximum resistance to mechanical fracture is determined by the manifestation of a constant minimum value of the dynamic coefficient of friction. This serves as an indicator of reduced friction force before reaching the fatigue limit. Another key factor is the number of separated particles produced per unit of integral work during the friction process. These evaluation parameters are lined up in a row by the number of points from 1 to 4. The maximum score corresponds to the maximum resistance, i.e., a lower value of the energy intensity of material wear and the minimum value of the stable friction coefficient. It has been determined that the same coincidence of these parameters according to the scores is almost at all stages of testing (I-III) was the coating formed by the gas-flame method with a yttrium concentration of 0.3%-0.5%. The exception was the coating formed by the ion-plasma method with a yttrium concentration of 0.1% at the fourth stage of testing.*

Keywords: sealing coating, ion-plasma method, gas-flame method, mechanical fracture resistance, cutting tracks, high-temperature loading, yttrium, mechanical stability, gas turbine engines.

1. Introduction

In the current technological environment of industrially countries, especially in the aerospace, energy and aviation industries, there is a growing need for materials that could provide reliable operation in high temperatures, aggressive environments: intense gas-erosion and gas-explosive exposures [1,2]. One of the most important areas of research and development in this context is the creation of heat-resistant sealing coatings that would be effective in conditions of high-temperature aggressive gas flow and will increase engine's efficiency. Among the modern materials that have high thermal endurance and excellent resistance to abrasive and gas-erosion wear, yttrium-containing coatings occupy a special place. The use of yttrium in coatings can increase wear resistance, heat resistance, provide reliable adhesion to the substrate material, and improve mechanical properties [3].

An example of application is the coatings of gas turbines. One of the main parameters in the design of modern gas turbine engines (GTEs) is the efficiency. One of the main directions of improving the engine design and to reduce gas flow losses and rationalizing fuel consumption is to reduce radial clearances in the

rotor-stator interface [4]. The control of the size of axial and radial clearances in the GTEs are the focus of research by many authors, but this problem has not been finally solved. It is quite difficult to ensure the size of the gap, so there is a need to use sealing coatings. In particular, coatings of the Ni-Co-Cr-Al-Y system [5].

The authors [6] note the prospects of using of rare earth metals in heat-resistant coatings. Active interaction with impurities – interstitial elements (mainly carbon and oxygen) promote the formation of stable carbides at the interfaces (phase boundaries, dislocation clusters). Yttrium in appropriate proportions stabilizes aluminum and chromium oxide films, improves the adhesion of coatings to the substrate material, increases the thermal stability of alloys, and slows down the coagulation of hardening phases [7-9]. It has been established that yttrium dissolved in a nickel matrix increases heat resistance [reference]. The introduction of yttrium in an amount exceeding its solubility limit leads to the precipitation of the phase close to Ni_3Y inside the grain and at the grain boundaries. [10]. The introduction of yttrium also contributes to the formation of Ni $(Al,Y)_2O_4$ and Y_2O_3 oxides on the alloy surface. In the coatings of the Ni-Co-Cr-Al-Y segregation of Y at the scale-coating interface leads to less cavity formation and, therefore, improves the adhesion of the oxide α-Al_2O_3 oxide scale. However, despite these studies, the experimental results of on the effect of yttrium on the high-temperature gas-erosion resistance of coatings are currently not sufficient to determine the required amount of Y to be added, as well as the efficiency of its use [11].

The main objective of the research is to determine the resistance of yttrium-containing coatings formed from KNA-82 alloy ligatures on small-sized samples using the gas-flame and plasma spray methods to mechanical destruction during the formation of the insertion tracks. In this case, the cut-in tracks perform a forcedly modeled wear profile of the material of coatings applied to the surface of the stator of a labyrinthine gas-dynamic seal, power turbine, etc. In this case, resistance is considered as a generalized quality of a multiligature material, which, according to the nature of friction and wear observed when the pointed ridges are cut in, reflects the pattern of destruction of cohesive bonds between the components of the formed powder coating [12,13].

2. Materials and research method

To conduct the research, the coatings were formed up to 5 mm thick on one side of cubic specimens of size 15×22×20 from a cylindrical forming work surface. The substrate for the sample was made of nickel alloy Inconel 600. The coatings tested were KHA-82 (nickel alloyed with silicon, aluminum, and solid lubricants (graphite and boron nitride) with the addition of 0.1%, 0.3%, and 0.5% yttrium. The coatings were applied by gas-flame and plasma sputtering methods, Fig. 1 c, d. The tribological tests were carried out at the SMC-2 unit at the modeled temperatures given in the presented stages of the study. Scheme of the rotating disk - fixed pad is presented in Figure 1a.

The prepared samples were subsequently subjected to

- high-temperature dynamic loading in the environment of a burning iso-octane-propane-butane gas mixture at a temperature of 950-1220 ℃ for 5 min., Fig 1, c,
- high-temperature static loading in a furnace at 1100℃ for 3 hours, which was considered as a static high-temperature loading with a limited amount of oxygen as an oxidizing agent;
- high-temperature dynamic loading in the environment of a burning gas iso-octane-propane-butane mixture at a temperature of 950-1020 ℃ for 5 min. with modeling of a constant mechanical load, Fig1, d.

Based on the above factors of high-temperature loading, the physical modeling of mechanical fracture of the sample surfaces was carried out in four stages:

- stage 1 - tribotechnical tests at a normal ambient temperature T = 25ºC after coating. The test cycle was 5 min. at a constant load;
- stage 2 - tribotechnical tests at a normal ambient temperature of T = 25ºC after exposure of the coating to a high-temperature dynamic load of a burning gas iso-octane-propane-butane mixture at a temperature of 950-1220 ℃. The test cycle was 5 min. at constant load;
- stage 3 - tribotechnical tests at an ambient temperature of T = 25ºC after exposure of the coating to a high-temperature static load in an oven at a temperature of 1100 ℃. The test cycle is 5 min. at constant load;
- stage 4 - tribotechnical tests in a burning gas iso-octane-propane-butane mixture at a temperature of 950-1020 ℃. The test cycle included mechanical loading without a burning gas mixture environment for 1 min, with a burning gas mixture environment for 3 min, and without a burning gas mixture environment for 1 min. The comparison of the resistance of yttrium-containing coatings to wear resistance was carried out relative to coatings that were not subjected to temperature loading and acted as reference coatings.

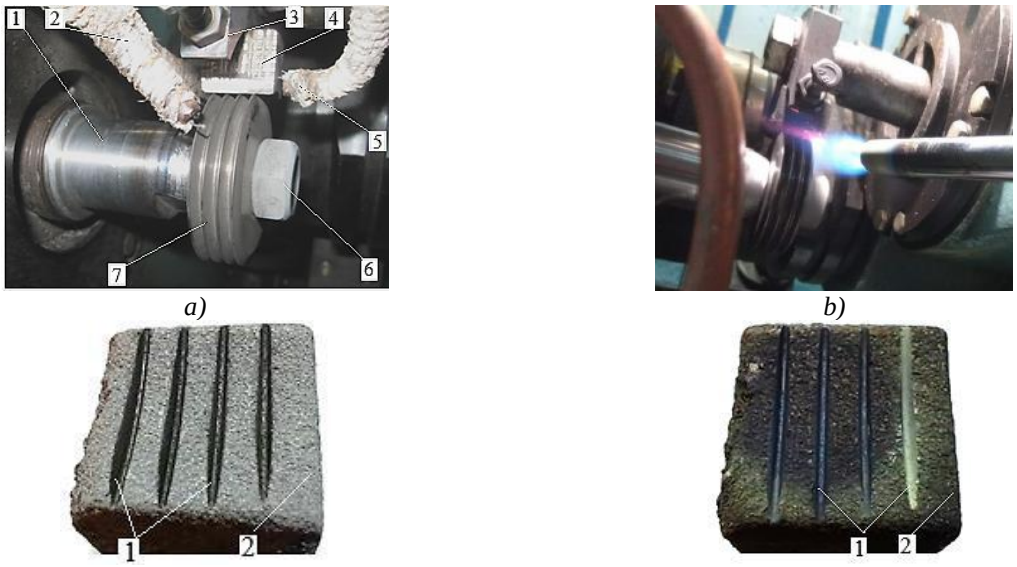

Fig. 1. Elements of methodological support for experimental studies: a) contact of the disk samples with the pad: 1 lower shaft of the SMC-2 friction machine; 2 - thermocouple casing; 3 - holder; 4 - coated sample pad; 5 - thermocouple casing; 6 - fixing nut; 7 - sample disk with ridges; b) contact of the sample disk with the pad in a burning gas mixture; c) the surface of the coating formed by the gas-flame method; d) the surface of the coating formed by the gas-flame method after temperature loading in a burning gas mixture: 1 - cut-in tracks; 2 – coating.

To evaluate the resistance of coatings to wear resistance, we used the components of the methodology for tribotechnical testing of materials for friction and wear proposed in [14,15], Fig 1, a. The tests were carried out on the SMC-2 test rig according to the friction scheme "rotating disk with ridges - fixed pad with a coating" under a static contact load with a force of P = 18.6 N and a disk rotation frequency of n = 300 min^{-1} without modeling the temperature state. The radius of the disk was 0.025 m, made of Inconel 617 alloy.

The test time was 5 min. The load during the tests of the samples after exposure to the furnace was P_1=18.6 N and P_2=3.5 N. A disk with four ridges of a trapezoidal profile with an outer diameter of d = 50 mm was installed on the lower shaft of the friction machine, Fig 1, a.

The direct parameters of tribotechnical tests were considered:

- weight loss of the coating material Δm, g
- friction torque Mt, P·m in the form of tribograms, the value of the scale of the friction recorder field was Mti=0.18 N·m.

The indirect parameters of tribotechnical tests were considered:

- dynamic friction coefficient μ;
- energy intensity of wear of the coating material I_m, $g \cdot J^{-1}$.
- friction path l_i = 235.5 m

The weight loss of the samples was measured on an electronic balance Radwag AS 220.R2 with an accuracy of 0.1 mg. The number of samples for each coating was n=3. The arithmetic mean values were used for analysis. The average standard deviation was σ = 0.0055 g.

$$I_m \approx \frac{\Delta m}{N \cdot l_1 \cdot \bar{\mu}_1 + P \cdot l_2 \cdot \bar{\mu}_2 + P \cdot l_3 \cdot \bar{\mu}_3} \approx \frac{\Delta m}{N \cdot \sum_{i=1}^{3} l_i \bar{\mu}_j}, g \cdot J^{-1}, \quad (1)$$

where Δm is the average mass wear of the coating, g; μj is the average current value of the friction coefficient during the corresponding test time; li is the average friction path over which the friction coefficient μj is manifested, m; P is the force of pressing the coated sample against the disk ridges, N.

To estimate the ranges of change in the energy intensity of wear due to the range of changes in the yttrium content and the predicted expected difference in weight wear, we propose to use the conditional maximum and minimum wear intensity, which was

$$I_{my_{max}} = \frac{\Delta m_{max}}{A_{\tau_{min}}} g \cdot J^{-1}, \quad (2)$$

$$I_{my_{min}} = \frac{\Delta m_{min}}{A_{\tau max}}, \ g \cdot J^{-1}, \quad (3)$$

where Δm_{max}, Δm_{min} are the maximum and minimum significant wear of the samples at the research stage, g; A(t_min), A_(t_max) are the minimum and maximum values of friction work, J.

The dynamic coefficient of friction (hereinafter referred to as the friction coefficient) was calculated according to the equation:

$$\mu = \frac{M_{t_i}}{P \cdot r}. \quad (4)$$

The analysis of the wear mechanism of the material of the studied coatings is based on the following judgment. The frictional interaction of the surfaces of the moving disk ridges with the components of the coating structures causes

- the action of a tangentially directed friction force, which in this direction loads the cohesive bonds between the microscopic particles of the coatings, and when repeatedly manifested, causes their fatigue to resist destruction, which in turn causes their gradual separation and removal from the friction zones. This is the main cause of coating failures, since during the experiments, active separation of these particles was observed, but with varying intensity;

- the effect of normal static load, which during the experiment caused the appearance of instantaneous macro and micro stresses in the surface layers of coatings that did not have time to relax and intensified the process of separation of microparticles.

Based on the above, the conditions of maximum wear resistance are constant minimum value of the dynamic friction coefficient, as an evidence of lower friction force before reaching the fatigue limit, and the number of separated particles that are accounted for the production of a unit of integrated friction force work [5]. That is, with a lower integral work of friction forces $\downarrow A_t$ and a greater separation of particles $\uparrow \Delta m$, the fracture resistance will be lower and the parameter Im will be higher, expression (1). Conversely, with a greater integrated work of friction forces $\uparrow A_t$ and a smaller separation of particles $\downarrow \Delta m$, the fracture resistance will be greater and the parameter Im will be smaller.

These parameters, in accordance with the research methodology, were taken into account in the form of the constructed laws $\mu=f(t)$ and the complex parameter Im.

3. Experimental data and results

Based on the results of processing the data from the obtained tribograms, graphical dependences of the change in the dynamic coefficient of friction over the test time were constructed using the arithmetic mean values, Fig 2-5,7. The energy intensities of wear of the coatings during the formation of the cut-in tracks are given in Tables 1-4 and Fig 6.

Results of the research at stage 1.

The analysis of the data obtained regarding the effect of the resistance of the initial coatings to mechanical destruction indicates the following:

- the minimum value of the weight of the separated particles was Δm_{min}=0.0747 g for the coating formed by the thermal spray method with a yttrium concentration of 0.5%, the maximum value Δm_{max}=0.2629 g was for the coating formed by the plasma spray method with a yttrium concentration of 0.5%;

- the minimum value of friction work At_{min}=1271 J was for the coating formed by the thermal spray method with a yttrium concentration of 0.5%, the maximum value At_{max}=8463 J was for the coating formed by the thermal spray method with a yttrium concentration of 0.3%.

Based on the above, the limit values of stability according to the parameters of expressions (2,3), against which the stability of the original coatings should be evaluated, were as follows:

- minimum durability corresponds to the maximum conditional energy intensity of wear $I_{mu}=20.6 \cdot 10^{-5}$ g·J^{-1};
- maximum resistance corresponds to the minimum conditional energy intensity of wear $I_{mu}=0.8 \cdot 10^{-5}$ g·J^{-1}.

The analysis of the data obtained regarding the manifestation of the resistance of the original coatings indicates the following. In general, an ambiguous effect of yttrium content, temperature load, and the method of coating formation on the manifestation of tribotechnical characteristics is noted.

Thus, in the absence of a temperature load (Table 1)

- The plasma spray method of coating formation compared to the thermal spray method causes a decrease in wear resistance by 1.65 times and 2.6 times with an increase in yttrium concentration from 0% to 0.3%,

except for a concentration of 0.5%, at which the resistance, on the contrary, increased by 1.5 times;

- the maximum resistance corresponded to the coatings formed with yttrium concentrations of 0.1% and 0.3%, but did not differ significantly from the original coating.

Table 1. Energy intensities of wear of experimental coatings $Im \cdot 10^{-5}$, $g \cdot J^{-1}$, obtained at the research stages 1 and 2

Yttrium content Y, %	Thermal spray method		Plasma spray method	
	No heating	Heating in a gas environment	No heating	Heating in a gas environment
0	3.3	8.16	5.4	7.82
0.1	3.1	8.37	5.03	9.66
0.3	2.79	6.08	7.15	10.13
0.5	5.87	8.13	3.78	11.28

For the assessment by two parameters, i.e., taking into account the friction coefficient, it is proposed to apply a point scale from 1 to 4. The maximum score corresponds to the maximum stability and the minimum value of the stable friction coefficient, the patterns of change of which are shown in Fig. 2

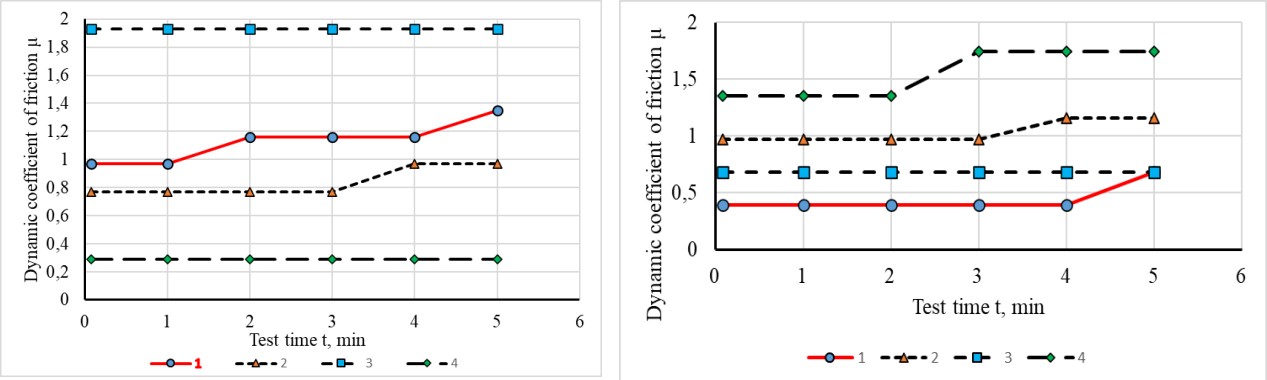

a) *b)*

Fig. 2. Dependence of the dynamic coefficient of friction on the time of tribotechnical testing of coatings at T = 25 °C before interaction with a stream of burning gases: a) at thermal spray forming; b) at plasma spray forming; 1 - original coating; 2 - yttrium 0.1%; 3 - yttrium 0.3%; 4 - yttrium 0.5%.

An increase in the coefficient of friction by more than one indicates pathological processes of destruction of cohesive bonds with the separation of particles. That is, the friction force significantly exceeds the bonding forces between the coating components.

Thus, in the absence of temperature load, the scores had the following distribution (Table 2).

Table 2. Evaluation of coatings without temperature load

Formation method	Parameter	Number of points min→max steadiness			
		1	2	3	4
Thermal spray	I_m	0.5	0	**0.1**	0.3
	μ	0.3	0	**0.1**	0.5
Plasma spray	I_m	0.3	0	**0.1**	0.5
	μ	0.5	0.1	**0.3**	0

From the data in Table 2, it should be assumed that the coating formed by the thermal spray method has a parameter coincidence of 3 points with yttrium concentration of 0.1%. That is, this coating has the maximum resistance to mechanical fracture when forming the insertion tracks. For the coating formed by the plasma spray method, there is no obvious coincidence, but the maximum resistance is close to the same number of points for concentrations from 0.1% to 0.3%.

Results of the research at stage 2.

The analysis of the data obtained regarding the resistance of coatings to mechanical destruction at a temperature of T = 25°C after their heating in a gas environment at a temperature of 950-1220 °C indicates the following:

- the minimum value of the mass of separated particles was Δm_{min}=0.1802 g for the coating formed by the thermal spray method with a yttrium concentration of 0.3%, the maximum value Δm_{max}=0.4707 g was for the coating formed by the plasma spray method with a yttrium concentration of 0.3%;

- the minimum value of friction work A_{tmin}=2964.3 J was for the coating formed by the thermal spray method with a yttrium concentration of 0.3%, the maximum value A_{tmax}=4648.1 J was for the coating formed by the plasma spray method with a yttrium concentration of 0.3%.

Based on the above, the conditional limit values of stability according to the parameters of expression (2.3) were as follows:

- minimum resistance corresponds to the maximum conditional energy intensity of wear $I_{mu}=15.87\cdot10^{-5}$ g·J^{-1};
- maximum resistance corresponds to the minimum conditional energy intensity of wear $I_{mu}=3.87\cdot10^{-5}$ g·J^{-1}.

Thus, in comparison with the ultimate limits of the stability of the original coatings, it can be seen that the range of stability of the coatings after heating in a gas environment narrowed by 1.65 times, and the stability decreased in general for both methods of formation, regardless of the yttrium concentration, Table 1. At the same time, the maximum stability remained for the coating formed by the thermal spray method with a yttrium content of 0.3%, but compared to the original structure, the stability decreased by 2.18 times. However, as for the coatings formed by the plasma spray method, the maximum resistance corresponded to the coating without yttrium. The resistance of the coating with a yttrium concentration of 0.5%, which was the maximum, decreased by almost 3 times. The nature of the friction coefficient for the coatings formed by the thermal spray method is shown in Fig, 2 a. The structural-phase transformations that took place caused obvious dispersion of the mechanical properties of the coatings along the depth, as indicated by the equality of the friction coefficients for yttrium coatings during the test period from 0 min to 1 min, when μ = 0.58-0.67, and from 4 min to 5 min, when μ = 0.77, Fig 3, a. But from 1 min to 4 min, the coefficients differed. This implies that different fracture resistance according to preliminary estimates of the depth of the cut-in tracks was observed at a distance from the surface of 0.5 mm to 2 mm.

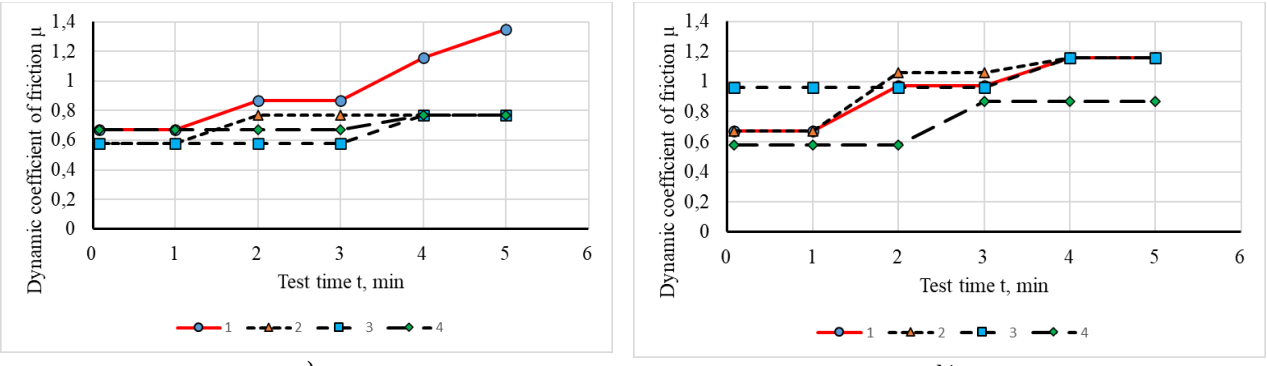

a) *b)*

Fig 3. Dependence of the dynamic coefficient of friction on the time of tribotechnical testing of coatings at T = 25°C after interaction with a stream of burning gases: a) at thermal spray forming; b) at plasma spray forming; 1 - initial coating; 2 - yttrium 0.1%; 3 - yttrium 0.3%; 4 - yttrium 0.5%.

For the coatings formed by the plasma method, Fig 3, b, no such distribution was observed. However, for almost all coatings, the friction coefficient μ = 1.16 was equal only in the period from 4 min to 5 min of testing, with the exception of the coating with a yttrium concentration of 0.5%, for which μ = 0.87. In this case, the same susceptibility to fracture processes was characteristic of the coating without yttrium and the coatings with its concentrations of 0.1% and 0.3%, which occurred from the 2nd min to the 3rd min of the test, Fig 3, b.

The interaction of the coatings with the high-temperature gas environment resulted in the following distribution of points in assessing their durability (Table 3). The values of the friction coefficients were selected according to the time of manifestation of obvious differences, i.e., from the 2nd min to the 3rd min of testing, Fig 3, a, b.

Table 3. Evaluation of coatings exposed to high-temperature gas loading.

Formation method	Parameter	Number of points min→max steadiness			
		1	2	3	4
Thermal spray	I_m	0.1	0	0.5	**0.3**
	μ	0	0.1	0.5	**0.3**
Plasma spray	I_m	0.5	0.3	**0.1**	0
	μ	0.1	0	**0.3**	0.5

From the data in Table 3, it should be assumed that the coating formed by the thermal spray method has a parameter coincidence of 4 points with a yttrium concentration of 0.3%, i.e., it has the maximum score. Based on this, this coating has the maximum resistance to mechanical fracture when forming the cut-in tracks. For the coating formed by the plasma method, there is no obvious coincidence, but the maximum resistance for concentrations from 0.1% to 0.3% with the same number of points borders on the number of points 3.

Research results at stage 3.

The analysis of the data obtained regarding the manifestation of the resistance of coatings to mechanical fracture at a temperature of T = 25ºC after exposure to a high-temperature static load in an oven at a temperature of 1100 ℃ indicates the following:

- the minimum value of the weight of the separated particles was Δm_{min}=0.004 g for the coating formed by the plasma method without yttrium, the maximum value Δm_{max}=0.1331 g was for the coating formed by the plasma spray method with a yttrium concentration of 0.1%;

the minimum value of friction work A_{tmin} =1710.2 J was for the coating formed by the thermal spray method with a yttrium concentration of 0.3%, the maximum value A_{tmax} =7542.1 J was for the coating formed by the ionoplasma method with a yttrium concentration of 0.3%.

Based on the above, the limit values of stability according to the parameters of expressions (2,3) were as follows:

- minimum resistance corresponds to the maximum energy conditional wear intensity $I_{mu}=7.8\cdot10^{-5}$ g·J^{-1};
- maximum resistance corresponds to the minimum energy conditional wear intensity $I_{mu}=0.05\cdot10^{-5}$ g·J^{-1}.

Thus, in comparison with the ultimate limits of resistance relative to the original coatings, it can be seen that the range of resistance of the coatings after exposure to the furnace narrowed by 2.5 times.

At the same time, the stability has generally increased for both formation methods, regardless of yttrium concentration. The increase in resistance for coatings formed by the thermal spray method was 6.6 times on average, and 3.8 times for the ion plasma spray method plasma method, respectively.

Table 4. Energy intensities of wear of experimental coatings Im·10-5, g·J^{-1}, obtained at the research stages 1 and 2.

Yttrium content Y, %	Thermal spray method		Plasma spray method	
	Aging in the furnace	Heating after the furnace	Aging in the furnace	Heating after the furnace
0	0.35	0.35	0.2	1.47
0.1	1.14	1.49	1.76	0.85
0.3	0.43	0.61	0.9	0.79
0.5	0.21	0.37	1.46	0.96

The coatings formed by the thermal spray method retain greater resistance. However, the highest resistance value was already achieved by the coating with a yttrium concentration of 0.5%. For coatings formed by the plasma spray method, there is no obvious pattern of increasing resistance, as is the case for gas flame coatings. A coating with a yttrium concentration of 0.3% has greater resistance. However, it should also be noted that there is a decrease in the resistance of coatings with yttrium compared to coatings without it. This is more pronounced for coatings formed by the plasma spray method.

The nature of the friction coefficient, Fig 4, indicates the following. For coatings formed by the thermal spray method, Fig 4, a, at the beginning of the experiments, a decrease in the friction coefficient is observed, which is due to the creation of surface structures capable of exerting less shear resistance with fewer separable wear particles, as indicated by the data in Table 4. However, this tribological state is not maintained in the subsequent test period, with the exception of the coating with a yttrium content of 0.3%. This indicates that

the gradients of mechanical properties with depth for coatings with yttrium content of 0.1% and 0.5% are not the same.

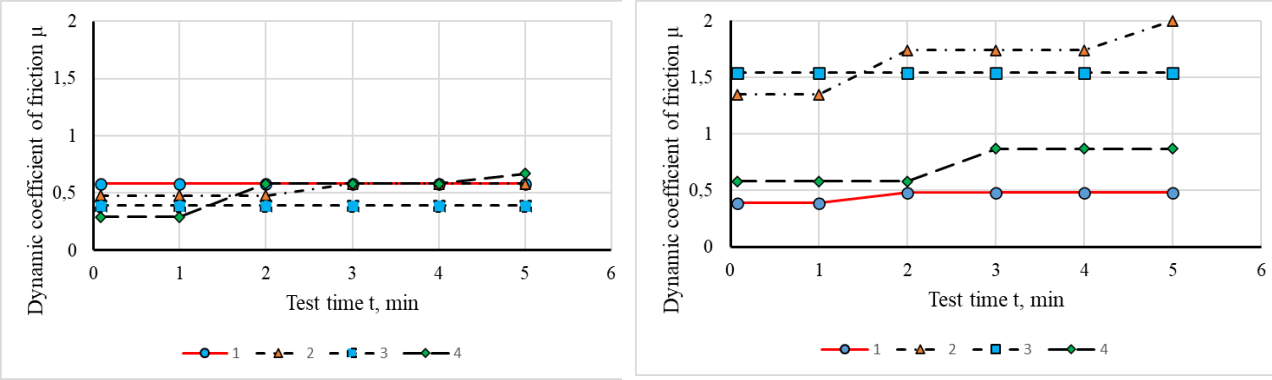

a) *b)*

Fig. 4. Dependence of the dynamic coefficient of friction on the time of tribotechnical testing of coatings at T = 25°C after exposure to the furnace: a) at thermal spray forming; b) at plasma spray forming; 1 - original coating; 2 - yttrium 0.1%; 3 - yttrium 0.3%; 4 - yttrium 0.5%.

For the coatings formed by the ionoplasma method, Fig 4, b, an increase in the friction coefficient is observed exclusively for all yttrium-containing coatings, which is due to the creation of surface structures capable of exerting greater resistance, but with a larger number of separable particles, as indicated by the data in Table 4. The lowest values of the friction coefficient were observed for the coating with a yttrium content of 0.5%, for which the wear rate was average between the coatings with a yttrium content of 0.1% and 0.3%. Again, this indicates the peculiarity of the distribution of gradients of mechanical properties of coatings along the depth. Thus, in this case, the coating with yttrium content of 0.5% is characterized by a lower resistance to the destruction of cohesive bonds between the coating components, which actively reduces the shear resistance and causes a lower friction coefficient. However, this resistance is 1.5 to 1.8 times higher than that of a yttrium-free coating during the test.

The exposure of the coatings to static high-temperature conditions resulted in the following distribution of points in the assessment of their durability (Table 5). The values of the friction coefficients were selected according to the time of manifestation of obvious differences, i.e., from the beginning of the tests to 1 min of testing, Fig 4, a, b.

Table 5. Evaluation of coatings after exposure to static high-temperature environment.

Formation method	Parameter	Number of points min→max steadiness			
		1	2	3	4
Thermal spray	I_m	**0.1**	**0.3**	**0**	**0.5**
	μ	**0**	**0.1**	**0.3**	**0.5**
Plasma spray	I_m	**0.1**	**0.5**	**0.3**	**0**
	μ	**0.1**	**0.3**	**0.5**	**0**

From the data in Table 5, it should be assumed that the coating formed by the thermal spray method has a parameter coincidence of 4 points with a yttrium concentration of 0.5%, i.e., it has the maximum score. Based on this, this coating has the maximum resistance to mechanical fracture when forming the cut-in tracks. For the coating formed by the plasma spray method, there is no obvious coincidence, but the maximum resistance for concentrations from 0.3% to 0.5% with a point 3.

Research results at stage 4.

The analysis of the data obtained regarding the manifestation of the resistance of coatings to mechanical fracture at a temperature of T=950-1020°C after exposure to high-temperature static load in an oven at a temperature of 1100 °C indicates the following:

- the minimum value of the weight of the separated particles was Δm_{min}=0.0131 g for the coating formed by the thermal spray method with yttrium concentration of 0.5%, the maximum value Δm_{max}=0.0832 g occurred for the coating formed by the thermal spray method with a yttrium concentration of 0.1%;

- the minimum value of friction work A_{tmin} =3140.9 J was for the coating formed by the plasma spray method with a yttrium concentration of 0.1%, the maximum value A_{tmax}=6074.7 J was for the coating formed by the thermal spray method without yttrium.

Based on the above, the limiting values of stability according to the parameters of expressions (2,3) were as follows:

- minimum resistance corresponds to the maximum energy conditional wear intensity $I_{mu}=2.64\cdot10^{-5}$ g·J$^{-1;}$
- maximum resistance corresponds to the minimum energy conditional wear intensity $I_{mu}=2.15\cdot10^{-5}$ g·J^{-1}.

Thus, in comparison with the ultimate limits of stability relative to the original coatings, it is clear that the range of stability of the coatings after exposure to high-temperature loading narrowed by almost 32.5 times. And compared to the resistance range that occurred at the previous stage, the range narrowed by 15.8 times. This indicates a significant influence of the high-temperature loading factor on the formation of fracture resistance when forming the insertion tracks.

At the same time, after repeated high-temperature loading, the resistance for coatings obtained by the thermal spray method with the addition of yttrium decreased by an average of 1.5 times, and without yttrium remained almost unchanged (Table 4). The coating with a yttrium concentration of 0.5% was more resistant. For coatings formed by the thermal spray method, the picture is the opposite, the resistance increased for coatings with yttrium by an average of 1.25 times. Coatings with a yttrium concentration of 0.5% had greater resistance (Table 4). The general picture of the trends in the energy intensity of wear of the experimental coatings is shown in Figure 5.

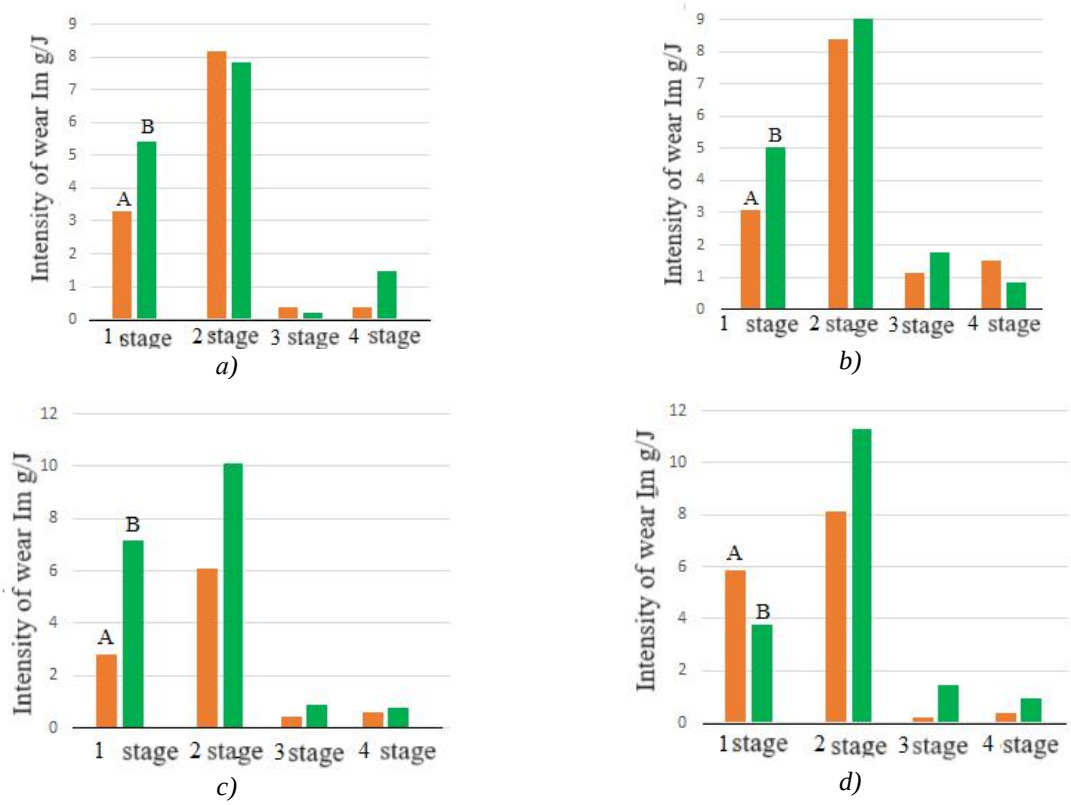

Fig. 5. Diagrams of ratios of wear intensities Im·10^{-5} of coating materials by stages of research: A - coating formed by the thermal spray method; B - coating formed by the plasma method; a) without yttrium; b) yttrium 0.1%; c) yttrium 0.3%; d) yttrium 0.5%.

The character of the friction coefficient for coatings, Fig 6, indicates the following. The general picture of the mechanical behavior of coatings, which was described for the identified typological condition at stage 4, is preserved. The exception is due to the change in some numerous values of the friction coefficient and the pattern of its manifestation over the test time, which is caused, firstly, by the temperature of the interaction medium, and secondly, by an increase in load, almost 1.8 times.

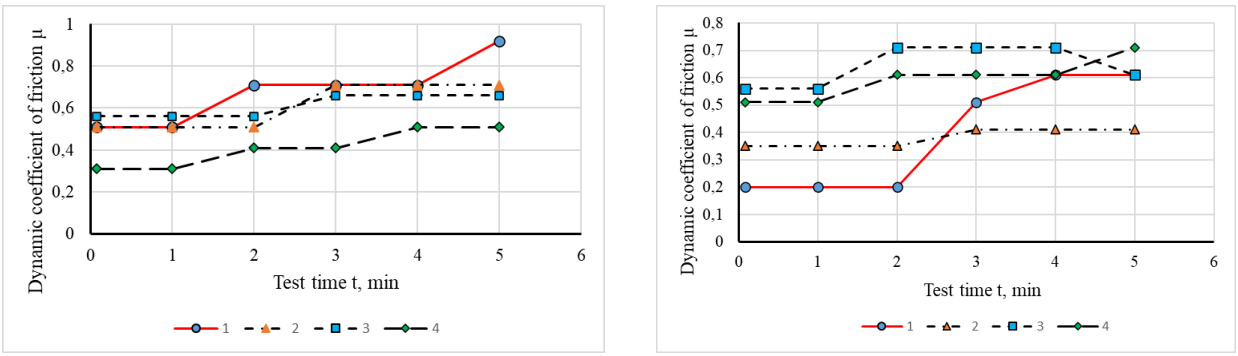

a) *b)*

Fig. 6. Dependence of the dynamic coefficient of friction on the time of tribotechnical testing of coatings at T = 950-1020ºC after exposure to the furnace: a) at thermal spray forming; b) at plasma spray forming; 1 - initial coating; 2 - yttrium 0.1%; 3 - yttrium 0.3%; 4 - yttrium 0.5%.

For all yttrium-containing gas-flame coatings, there is an increase in the friction coefficient over the test time, which indicates an increase in the resistance to movement and the manifestation of gradients in the mechanical properties of their near-surface layers. For all yttrium-containing ion-plasma coatings, a decrease in the friction coefficient by 1.3-2.6 times is observed, indicating an additional formation of surface structures capable of exerting less resistance to movement.

Table 6. Evaluation of coatings after exposure to static high-temperature environment.

Formation method	Parameter	Number of points min→max stability			
		1	2	3	4
Thermal spray	I_m	0.1	**0.3**	0.5	0
	μ	0	**0.3**	0.1	0.5
Plasma spray	I_m	0	0.5	**0.1**	0.3
	μ	0.3	0.5	**0.1**	0

From the data in Table 6, it should be assumed that the coating formed by the thermal spray method has a parameter coincidence of 2 points with yttrium concentration of 0.3%, i.e., it has an average score. Based on this, this coating has an average resistance to mechanical fracture when forming the cut-in tracks. For the coating formed by the plasma spray method, there is a coincidence of parameters in terms of the number of points, which is equal to 3 with yttrium concentration of 0.1%, i.e., it also has an average score, but higher than the gas flame coating.

4. Conclusion

The results of the four-stage experiment indicate the importance of taking into account the influence of various factors on the mechanical resistance of coatings. The first stage of the study showed that the effect of yttrium content, high-temperature, and coating formation method on their resistance to mechanical fracture is ambiguous. A decrease in resistance is observed when using the plasma spray method compared to the thermal spray method, when there is no temperature load. The second stage confirmed that the coatings obtained by the thermal spray method have the maximum resistance to mechanical fracture compared to other methods, but their properties can change after heating. The third stage indicates an increase in the stability of coatings after exposure to high-temperature loading in a furnace, regardless of yttrium concentration, but a narrowing of the stability range after such exposure is observed. At the fourth stage, it was confirmed that high-temperature loading significantly affects the mechanical stability of coatings, and the addition of yttrium can affect their stability, depending on the method of coating formation and its concentration.

In conclusion, high-temperature loading has a significant impact on the mechanical resistance of coatings, and this factor should be taken into account when using them in appropriate conditions. The addition of yttrium can be useful for improving resistance, but the effect of this element depends on the method of coating formation and its concentration. Thus, the optimal choice of coating formation parameters can only be made based on a comprehensive analysis of all these factors. To confirm the results, further studies of the microstructure and phase composition of the coatings will be carried out.

Conflict of interest statement
The authors declare that they have no conflict of interest in relation to this research, whether financial, personal, authorship or otherwise, that could affect the research and its results presented in this paper.

CRediT author statement
Kubich V.: supervision, conceptualization, methodology; **Fasol Ye.:** investigation, data curation, software; **Cherneta O.**: validation, writing - review & editing; visualization; Yershina A.K., Sakipov N.Z.: formal analysis, writing-original draft.
The final manuscript was read and approved by all authors.

References

1 Čížek M., Pátek Z. (2020) On CFD investigation of radial clearance of labyrinth seals of a turbine engine. *Acta Polytechnica*, 60(1), 38–48. DOI: 10.14311/ap.2020.60.0038.

2 Yu B., Ke H., Shen E., Zhang T. (2020) A review of blade tip clearance–measuring technologies for gas turbine engines. *Measurement and Control*, 53(3-4), 339–357. DOI: 10.1177/0020294019877514.

3 Zhang B., Li J., Li W., Ji H. (2021) Influence of Geometric Tooth Shape Parameters of Labyrinth Seals on the Flow Law and the Algorithm for Designing Straight Grate Teeth. *Russian Physics Journal*, 64(6), 1122–1129. DOI:10.1007/s11182-021-02432-0.

4 Enache M., Carlanescu R., Mangra A., Florean F., Kuncser R. (2021) Investigation of Flow through a Labyrinth Seal. *Incas Bulletin*, 13(2), 51–58. DOI: 10.13111/2066-8201.2021.13.2.6.

5 Dai X., Yan X., He K., Li J., Feng Z. (2020) Numerical Investigations of Leakage Performance Degradations in Labyrinth and Flexible Seals Due to Wear. *Journal of Engineering for Gas Turbines and Power*, 143 (5). DOI:10.1115/1.4049008.

6 Ullah A., Khan A., Bao Z.B., Yang, Y.F., Xu M.M., Zhu S.L., Wang F.H. (2021) Temperature Effect on Early Oxidation Behavior of NiCoCrAlY Coatings: Microstructure and Phase Transformation. *Acta Metallurgica Sinica (English Letters)*, 35(6). DOI: 10.1007/s40195-021-01310-5.

7 Hao E., Zhao X., An Y., Deng W., Zhou H., Chen J. (2019) The effect of pre-oxidation on microstructure, mechanical properties and high-temperature tribological behaviors of HVOF-sprayed NiCoCrAlYTa coating. *Applied Surface Science*, 489, 187–197. DOI: 10.1016/j.apsusc.2019.05.334.

8 Jojith R., Sam M., Radhika N. (2021) Recent advances in tribological behavior of functionally graded composites: A review. *Engineering Science and Technology, an International Journal*, 25(5). DOI:10.1016/j.jestch.2021.05.003.

9 Szala M., Walczak M., Świetlicki A. (2021) Effect of Microstructure and Hardness on Cavitation Erosion and Dry Sliding Wear of HVOF Deposited CoNiCrAlY, NiCoCrAlY and NiCrMoNbTa Coatings. *Materials*, 15(1), 93. DOI: 10.3390/ma15010093.

10 Elsaß M., Kontermann C., Oechsner M. (2021) Temperature influence on the development of interdiffusion phenomena in MCrAlY-coated nickel-based superalloys. *Materialwissenschaft und Werkstofftechnik*, 52(2), 248–260. DOI: 10.1002/mawe.202000270.

11 Paul S. (2017) Stiffness of Plasma Sprayed Thermal Barrier Coatings. *Coatings*, 7(5), 68. DOI:10.3390/coatings7050068.

12 Wu Y., Li Y., Xu Y., Kang M., Wang J., Sun B. (2021) Unveiling the mechanism of yttrium-related microstructure inhibiting or promoting high-temperature oxidation based on Ni-Al-Y alloys. *Acta Materialia*, 211, 116879. DOI: 10.1016/j.actamat.2021.116879.

13 Wu Y., Li Y., Xu Y., Kang M., Wang J., Sun B. (2021b) Unveiling the precipitation-induced high-temperature oxidation behavior in a Ni-Al-Y alloy. *Materials Letters*, 297, 129977. DOI: 10.1016/j.matlet.2021.129977.

14 Boguslaiev V.O., Greshta V.L., Kubich V.I., Tkach D.V., Fasol Y.O., Lekhovitser V.O. (2020) Effect of alloying heat-resistant packing coatings on their tribotechnical, physical and mechanical properties. *Naukovyi Visnyk Natsionalnoho Hirnychoho Universytetu*, (6), 41–47. DOI: 10.33271/nvngu/2020-6/041.

15 Boguslaev V.O., Greshta V.L., Tkach D.V., Kubich V.I., Sotnikov E.G., Lekhovitser Z.V., Klymov O.V. (2019) Evaluation of the Tribotechnical Characteristics of Therma-Barrier Sealing Coatings under Critical Loads. *Journal of Friction and Wear*, 40(1), 80–87. DOI:10.3103/s1068366619010033.

AUTHORS' INFORMATION

Kubich, Vadim Ivanovich – PhD, Associate Professor, Department of Automobiles National University «Zaporizhzhia Polytechnic», Zaporizhzhia, Ukraine, 69063, Scopus Author ID 57203875007; https://orcid.org/0000-0001-6230-9263; schmirung@gmail.com

Fasol, Yelyzaveta Oleksandrivna – Master, Senior Lecturer, Department of Physical Materials Science, National University «Zaporizhzhia Polytechnic», Zaporizhzhia, Ukraine, 69063, Scopus Author ID: 57221413434; https://orcid.org/0000-0003-4846-9046; selvluna@gmail.com

Cherneta, Oleg Georgievich - PhD, Associate Professor, Associate Professor, Department of automobiles and automotive industry, Dniprovsky State Technical University, Kamenske, Ukraine, 51918, Scopus Author ID: 57203871112; https://orcid.org/0000-0002-3871-6923; OCherneta@gmail.com

Yershina, Ainagul Kappasovna - Doctor of Phys. and Math. Sciences, Professor, Kazakh National Women's Teacher Training University, Almaty, Kazakhstan; Scopus Author ID: 55849381800; https://orcid.org/0000-0002-6811-3904; 123ainakul.yershina@gmail.com

Sakipov, Nurlan Zarkeshovich – Candidate of Phys. and Math. Sciences, Associate Professor, Civil Aviation Academy, Almaty, Kazakhstan; Scopus Author ID:6505664666; https://orcid.org/0000-0001-9853-2491; nsakipov@mail.ru

EURASIAN PHYSICAL TECHNICAL JOURNAL

2024, Volume 21, No.3 (49)

https://doi.org/10.31489/2024No3/93-98

Received: 14/06/2024 Revised: 17/09/2024 Accepted: 26/09/2024 Published online: 30/09/2024

Research Article

UDC: 537.874.4

SCIENTIFIC AND TECHNICAL SUBSTANTIATION OF THE PARAMETERS OF THE RADIOLOCATION DEVICE FOR THE DETECTION OF PROHIBITED ITEMS

Zhantlessov Y.Zh.[2], Smakova N.S.[2*], Gruzin V.V.[1], Togussov A.K.[1], Jussupbekov T.Kh.[1], Zhantlessov Zh.Kh.[2]

1 - National Defense University

2 - K.Kulazhanov Kazakh University of Technology and Business

*Corresponding author: nuri_5@mail.ru

Abstract. *The paper presents a scientific and technical substantiation of the parameters of the radar device, which allows to detect and visualize forbidden objects by means of electromagnetic radiation of the microwave range. A model of a multistatic scheme for measuring waves reflected from an object based on the holographic method is developed. A software complex of simulation modeling of radar device operation has been developed, by means of which reconstructions of object images for different configurations of sparse sensor subsystems of the radar device have been obtained. An optimal configuration of the sparse sensor subsystem was selected by the method of peak signal-to-noise ratio analysis, for which a multi static hologram was modeled and a reconstruction of the metal rod image was generated. The reconstruction of the metal rod image obtained as a result of simulation modeling has a recognizable contour, which confirms the prospect of developing an experimental prototype of a radar device for detecting prohibited objects.*

Keywords: microwave imaging, holography, multi static array, detection of prohibited items, visualization.

1. Introduction

Places of mass gatherings require special measures to ensure safety. This is due to the fact that mass events involve large numbers of people, which may be associated with security threats due to unlawful actions of certain groups of people. To reduce the surprise factor from the use of various types of prohibited items, it is necessary to use technical systems to detect the presence of prohibited items hidden under clothing or in any hand-held items, such as bags [1].

Prohibited items to be detected are traditionally made of durable materials that have a high reflection coefficient for electromagnetic waves: metal, plastic, rubber, ceramics, and others. [2].

The radio wave method of object detection is promising in terms of in formativeness, safety and non-contact action in the process of scanning various objects. Based on the radio wave method, research is underway to develop inspection systems that allow remote detection of prohibited objects [3,4].

Currently created means of remote detection and visualization of prohibited items, based on radio waves have a rather high price, which is one of the factors limiting their widespread use. Based on the above, it can be stated that the development of an affordable radar device that allows remote detection of hidden prohibited items is an urgent scientific and technical task that requires research.

In the presented work, a scientific and technical justification of the parameters of a radar device for the detection of forbidden objects by means of a holographic method of image acquisition using a multi static measurement scheme is proposed [5,6].

The concept of radar device application is as follows: the object of inspection is installed at a certain distance from the sensor subsystem, which is an array of measuring and radiating antennas evenly distributed in the plane of the sensor subsystem (Figure 1).

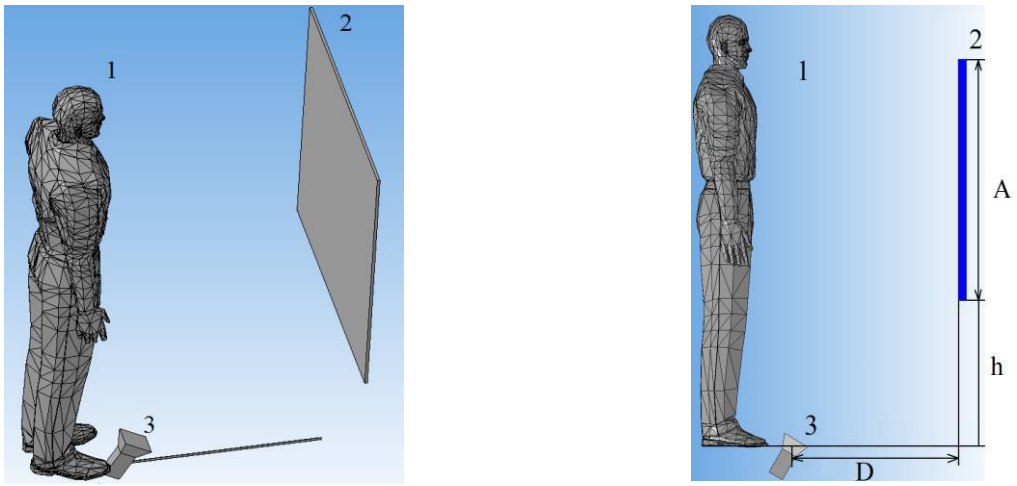

a *b*

a - general view of the arrangement; b - side view; A - aperture size of the sensor subsystem; D - distance from the base of the sensor subsystem to the reference source; 1 - detection object; 2 - sensor system; 3 - reference source

Fig 1. Location of the detection object in relation to sensor system and reference source.

The reference source is installed opposite the sensor subsystem in such a way as to ensure a high stable level of the reference signal over the entire measuring plane. Radiators of the sensor subsystem in turn irradiate the object with electromagnetic wave of the microwave range. As a result of interaction between the wave reflected from the object and the reference source, a hologram is formed, which is registered by the measuring antennas of the sensor subsystem [7].

For most prohibited items, the most common place to carry prohibited items is the torso area. It is in this area that the best authorization should be concentrated. The average height of a person is 1.7 meters, but occasionally people with a height of about two meters are encountered, so the maximum dimensions of a person are assumed to be 2 meters.

In [8], studies of spatial resolution depending on aperture parameters and location of the object of inspection relative to the sensor subsystem were carried out, and rational parameters of the radar device for human inspection for the presence of prohibited items were scientifically substantiated (Table 1).

Table 1. Rational parameters for inspection of a person up to two meters tall.

Parameter name	Minimum value	Maximum value
Distance to the object, m	L = 0,6 м	L = 1 м
Aperture size of radiolocation device sensor subsystem, m	D = 1 м	
Height of radiolocation device sensor subsystem center, m	J = 1 м	

The presented location of the sensor subsystem relative to the scanning object allows its inspection with a resolution in the range from half-length to 0.9 wavelength. One of the main criteria in the process of creating a radar device for the detection of prohibited items is for the assembly of the system to select according to certain parameters the necessary components with operating frequency up to 6 GHz and wavelength of 50 mm.

2. Formulation of the problem

The research task of designing a radar device for the detection of prohibited objects is to find its best configuration that combines a rational ratio between the quality of the received image and the technical characteristics of its subsystems. The standard approach of designing sensor subsystems is based on the fact

that the distance between neighboring radiating and measuring antennas should be no more than half a wavelength of radiation, which provides a high-quality image [9]. However, the design of such a sensor subsystem is not economically feasible due to the high requirements for the measurement electronics and computing module.

The main advantage of wave systems based on a multi static sensing scheme is that the reconstruction algorithm is robust to the aperture sparsity of the sensor subsystem. This means that it is possible to use a sensor subsystem in image computation where the distance between the emitting and measuring elements of the sensor subsystem is greater than half the wavelength of the sensing signal.

The use of a sparse sensor subsystem will result in the appearance of systematic noise in the image reconstruction [10]. However, despite the presence of systematic noise, the image quality can remain at the required level, sufficient for detection and unambiguous recognition of the forbidden object, at different coefficients of the sensor subsystem sparse.

In view of the existence of many combinations of parameters and configurations of the radar device, the task of searching for rational parameters by experimental methods is quite laborious, so in this case the method of simulation modeling is the most effective [11].

3. Model Development

To analyze the influence of sensor subsystem parameters on the quality of image reconstruction, a spatial diagram of one transmitter-receiver pair of sensor and reference source subsystems was initially drawn (Figure 2).

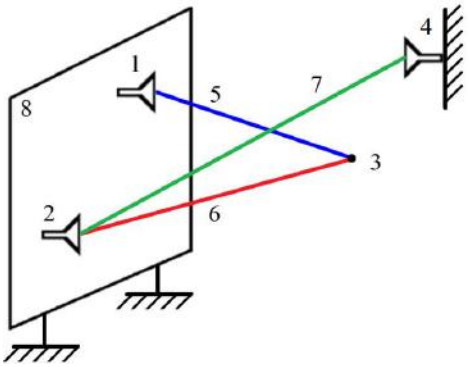

1 - transmitter; 2 - receiver; 3 - reflection point; 4 - reference source;
5 - wave path from the transmitter to the reflection point; 6 - wave path from the reflection point to the receiver; 7 - wave path from the reference source to the receivers; 8 - measurement plane of reflected signals

Fig 2. Spatial diagram of one pair “transmitter - receiver” sensor subsystem of the radar device.

In the process of forming the simulation area, which is bounded by the cube ABCDEFGH with an edge equal to 1 m, the sensor system 1 (see Figure 3) was located on the face ABCD. In the center of the EFGH face there is an object 2 (see Figure 3) of scanning, for which analytical studies with the help of simulation were performed.

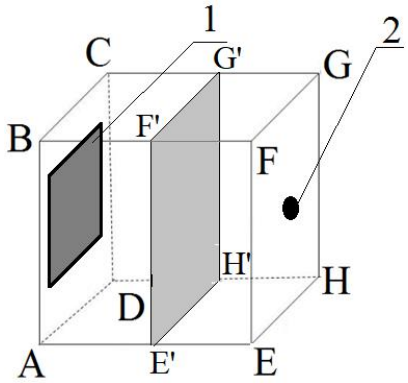

1 - location of the sensor subsystem; 2 - location of the modeling object

Fig 3. Simulation modeling area.

The flat image of the scanning object for simulation modeling is a two-dimensional array of 256 x 256 points, each of which of the simulation object has two states:

1 - 100% reflection;

2 - 0% reflection.To control the noise level of image reconstruction we will use the peak signal-to-noise ratio (hereinafter referred to as PSNR) [12]:

$$\mathrm{PSNR} = 20\lg\left(\frac{\mathrm{MAX}}{RMS}\right), \quad (1)$$

where, *MAX* – maximum value of the reconstruction intensity;

RMS – the standard deviation of the image reconstruction [13].

$$RMS = \frac{1}{\mathrm{X}\cdot\mathrm{Y}}\sum_{i=o}^{X-1}\sum_{j=0}^{Y-1}\left(I_0(i,j) - \mathrm{I}(i,j)\right)^2, \quad (2)$$

where, $I_0(i,j)$ - image reconstruction obtained by the sensor subsystem with the distance between neighboring emitters and receivers equal to half wavelength, two-dimensional array;

$I(i,j)$ - image reconstruction obtained by a sparse sensor subsystem with the distance between neighboring emitters and receivers exceeding half a wavelength, two-dimensional array;

i, j - coordinates of the image point, pixel;

X, Y - length and width of the image reconstruction, pixel.

4. Results of simulation modeling

Using the simulation software package, the influence of the rarefaction coefficients of transmitters and receivers in the sensor subsystem was investigated of the sensor subsystem of the radiolocation device on the PSNR of the image reconstruction (Figure 4).

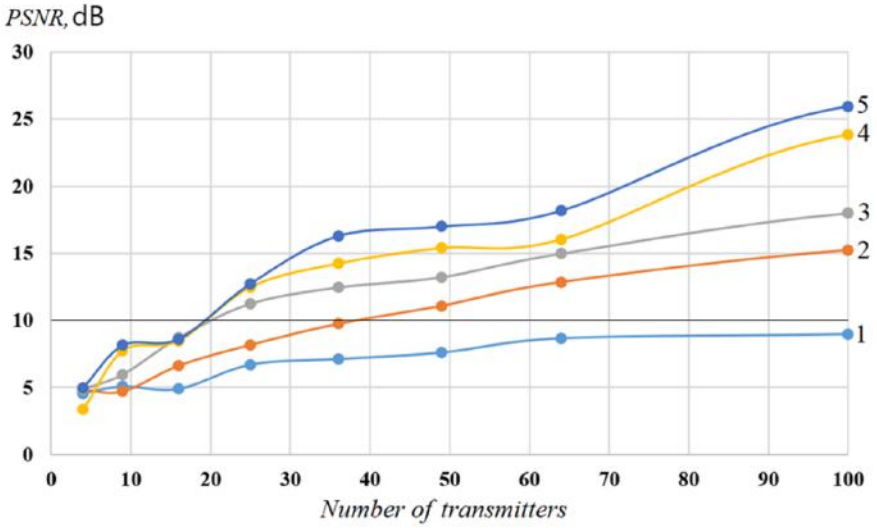

1 - PSNR for 144 receivers; 2 - PSNR for 196 receivers; 3 - PSNR for 256 receivers;
4 - PSNR for 324 receivers; 5 - PSNR for 400 receivers;

Fig 4. Plots of peak signal-to-noise ratio as a function of the number of transmitters in the sensor system.

As a criterion for selecting the configuration of the sensor subsystem we will use the value of peak signal-to-noise ratio equal to 10 dB. Such peak signal-to-noise ratio will allow to detect, unambiguously recognize and classify the object as forbidden.

Further parameters of the sensor subsystem are selected based on the principle of minimizing the number of measurement channels.

As a result of optimization, a sensor subsystem configuration consisting of 49 emitting and 196 measuring channels was selected. Simulation modeling was performed for the selected sensor subsystem configuration, and the contour of a metal rod with a length of 500 mm and a diameter of 20 mm was used as a modeling object (Figure 5-A). As a result of the simulation, image reconstructions were obtained for a full sensor subsystem consisting of 1600 emitters and 1600 receivers (Figure 5-B) and a sparse sensor subsystem consisting of 49 emitters and 196 receivers (Figure 5-C).

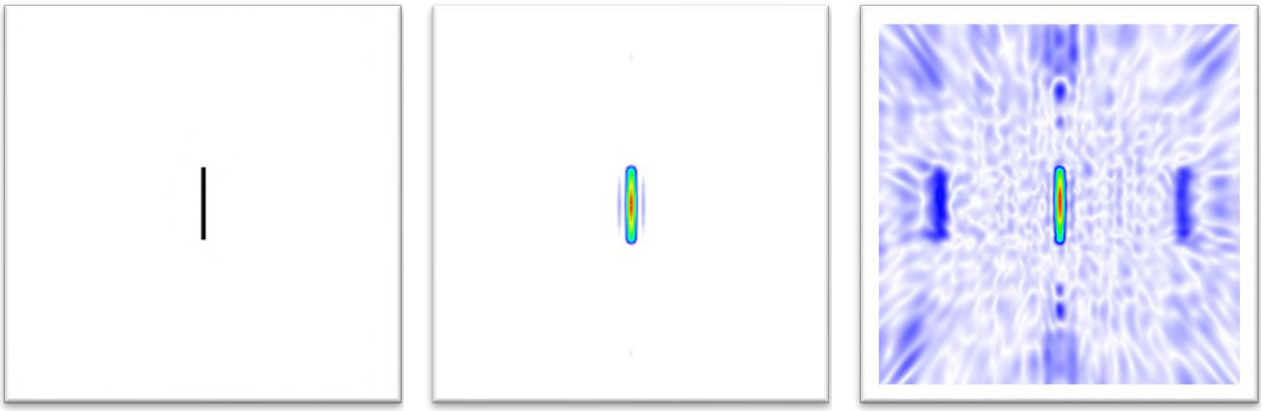

A B C

A - modeling object; B - image reconstruction for sensor subsystem with C

Fig 5. Modeling object and its image reconstruction depending on the number of measurement channels.

5. Conclusions

As a result of this study, the possibility of developing an affordable radar device for detecting hidden prohibited objects using a sparse sensor subsystem has been confirmed.

For different configurations of sparse sensor subsystems, the simulation modeling of radar device operation was carried out. Dependences of the peak signal-to-noise ratio depending on the sparse aperture configuration are obtained.

An optimization strategy based on the requirements of image reconstruction quality equal to 10 dB and minimization of the number of measurement channels is formed.

As a result of the optimization, a sensor subsystem consisting of 49 transmitters and 196 receivers is selected, with:

- aperture equal to 1 m;
- center of the sensor subsystem placed at a height of 1 m;
- distance to the scanning object equal to 1 m.

The reconstruction of the image of the metal rod obtained as a result of simulation modeling has a recognizable contour, which confirms the possibility of developing an experimental prototype of the radar device for the detection of prohibited objects, despite the existing noise.

Conflict of interest statement

The authors declare that they have no conflict of interest in relation to this research, whether financial, personal, authorship or otherwise, that could affect the research and its results presented in this paper.

CRediT author statement

Zhantlessov Y.Zh.: conceptualization, project administration; Smakova N.S.: investigation, validation;
Gruzin V.V.: Methodology; Formal analysis; Togusov A.K.: investigation; Jusupbekov T.Kh: research strategy; Zhantlessov Z.Kh: mathematical model concept.
The final manuscript was read and approved by all authors.

Funding

The scientific article was published within the framework of the implementation of the scientific project of grant funding for 2022-2024 years IRN № AP148038/0222
(The research is funded by the Committee of Science of the Ministry of Science and Higher Education of the Republic of Kazakhstan).

References

1. Harmer S., Cole S., Bowring N., Rezgui N., Andrews D. (2012) On body concealed weapon detection using a phased array. *Progress in Electromagnetics Research*, 124, 187 – 210, DOI:10.2528/PIER11112105.

2. Yermakhanova A., Kenzhegulov A., Meiirbekov M., Samsonenko A., Baiserikov, B. (2023) Study of radio transparency and dielectric permittivity of glass- and aramid epoxy composites. *Eurasian Physical Technical Journal*, 20(2(44), 70–78. DOI: 10.31489/2023No2/70-78.

3. David M. Sheen. (2015) Noise analysis for near-field 3D FM-CW radar imaging systems. *Proceedings of the SPIE*, 9462. DOI: 10.1117/12.2180032.

4. Corredoura P., Baharav Z., Taber B., Lee G. (2006) Millimeter-Wave Imaging System for Personnel Screening: Scanning 10^7 Points a Second and Using No Moving Parts. *SPIE Passive Millimeter-Wave Imaging Technology*, 62110B.DOI: 10.1117/12.669664.

5. Sheen D.M. (2013) Sparse multi-static arrays for near-field millimeter-wave imaging. *2013 IEEE Global Conference on Signal and Information Processing*, Austin, TX, USA, 699-702, DOI:10.1109/GlobalSIP.2013.6736987.

6. Sherif A. (2013) *Electronic Microwave Imaging with Planar Multistatic Arrays*. Faculty of Engineering Friedrich-Alexander - Universitaet Erlangen - Noernberg for the doctoral degree Doctor of Engineering. - Erlangen. - 226 p. https://www.researchgate.net/profile/Sherif-Ahmed-5

7. Zhantlessov Zh.Kh, Gruzin V.V., Zhantlessov Y.Zh. (2017) Object scanning method. *Patent for invention № 32026.* National institute of intellectual property. Astana, Kazakhstan 31.03.2017.

8. Zhantlessov Y.Zh. (2020) *Justification of parameters and development of hardware-software complex of radio- and acoustic tomography of static objects*. National Defense University of the Republic of Kazakhstan. Astana, 2020. 151 p. [in Russian], For official use.

9. Zhuravlev A., Razevig V., Rogozin A., Chizh M. (2023). Microwave Imaging of Concealed Objects With Linear Antenna Array and Optical Tracking of the Target for High-Performance Security Screening Systems. *IEEE Transactions on Microwave Theory and Techniques*, 71 (3), 1326-1336, DOI:10.1109/TMTT.2022.3217593.

10. Muhammad A. E., Martin G., Edward J., Martin O'H. (2013) Artifact Removal Algorithms for Microwave Imaging of the Breast. *Progress In Electromagnetics Research,* 141, 185-200. http://dx.doi.org/10.2528/PIER13052407.

11. Shumakov D.S., Tu S., Nikolova N.K. (2015) Fast quantitative microwave imaging based on measured point spread functions and inversion in real space. *2015 IEEE International Symposium on Antennas and Propagation & USNC/URSI National Radio Science Meeting.* Vancouver, BC, Canada, 687-688. DOI: 10.1109/APS.2015.7304730.

12. Yang X. (2018) *Signal processing for microwave imaging systems with very sparse array*. Doctoral Dissertation. Missouri University of Science and Technology. 116 p. https://scholarsmine.mst.edu/doctoral_dissertations/2733

13. Zhang B., Hong W., Wu Y. (2012) Sparse microwave imaging: Principles and applications. *Sci. China Inf. Sci.*, 55, 1722–1754. DOI: 10.1007/s11432-012-4633-4.

AUTHORS' INFORMATION

Zhantlessov, Y.Zh - PhD, Senior Lecturer, K. Kulazhanov Kazakh University of Technology and Business, Astana, Kazakhstan; Scopus Author ID: 55772588800; ORCID ID: 0000-0001-7209-5844; yerbolzh@mail.ru

Smakova, N.S. - PhD, Associate Professor, K. Kulazhanov Kazakh University of Technology and Business, Astana, Kazakhstan; Scopus Author ID: 56669706400; ORCID ID: 0009-0002-5754-4001; nuri_5@mail.ru

Gruzin, V.V. - Doctor of techn. sciences, Professor of the Technical Support Department of the National Defense University of the Republic of Kazakhstan, Astana, Kazakhstan; Scopus Author ID: 57191036631; ORCID ID: 0000-0002-1128-5246; gruzinvv@mail.ru

Togussov, A.K. - Doctor of techn. sciences, Professor of the Technical Support Department of the National Defense University of the Republic of Kazakhstan, Astana, Kazakhstan; Scopus Author ID: 57222548232; ORCID ID: 0009-0009-5810-1940; tak_70@mail.ru

Jussupbekov, T.Kh. - Doctoral student of the Department of Technical Support of the National Defense University of the Republic of Kazakhstan, Astana, Kazakhstan; ORCID ID: 0009-0007-7119-4681; timur607@mail.ru

Zhantlessov, J.Kh. - Candidate of Physical and Mathematical Sciences, Associate Professor, K. Kulazhanov Kazakh University of Technology and Business, Astana, Kazakhstan. ORCID ID: 0009-0004-9294-8292; jangabil@mail.ru

EURASIAN PHYSICAL TECHNICAL JOURNAL

2024, Volume 21, No. 3 (49)

https://doi.org/10.31489/2024No3/99-107

Received: 29/06/2024 Revised: 11/09/2024 Accepted: 19/09/2024 Published online: 30/09/2024

Research Article

UDC 549.641.1, 620.3

EFFECT OF ANNEALING DURATION ON PHOTOCATALYTIC PROPERTIES OF $LaFeO_3$ PEROVSKITE

Zhanbirbayeva P.A., Baltabekov A.S., Kayumova A.S., Kuanyshbekova A.B., Adambay T.N., Serikov T.M. *

E.A. Buketov, Karaganda University, Karaganda, Kazakhstan
*Corresponding authors: serikov-timur@mail.ru

Abstract. *In this paper, the effect of the annealing duration on the photocatalytic properties of lanthanum ferrite perovskite synthesized by the hydrothermal method is investigated. Lanthanum ferrite was chosen as the object of study due to its high activity under the influence of visible light. During the experiments, the structural changes occurring in the material during annealing during 2, 4 and 6 hours were studied. The main attention was paid to the analysis of the morphology of nanoparticles, phase composition, crystallinity, absorption spectra and photocatalytic activity. The results show that an increase in the annealing time leads to an improvement in the crystal structure, an increase in the size of crystallites and a higher level of oxygenation. The optimal annealing time to achieve maximum photocatalytic activity was determined to be 6 hours. The work confirms the prospects of using long-term annealing to improve the photocatalytic properties of perovskite-based materials.*

Keywords: Lanthanum ferrite, annealing duration, photocatalytic activity.

1. Introduction

Currently, solar energy, as a bright and renewable source, is used as an alternative to fossil fuels [1]. Photocatalysis is a promising environmentally friendly method based on the use of semiconductor photocatalysts with high chemical and thermal stability. These processes are usually carried out with the participation of photoinduced charge carriers under mild operating conditions without the addition of chemicals. This gives photocatalysis an advantage over traditional methods such as biological and electrocatalytic treatment, which are often accompanied by instability, low mechanical strength, poisoning of catalysts and corrosion of electrodes [2,3]. The use of solar energy by semiconductor photocatalysts makes it possible to obtain hydrogen by reducing water, convert CO_2 into useful chemicals and oxidize various pollutants [4]. Thus, semiconductor-based photocatalysis is considered as a clean, cost-effective, renewable and safe technology [5]. Since the first report on photocatalysis using TiO_2 [6], this area has attracted considerable attention from scientists around the world. To date, there are many semiconductor photocatalysts, such as ZnO [7], SnO_2 [8], $BiVO_4$ [9], BiOCl [10], $SrTiO_3$ [11], WO_3 [12], Fe_2O_3 [13], Ta_2O_5 [14], $BiFeO_3$ [15], Bi_2WO_6 [16], Cu_2O [17], g-C_3N_4 [18], graphene [19] and carbon nanotubes [20] are actively used in the photocatalytic production of solar fuels and environmental purification.

Many promising environmentally friendly methods have been developed for photocatalytic disinfection of water and reduction of CO_2 emissions aimed at use in green and renewable energy [21]. During the process of semiconductor photocatalysis, highly reactive and transient particles are generated on the surface of a semiconductor material when it is exposed to light with a wavelength corresponding to or exceeding the band gap of the substance [22]. These particles exhibit a remarkable capacity for oxidation and reduction, enabling

them to break down pollutants, mitigate CO_2 emissions, and facilitate the splitting of water [23]. Recently, materials such as perovskites have garnered significant attention within the realm of photocatalytic research. Perovskites are crystalline materials with a stable structure of the ABO_3 type, which exhibits remarkable flexibility in its composition. This flexibility arises from the capacity to replace ions of rare-earth or alkaline-earth metals in position A, as well as transition metals in position B. The exceptional properties of perovskites as photocatalysts stem from their ability to manipulate valence and vacancy states, significantly enhancing their catalytic capabilities. Moreover, perovskite-based photocatalytic materials boast a narrow bandgap, enabling more efficient utilization of solar energy compared to other semiconductor-based counterparts [24].

Of particular relevance in this context is the lanthanum ferrite compound, $LaFeO_3$, which exhibits remarkable photocatalytic properties when exposed to visible light with an energy gap of 2.0 eV [25]. Within the perovskite structure of $LaFeO_3$, the rare-earth metal ion assumes position A, while the transition metal cation takes up position B [26].

There are various methods for the synthesis of $LaFeO_3$ nanostructures, which are used in the fields of energy and ecology. These include hydrothermal, solvothermal, sol-gel, microwave, and sonochemical methods. In this study, the hydrothermal method was employed for the synthesis of $LaFeO_3$, as it has several advantages. The hydrothermal method enables the material to be produced at relatively low temperatures, contributing to the formation of high-quality crystalline structures with controlled morphology and a narrow range of particle sizes. This approach also ensures a high degree of uniformity and purity in the sample, which is crucial for subsequent investigations of photocatalytic properties.

This work is aimed at studying the effect of annealing duration on the structural and photocatalytic properties of $LaFeO_3$ synthesized by the hydrothermal method.

2. Experimental part

Synthesis of $LaFeO_3$

During hydrothermal synthesis of $LaFeO_3$: 5 mmol $La(NO_3)_3$ $6H_2O$ and 5 mmol $Fe(NO_3)_3$ $9H_2O$ is dissolved in 10 ml of deionized water. Then 10 mmol of citric acid was added to the mixture and continuously stirred for 2 hours at room temperature. The pH value was adjusted to 9 using ammonium hydroxide, after which the mixture was stirred for another 1 hour. The resulting solution was transferred to a 50 ml Teflon autoclave and heated at 180 ° C for 12 hours. The solids were separated by centrifugation, washed with deionized water and ethanol, dried at 80 °C for 5 hours, and then calcined in air at 800 °C for 2, 4 and 6 hours.

The morphology of nanocomposite materials was studied using the Mira scanning electron microscope in 3 LMU (Tuscan), which is based on the energy dispersion analysis (EDA) function. The images of Pam, Pam paintings and Said were obtained using a transmission electron microscope DSR-1400 plus (JEOL) with an accelerating voltage of 120 kV. The phase composition of the samples was studied using X-ray diffraction on an XRD analysis diffractometer (Rigaku Ultima IV). X-ray diffraction analysis was measured using a Confotec MR520 scanning Raman microscope (SOL Instruments, Belarus). The absorption spectra of the studied samples were measured on the CM 2203 device (Solar, Belarus). The specific surface area and pore size of the samples were studied using the ASAP 2460 analyzer. To study the photocatalytic properties, a single-channel potentiostat, the Corrtest CS 350 galvanostat with an integrated FRA module, was used. The photocatalytic activity of the samples was assessed by the response of the photocurrent under artificial sunlight with a 10-second intermittent on/off switch.

3. Results and Discussion

Figure 1 shows images of $LaFeO_3$ nanoparticles obtained using a scanning electron microscope (SEM) synthesized by the hydrothermal method with different annealing durations (2 hours, 4 hours and 6 hours). The formation of microspheres was observed after 2 hours (Fig. 1 a, b), however, few aggregated nanoparticles were observed, which proves that the formation of $LaFeO_3$ microspheres occurs due to the process of self-assembly of nanoparticles [27]. After annealing for 4 hours of $LaFeO_3$ (see Figure 1 d, e), a more uniform particle size distribution is observed, they have a rounded shape and the average size was ~104 nm. The SEM image for the extended reaction time of $LaFeO_3$_6h in Fig. 1g, h shows microspheres with a smooth surface and with an average size of ~110 nm. No cavities or defects were found in the microspheres. The particles have acquired a smoother and more spherical shape, which indicates a further improvement in the crystal structure.

Also depicted in Figure 1 are energy dispersion analysis spectra showing the constituent elements La, Fe and O for each sample. The EDA spectrum of $LaFeO_3$_2h (Figure 1c) shows the percentage of elements: La

— 57%, O — 21.5%, Fe — 21.5%. These data confirm the presence of all the necessary elements in the composition of $LaFeO_3$. And for the $LaFeO_3$_4h sample, the EDA (Figure 1f) spectrum shows a decrease in the La content to 54.5%, an increase in the oxygen content to 25.5% and a decrease in the Fe fraction to 19.9%. This may indicate an improvement in the oxygenation of the structure. As a result of annealing, oxygen atoms can better integrate into the crystal lattice of $LaFeO_3$, which leads to an increase in the oxygen content relative to other elements (lanthanum and iron). In the EDA spectra, we see an increase in the percentage of oxygen as the annealing time increases, which indicates a more complete incorporation of oxygen into the structure of the material. The EDA spectrum of $LaFeO_3$_6h (Figure 1i) shows a further decrease in the La content to 53.2%, an increase in the O content to 26%, and the Fe content is 20.8%. These changes show that long waiting contributed to even more complete oxygenation and crystallization of the material. Oxygenation contributes to the formation and stabilization of the correct crystal structure of perovskite, in which each atom takes its place in the lattice. This is important to ensure uniform charge distribution and improve the photocatalytic properties of the material.

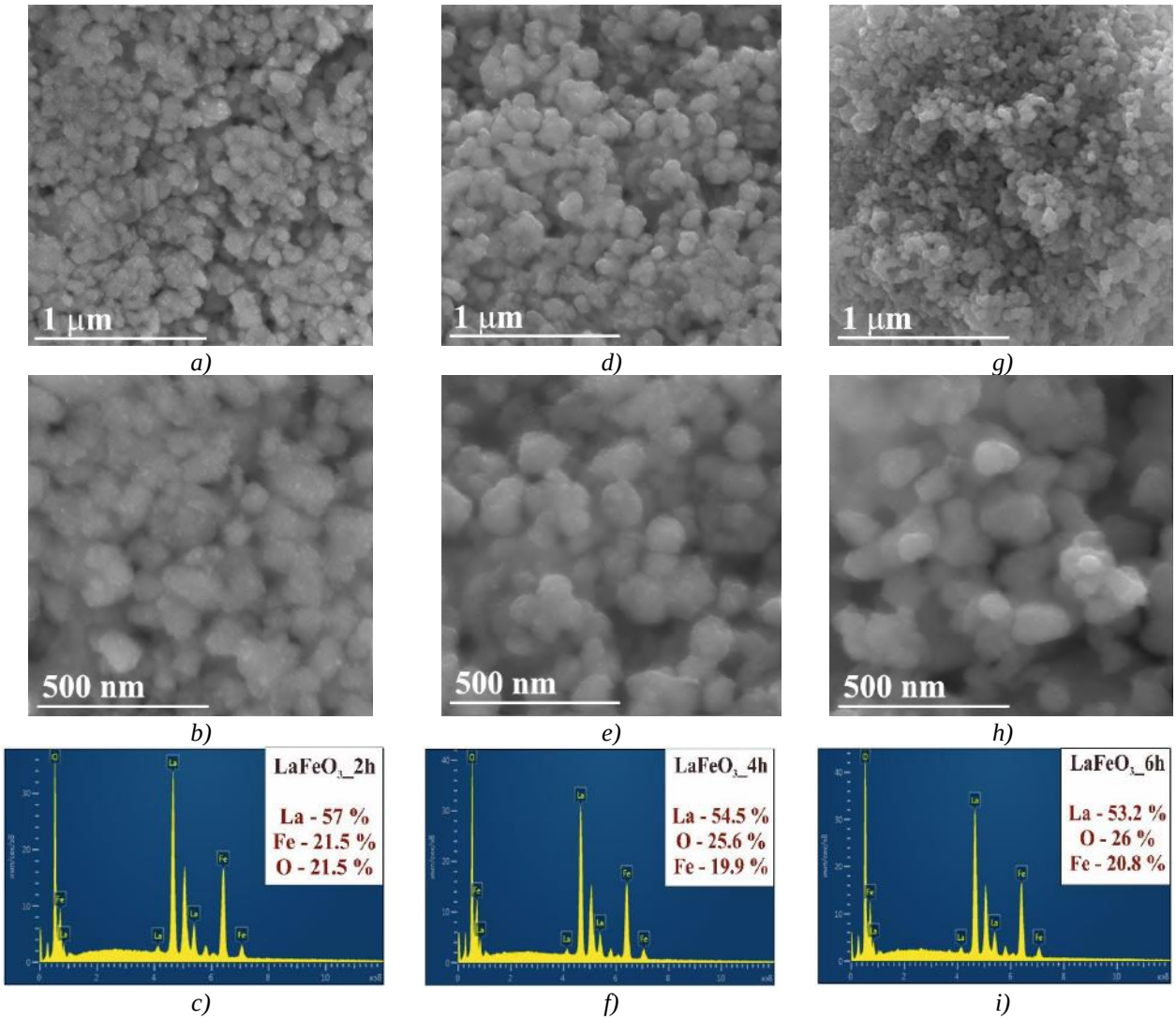

Fig.1. SEM of $LaFeO_3$ perovskite nanoparticles (a,b) $LaFeO_3$_2h, (d,e) $LaFeO_3$_4h, (g,h) $LaFeO_3$_6h and EDA (c) $LaFeO_3$_2h, (f) $LaFeO_3$_4h, (i) $LaFeO_3$_6h

Figure 2 shows a series of images obtained using transmission electron microscopy (TEM) and the elemental composition of $LaFeO_3$ samples after annealing for different time intervals: 2, 4, and 6 hours. After 2 hours of annealing, weakly agglomerated nanoparticles with irregular shapes are visible (Fig. 2 a, b, and c).

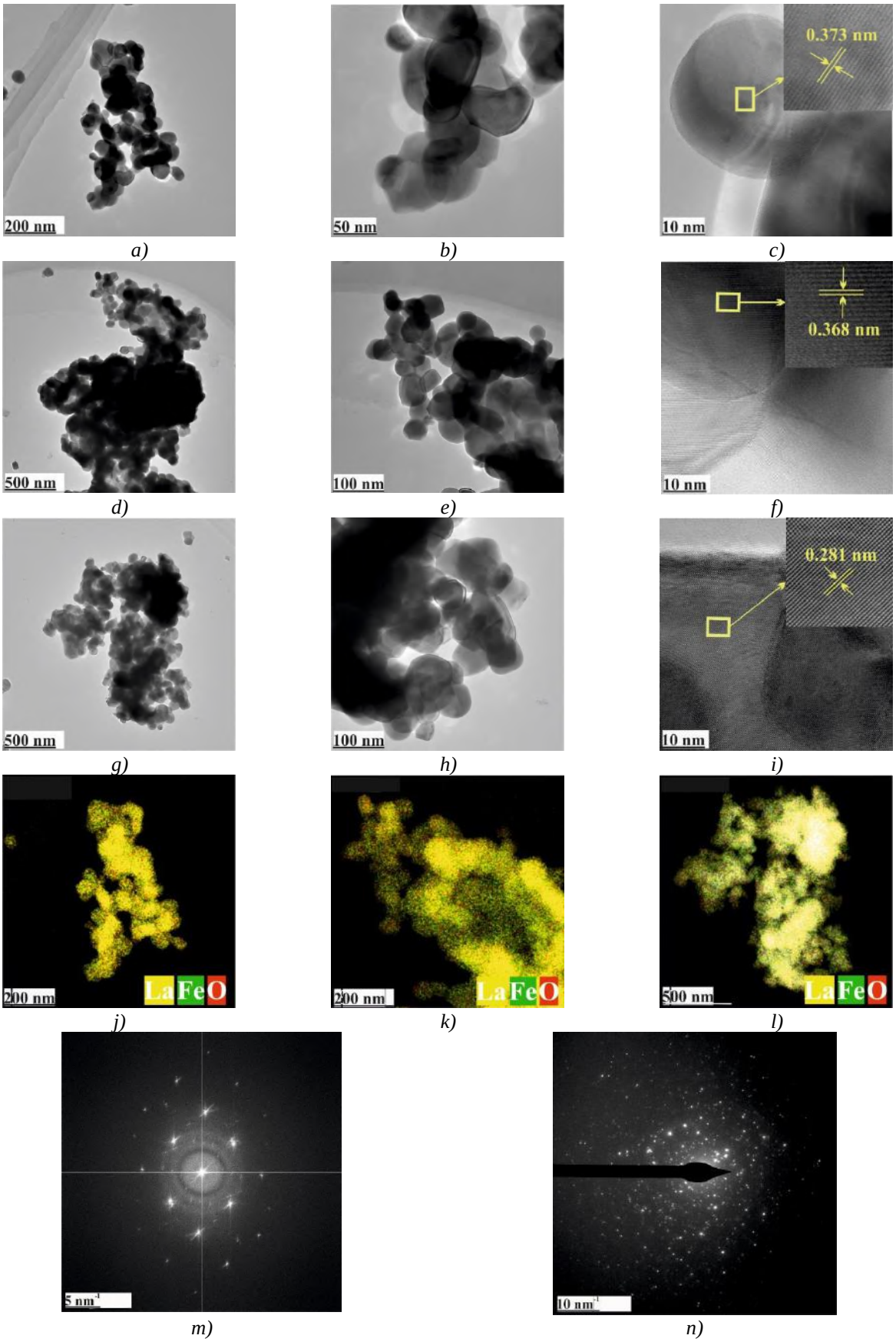

Fig.2. TEM of $LaFeO_3$ perovskite nanoparticles (a,b,c) $LaFeO_3$_2h, (d,e,f) $LaFeO_3$_4h, (g,h,i) $LaFeO_3$_6h and elemental composition (j) $LaFeO_3$_2h, (k) $LaFeO_3$_4h, (l) $LaFeO_3$_6h and electron diffraction patterns (m,n)

The particles appear to be amorphous or poorly crystallized. The particles remain relatively large, but their boundaries are still blurred, indicating insufficient crystallization. $LaFeO_3$ after annealing for 4 hours, a higher degree of particle agglomeration is observed, and the particles themselves have become more ordered compared to samples annealed for 2 hours. The particles become more uniform in size and shape. The boundaries of the particles are better distinguishable, which indicates a higher degree of crystallization. At high magnification (Figure 2f), the crystal structure characteristic of perovskite with pronounced atomic planes is clearly visible. This indicates an improvement in crystallinity compared to samples annealed for 2 hours. $LaFeO_3$ after 6 hours of annealing, the samples continue to exhibit agglomeration, but the particles become more compact and less porous (Figure 2 g, h, and i). The particles achieve greater uniformity in size, with clear boundaries, which indicates an improvement in crystallinity. A clear crystal structure is visible, with well-defined atomic planes, which confirms a high degree of crystallization during longer annealing. Electron diffraction patterns are shown in Figure 2m and 2n. The distribution of the elements La, Fe and O in each of the samples is shown in Figure 2 j, k, l. At all stages of annealing, a relatively uniform distribution of elements is observed, which confirms the successful formation of $LaFeO_3$ phases.

The X-ray diffraction (XRD) graph shown in Figure 3a demonstrates changes in the crystal structure of Lafeo₃ perovskite at different annealing durations of 2, 4 and 6 hours. $LaFeO_3$ perovskite is characterized by specific diffraction angles corresponding to its crystallographic planes, such as (101), (121), (220), (202), (141), (240), (242), (204). After two hours of $LaFeO_3$ annealing, diffraction peaks are observed, indicating the beginning of crystallization of the material. However, these peaks are relatively wide and have low intensity, which indicates the small size of the crystallites and the presence of structural defects. In this state, the crystals have not yet fully formed, and a significant part of the material may remain amorphous or not fully crystallized. Compared to 2-hour annealing, 4-hour annealing results in a noticeable improvement in the crystal structure. The peaks become narrower and more intense, which indicates an increase in the size of the crystallites and a decrease in the number of defects. The structure becomes more ordered, and the material undergoes a stage of active crystallization, with a better distribution of atoms in the lattice. The sample subjected to 6-hour annealing shows an even higher degree of crystallinity. The peaks on the chart become the narrowest and most intense among all three samples. This indicates that the material has reached a high level of crystalline ordering, and the crystallites have grown to significant sizes. Defects in the structure are minimized, and the material has acquired a stable crystal lattice.

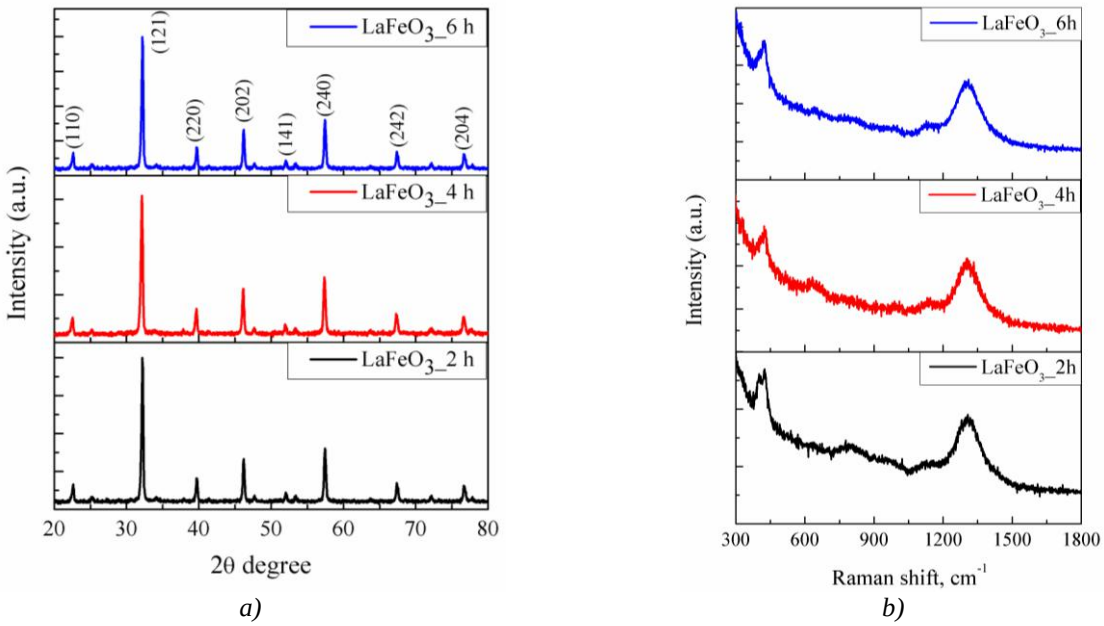

Fig.3. X-ray diffraction (a) and Raman spectroscopy (b) of $LaFeO_3$ perovskite.

With increasing annealing time, there is a noticeable narrowing of peaks on the XRD graph. This indicates an increase in the size of crystallites and an improvement in the ordering of atoms in the lattice. The intensity of the diffraction peaks also increases as the annealing time increases. This is due to the reduction of defects

and improvement of crystallinity. Two—hour annealing is characterized by the weakest peaks, whereas six-hour annealing is characterized by the most intense, which indicates a high degree of order in the structure.

As a result of prolonged annealing, the structure of $LaFeO_3$ becomes more ordered, which is expressed in increased intensity and sharpness of peaks. Samples annealed for 4 and 6 hours demonstrate significantly better crystalline properties compared to two-hour annealing, which indicates that a long heat treatment time contributes to the formation of a stable and homogeneous crystal lattice.

Figure 3b shows three graphs of Raman spectroscopy demonstrating the dependence of intensity (in arbitrary units, a.u.) on the Raman shift (in cm^{-1}) for samples of $LaFeO_3$ (lanthanum ferrite) subjected to heat treatment for 2, 4 and 6 hours. The main characteristic peaks of $LaFeO_3$ are observed in the region of 450 cm^{-1} and 1350 cm^{-1}. The annealing duration directly affects the crystal structure of $LaFeO_3$. With increasing processing time, the material gradually crystallizes, which manifests itself in clearer and more intense peaks in the Raman spectra. The sample processed for 6 hours shows the highest degree of crystallization, with pronounced peaks and high intensity. This indicates a more perfect crystal lattice compared to other samples. $LaFeO_3$ treated for 4 hours shows an intermediate degree of crystallization. Peaks are present, but their intensity and clarity are lower than in the 6-hour sample, indicating a transitional phase. Compared with the rest of the samples, $LaFeO_3$ treated for 2 hours demonstrates the initial stage of crystallization or the presence of a significant amorphous phase. The peaks are wide and weakly pronounced, which indicates that the material has not yet reached a high degree of crystallinity. Longer processing leads to an improvement in the crystal structure, with a transition from an amorphous or polycrystalline phase to a more ordered phase. This can be seen by the improvement in the intensity and clarity of peaks in the spectrum.

Figure 4 shows a graph of the absorption spectrum for samples of $LaFeO_3$ treated for different times: 2, 4 and 6 hours, the absorption peak of lanthanum ferrite is observed at about 300–500 nm. $LaFeO_3$_2h has the lowest absorption compared to the rest of the samples. $LaFeO_3$_4h shows higher absorption compared to the 2-hour sample, and $LaFeO_3$_6h also has a pronounced peak in the range of 300-500 nm. With increasing processing time (from 2 to 6 hours), the absorption of light in the visible range increases. This may indicate an improvement in the crystal structure or an increase in particle size, which leads to more efficient light absorption.

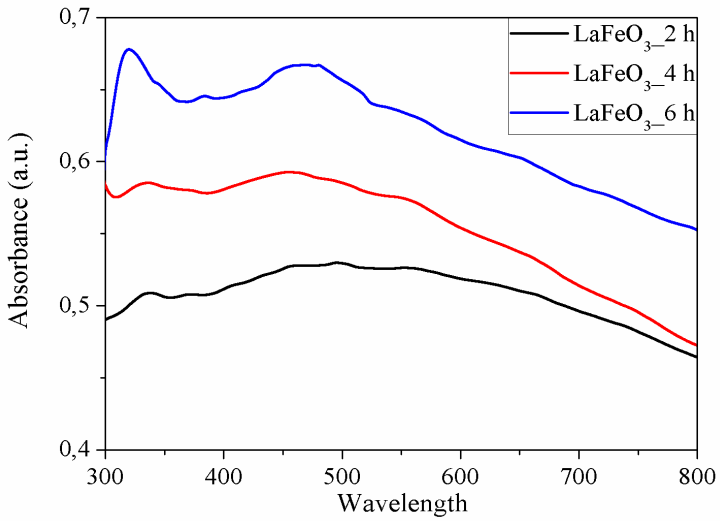

Fig.4. Absorption spectrum of $LaFeO_3$ perovskite.

The figure 5a shows the $LaFeO_3$ adsorption-desorption isotherm obtained under various heat treatment conditions (2, 4 and 6 hours) depending on the relative pressure P/P_0. All three samples show the presence of a hysteresis loop, which means the difference between sorption and desorption processes characteristic of porous materials. Hysteresis indicates the presence of capillary condensation in mesopores. At high pressure areas (P/P_0 >0.8) there is a sharp increase in adsorption for all samples, which is associated with pore filling. The sample with a longer annealing time $LaFeO_3$_6h shows the most pronounced growth, which indicates a more developed porous structure.

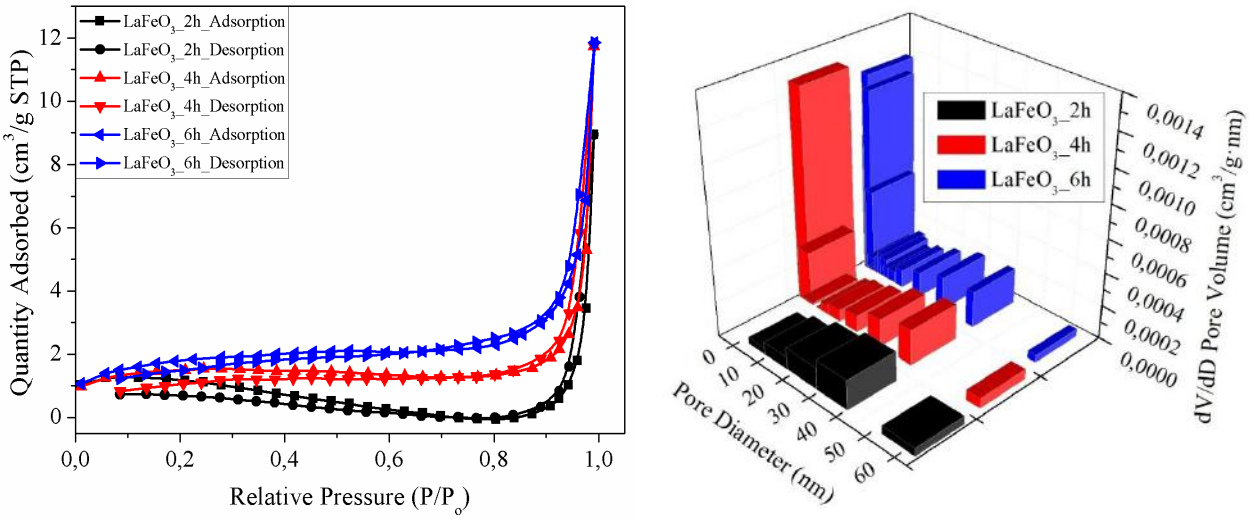

a) *b)*

Fig.5. N_2 adsorption–desorption isotherms (a) and pore size distribution curves (b) of $LaFeO_3$ perovskite.

The distribution of the pore volume depending on their diameter is presented for three samples of $LaFeO_3$ subjected to heat treatment for 2, 4 and 6 hours in Figure 5b. This is a three-dimensional diagram that illustrates how the pore volume changes (along the z axis) at different pore diameters (along the x axis) for each of the samples. In $LaFeO_3$_2h, the pore volume is relatively small compared to other samples, indicating a less developed pore system. The greatest development of the porous structure among all three samples is shown by $LaFeO_3$_6h. In this regard, it was found that an increase in the annealing time leads to an expansion of the pore distribution and an increase in their volume.

Figure 6 shows the change in current density as a function of time for samples of $LaFeO_3$ annealed for 2, 4 and 6 hours. The current density increases with increasing annealing time. The $LaFeO_3$ sample annealed for 6 hours shows the highest current density, which suggests that a longer annealing time leads to better photocatalytic activity.

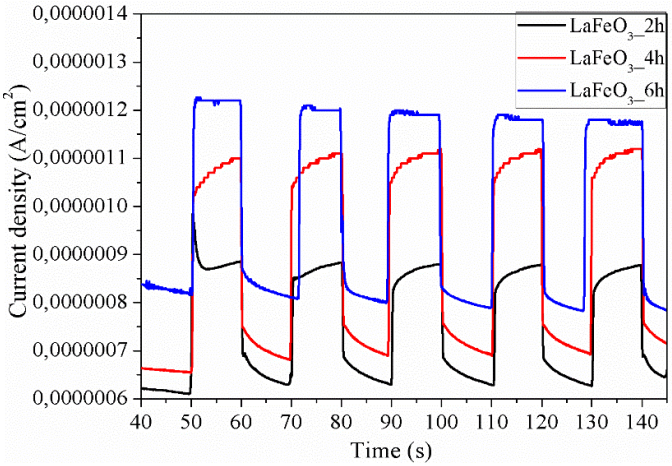

Fig.6. Photocurrent density for $LaFeO_3$ perovskite.

4. Conclusions

In the course of the study, it was found that the duration of annealing has a significant effect on the structural and photocatalytic properties of $LaFeO_3$ perovskite. The $LaFeO_3$ synthesized by the hydrothermal method demonstrates significant changes in morphology and crystal structure with increasing annealing time. Morphological changes in the material also have a significant impact on its catalytic properties. The transition from agglomerated nanoparticles to more uniform and well-formed microspheres with a smooth surface improves light absorption and interaction with reagents on the surface of the material. Experimental results have shown that an increase in the duration of annealing leads to an improvement in the crystallinity of the material, an increase in the size of crystallites and an increase in oxygenation. The improvement of the crystal structure leads to a better distribution of charges inside the material, which prevents their recombination and

thereby increases the photocatalytic activity. The highest rates of photocatalytic activity were achieved during annealing for 6 hours, which is associated with the highest degree of crystallization and improvement of the structure of the material. This study confirms the importance of controlling the heat treatment time to optimize the properties of perovskite materials, which opens up new prospects for their use as effective photocatalysts.

Conflict of interest statement

The authors declare that they have no conflict of interest in relation to this research, whether financial, personal, authorship or otherwise, that could affect the research and its results presented in this paper.

CRediT author statement: Zhanbirbayeva P.A.: Methodology, Writing - Review & Editing**,** Baltabekov A.S.: Writing**-** Original draft preparation, Kayumova A.S.: Visualization, Kuanyshbekova A.B.: Data Curation, Adambay T.N.: Data Curation, Serikov T.M.: Conceptualization, Writing - Review & Editing.
The final manuscript was read and approved by all authors.

Acknowledgments

This study was supported by the Ministry of Education and Science of the Republic of Kazakhstan (project AP23487860).

References

1 Marschall R. (2014) Semiconductor composites: strategies for enhancing charge carrier separation to improve photocatalytic activity. *Advanced Functional Materials,* 24, 2421–2440. DOI: 10.1002/adfm.201303214.

2 Boyjoo Y., Sun H., Liu J., Pareek V.K., Wang S. (2017) A review on photocatalysis for air treatment: From catalyst development to reactor design. *Chemical Engineering Journal,* 310, 537– 559. DOI:10.1016/j.cej.2016.06.090.

3 Humayun M., Qu Y., Raziq F., Yan R., Li Z., Zhang X., Jing L. (2016) Exceptional Visible-Light Activities of TiO_2-Coupled N-Doped Porous Perovskite $LaFeO_3$ for 2,4-Dichlorophenol Decomposition and CO_2 Conversion. *Environmental Science and Technology,* 50 (24), 13600-13610. DOI:10.1021/acs.est.6b04958.

4 Li J., Li H., Zhan G., Zhang L. (2016) Solar Water Splitting and Nitrogen Fixation with Layered Bismuth Oxyhalides. *Accounts of Chemical Research,* 50 (1), 112-121. DOI: 10.1021/acs.accounts.6b00523.

5 Kumar A., Sharma P., Sharma G., Dhiman P., Shekh M., Sillanpää M., Stadler F.J. (2024) Recent progress in advanced strategies to enhance the photocatalytic performance of metal molybdates for H_2 production and CO_2 reduction. *Journal of Alloys and Compounds,* 971. DOI:10.1016/j.jallcom.2023.172665.

6 Paramasivam I., Jha H., Liu N., Schmuki P. (2012) A Review of Photocatalysis using Self-organized TiO_2 Nanotubes and Other Ordered Oxide Nanostructures. *Journal of Photochemistry and Photobiology C,* 13, 1–29. DOI: 10.1002/smll.201200564.

7 Wang X., Liao M., Zhong Y., Zheng J.Y., Tian W., Zhai T., Zhi C., Ma Y., Yao J., Bando Y., Golberg D. (2012) ZnO hollow spheres with double-yolk egg structure for high-performance photocatalysts and photodetectors. *Advanced Materials,* 24 (26), 3421–3425. DOI: 10.1002/adma.201201139.

8 Liu S., Huang G., Yu J., Ng T.W., Yip H.Y., Wong P.K. (2014) Porous Fluorinated SnO_2 Hollow Nanospheres: Transformative Self-assembly and Photocatalytic Inactivation of Bacteria. *ACS Applied Materials & Interfaces,* 6 (5), 2407–2414. DOI: 10.1021/am4047975.

9 Zhang H., Li H., Wang Z., Zheng Z., Wang P., Liu Y., Zhang X., Qin X., Dai Y., Huang B. (2018) Fabrication of $BiVO_4$ photoanode consisted of mesoporous nanoparticles with improved bulk charge separation efficiency. *Applied Catalysis B: Environmental,* 238, 586–591. DOI: 10.1016/j.apcatb.2018.07.050.

10 Li Z., Qu Y., Hu K., Humayun M., Chen S., Jing L. (2017) Improved photoelectrocatalytic activities of BiOCl with high stability for water oxidation and MO degradation by coupling RGO and modifying phosphate groups to prolong carrier lifetime. *Applied Catalysis B: Environmental,* 203, 355–362. DOI: 10.1016/j.apcatb.2016.10.045.

11 Humayun M., Xu L., Zhou L., Zheng Z., Fu Q., Luo W. (2018) Exceptional co-catalyst free photocatalytic activities of B and Fe co-doped $SrTiO_3$ for CO_2 conversion and H_2 evolution. *Nano Research,* 11, 6391–6404. DOI:10.1007/s12274-018-2164-z.

12 Reyes-Gil K.R., Wiggenhorn C., Brunschwig B.S., Lewis N.S. (2013) Comparison between the Quantum Yields of Compact and Porous WO_3 Photoanodes. *The Journal of Physical Chemistry C,* 117 (29), 14947–14957.

13 Zhou X., Xu Q., Lei W., Zhang T., Qi X., Liu G., Deng K., Yu J. (2014) Origin of Tunable Photocatalytic Selectivity of Well-Defined α-Fe_2O_3. *Nanocrystals,* 10 (4), 674–679. DOI: 10.1002/smll.201301870.

14 Sakamoto H., Ohara T., Yasumoto N., Shiraishi Y., Ichikawa S., Tanaka S., Hirai T. (2015). Hot-Electron-Induced Highly Efficient O_2 Activation by Pt Nanoparticles Supported on Ta_2O_5 Driven by Visible Light. *Journal of the American Chemical Society,* 137 (27), 9324–9332. DOI: 10.1021/jacs.5b04062.

15 Humayun M., Zada A., Li Z., Xie M., Zhang X., Qu Y., Raziq F., Jing L. (2016) Enhanced visible-light activities of porous $BiFeO_3$ by coupling with nanocrystalline TiO_2 and mechanism. *Applied Catalysis B: Environmental*, 180, 219–226. DOI: 10.1016/j.apcatb.2015.06.035.

16 Xie M., Feng Y., Fu X., Luan P., Jing L. (2015) Phosphate-bridged TiO_2–$BiVO_4$ nanocomposites with exceptional visible activities for photocatalytic water splitting. *Journal of Alloys and Compounds*, 631, 120–124. DOI:10.1016/j.jallcom.2015.01.091.

17 An X., Li K., Tang J. (2014) Cu_2O/Reduced Graphene Oxide Composites for the Photocatalytic Conversion of CO_2. *ChemSusChem.*, 7 (4), 1086–1093. DOI: 10.1002/cssc.201301194.

18 Xing W., Tu W., Han Z., Hu Y., Meng Q., Chen G. (2018) Template-Induced High-Crystalline g-C_3N_4 Nanosheets for Enhanced Photocatalytic H_2 Evolution. *ACS Energy Letters*, 3 (2), 514–519.

19 Zhang F., Li Y.-H., Li J.-Y., Tang Z.-R., Xu Y.-J. (2019) 3D graphene-based gel photocatalysts for environmental pollutants degradation. *Environmental Pollution*, 253, 365–376. DOI: 10.1016/j.envpol.2019.06.089.

20 Ge J., Zhang Y., Park S.-J. (2019) Recent Advances in Carbonaceous Photocatalysts with Enhanced Photocatalytic Performances: A Mini Review. *Materials*, 12, 1916. DOI: 10.3390/ma12121916.

21 Khan N.A., Humayun M., Usman M., Ghazi Z.A., Naeem A., Khan A.L., Khan A.A., Tahir A.A., Ullah H. (2021) Structural Characteristics and Environmental Applications of Covalent Organic Frameworks. *Energies*, 14 (8), 2267. DOI: 10.3390/en14082267.

22 Yaseen M., Humayun M., Khan A., Usman M., Ullah H., Tahir A.A., Ullah H. (2021) Preparation, Functionalization, Modification, and Applications of Nanostructured Gold: A Critical Review. *Energies*, 14 (5), 1278. DOI:10.3390/en14051278.

23 Ashraf M., Khan I., Usman M., Khan A., Shah S.S., Khan A.Z., Saeed K., Yaseen M., Ehsan M.F., Tahir M.N., Ullah N. (2020) Hematite and Magnetite Nanostructures for Green and Sustainable Energy Harnessing and Environmental Pollution Control: A Review. *Chemical Research in Toxicology*, 33 (5), 1292–1311. DOI: 10.1021/acs.chemrestox.9b00308.

24 Tijare S.N., Joshi M.V., Padole P.S., Mangrulkar P.A., Rayalu S.S., Labhsetwar N.K. (2012) Photocatalytic hydrogen generation through water splitting on nano-crystalline $LaFeO_3$ perovskite. *International Journal of Hydrogen Energy*, 37 (13), 10451–10456. DOI: 10.1016/j.ijhydene.2012.01.120.

25 Jiang Y., Lv Q., Xu F., Sun X., Ding Y. (2021) Synthesis of TiO_2/$LaFeO_3$ composites for the photoelectrochemical hydrogen evolution. *Journal of Materials Science*, 56 (26), 15188–15204. DOI:10.1007/s10853-021-06188-3.

26 Assirey E.A.R. (2019) Perovskite synthesis, properties and their related biochemical and industrial application. *Saudi Pharmaceutical Journal*, 27 (6), 817–829. DOI: 10.1016/j.jsps.2019.05.003.

27 Thirumalairajan S., Girija K., Ganesh I., Mangalaraj D., Viswanathan C., Balamurugan A., Ponpandian N. (2013) Controlled synthesis of perovskite $LaFeO_3$ microsphere composed of nanoparticles via self-assembly process and their associated photocatalytic activity. *Journal of Physical Chemistry C*, 117 (8), 3219–3227. DOI:10.1016/j.cej.2012.08.012.

AUTHORS' INFORMATION

Zhanbirbayeva, Perizat Amangeldievna - Doctoral student, Karaganda University named after academician E.A. Buketov, Karaganda, Kazakhstan. Scopus Author ID: 58091458000, ORCID iD: 0000-0002-9351-956X, perizat.zhanbirbaeva@mail.ru

Baltabekov, Askhat Sekerbaevich - PhD, associate professor, Karaganda University named after academician E.A. Buketov, Karaganda, Kazakhstan. Scopus Author ID: 35193461600, ORCID iD: 0000-0001-8829-2527, abskargu@mail.ru

Kayumova, Ainur Serikovna - Doctoral student, Karaganda University named after academician E.A. Buketov, Karaganda, Kazakhstan. Scopus Author ID: 58547258400, ORCID iD: 0000-0003-4684-0083, aneka.08@mail.ru

Kuanyshbekova, Ayazhan Bakhtiyarovna – Magistr, Karaganda University named after academician E.A. Buketov, Karaganda, Kazakhstan. ORCID iD: 0009-0002-7300-868X, kuanyshbekovaaya@mail.ru

Adambay, Tolganay Nurbolatkyzy – Student, Karaganda University named after academician E.A. Buketov, Karaganda, Kazakhstan. ORCID iD: 0009-0009-8127-8090, adambay.tolganay@mail.ru

Serikov, Timur Maratovich - PhD, associate professor, Karaganda University named after academician E.A. Buketov, Karaganda, Kazakhstan. Scopus Author ID: 56669712000, ORCID iD: 0000-0003-4302-9674, serikov-timur@mail.ru

EURASIAN PHYSICAL TECHNICAL JOURNAL

2024, Volume 21, No.3 (49)

https://doi.org/10.31489/2024No3/108-116

Received: 31/01/2024 Revised: 17/05/2024 Accepted: 20/09/2024 Published online: 30/09/2024

Original Research Article

UDC 53.05; 524.4

FRACTAL DIMENSION OF STAR CLUSTERS

Ussipov N.[1], Akhmetali A.[1]*, Zaidyn M.[1], Akniyazova A.[1], Sakan A.[1], Kalambay M.[1,2,3,4,5], Shukirgaliyev B.[2,3,4,5]

[1] Department of Solid State Physics and Nonlinear Physics, Al-Farabi Kazakh National University, Almaty, Kazakhstan,
[2] Energetic Cosmos Laboratory, Nazarbayev University, Astana, Kazakhstan
[3] Fesenkov Astrophysical Institute, Almaty, Kazakhstan
[4] Heriot-Watt University, Edinburgh, UK
[5] Heriot-Watt branch in Kazakhstan, K.Zhubanov Aktobe Regional University, Aktobe, Kazakhstan
*Corresponding author: akhmetalialmat@gmail.com

Abstract. *Quantitative analysis of the structure of star clusters is crucial for understanding their formation and evolution. In this article, we explore the application of fractal dimension analysis to study the evolution of star clusters, also fractal dimension, a concept from fractal geometry, provides a quantitative measure of the complexity and self-similarity of geometric objects. By considering star clusters as complex networks, we employ the box covering method to calculate their fractal dimension. Our methodology combines the well-established Minimum Spanning Tree (MST) and Box-Covering (BC) methods and using these methods, the fractal structure of the clusters was determined. It was revealed that star clusters disintegrate at a fractal dimension of 1.3 and obey a power law. It should be noted that the obtained result was compared with the results of the McLuster.*

Keywords: Star cluster, Fractal dimension, Box-covering, Star formation effiency.

1. Introduction

A star cluster is a gravitationally bound complex stellar structure with a radius ranging from 0.5 to several parsecs and a mass ranging from 10^3 to 10^7 solar masses [1].

Clusters of stars originate within massive molecular clouds triggered by the gravitational collapse of dense gas concentrations [2-3]. The influential impact of massive stars comes from various forms of stellar feedback, such as ionizing radiation, stellar winds, and radiation pressure, which can swiftly dismantle an entire molecular cloud [4-5]. The ejection of gas occurs at an approximate velocity of 10 km/s on average [6, 7]. Consequently, for star-forming areas with dimensions smaller than 10 pc, gas could be blown within a span of less than 1 million years. The star formation process is assessed through a quantitative measure known as the star formation efficiency (SFE), revealing the connection between neutral gas and the law of star formation [8, 9]. Star Formation Efficiency (SFE) is measured when a gas turns into stars. In nearby areas where star formation takes place, the SFE is estimated to be less than 30% [2, 10-11]. On a larger galactic scale, the average SFE is only a few percent [12]. When gas is ejected quickly and star formation efficiency is low, it can destroy star clusters [13-14]. If a cluster experiences gas expulsion, it will lose both mass and density [14-17]. Star clusters are direct products of the star formation process within galaxies and exhibit a significantly brighter nature compared to individual stars. Consequently, star clusters represent essential objects of study in star formation research [18].

Most star clusters have a hierarchical structure [19-21]. Quantitative and objective statistical measurements are used to comprehend the evolution of complex hierarchical structures of star clusters [22]. Additionally, it is important to evaluate the observed clusters using numerical modeling methods. This paper is aimed at studying the structure of star clusters through the analysis of their fractal dimension, considering star clusters as a complex network [23]. The primary issue in analyzing the fractality of complex networks lies in selecting a method for determining the dimension. When assessing the fractal properties of complex networks, the box-covering method is commonly employed [24]. The goal of this method is to identify the minimum number of boxes required to cover the entire network. Numerous algorithms have been proposed to address this challenge [25]. Minimum Spanning Tree (MST) was initially introduced in astronomy by Barrow et al. (1985) and finds applications in cosmology for the classification of large-scale structures, as well as for dynamic mass segregation in star clusters [26-31].

In this study, we introduce a novel approach by integrating Box-Covering (BC) and MST methods to analyze the fractal properties of star clusters across different stages of their evolution. While both methods have been applied separately in the study of fractal systems, their combination in the context of stellar clusters is innovative. The BC method is adapted to account for stellar mass loss during evolutionary stages, correlating this mass change with shifts in the cluster's fractal structure. Additionally, MST, which has traditionally been used to describe static topological structures, is applied dynamically to track the fragmentation and collapse of star-forming regions over time. This dual application of BC and MST provides new insights into the evolving fractal properties of star clusters, offering a deeper understanding of their structural development throughout their lifecycle.

In Section 2, we present a proposed methodology that explains the process of analyzing the fractal dimensions of star clusters with varying SFE, considering them as complex networks. In Section 3, we present and discuss our results, while the main conclusions of our work are outlined in Section 4.

2. Methodology

In this study, we calculated the fractal dimensions of star clusters at various stages of evolution. We ran simulations of SCs with different SFE, including 0.15, 0.17 and 0.20. The initial mass of the cluster was $M = 6000$ solar masses and it was simulated on a solar orbit, 8178 pc away from the Galactic center. The density profile of the initial cluster was modeled on the Plummer model [32]. After the start of the simulation, the effect of the gas explosion and the gravity of the host galaxy greatly change the shape of the initial cluster (see APPENDIX Fig. A1). And the lifetime of clusters can vary based on the SFE, so SCs with higher SFEs live longer [16-17] (also see the Table 1 in APPENDIX 2). We have created a star cluster model with a coefficient of (lambda) $\lambda = 0.05$ (1).

$$\lambda = \frac{r_h}{r_j} \tag{1}$$

The Jacobi radius, r_j refers to the distance from the center of a cluster at which its gravitational potential becomes stronger than that of the host galaxy. And, the half-mass radius, r_h is the radius within which half of the cluster's total mass is located [12]. Since many stars fly apart into the galaxy's space, the cluster loses its stars, reducing the r_j and the r_h (red circle in APPENDIX 1 Fig. A1).

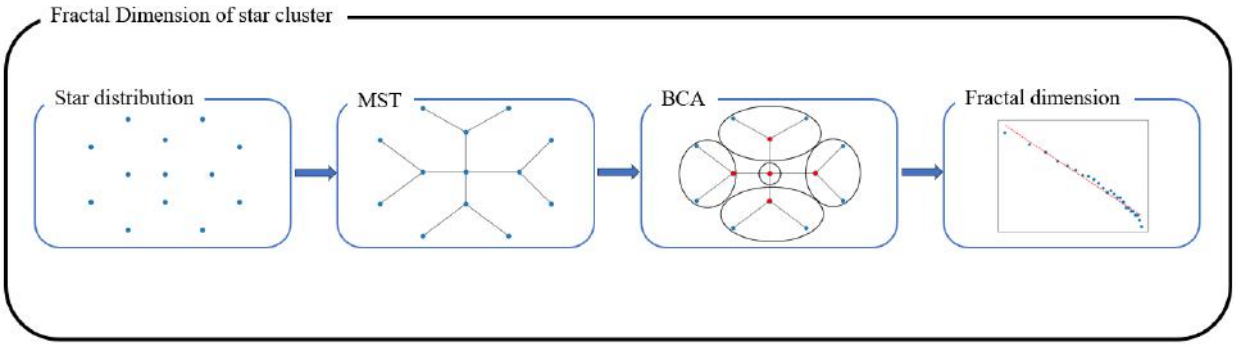

Fig.1. The flowchart demonstrates the algorithm of this study

.

To quantify the fractal dimension of the simulated star clusters, we used the MST and BC methods.

The Minimum Spanning Tree (MST) is a unique network with minimal weight that connects any distribution of points in space. In this context, the weight of the tree is understood as the sum of the weights of the edges included in the network. However, in our case, instead of considering the weights of the edges, we evaluate the distances of stars relative to each other. The MST algorithm should build a network by connecting stars within a cluster with a minimum total length. The resulting MST represents the basis of the cluster's connectivity, revealing the underlying hierarchical organization and relationships between the stars The minimum spanning tree can be used to determine the network topology [32-33]. The next step was to determine the fractal dimension of the network using the well-known box coverage method [26]. The box coverage method is widely used to calculate the fractal dimension of complex networks, but its effectiveness relies on determining the minimum number of boxes needed to cover the entire network. If the distribution of the number of boxes, $N_b(l_b)$, corresponds to a power law, it indicates that D represents the fractal dimension of a complex network. The concept of fractal dimension, as a measure of occupancy and complexity within object space, holds great importance for the study of the reliability of complex networks [33-34].

$$N_b(l_b) \sim l_b^{-D} \tag{2}$$

where l_b is the radius of the boxes, N_b is the number of boxes.

The discovery of fractal features and self-similarity in star clusters not only opens up a new perspective for improving our understanding of the internal structure and characteristics of these clusters but also provides a new basis for explaining the mechanisms underlying their formation, evolutionary processes, and the coexistence of various characteristics within them.

3. Results and discussion

According to the calculations, it can be asserted that the star cluster has a certain fractal dimension. As an example, Figure 2 illustrates the results of calculating the fractal dimension for SFE=0.15 at the age of 10 million years. It is evident that the number of boxes decreases rapidly, depending on the radii, and follows a power law. However, there is a noticeable deviation from the power-law behavior when $\log(l_b) > 3.5$. This flattening suggests that at larger box sizes, the fractal nature of the star cluster begins to break down. In this case, the deviation is likely due to the fact that, at larger scales, the global structure of the cluster becomes more coherent and less fragmented, resulting in fewer boxes required to cover the structure.

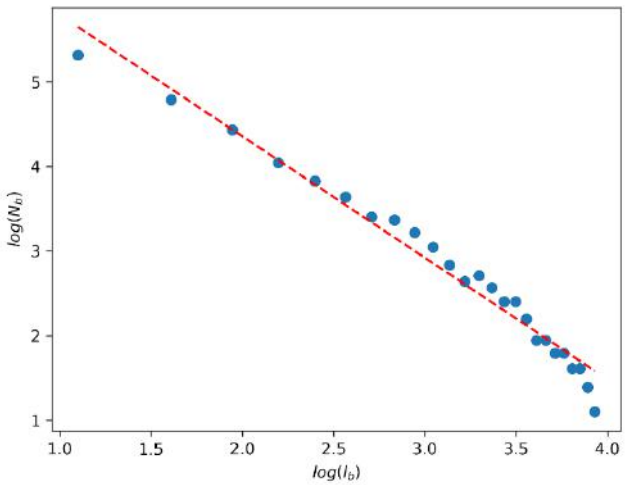

Fig.2. Fractal dimension of the cluster with SFE = 0.15 at 10 Myr age.

The main results of our study are illustrated in Figure 3. We compared the fractal dimensions for various SFE values in the time range of 50-950 million years for a Jacobi radius of 1. At SFE=0.15, the fractal dimension values exhibit a sharp decrease over time, while at SFE=0.17 and SFE=0.20, the rates of change are the same. It is evident that the fractal dimension of the star cluster depends on its evolution and undergoes changes with alterations in its structure.

Figure 3 shows the dynamics of changes in fractal dimension during the evolution of star clusters. In the initial stages of young cluster evolution, a consistent increase in fractal dimension is observed, reaching its peak value after approximately 200 million years. This phenomenon can be explained by a more complex structure and active cluster formation processes that enhance fractal characteristics. The growth of fractal dimension observed at later times in Figure 3 reflects the re-structuring of the cluster as new hierarchical patterns form due to dynamical interactions and external perturbations. As the cluster evolves, mass loss from stellar evolution (particularly from massive stars) and gravitational interactions between stars lead to the emergence of new substructures, increasing the fractal dimension. The increase in fractal dimension at 800 million years, for instance, is associated with the formation of subclusters or the merging of previously distinct structures.

However, after reaching the specified time interval, it becomes evident that the clusters start to lose their fractal dimension. This phenomenon is attributed to the loss of complexity or organization within the cluster's structure. It can be triggered by dynamic interactions between stars, leading to a gradual reduction in the number of stars in the cluster and, ultimately, a decrease in its fractal dimension. In the final stage of their life, clusters lose their structure and become more dispersed [9]. From Figure 3, it can be noted that when the fractal dimension of a cluster falls below a certain 'threshold' value of 1.3, the cluster is prone to decay.

Thus, analyzing the dynamics of changes in fractal dimension during the evolution of star clusters allows us to track the processes that shape and dismantle cluster structures.

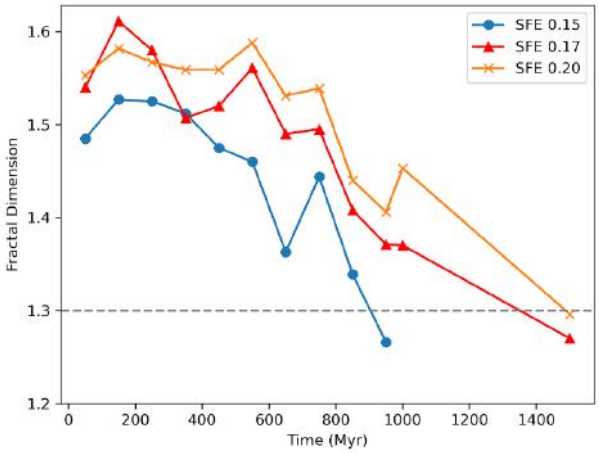

Fig.3. Comparison of fractal dimensions of different SFEs according to the evolution of star cluster formation.

To validate our method, we measured the fractal dimensions of model star clusters generated using the publicly available code MCLUSTER [35]. We created star clusters with the following fractal dimensions: 1.6, 2, 2.6, and 3. The results are shown in Figure 4 and Table 1. Due to errors and the inherent randomness of the MCLUSTER model, the fractal dimensions exhibit variations, but the structure in the generated star clusters follows to the power law. Therefore, we can assert that our method effectively captures the fractal structure in the distribution of star clusters.

Table 1.

No.	Fractal dimension with our methods	Fractal dimension with Mcluster
1	1.35	1.6
2	1.44	2
3	1.59	2.6
4	1.70	3

.

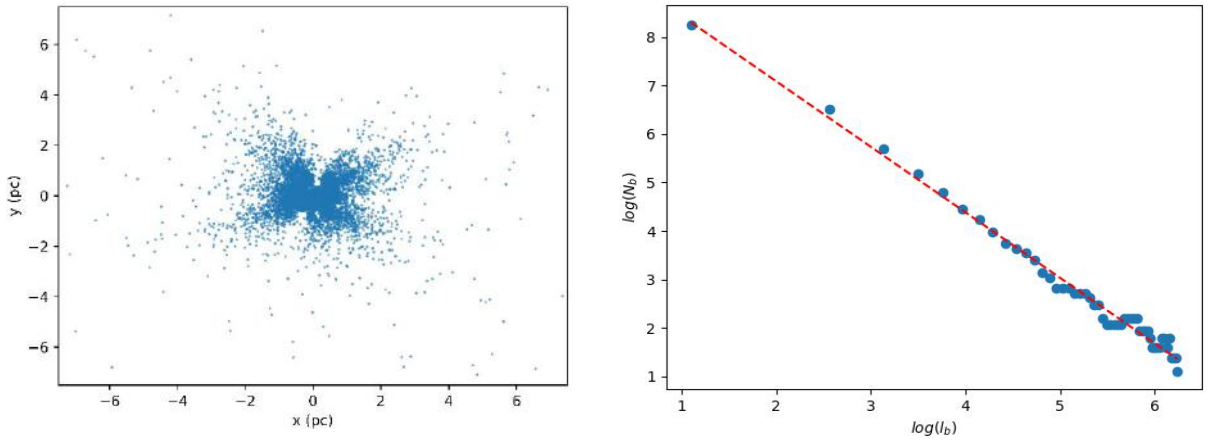

a) *b)*

Fig.4. a) Distribution of a model star cluster constructed using MCLUSTER for fractal dimension $D = 1.6$; b) Power law for fractal dimension $D = 1.6$.

4. Conclusion

In this paper, we used algorithms that had not previously been used in the field of astronomy, specifically in the study of star clusters: MST and BC. To illustrate the proposed method, we modeled star clusters with varying initial SFE from birth to decay. We examined the moments of the cluster's life at intervals of 50 million years and calculated their fractal dimensions within a 1 Jacobi radius. The following conclusions were drawn:

Firstly, a star cluster has a specific fractal dimension and exhibits both fractal and hierarchical structures.

Secondly, the fractal dimension of the star cluster depends on the cluster's structure and varies significantly throughout its evolution. The importance of fractal dimension increases primarily due to rapid dynamic relaxation, which leads to a complexity of the structure. Subsequently, it begins to decrease because of a reduction in the number of stars within the cluster, leading to the structure of the star cluster becoming more homogeneous and less complex.

Thirdly, when the fractal dimension of a star cluster falls below a certain "threshold" (D~1.3), it tends to decay. To compare our results, we used the distribution of star clusters generated by the publicly available code MCLUSTER. Our method was then employed to determine the fractal structure of these clusters.

Our results indicate that our method can serve as an effective tool for studying the structure and topology of complex clusters.

Conflict of interest statement

The authors declare that they have no conflict of interest in relation to this research, whether financial, personal, authorship or otherwise, that could affect the research and its results presented in this paper.

CRediT author statement

Ussipov N., Akhmetali A.: Methodology, Data curation, Conceptualization; Akniyazova A., Sakan.A.: Writing –original draft, Visualization; Ussipov N., Zaidyn M.: Writing –review & editing, Validation, Supervision; Shukirgaliyev B., Kalambay M.: Formal analysis; Investigation.

The final manuscript was read and approved by all authors.

Funding

This research has been funded by the Science Committee of the Ministry of Science and Higher Education of the Republic of Kazakhstan (Grant AP19674715).

Acknowledgments

We would like to express our sincerest gratitude to the Department of Solid State Physics and Nonlinear Physics of the Al-Farabi Kazakh National University for supporting this work by providing computing resources (Department of Physics and Technology).

References

1 Portegies Zwart S. F., McMillan S. L., Gieles M. (2010). Young massive star clusters. *Annual review of astronomy and astrophysics*, 48(1), 431-493. DOI:10.1146/annurev-astro-081309-130834.

2 Lada C.J., Lada E.A. (2003) Embedded clusters in molecular clouds. *Annual Review of Astronomy and Astrophysics*, 41(1), 57-115. DOI: 10.1146/annurev.astro.41.011802.094844.

3 Krumholz M.R., McKee C.F., Bland-Hawthorn J. (2019) Star clusters across cosmic time. *Annual Review of Astronomy and Astrophysics*, 57(1), 227-303. DOI: 10.1146/annurev-astro-091918-104430.

4 Rahner D., Pellegrini E.W., Glover S.C., Klessen R.S. (2019) WARPFIELD 2.0: feedback-regulated minimum star formation efficiencies of giant molecular clouds. *Monthly Notices of the Royal Astronomical Society*, 483(2), 2547-2560. DOI: 10.1093/mnras/sty3295.

5 McLeod A.F., Ali A.A., Chevance M., Della Bruna L., Schruba A., Stevance H.F., Zeidler P. (2021) The impact of pre-supernova feedback and its dependence on environment. *Monthly Notices of the Royal Astronomical Society*, 508(4), 5425-5448. DOI: 10.1093/mnras/stab2726.

6 Banerjee S., Kroupa P. (2013) Did the infant R136 and NGC 3603 clusters undergo residual gas expulsion? *The Astrophysical Journal*, 764(1), 29. DOI: 10.1088/0004-637X/764/1/29.

7 Grasha K., Calzetti D., Adamo A., Kennicutt R.C., Elmegreen B.G., Messa M., Meidt S.E. (2019) The spatial relation between young star clusters and molecular clouds in M51 with LEGUS. *Monthly Notices of the Royal Astronomical Society*, 483(4), 4707-4723. DOI: 10.1093/mnras/sty3424.

8 Kennicutt Jr.R.C. (1989) The star formation law in galactic disks. *Astrophysical Journal*, Part 1, 344, 685-703. DOI: 10.1086/167834.

9 Krause M.G., Offner S.S., Charbonnel C., Gieles M., Klessen R.S., Vázquez-Semadeni E., Zinnecker H. (2020) The physics of star cluster formation and evolution. *Space Science Reviews*, 216, 1 - 46. DOI: 10.1007/s11214-020-00689-4.

10 Murray N. (2011) Star formation efficiencies and lifetimes of giant molecular clouds in the Milky Way. *The Astrophysical Journal*, 729, 2, 133. doi: 10.1088/0004-637X/729/2/133.

11 Higuchi A.E., Kurono Y., Saito M., Kawabe R. (2009) A mapping survey of dense clumps associated with embedded clusters: evolutionary stages of cluster-forming clumps. *The Astrophysical Journal*, *705*(1), 468. doi: 10.1088/0004-637X/705/1/468.

12 Kruijssen J.D., Schruba A., Chevance M., Longmore S.N., Hygate A.P., Haydon D.T., van Dishoeck E.F. (2019) Fast and inefficient star formation due to short-lived molecular clouds and rapid feedback. *Nature*, *569*(7757), 519-522. DOI: 10.1038/s41586-019-1194-3.

13 Lada C.J., Margulis M., Dearborn D. (1984) The formation and early dynamical evolution of bound stellar systems. *Astrophysical Journal*, 285, 141-152. DOI:10.1086/162485.

14 Baumgardt H., Kroupa P. (2007) A comprehensive set of simulations studying the influence of gas expulsion on star cluster evolution. *Monthly Notices of the Royal Astronomical Society*, 380(4), 1589-1598. DOI: 10.1111/j.1365-2966.2007.12209.x.

15 Geyer M.P., Burkert A. (2001) The effect of gas loss on the formation of bound stellar clusters. *Monthly Notices of the Royal Astronomical Society*, 323, 4, 988 – 994. DOI: 10.1046/j.1365-8711.2001.04257.x.

16 Shukirgaliyev B., Parmentier G., Berczik P., Just A. (2017) Impact of a star formation efficiency profile on the evolution of open clusters. *Astronomy & Astrophysics*, 605, A119. DOI: 10.1051/0004-6361/201730607.

17 Shukirgaliyev B., Otebay A., Sobolenko M., Ishchenko M., Borodina O., Panamarev T., Just A. (2021) Bound mass of Dehnen models with a centrally peaked star formation efficiency. *Astronomy & Astrophysics*, 654, A53, DOI: 10.1051/0004-6361/202141299.

18 Lada C.J., Lada E.A. (2003) Embedded clusters in molecular clouds. *Annual Review of Astronomy and Astrophysics*, 41(1), 57-115. DOI:10.1146/annurev.astro.41.011802.094844.

19 Bastian N., Covey K.R., Meyer M.R. (2010) A universal stellar initial mass function? A critical look at variations. *Annual Review of Astronomy and Astrophysics*, 48(1), 339-389. DOI:10.1146/annurev-astro-082708-101642.

20 Grasha K., Calzetti D., Adamo A., Kim H., Elmegreen B.G., Gouliermis D.A., Ubeda L. (2017) The hierarchical distribution of the young stellar clusters in six local star-forming galaxies. *The Astrophysical Journal*, 840(2), 113. DOI: 10.3847/1538-4357/aa6f15.

21 Lahén N., Naab T., Johansson P. H., Elmegreen B., Hu C. Y., Walch S., Moster B.P. (2020) The GRIFFIN Project—Formation of Star Clusters with Individual Massive Stars in a Simulated Dwarf Galaxy Starburst. *The Astrophysical Journal*, 891(1), 2. DOI:10.3847/1538-4357/ab7190.

22 Komjáthy J., Molontay R., Simon K. (2019) Transfinite fractal dimension of trees and hierarchical scale-free graphs. *Journal of Complex Networks*, 7 (5), 764-791. DOI: 10.1093/comnet/cnz005.

23 Mandelbrot B.B. (1983) The fractal geometry of nature. 286. Revised and enlarged edition. New York. DOI:10.1119/1.13295.

24 Kim J.S., Goh K.I., Kahng B., Kim D. (2007) A box-covering algorithm for fractal scaling in scale-free networks. *Chaos: An Interdisciplinary Journal of Nonlinear Science*, 17(2). DOI: 10.1063/1.2737827.

.

25 Wen T., Cheong K.H. (2021) The fractal dimension of complex networks: A review. *Information Fusion*, 73, 87-102. DOI: 10.1016/j.inffus.2021.02.001.

26 Barrow J.D., Bhavsar S.P., Sonoda D.H. (1985) Minimal spanning trees, filaments and galaxy clustering. *Monthly Notices of the Royal Astronomical Society*, 216(1), 17-35. DOI:10.1093/mnras/216.1.17.

27 Bonanno G., Caldarelli G., Lillo F., Mantegna R.N. (2003) Topology of correlation-based minimal spanning trees in real and model markets. *Physical Review E*, 68(4), 046130. DOI: 10.1103/ PhysRevE.68.046130.

28 Bhavsar S.P., Ling E.N. (1988) II. Large-Scale Distribution of Galaxies: Filamentary Structure and Visual Bias. *Publications of the Astronomical Society of the Pacific*, 100(633), 1314. DOI:10.1086/132325.

29 Libeskind N.I., Van De Weygaert R., Cautun M., Falck B., Tempel E., Abel T., Yepes G. (2018) Tracing the cosmic web. *Monthly Notices of the Royal Astronomical Society*, 473(1), 1195-1217. DOI:10.48550/arXiv.1705.03021 .

30 Allison R.J., Goodwin S.P., Parker R.J., De Grijs R., Zwart S.F.P., Kouwenhoven M.B.N. (2009) Dynamical mass segregation on a very short timescale. *The Astrophysical Journal*, *700*(2), L99. DOI:10.1088/0004-637X/700/2/L99.

31 Naidoo K., Whiteway L., Massara E., Gualdi D., Lahav O., Viel M., Font-Ribera A. (2020). Beyond two-point statistics: using the minimum spanning tree as a tool for cosmology. *Monthly Notices of the Royal Astronomical Society*, 491(2), 1709-1726. DOI:10.1093/mnras/stz3075.

32 Plummer H.C. (1911) On the problem of distribution in globular star clusters. *Monthly Notices of the Royal Astronomical Society*, 71, 460-470. DOI: 10.1093/mnras/71.5.460.

33 Zhanabaev Z., Ussipov N., Khokhlov S. (2021) Scale-invariant and wave nature of the Hubble parameter. *Eurasian Physical Technical Journal*, 18(2 (36)), 81-89. DOI:10.13140/RG.2.2.31792.61449/1.

34 Küpper A.H., Maschberger T., Kroupa P., Baumgardt H. (2011) Mass segregation and fractal substructure in young massive clusters–I. The McLuster code and method calibration. *Monthly Notices of the Royal Astronomical Society*, 417(3), 2300-2317. DOI: 10.1111/j.1365-2966.2011.19412.x.

AUTHORS' INFORMATION

Ussipov, Nurzhan – Senior Lecturer, Department of Physics and Technology, Al-Farabi Kazakh National University, Almaty, Kazakhstan; Scopus Author ID: 57226319348; ORCID: 0000-0002-2512-3280; ussipov.nurzhan @kaznu.kz,

Akhmetali, Almat – Bachelor (Sci.), Department of Physics and Technology, Al-Farabi Kazakh National University, Almaty, Kazakhstan; Scopus Author ID: 58759186800; ORCID: 0009-0005-7254-524X; akhmetalialmat @gmail.com

Zaidyn, Marat – Student, Department of Physics and Technology, Al-Farabi Kazakh National University, Almaty, Kazakhstan, Scopus Author ID: 59194267200; ORCID: 0009-0006-8505-7277; zaidyn_marat@live.kaznu.kz

Akniyazova, Aigerim – Master (Sci.), Lecturer, Department of Physics and Technology, Al-Farabi Kazakh National University, Almaty, Kazakhstan; ORCID: 0000-0002-9185-3185; aigerimakniyazova@gmail.com

Sakan, Aknur – Bachelor of natural sciences, Department of Physics and Technology, Al-Farabi Kazakh National University, Almaty, Kazakhstan; ORCID: 0009-0001-8784-4470 ; aknursakan47@gmail.com

Mukhagali, Kalambay – PhD, Senior Lecturer, Heriot-Watt branch in Kazakhstan, K.Zhubanov Aktobe Regional University, Aktobe, Kazakhstan; Scopus Author ID: 57224666055; ORCID:0000-0002-0570-7270; mukhagaly@gmail.com

Bekdaulet, Shukirgaliyev – PhD, Associate Professor, Heriot-Watt branch in Kazakhstan, K.Zhubanov Aktobe Regional University, Aktobe, Kazakhstan; Scopus Author ID: 57163629900; ORCID: 0000-0002-4601-7065; b.shukirgaliyev@hw.ac.uk

APPENDIX 1

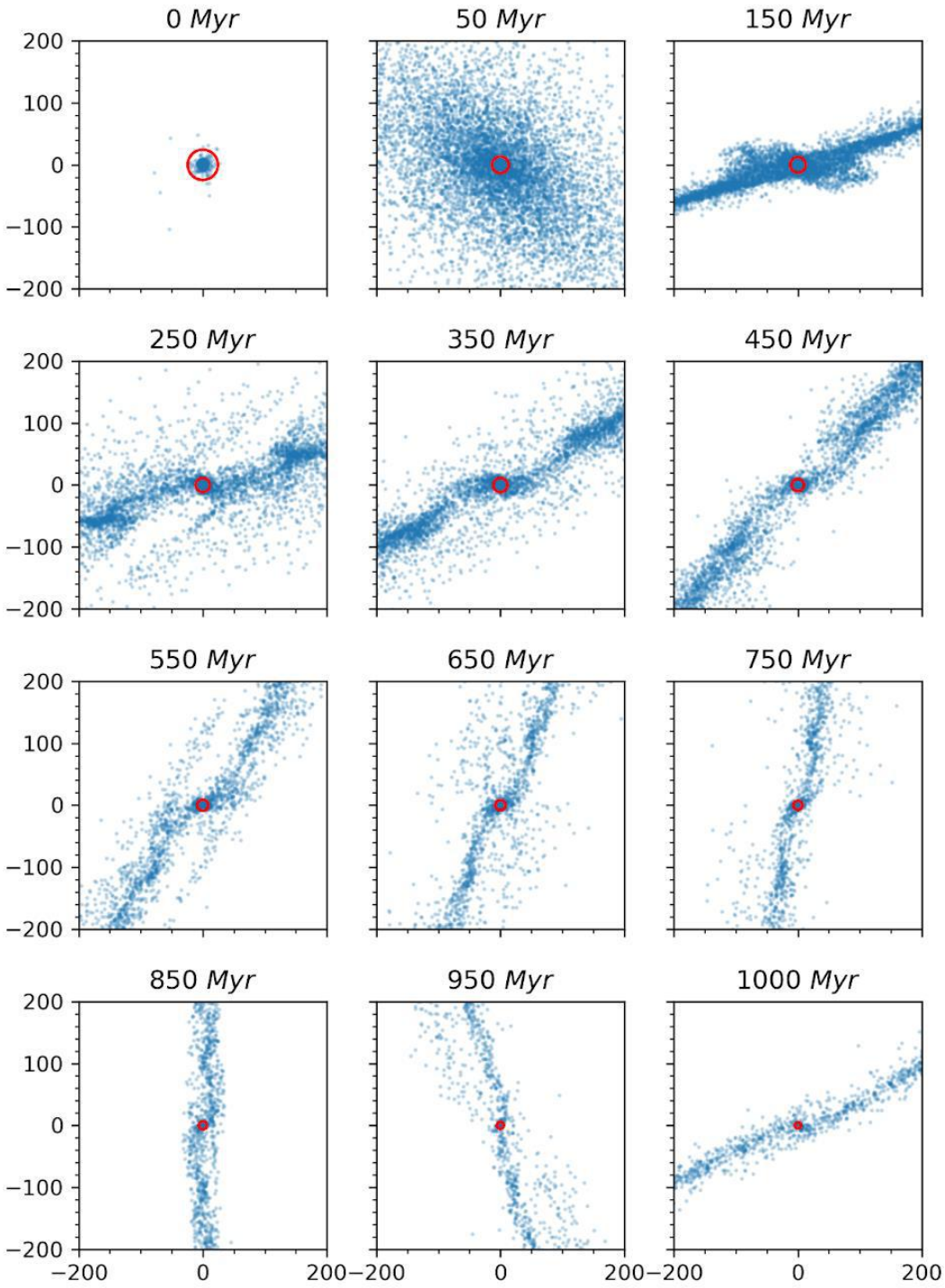

Fig.A1. Evolution of the cluster with SFE=0.15 (red circle is a Jacobi radius).

Figure A1 shows the evolution of the cluster with an SFE=15% and a time interval of 50 Myr. The red circle marks the Jacobi radius which decreases as the cluster dissolves.

.

APPENDIX 2

Table A1. Statistical analysis of clusters: SFE=0.15, 0.17, 0.20. In Table A1, the Jacobi radius at various stages of SC's lifetime, along with mass and number of stars within that radius, are shown.

Age (Myr)	SFE=0.15			SFE=0.17			SFE=0.20		
	R_J (pc)	N	M_J ($M_\odot$)	R_J (pc)	N	M_J ($M_\odot$)	R_J (pc)	N	M_J ($M_\odot$)
0	24.40	10454	6000	24.44	10433	6000	24.51	10432	6000
50	13.50	2138	998.1	15.19	3068	1424.8	16.33	3902	1766.3
150	12.50	1803	793.7	14.44	2768	1224.0	15.53	3502	1521.6
250	11.35	1307	591.9	13.51	2287	1007.4	14.70	3018	1291.3
350	10.55	1002	476.4	13.03	1958	898.8	14.21	2675	1161.5
450	9.80	750	383.2	12.53	1661	799.9	13.65	2304	1034.2
550	8.88	532	283.9	11.94	1376	691.6	13.19	2009	931.5
650	8.14	356	219.4	10.40	1140	601.4	12.71	1712	833.1
750	7.21	211	152.5	10.74	899	503.07	12.08	1390	718.7
850	6.52	137	112.3	10.00	673	406.8	11.58	1150	632.2
950	5.47	75	66.6	9.11	454	307.5	11.01	931	542.9
1000	4.90	51	47.8	8.72	377	269.7	10.83	840	514.6

EURASIAN PHYSICAL TECHNICAL JOURNAL

2024, Volume 21, No.3 (49)

Special Issue

https://doi.org/10.31489/2024No3/117-124

Received: 22/05/2024 Revised: 22/06/2024 Accepted: 23/09/2024 Published online:30/09/2024

Original Research Article

UDC 53.093

INFLUENCE OF MOISTURE CONDITION AND SILICA SAND ON FRICTION COEFFICIENT OF WIND TURBINE BRAKE SYSTEM

Mohammed O.A.[1], Mohammed S.A. [1], Ghazaly N.M.*[2,3]

[1] Department of Mechanical Engineering, College of Engineering, University of Mosul, Mosul, Iraq.

[2] Technical College, Imam Ja'afar Al-Sadiq University, Baghdad, Iraq.

[3] Department of Mechanical Engineering, South Valley University, Qena, Egypt.

*Corresponding author: nouby.ghazaly@eng.svu.edu.eg

Abstract. *Major drive train parts for the horizontal wind turbines including the gearbox, generator, and brake system have very high repair and replacement costs and take a long time to complete. This paper investigates the impact of environmental air pollution on drivetrain tribology behaviors. Experimental research of the wind turbine's drive train system is simulated and investigated. The mechanical brake system of wind turbines is the subject of one case study chosen for this research paper. This research paper is examined how impurities affect the friction coefficient of the brake on wind turbines. According to the findings, the friction coefficient rises with each increase in wind turbine shaft speed. Also, it has been discovered that the size of the contaminants' particles significantly affects the friction coefficient. Furthermore, the findings may offer helpful insights of the drive train system that as humidity increased from 30 mm^3 to 90 mm^3, the coefficient of friction significantly decreased.*

Keywords*:* wind turbines; moisture condition; silica sand; friction coefficient.

1. Introduction

Recently, the global use of power has tripled, in large part due to economic expansion. While developed countries like the United States, Japan, and Europe still require more electricity production to keep up with their higher consumption levels and to satisfy the expanding number of applications, Egypt's ongoing economic growth has resulted in a significant increase in the demand for electricity. The need for alternatives to finite fossil fuels and their negative environmental effects has propelled the wind industry's explosive growth during the last 20 years. A wind turbine design needs to undergo advanced engineering analysis to further increase the cost effectiveness of wind turbines, both in terms of dependability and the design of larger turbines as well as overall cost effectiveness. From several angles, it is possible to examine the cost effectiveness in the wind turbine sector. One of the biggest problems in this industry is the high maintenance costs and unproductive downtime caused by faults and failures in the functioning drive train components including bearings, gearboxes, and couplings, as cited by B. Lu et al., 2009 [6] and K.K. Borum et al., 2006 [12]. Also, many researchers including Alex Alsyouf I. and El-Thalji I., 2008 [1], H. Peng et al., 2023 [20] reported that the mechanical reliability of wind turbine-based renewable electricity generation has unique challenges when compared to utility-scale fossil fuel-based power. Due

to the sheer number of turbines and their dispersion, maintenance is a challenging and infrequent undertaking, and peak loads—due to unstable winds and grid faults as well as challenging environmental factors like temperature swings and moisture lead to excessive operation. Thus, one of the more difficult current practical tribological problems is presented by wind turbine systems. The actuators and drivetrain of the turbine have experienced costly repairs due to contact failures in gear and bearing components.

Maalawi K.Y. and Badr M.A. 2023 [14], Babu B.C., Mohanty K.B. 2010 [4] mentioned that the primary mechanical parts of the system are housed in the wind turbine's exterior housing, or nacelle. These components include the power electronics, the generator, bearings, the rotor shaft, the gearbox unit, the filtering system for lubricants, the mechanical braking mechanism, and the brakes, as shown in Figure 1. The generator is driven by the high-speed shaft, which receives energy from the main shaft via the gearbox. The nacelle cover and drivetrain parts are attached to a bedplate, It sits atop of a yaw mechanism which actively points the rotor toward the wind.

Despite the wide range of wind turbine powertrain types now in use, utility-scale systems typically fall into one of three groups as described by Q. Sun et al., 2002 [18]. The first idea entails employing two bearings to support the primary shaft. Radial loads are carried by the bearing closest to the gearbox, whereas loads axial and radial are carried by the bearing closest to the rotor. The primary shaft therefore solely sends torque to the gearbox. Torque arms can be added to the gearbox unit to transfer response torque to the bedplate since the gearbox may direct reaction torque in that direction Randall, R.B. and J. Antoni 2011 [19], Y. Amirat et al., 2007 [24]. The second idea, referred to as a "three-point suspension" design, an axial bearing is used to support the primary shaft close to the rotor, while the opposite end of the shaft can be support by a radial bearing from inside the gearbox. The actual gearbox is supported by two torque arms and positioned on the bed plate. The gearbox is directly integrated into the nacelle in the third category of drivetrain. This design incorporates all rotor support bearings into the gearbox, which also receives all rotor load inputs. Although this design can be viewed as favorable for reducing the weight of the nacelle., compatibility issues between the gearbox and the other nacelle components may cause early failure as mentioned by B. Lu et al., 2009 [6], A. Staino, B. Basu 2013[2], Peng Guo and David Infield 2012 [17].

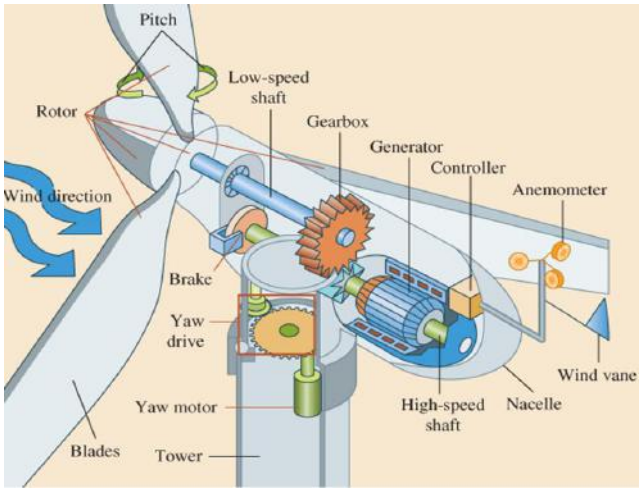

Fig.1. A horizontal-axis wind turbine's main part.

The high-speed portion of the powertrain of contemporary wind turbines typically includes a mechanical brake between the gearbox and the generator. The major function of this mechanical brake, which is nearly always shaped like a disc brake, is to shut off the rotor when it is shutting down in order to perform maintenance and repair work. Some turbines use the mechanical brake as a supplementary braking method in addition to serving as a parking brake so that aerodynamic braking can be used as well. In order to reduce the size and weight of the brake disc in larger wind turbines, the mechanical brake is located on the gearbox's high-speed side. The mechanical brake may reduce a gearbox's dependability because it is mounted on a high-speed shaft. When the vehicle is at rest, the braking loads often collide with the wind turbulence forces, causing minute oscillatory movements of the gear teeth. As a result of

these movements, the gear teeth may wear as found in M. Ragheb et al., 2011 [15], Gasch, R. and J. Twele 2012 [8], Sørensen, J. D. et al., 2011, Bhutta, et al., 2012 [5].

Howell R, et al., 2010 [10], Nadica Stojanovic, et al., 2022 [16], Zhang et al., 2023 [25] reported that the cutting and grinding from manufacturing, as well as internally induced wear wrench age, metal oxide corrosion products, airborne abrasives entering through vents, and mechanical seals are other sources of contaminated particles. Additionally, to particle pollution, Lubricating and hydraulic fluids also contain trace amounts of water that dissolve. Depending on the base stock and additions. The saturation level (maximum dissolved water content) is normally between 300 and 500 ppm. Also, Leung DY and Yang Y 2012 [13], Roman, et al., 2022 [21] showed that the free water, which collects in the system's low points, is defined as water contamination that exceeds the saturation limit. Depending on the amount, A bout 1 lm worth of emulsified free water droplets are remained suspended in the oil, giving it a hazy to milky appearance. Sources of water include liquid water acquired during transit and storage as well as humidity entering through vents and mechanical seals as mentioned by Roy Saha 2015 [22], Islam, M.R. et al., 2013 [11], G. Yu, et al., 2011 [9], Belhocine and Nouby, 2015 [3], Chellaganesh Durai, et al., 2021 [7].

According to the previously described discussions, fabrication of a new drivetrain test system to assess the tribology behaviors of wind turbine is conducted. The effect of contaminates on the tribology behaviors of the wind turbine brake system is studied. The effects of various-sized sand particles as pollutants is investigated. In additions, the humidity as water spray on the mechanical brake system are examined under different speeds and several loads.

2. General Description of Bearing Test-rig

As depicted in Figure 2, a sophisticated test apparatus is created to capture precise and trustworthy data which are utilized to assess gearbox performance by utilizing a variety of signal processing methods. The major goal of these experimental research is to keep an eye on how an automobile gearbox is performing at various speeds. A 100 mV/g-sensitivity piezoelectric accelerometer is mounted on the casing to provide vibration signatures of gearboxes. AC motor of A 7.5 kW power with a variable speed controller and a maximum speed of 1500 rpm makes up the drive unit. A tachometer S119-LT photo-type with 0.1 rpm resolution is used to detect the rotational speed directly. The type of bearings used is ball bearings, where they are positioned between brake assembly and motor, and the brake mechanism is connected to the AC motor by a mild steel shaft. A control valve-equipped hydraulic braking system is employed in order to enforce the necessary load and show its value on a pressure gauge.

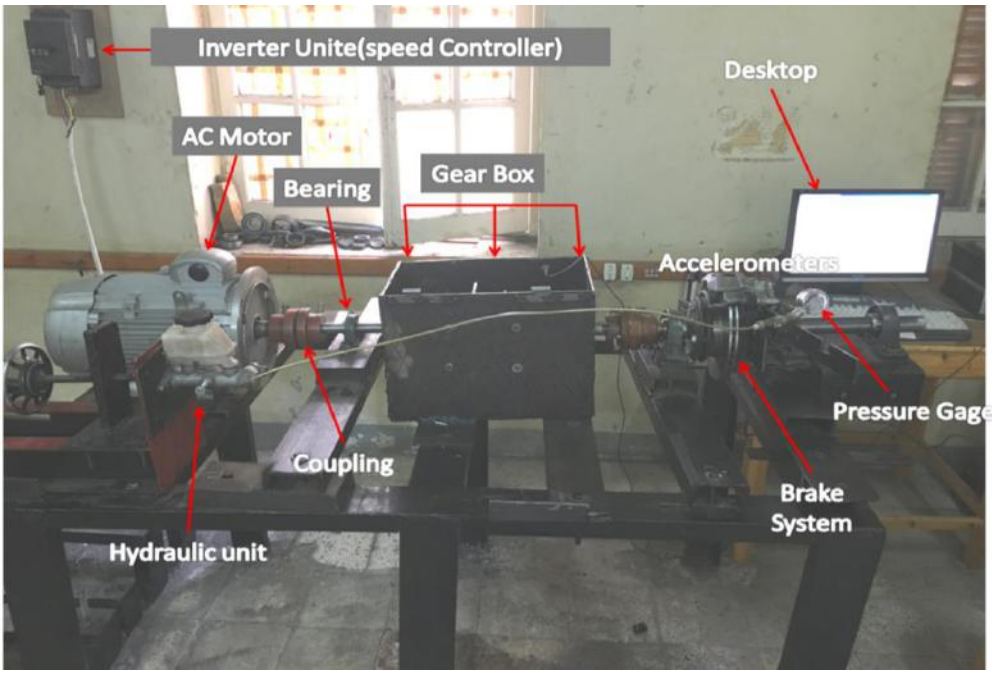

Fig.2. Test rig of wind turbine's drive train system

To collect the vibration information, a magnetic base is used to mount a piezoelectric accelerometer directly above the gearbox. The accelerometer's output signal is received by the dual channel vibration analyzer, which saves it as vibration signatures. Using PULSE software and a connection linked to a computer, the vibration analyzer's recorded data can be retrieved. The data Acquisition System that used is 3560-B Brüel & Kjaer Vibro-Acoustics type. To get reference signatures, the gearbox is tested without any load. The test rig's vibrations are recorded and confirmed prior to the experiment in order to determine whether there is a misalignment. To stabilize the vibration, the setup is run for 15 minutes.

3. Results and Discussion

This section defines the drive train system as the electromechanical component of a wind turbine that transmits mechanical power from the rotor hub to the electric power generator. It consists of shafts, bearings, gearboxes, shaft couplings, mounts, mechanical brake systems, and other functional components. This system is crucial to the tribology of wind turbines. The mechanical braking system is chosen so that the impact of impurities on friction coefficient, a key determinant of tribology behaviors can be studied. The investigation of the brake system uses actual disc brakes.

The high-speed section of the powertrain of contemporary wind turbines often has a mechanical brake, which is located between the gearbox and the generator. The main purpose of this mechanical brake during shutdown is to lock down the rotor so that maintenance and repair work may be done. It nearly always resembles a disc brake. Several turbines use the mechanical brake in addition to acting as a parking brake so that aerodynamic braking can be employed as well. The mechanical brake on larger wind turbines is located on the gearbox's high-speed side to reduce the brake disc's size and weight. Due to its placement on a high-speed shaft, the mechanical brake may make a gearbox less dependable. At rest, braking loads frequently clash with wind turbulence forces, causing minute oscillations in the gear teeth.

The experiment involved measuring the coefficient of friction once every second. Averaged over 60 seconds is the coefficient of friction. The friction coefficient varies over time while the testing is continuing because the metal-to-metal contact causes deformation on the contact surface. The coefficient friction stabilizes once the machine has been running. Figure 3 show the friction coefficient vs time for a wind shaft rotating at 1000 rpm and 10 bar of applied pressure. At dry, standard temperature, the friction coefficient is typically 0.35.

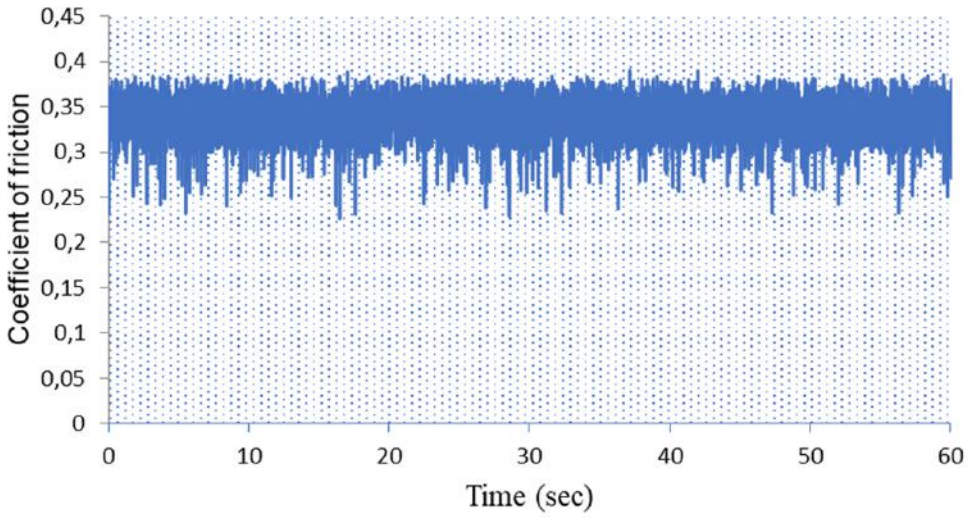

Fig.3. Variation over time of the friction coefficient at 1000rpm and 10 bar.

3.1 Effect of Silica Sand Particles on Wind Turbine Brake

When braking, both the brake rotor and the brake pads are exposed to weather environmental particles, which may have an impact on the surface quality of the brake pads in the form of moisture, humidity, or other impurities. Several vibration experiments are conducted to determine the effect of this particle on the brake friction coefficient. The effects of various-sized sand particles as pollutants on the mechanical brake system are examined. As indicated in Figure 4, this experiment used silica sand particles with a size range between 0 and 300 μm that are most frequently found in the weather. There were three different silica sand

size ranges used: 0-100 μm, 100-200 μm, and 200-300 μm. On a brake test apparatus that is vertically oriented, the experiments are run at various sliding speeds and applied contact forces. The outcome demonstrates that the silica sand particles had an impact on the disc brake's surface behavior. The disc brake's silica sand particle friction coefficient results reveal a rougher surface region with several primary contact plateaus, wear scars, and groove structures with varying levels of roughness and sliding direction. Figure 4 shows a plot of the impact of tiny silica sand particles at various rotational speeds.

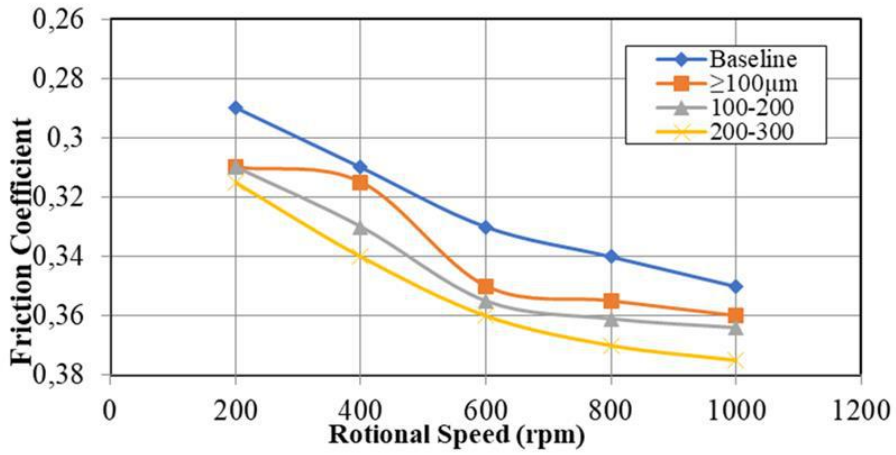

Fig.4. Effect small particles of silica sand with different rotational speed.

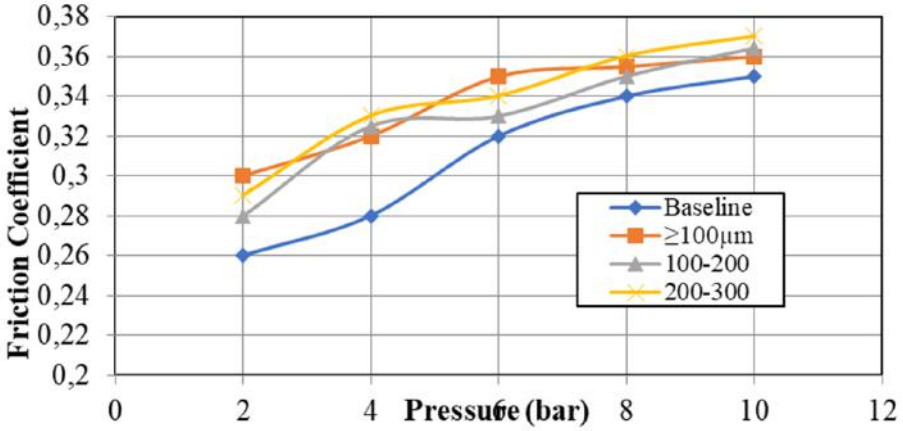

Fig.5. Effect small particles of silica sand with different brake pressure.

The results reveal that the friction coefficient is discovered to rise with every braking speed. Additionally, it has been discovered that the size of the particles significantly affects the friction coefficient. Figure 5 depicts the impact of tiny silica sand particles with various braking pressures on friction coefficient. The friction coefficient is discovered to rise with applied load. Additionally, it has been discovered that the particles' sizes significantly influence the friction coefficient, which rises as the load increases.

3.2 Influence of Moisture Condition on Friction Coefficient

As a quick technique to introduce the moisture condition, water was sprayed on the wind turbine mechanical braking system. This experiment demonstrated how humidity could affect the mechanical braking mechanism of a wind turbine. As the wind turbine shaft speed grew from 200 rpm to 1000 rpm, moisture is added to the friction, which significantly increased the coefficient friction. Additionally, it is demonstrated that as humidity increased at each speed from 30 mm^3 to 90 mm^3, there is a significant drop in coefficient friction.

The change in shear rate, which can affect the mechanical characteristics of the mating materials, may be the cause of the increase in coefficient of friction with an increase in rational speed. At larger shear strain

rates, these materials' strength increases. However, in the dry test, the friction coefficient likewise increased when the speed was increased. Figure 6 depicts the impact of humidity on coefficient of friction as a function of rotational speed. Additionally, Figure 7 illustrates the impact of humidity on various braking pressures.

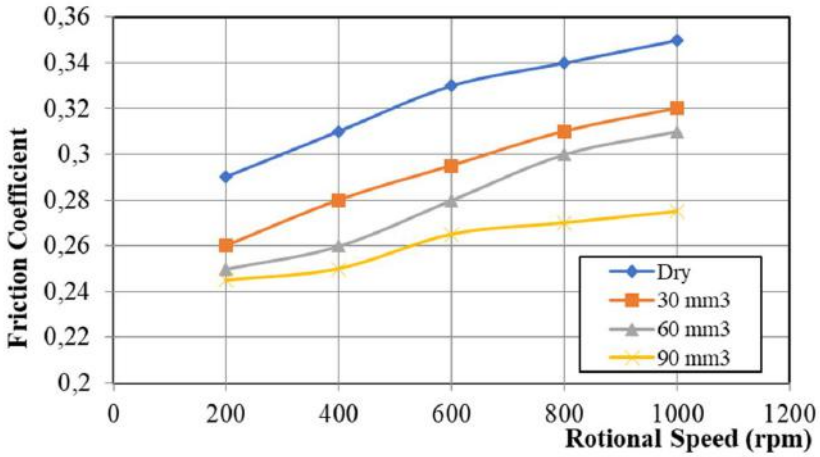

Fig.6. Effect humidity with different rotational speed.

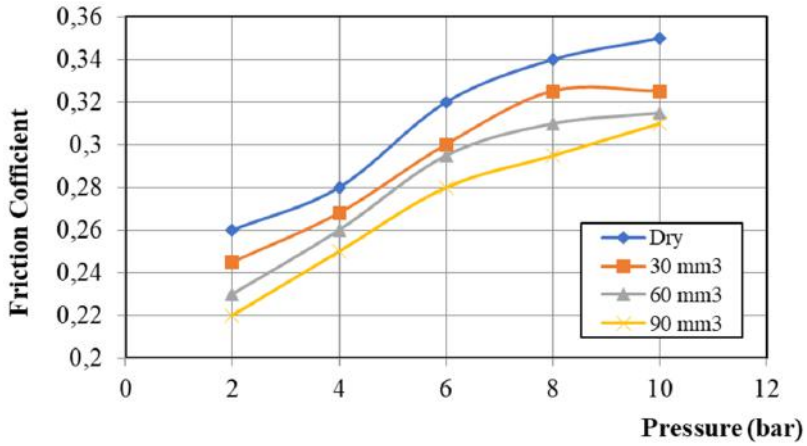

Fig.7. Effect humidity with different brake pressure.

4. Conclusions

From the experimental results indicate that humidity and silica sand under the braking speeds and load have a prominent influence on the wind turbine braking system. In additions, the following inferences can be made in light of the experimental findings:

1. The outcome demonstrates that the silica sand particles had an effect on the surface behavior of the wind turbine disc brake.
2. It has been discovered that friction coefficient rises with every wind turbine shaft speed.
3. The friction coefficient is shown to be significantly influenced by the particle size, and when the load on the wind turbine brake system grows, the friction coefficient also increases.

For each speed of wind turbine, it was demonstrated that as humidity increased from 30 mm^3 to 90 mm^3, the coefficient of friction significantly decreased.

Conflict of interest statement

The authors declare that they have no conflict of interest in relation to this research, whether financial, personal, authorship or otherwise, that could affect the research and its results presented in this paper.

CRediT author statement

Mohammed Omar A.: Conceptualization, Software; Mohammed; Sufyan A.: Writing - Review & Editing; Ghazaly Nouby M.: Supervision, Methodology. The final manuscript was read and approved by all authors.

References

1 Alsyouf I., El-Thalji I. (2008) Maintenance practise in wind power systems: a review and analysis. *Proceeding of the European Wind Energy Conference and Exhibition*, Brussels, Belgium, 2588 – 2597. https://www.proceedings.com/content/005/005469webtoc.pdf.

2 Staino A., Basu B. (2013) Dynamics and control of vibrations in wind turbines with variable rotor speed. *Enginnering Structures,* 58 – 67. DOI: 10.1016/j.engstruct.2013.03.014.

3 Belhocine A., Ghazaly N.M. (2015) Effects of Material Properties on Generation of Brake Squeal Noise Using Finite Element Method. *Latin American Journal of Solids and Structures,* 12, 2 (8). DOI:10.1590/1679-78251520.

4 Babu B.C., Mohanty K.B. (2010) Doubly-fed induction generator for variable speed wind energy conversion systems–modeling and simulation. *Int. J. Comput. Electr. Eng.,* 2(1), 141–147. DOI:10.7763/IJCEE.2010.V2.127.

5 Bhutta M.M.A., Hayat N., Farooq A.U., Ali Z., Jamil S.R., Hussain Z. (2012) Vertical axis wind turbine–A review of various configurations and design techniques. *Renewable and Sustainable Energy Reviews*, 16(4), 1926-1939. DOI: 10.1016/j.rser.2011.12.004.

6 Lu B., Li Y., Wu X., Yang Z. (2009) A review of recent advances in wind turbine condition monitoring and fault diagnosis. *IEEE Power Electron. Mach. Wind Appl.*, 1–7. DOI:10.1109/PEMWA.2009.5208325.

7 Chellaganesh Durai, M. Adam Khan, J. T. Winowlin Jappes, Nouby M. Ghazaly, P. Madindwa Mashinini (2021) Solid particle erosion studies on thermally deposited alumina– titania coatings over aluminium alloy. *International Journal of Minerals, Metallurgy and Materials,* 28, 1186–1193. DOI:10.1007/s12613-020-2099-8.

8 Gasch R., Twele J. (2012) Wind Power Plants - Fundamentals, Design, Construction and Operation, Springer. DOI:10.1007/978-3-642-22938-1.

9 Yu G., Shen X., Zhu X., Du X.Z. (2011) An insight into the separate flow and stall delay for hawt, *Renew. Energy,* 36 (1), 69–76. DOI: 10.1016/j.renene.2010.05.021.

10 Howell R., Qin N., Edwards J., Durrani N. (2010) Wind tunnel and numerical study of a small vertical axis wind turbine. *Renewable energy*, 35(2), 412-422. DOI:10.1016/j.renene.2009.07.025.

11 Islam M.R., Mekhilef S., Saidur R. (2013) Progress and recent trends of wind energy technology. Renew. Sustain. Energy Rev. *Renewable and Sustainable Energy Reviews,* 21, 456 – 468. DOI:10.1016/j.rser.2013.01.007.

12 Borum K.K., McGugan M., Brøndsted P. (2006) Condition monitoring of wind turbine blades. *Proc. of the 27th Risøe Intern. Symposium on Materials Science. Polymer Composite Materials for Wind Power Turbines*, 139–145. http://www.risoe.dk/rispubl/AFM/sympsale.htm

13 Leung D.Y., Yang Y. (2012) Wind energy development and its environmental impact: a review. *Renewable and Sustainable Energy Reviews*, 16(1), 1031-1039. DOI: 10.1016/j.rser.2011.09.024.

14 Maalawi K.Y., Badr M.A. (2003) A practical approach for selecting optimum wind rotors. *Renewable Energy,* 28, 803–822. DOI:10.1016/S0960-1481(02)00028-9.

15 Ragheb M., Ragheb A.M. (2011) Wind Turbines Theory - The Betz Equation and Optimal Rotor Tip Speed Ratio. *Fundam. Adv. Top. Wind Power*, 1(1). DOI:10.5772/21398.

16 Nadica Stojanovic, Ghazaly N.M., Grujic I., Doric J. (2022) Determination of Noise Caused by Ventilated Brake Disc with Respect to the Rib Shape and Material Properties Using Taguchi Method. *Transactions of FAMENA,* 46 (4). DOI:10.21278/TOF.464011219.

17 Guo P., Infield D. (2012) Wind turbine tower vibration modelling and monitoring by the non-linear state estimation technique. *Energies*, 5(12), 5279 – 5293. DOI:10.3390/en5125279.

18 Sun Q., Chen C., Zhang D., Xi F. (2020) Pattern recognition for automatic machinery fault diagnosis," *Mechanical Systems and Signal Processing*, 142, 106680. DOI:10.1016/j.ymssp.2020.106680.

19 Randall R.B., Antoni J. (2011) Rolling element bearing diagnostics—A tutorial, *Mechanical Systems and Signal Processing. 2*5, 2, 485 – 520. DOI:10.1016/j.ymssp.2010.07.017.

20 Peng H., Li S., Shangguan L., Fan Y., Zhang H. (2023) Analysis of Wind Turbine Equipment Failure and Intelligent Operation and Maintenance Research. *Sustainability,* 15(10), 8333. DOI:10.3390/su15108333.

21 Roman A., Lemos, G.V.B., Gasparin A.L. (2022) Friction material wear: Effects and interactions between service brake temperature, lining contact pressure, and vehicle speed. *Proceedings of the Institution*

of Mechanical Engineers, Part J: Journal of Engineering Tribology, 236(12), 2468 – 2476. DOI:10.1177/13506501221080282.

22 Roy S., Saha U.K. (2015) Wind tunnel experiments of a newly developed two-bladed Savonius-style wind turbine. *Appl Energy*.,137, 117–125. DOI:10.1016/j.apenergy.2014.10.022.

23 Jens N.S. (2011) Wind Energy Systems: Optimising Design and Construction for Safe and Reliable Operation. *Woodhead Publishing*, DOI:10.1533/9781857090638.

24 Amirat Y., Benbouzid M.E.H., Bensaker B., Wamkeue R. (2007) Condition Monitoring and ault Diagnosis in Wind Energy Conversion Systems: *A Review in Electric Machines and Drives Conference*. IEMDC '07, IEEE International. DOI:10.1109/IEMDC.2007.383639.

25 Zhang M.X., Ou Y.D., Yuan H.B., Pan J.L., Ma L. (2023) Simulation experiment study on friction and wear of materials under high humidity conditions. *Industrial Lubrication and Tribology*, 75, 6, 672 – 678. DOI:10.1108/ILT-04-2023-0090.

AUTHORS' INFORMATION

Mohammed, Omar A. – MSE, Lecturer, Department of Mechanical Engineering, College of Engineering, University of Mosul, Mosul, Iraq; 55175671700; SCOPUS Author ID: 57212494891; ORCID: 0000-0001-7126-1599; Omar.a.mohammed@uomosul.edu.iq

Mohammed, Sufyan A. – M.E, Lecturer, Department of Mechanical Engineering, College of Engineering, University of Mosul, Mosul, Iraq; SCOPUS Author ID: 57467887400; ORCID:0000-0001-9291-8297; Sufyan.a.mohammed@uomosul.edu.iq

Ghazaly, Nouby M. – PhD, Professor, Technical College, Imam Ja'afar Al-Sadiq University, Baghdad, Iraq; Department of Mechanical Engineering, South Valley University, Qena, Egypt; SCOPUS Author ID: 55175671700; ORCID: 0000-0001-8460-4407; nouby.ghazaly@eng.svu.edu.eg

EURASIAN PHYSICAL TECHNICAL JOURNAL

2024, Volume 21, No.3 (49)

Special Issue

https://doi.org/10.31489/2024No3/125-131

Received: 06/08/2024 Revised: 07/09/2024 Accepted: 23/09/2024 Published online:30/09/2024

Original Research Article

UDC 531.46

NUMERICAL STUDY OF GRADUAL CHANGE IN SHAFT DIAMETER AND RELIEF GROOVE RADIUS ON STRESS CONCENTRATION FACTOR

Sinossi M.I., Sadak T.W.

Mechanical Design and Production Department, Faculty of Engineering, Beni-Suef University, Egypt

*Corresponding author: tahany@eng.bsu.edu.eg

Abstract. *The purpose of this work is to investigate the effect of relief groove radius and the taper in gradual diameter change of shaft on stress concentration factors. Finite element analysis was used to conduct theoretical research in order to reduce the maximum value of stress in stepped shafts. In comparison based on a straight shaft without relief groove, the results show the decrease of taper angle has a significant effect in decrease the values of stress concentration factors. On the other hand, the increase of location of relief grooves from shaft shoulder tends to increase the stress concentration factors values, especially at high taper angle.*

Keywords: stepped shafts, shaft shoulder fillet, relief groove, stress concentration factors (SCF), finite element analysis (FEA).

1. Introduction

Most machine parts have varying cross sections, and shafts often include steps or shoulders to accommodate bearings, gears, and other mechanical elements. These changes in cross – sectional geometry cause local stress concentration and, while it is not practical to eliminate such features, it is necessary to minimize their effects, given that the degree of stress concentration is a factor in the evaluation of fatigue strength and fatigue life.

The stress concentration factors (SCF) are based on the nominal stress at the minimum diameter or width can be defined as the following,

$$k_t = \frac{\sigma_{max}}{\sigma_{nom}}$$

where σ_{max} is the maximum stress at the root of relief groove obtained from numerical simulation, and σ_{nom} is the nominal stress calculated by $\sigma_{nom} = 4F/(\pi d^2)$ for step shaft cross section.

Shoulders, grooves, keyways, and threads all contribute to increased localized high stresses in the parts. Stress concentration refers to the localization of high stress. The ratio of peak stress in the body to nominal stress is known as the stress concentration factor (K_t). In experimental and analytical researches, Pertson and Roak presented a lot of data in the form of graphs to evaluated the effect of geometrical discontinuities on the stress concentration factor (kt) [1].

Amaral Dias et al., presented a method for numerically evaluating stress concentration factors in shafts when radial bearings are used under three pure load conditions: traction, bending, and torsion. Two designs of simple fillet bearing shoulder is used in studies. Ansys® software was used to carry out the study. A

validation is achieved by comparing data from the literature works. The results showed that, in some case, simple fillet present low stress concentration factor compared to the standard design, [2]. Finite element analysis by Solid Works program was used to study a rounded shaft with shoulder fillet. The stress concentration factors for various fillet radius were investigated under applying tensile load on the round shaft. The results showed that the error not exceed that 5% between theoretically stress compared to the maximum stress computed with Solid Works. In addition to, the error deceases with the increase of fillet radius [3].

The effect of stress concentration on fatigue life were numerically evaluated using finite element analysis by applying changes in geometric parameters related to the size and location of the relief grooves. The results showed that the stress concentration reduced by 22.3% compared with that without the relief grooves. In addition to, using of the relief grooves extends the fatigue life by a factor of more than 3.3 times compared with the case without relief grooves [4]. Park et al., showed that Stress relief grooves were more effective than side fillet cutting at reducing stress concentration. The stress concentrations under bending and torsion loading conditions were lowered by 27.3 % and 18.2 %, respectively, when the radius of the stress relief groove was increased up to 2.0 mm. According to this study, the stress concentration increased when the radius of the relief groove was small [5].

Masanobu et al., studied that the effect of stress relief groove design variables such as radius, tangential angle, and depth on fretting fatigue strength. The results showed that the stress relief groove increases the fretting fatigue strength under the loading conditions of a bending moment combined with fretting fatigue.[6]

Prajwal et al., investigated the stress concentration and fatigue life of stepped shaft subject to axial stress. Reduction of stress concentration in the range of 13% and 34% were achieved for d_o/d_i from 1.08 to 1.22 [7].

Stress concentration factor of stepped shaft subject to twisting moment was investigated, the shaft has circular-to-square cross-section. Diameter to diagonal ratio (D/d) and radius of fillet to diagonal ratio (r/d) were studied for different ratios. The results indicated that the maximum shear stress located at the root of square in the middle location [8]. The results of FEA based on ANSYS program to compute the stress concentration factor (K_t) give a good result. The method can be considered good to produce accurate results for a wide range of geometry and loading conditions [9].

Stress concentration factor was studied by FEA analysis for keyway as discontinuity on shaft. The result shows the conformed agreement with theoretical calculations using Peterson equations. Torsion, bending and axial were applied as loading conditions. The results concluded that the increase of fillet radius of keyway tends to decrease the stress concentration factor (SCF) [10]. Different shapes and sizes of notched formed in cylindrical specimen subject to axial load, in order to reduce the effect of stress concentration. Studies were carried out by ANSYS software. The results showed notched shape, especially U shape notch, has a significant effect on stress concentration factor and fatigue life cycles [11].

2. Finite element analysis

The finite element method is a computational procedure for obtaining solutions to a wide range of engineering problems with complicated geometries that involve stress analysis. All models are studied using the ANSYS workbench 2019 R1 software. In this work, a round shaft with a constant D/d ratio of 1.5 was used, the effect of relief groove geometry has been investigated using finite element analysis (FEA). The different geometric are shown in Figure 1 can be described as the following.

1) The angles of tapered shaft are 5, 10, 15 and 20^o
2) Ratio of circular groove shaft diameter (r_g/d) are 0.1, 0.15 and 0.2
3) Distance between relief groove and shaft shoulder respect to shaft diameter (L/d) are 0.25, 0.5 and 0.75.

Steel material is used for simulations as an isotropic material with elastic modulus of 207 GPa, Poisson's ratio of 0.3. Figure 1 illustrates the geometric dimensions of the model used in the study.

1) The greater and lower diameters are (D) and (d) simultaneously,
2) Distance between the shoulder fillet and the circular groove is (L),
3) Applied normal force (F) of 1 kN.

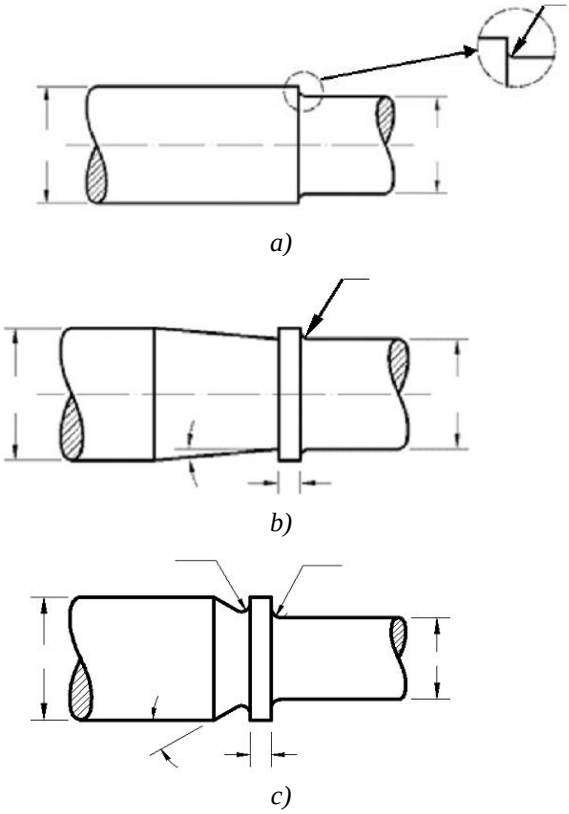

Fig.1. Geometric parameters of FEA models: a) Stepped shaft with shoulder fillet; b) Stepped shaft without relief groove; c) Stepped shaft with relief groove.

2.1 Mesh convergence

Different FEA models were studied with several different mesh sizes to determine the best mesh size to meet good results. Figures 2 and 3 show mesh refinement of fillet shoulder and equivalent stress distribution. 8 node elements with size of 0.25 mm along the fillet were applied to achieve high stress level. The relation between mesh densities on the stress concentration factor can be seen in Figure 4, the results showed that the stresses are increased by 17% when increasing the number of elements in the model.

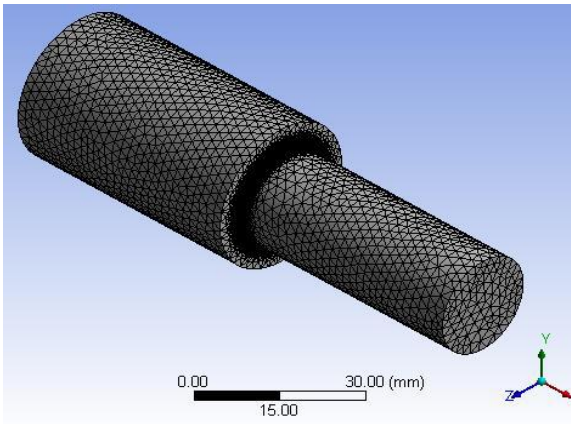

Fig.2. Mesh refinement of shaft model with shoulder.

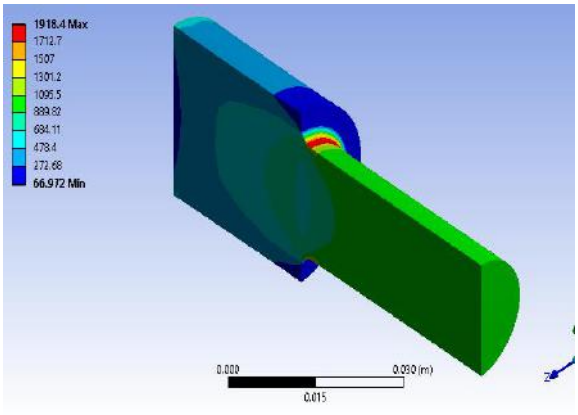

Fig. 3. Equivalent (von Mises) stress distribution of shaft model with shoulder fillet.

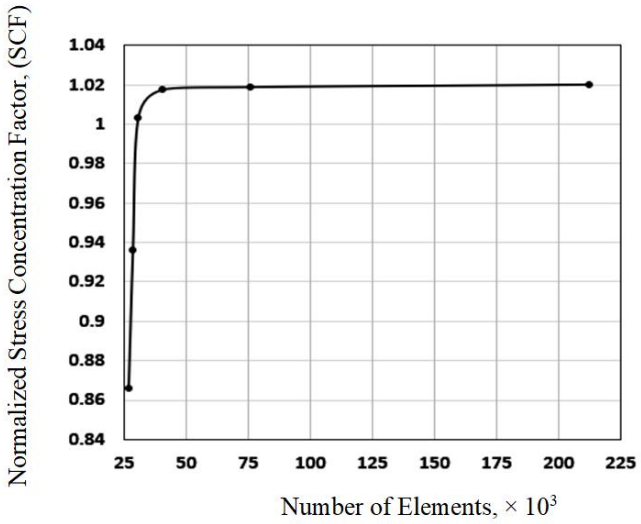

Fig.4. Stress concentration factor respect to mesh densities.

2.2 Verification of finite element model

ANSYS 2019 R1 is used to carry out FEA analysis. The validation of results obtained was compared to analytical data from Peterson,[1]. The shaft model has a circumferential groove. The material model is steel with a yield strength of 304 MPa, a Young's modulus of 207 GPa, and a Poisson ratio of 0.3 were used as input data in the FEA software.

Based on the results from the previous studies [1] and results from finite element analysis, Figure 5 illustrates the comparison between the stress concentration factor (SCF) for different ratios of (r/d) of stepped shaft (D/d) equal to 1.5 It may be noticed that a good agreement between two results in the range from 0.5 to 0.3.

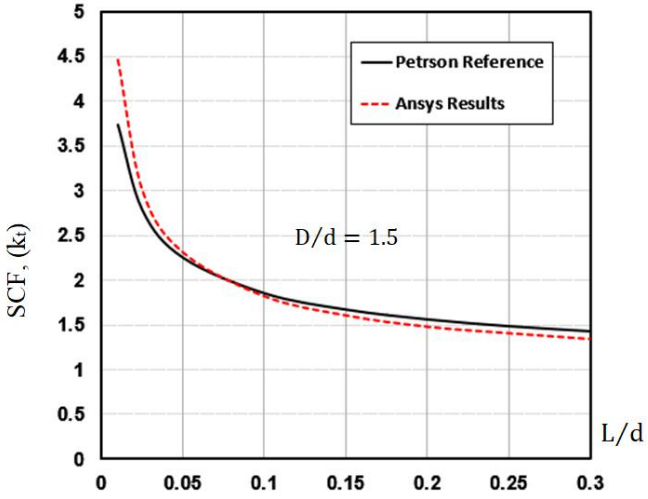

Fig.5. Validation of FEA results with the Analytical results given in reference, [1].

3. Results and Discussion

Figure 6 illustrates the effect of tapered shaft angle (θ^o) on stress concentration factor (SCF). The first curve shows the (SCF) of tapered shaft without relief groove, and the other is the percentage of these values relative to step shaft. The results show that the angle of tapered shaft has a significant effect, lowest values of (SFC) can be achieved at small angle value.

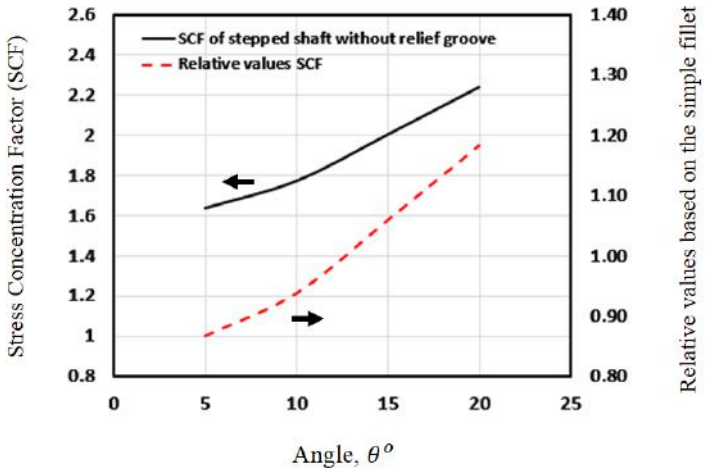

Fig.6. (SCF) of tapered shaft without relief groove.

As seen in Figure 7, The effect of groove location on stress concentration factor (SCF) is investigated. The increase in the distance ratio (L/d) between the shaft shoulder and relief groove tends to increase the values of stress concentration factors (SCF) values.

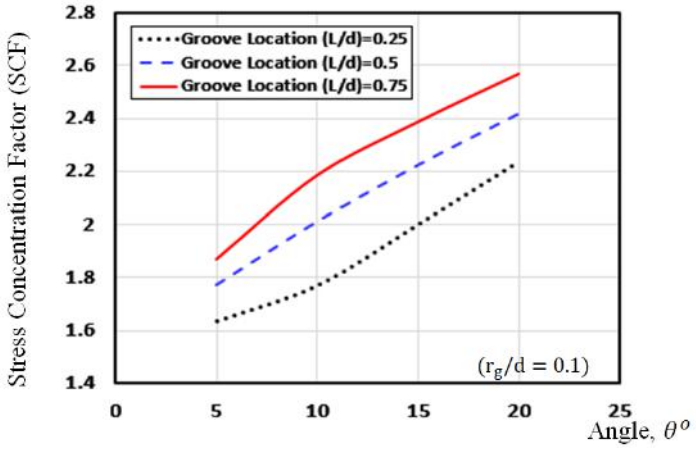

Fig.7. Effect of groove location of relief groove on (SCF).

The parameter of relief groove radius at different locations on the stress concentration factor (SCF) were studied. Figure 8, 9 and 10 illustrate the relationship between the stress concentration factor (SCF) versus the angle of tapered shaft at different ratio of relief groove radius (r_g/d). With constant locations of relief groove (L/d), It is clear that, the tapered shaft angle affects significantly the stress concentration factors (SCF). Furthermore, the effect of relief groove radius (r_g/d) on the values of (SCF) can be clear observed at angles 15^o and 20^o.

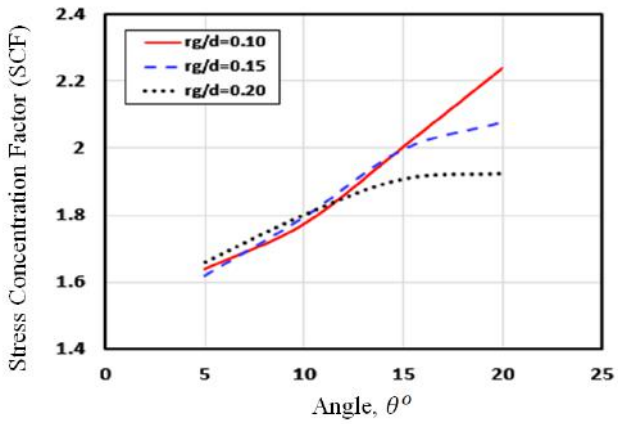

Fig.8. Effect of taper angle on (SCF), L/d= 0.25

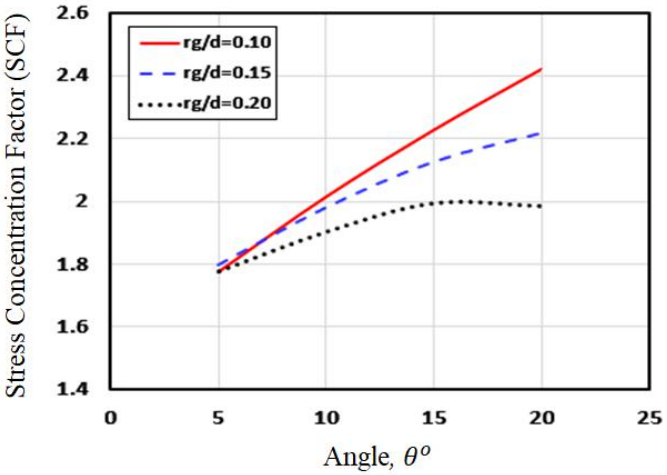

Fig.9. Effect of taper angle on (SCF), L/d= 0.5

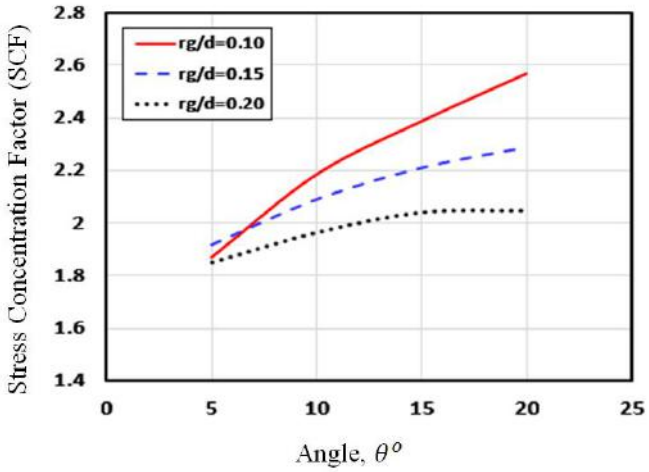

Fig.10. Effect of taper angle on (SCF), L/d= 0.75

4. Conclusions

In this study, a numerical model using ANSYS software is developed to study the effect of geometric parameter such as radius of relief groove (r_g) and angle of tapered shaft (θ^o) on stress concentration factor (SCF). Based on the results, the following conclusions can be drawn:

1) ANSYS software can be considered as a suitable FEA tool to study the stress concentration factor (SCF).

2) The angle of tapered shaft (θ^o) has a significant effect on the values of stress concentration factor (SCF).

3) The increase of relief groove radius (r_g) tends to increase the values stress concentration factor (SCF).

4) The stress concentration factor (SCF) of tapered stepped shaft is lower than that of a stepped shaft without a taper by 5-10% at small values of taper angles.

Conflict of interest statement
The authors declare that they have no conflict of interest in relation to this research, whether financial, personal, authorship or otherwise, that could affect the research and its results presented in this paper.
CRediT author statement
Sinossi M.I.: Conceptualization, Software; **Sadak T.W.:** Writing - Review & Editing, Methodology.
The final manuscript was read and approved by all authors.

References

1 Pilkey W.D, Pilkey D.F. (2020) Peterson's stress concentration factors. 3rd Edition. https://pdfcoffee.com/pilkey-w-d-peterson-s-stress-concentration-factors-3rd-ed-pdf-free.html

2 do Amaral Dias, do Vale G.C., J.L., da Silva J. (2019) Numerical Evaluation of Stress Concentration Factor for Different Designs of Shaft Shoulder Applied to Radial Bearings Housings. *Proceeding of the Conference: 25th International Congress of Mechanical Engineering.* DOI: 10.26678/ABCM.COBEM2019.COB2019-0196.

3 Singh A.P., Vidya S., Suresh P., Kumar A., Srikanth K. (2022) Comparative stress analysis of round shaft with shoulder fillet using finite element and analytical method. *Mater. Today Proc.*, 56, 497–501. DOI: 10.1016/j.matpr.2022.02.168.

4 Shin J.-M., Han D.-S., Lee K.-H., Han S.-H., et al. (2014) Using stress relief grooves to reduce stress concentration on axle drive shaft. *Journal of Mechanical Science and Technology*, 28(6), 2121-2127. DOI: 10.1007/s12206-014-0409-7.

5 Park I., Shim J.J. (2010) The Study for Reduction of Stress Concentration at the Stepped Shaft According to Two Types of External Force. *Journal of Power System Engineering*, 14(1), 47-52. https://www.researchgate.net/publication/263435600_The_Study_for_Reduction.

6 Kondo Y., Kubota M., Kataoka S., Sakae C. (2007). Effect of stress relief groove shape on fretting fatigue strength and index for the selection of groove shape. *Zairyo/Journal of the Society of Materials Science*, 56(12), 1156-1162. DOI: 10.2472/jsms.56.1156.

7 Kubota M., Kataoka S., Kondo Yo. (2009) Effect of stress relief groove on fretting fatigue strength and index for the selection of optimal groove shape. *International Journal of Fatigue*, 31(3), 439-446. DOI: 10.1016/j.ijfatigue.2008.07.007.

8 Prajwal S., Dhinakaran V., Jagadeesha T. (2020) Size optimization of shoulder filleted shafts with relief grooves for improving their fatigue life. *AIP Conf. Proc.*, 2283, 020057. DOI: 10.1063/5.0024911.

9 Lubis A., Akmal J. (2008) Stress Concentration Factors of Stepped-Shafts of Circular-to-square Cross Section under Twisting Moment. *Engineering, Materials Science*, 3(2), 48 - 52. https://www.semanticscholar.org/paper/Stress.

10 Parle D., Patil A., Ambulgekar A. (2011) Evaluation of Stress Concentration Factor using ANSYS. *Ansys Users Conference*, 35-38. https://www.researchgate.net/publication/306017771.

11 Prajapati H.R., Patel B.P., Patel N.V. (2014) Investigation of Stress Concentration Factor for Keyway on Shaft under Different Loading Conditions: A Case Study. DOI: 10.13140/RG.2.2.24744.67840

12 Raychev R., Delova I. (2021) Methods for Reducing the Stress Concentration in Cylindrical Specimens, at Axial Loading. Environment. Technology. Resources. *Proceedings of the 13th International Scientific and Practical Conference*, 3. DOI: 10.17770/etr2021vol3.6535.

AUTHORS' INFORMATION

Sinossi, Muhammad I. – PhD (Eng.), Assistance professor, Mechanical Design and Production Department, Faculty of Engineering, Beni-Suef University, Egypt; Scopus Author ID: 579215611206; ORCID iD: 0000-0002-9581-4386;
Sadak, **Tahany, W** – PhD (Eng.), Associate Professor, Former Vice Dean for Education and Student Affairs, Faculty of Engineering, Beni-Suef University, Egypt; Scopus Author ID: 55960111700; ORCID iD: 0000-0002-8101-6105.

EURASIAN PHYSICAL TECHNICAL JOURNAL

2024, Volume 21, No.3 (49)

Special Issue

https://doi.org/10.31489/2024No3/132-139

Received: 20/06/2024 Revised: 07/09/2024 Accepted: 23/09/2024 Published online:30/09/2024
Original Research Article

UDC 531.43; 51-72

RESIDUAL - STRESS AND TEMPERATURE FIELDS IN SURFACE TESTING: FINITE-ELEMENT ANALYSIS

Hasan Nazieh

Mechanical Engineering Department, Zarqa University, Zarqa, Jordan

Corresponding author: nazieh@ymail.com

Abstract. *Numerous advancements have been made to treat part surfacing, however, the presence of surface imperfections resulting from finishing processes has raised concerns about their potential to serve as stress concentrators. To address this concern, the present study utilized the power of the finite element method and cutting-edge software applications. The main aim of the study is to evaluate the stress-strain condition of material surfaces post-finishing, leveraging the comprehensive capabilities offered by these software systems. A significant component of the investigation centered on the influence of non-stationary temperature fields, as monitored by dynamic thermoelements, on the stress-strain dynamics within material surfaces. Visualization techniques were employed to depict the specified field functions, revealing notable variations in temperature distribution. The findings demonstrated that the standard function identified the highest temperature area within the 3-7-4 node segment, while the alternative function pinpointed it within the 4-node segment, indicated by the red area. These outcomes highlight the valuable role of non-stationary temperature fields in balancing the mechanical and physical aspects of the finishing process. This study contributes significant insights into the post-finishing stress-strain state of material surfaces, emphasizing the potential advantages of using modern software systems for in-depth exploration.*

Keywords: finite element method, information technology, serendipity finite element, stress-strain state.

1. Introduction

Surface quality plays a crucial role in determining the reliability and durability of equipment parts during operation. The roughness of air-engine blade surfaces, for instance, serves as a quality criterion for blade durability, fuel consumption, and engine efficiency [1]. A diamond stylus moving on an investigated surface is used to determine roughness parameters such as Ra and Rz [2]. Additionally, the quality of surface processing significantly influences the strength of parts [3]. For instance, imperfections formed during surface finishing are known to reduce significantly the fatigue strength of parts.

Various technologies are used for part surface treatment, including electric-powered diamond grinding, belt grinding, creep-feed grinding, polishing, electrochemical treatment, electrolytic plasma polishing, and ionic plasma hardening [4-6]. To eliminate the adverse influence of technological heredity, finishing treatment should be applied during the next processing operation to form compressive residual stresses in the surface layer. Uneven allowance removal leads to considerable instability in the residual stress indicator in surface layers. The process line for finishing material surfaces consists of units such as machine-tool fleet with numeric control (for example, grinding machine Metabo6NC-1000 [8] control equipment (measuring system BLAZER) [8], X-ray diffractometers X stress 3000 G3R [9], laser interferometers, robot manipulators with goniometers X stress Robot, etc.); and software systems for investigation of physical and

mechanical components of surface processing. The use of ANSYS software is essential in investigating the physical and mechanical components of surface processing [1, 6]. In addition, Fused deposition modeling (FDM) is the most commonly adopted technique in additive manufacturing, as it is useful in the enhancement of the tensile strength of 0° raster specimens. According to Garg and Bhattacharya [10], Fused deposition modeling (FDM) is the most commonly adopted technique that is used in additive manufacturing techniques. Burley et al. [11] conducted an experimental study and addressed the impact of residual stresses in the near-surface region after the adoption of the plastometry technique. Liu and Guo [12] used a thermo–elastic–viscoplastic model using explicit finite element code to develop Abaqus.

The present study focuses on the profound impact of surface finishing on the fatigue strength of mechanical parts. In particular, the study observes the effectiveness of creep-feed grinding and polishing techniques in enhancing the fatigue strength of these components. This in-depth analysis emphasizes an examination of the microgeometry and microstructure of the upper boundary layers of the surface. The comprehensive insights gained from the study include revealing the complexities of the physical and mechanical properties of these components facilitated through the use of ANSYS software. This will help in identifying the optimal operational conditions for both the creep-feed grinding and polishing techniques. In parallel, it suggests that adopting these techniques could indeed lead to a significant enhancement in the fatigue strength of components.

The significance of this study lies in its unique contributions, particularly in shedding light on the transformative role of surface finishing, with specific emphasis on creep-feed grinding and polishing techniques, in strengthening component fatigue strength. Through these findings, the study enriches the understanding of the surface finishing process and its far-reaching implications on the mechanical attributes of components. Beyond this, the study has evolved to offer practical recommendations, aimed at refining the surface finishing process to enhance the longevity and reliability of equipment components during their operational lifecycle.

2. Related Work

The finite element method is a mathematical technique used to analyze and investigate the stress-strain state and field functions of materials based on the theory of elasticity. It is widely used in engineering and material science research to model and simulate the behavior of complex structures and systems. One important aspect of the finite element method is the use of finite element approximations, which are mathematical models used to estimate the behavior of a system. One such approximation is the serendipity finite element, which is a type of quadrilateral element with nodes at the corners and in the middle of each side. The serendipity finite element was originally developed to simplify the calculation process by reducing the number of internal nodes required for accurate modeling. However, the standard functions of serendipity finite elements have been criticized for their unnatural nodal load distribution, which can result in inaccurate calculations.

The apparatus of the finite element method [12-13], is used to analyze and investigate the stress-strain state and field functions based on the theory of elasticity. The mathematical support of the finite element method serves as an algorithmic basis for the following software systems: Nastran, Ansys, Solid Works, etc. Lagrangian finite elements have nodes in the middle of the final element. Internal nodes increase the calculation scope and are not used for assembling finite elements. There are unidentified disadvantages in serendipity finite elements. The initial goal of creating serendipity finite elements is the ability to convert an arbitrary quadrilateral into a square and to reduce the calculation scope by removing extra internal nodes. This curvilinear element appeared in the calculation of structures as a serendipity finite element.

The higher the order of the serendipity finite element, the more accurate the calculation is. A square finite element combines well with a triangular simplex, forming an effective mesh of the finite element method. The square cells are convenient within the area, and triangular–in the boundary area during digitization of a planar area in arbitrary configuration. The basic function plays a key role in the finite element method; therefore, its physically adequate form is important. A serendipity finite element interpolates the element boundary function and approximates the nodes inside it. The main drawback of standard functions of the serendipity finite elements is unnatural nodal load distribution from a single mass force because loads are negative in corner nodes [13]. These standard functions [14] play a double role in isoperimetric technology. In Zienkiewicz's [14], standard model, there are no additional degrees of freedom (df), because it is designed according to hard recipes of matrix algebra within the La-grange interpolation formula [15].

The first alternative (physically adequate) model of serendipity finite elements appeared in 1982 due to the inability to find a rational explanation for unnaturally distributed uniform mass force [14]. Serendipity finite elements with negative loads at nodes are not suitable for computer testing. Doudkin et al. [16] presented a three-dimensional solid-state model based on computation. This study also analyzed feed elements of rods of vibroscreen. According to the results, the strengths of materials varied but their parameters did not report a change for the bulk materials. A study by Shukla, Murmu, and Deo [17] used Finite Element Method software for modeling the fracture behavior of plain concrete (PC) and basalt fiber concrete beams for Mode I (Three-point bending). The findings outlined that the results of the finite element simulation were favorable and no effect was reported in the fracture energy along with the varying sizes of specimens. Campaner [18] reported that despite restorative material, the tensile stress magnitude of the region of the prosthetic connectors was the highest. However, none of the modern software systems (finite element method oriented) contains alternative functions of the serendipity finite elements. Results of the constructive theory of serendipity approximations are laid down (as algorithmic functions) in two information technologies [19], developed based on Turbo Pascal and C#, respectively, and in the automated subsystem, developed based on Delphi.

2.1 Research Gap

The finite element method is a mathematical technique used to analyze and investigate the stress-strain state and field functions of materials based on the theory of elasticity. It is widely used in engineering and material science research to model and simulate the behavior of complex structures and systems. One important aspect of the finite element method is the use of finite element approximations, which are mathematical models used to estimate the behavior of a system. One such approximation is the serendipity finite element, which is a type of quadrilateral element with nodes at the corners and in the middle of each side. The serendipity finite element was originally developed to simplify the calculation process by reducing the number of internal nodes required for accurate modeling. However, the standard functions of serendipity finite elements have been criticized for their unnatural nodal load distribution, which can result in inaccurate calculations.

3. Materials and Methods

3.1 Field Functions for Residual Stress Prediction

The field functions $U(x, y, t)$ is used for conducting visualization and analysis tests of surfaces or non-stationary physical tests, which include temperature field and stress field. These field functions are custom-tailored to the requirements of residual stress prediction and represent a fundamental component of the present study. Equation 1 summarizes the field functions needed:

$$U(x, y, t) = \sum_{i=1}^{m} N_i * f_i(t) \quad (1)$$

Where: Ni is the standard or alternative basis of the serendipity finite element, t is time, I is node number, m is the number of nodes of the serendipity finite element, fi(t) is the law of time variation of a physical quantity (residual stress, temperature, etc.) at the boundary nodes of the serendipity finite element.

The field functions defined by Equation 1 are employed to visualize and analyze non-stationary temperature fields and stress fields. In particular, they are utilized for the prediction of residual stress in materials. Through the application of these field functions, the residual stress fields within the material samples are visualized and analyzed. The functions are integral to this process, and their unique design allows for the precise identification of regions with residual compressive stress, residual tensile stress, thermo-elastic stress, and residual stress in our specimens. The field functions are systematically adapted to the preferred physical quantities in the surface control points. This facilitates the investigation of residual stress in materials and ensures their direct relevance to our study objectives.

The applicability of these field functions is not confined to material surfaces with linear boundaries. Through the incorporation of isoperimetric transformation techniques, they can effectively handle surfaces with curvilinear boundaries, thus extending their utility. The surface area with a curvilinear boundary does not matter, due to the isoperimetric transformation. The standard and alternative function fields are presented in the following equations. The standard function [19].

$$N_i = \frac{1}{4}(1 + x_i x)(1 + y_i y), x_i, y_i = \pm 1, 1, 4$$

$$N_i = \frac{1}{4}(1 + x_i x)(1 + y_i y)(x_1 x + y_i y - 1), x_i, y_i = \pm 1, 1, 4$$
$$N_i = \frac{1}{2}(1 - x^2)(1 + y_i y), y_i = \pm 1, i = 5, 7$$
$$N_i = \frac{1}{2}(1 - y^2)(1 + x_i x), x_i = \pm 1, i = 6,8$$

The alternative function:

$$N_i = \frac{1}{4}(1 + x_i x)(1 + y_i y)x_i y_i xy, x_i, y_i = \pm 1, i = \overline{1,4}$$
$$N_i = \frac{1}{4}(1 - x^2)(1 + y_1 y)^2, y_i = \pm 1, i = 5, 7$$
$$N_i = \frac{1}{4}(1 - y^2)(1 + x_1 x)^2, x_i = \pm 1, i = 6, 8$$

3.2 Sensitivity Analysis and Optimization

To address the effects of various input parameters on the simulation results and to identify critical parameters that require control or optimization, the methods incorporate a sensitivity analysis. Furthermore, optimization techniques are seamlessly integrated to determine optimal design parameters and processing conditions that lead to the desired stress-strain state within the material surfaces.

A two-dimensional finite model was adopted in the study, and the length of the edge was 20 times larger than that of the uncut layer to ensure steady-state cutting. The type of element used was a four-node bilinear, but not all elements in the mesh were placed longer in the horizontal direction to account for intense compression and shear straining for the movement of the tool from right to left. This shape was selected to reduce the likelihood of numerical problems that may be encountered due to the distortion of elements.

The detailed algorithm with considerations for temperature fields, stress fields, sensitivity analysis, and optimization techniques has been provided in Appendix A.

3.3 Validation of Method for Residual Stress Prediction

Tests were conducted on material samples with known residual stress profiles. Residual stress was measured directly using established techniques. The measurements were then compared to the predictions generated by the method, calculating performance metrics such as MAE and RMSE. When experimental validation is not feasible, benchmark data with known residual stress profiles is used. The method was applied to predict residual stress within the same materials and geometries used in the benchmark data. Performance was evaluated through metrics and visual comparisons. The method's response to variations in input parameters was assessed, evaluating its robustness and reliability. The results of both experimental and numerical validation validated its applicability in scientific studies and practical applications.

4. Results and discussion

The square area of the processed surface area based on serendipity finite element of the first and second order is presented in Fig. 1 and 2. For a square of the first order (Fig. 1), a visualization and analysis test has been conducted using the MATLAB software package for a stationary field of residual stress. The values of residual stress ($\sigma_{residual}$) in four control nodes were determined by X-ray diffractometer stress 3000 G3R (second node of the process line) based on the electric-powered diamond grinding. The required range of computed values of residual stresses are:

$$\sigma_{1residual} = 25MPa, \sigma_{2residual} = 34MPa, \sigma_{3residual} = 42MPa, \sigma_{4residual} = 37MPa$$

The two-dimensional surface of the test stationary field of residual stress is shown in Fig. 3. The field has a clear gradient, and permanent relief (due to zero curvature), the highest concentration of residual stress is concentrated at the third node (purple area), and the lowest in the first (green area). In the element barycenter, the value of the residual stress is σcenter=residual = 34.5 MPa (arithmetic mean), which is confirmed by a uniform gradient. There are no anomalous areas (vortices) on the field surface. Recommendations for subsequent finishing are identified from the removal of stresses in the third node area.

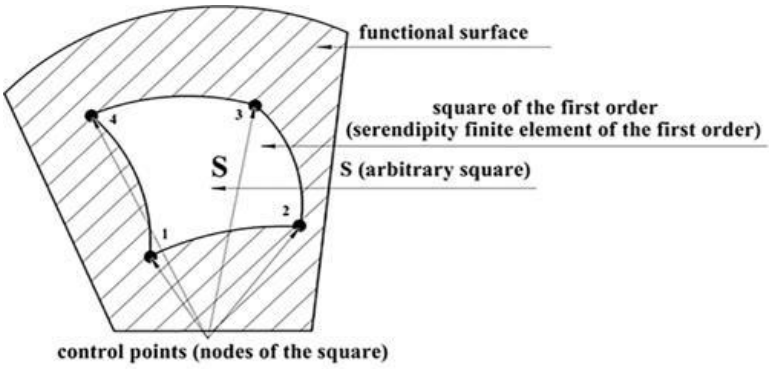

Fig.1. Square of the first order.

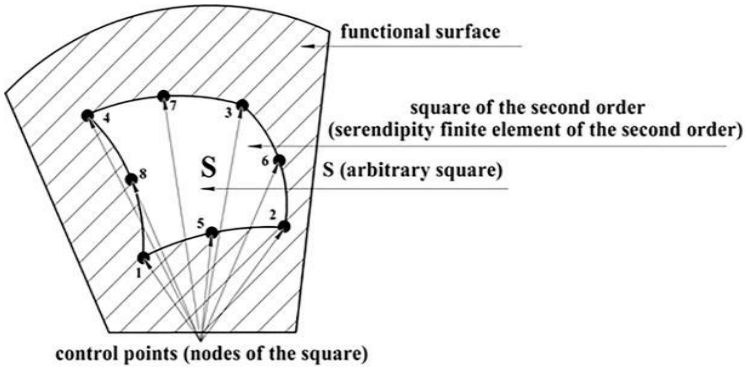

Fig.2. Some functions of the Square of the second order.

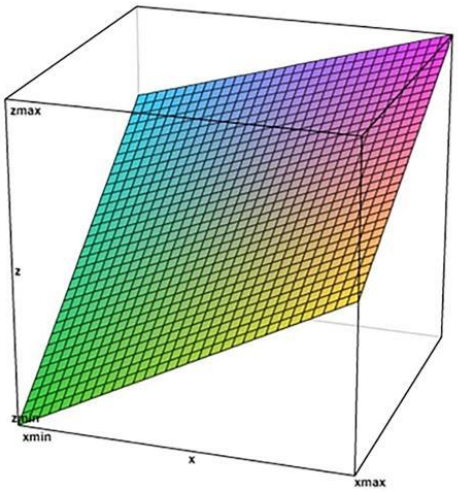

Fig.3. Testing in MATLAB.

A visualization and analysis test has been conducted for a stationary temperature field using dynamic thermos-elements for a square of the second order. Equation 3 presents the following function:

$$U(x,y) = \sum_{i=1}^{8} N_I * T_i$$

The temperature values in eight control nodes were determined with a contact thermocouple (the second node of the process line) because of the belt grinding (temperature perturbations at the points of changed trajectory of the tool moving). The desired range of values: T1=120°C, T2=134°C, T3=147°C, T4=151°C, T5=125°C, T6=139°C, T7=148°C,

T8=118°C. Fig. 4 shows the two-dimensional surface of the tested stationary field using the standard function. The field has a smooth gradient, and saddle-shaped relief (hyperbolic paraboloid). The highest temperature area is concentrated in the 3-7-4 node segment, whereas the lowest temperature area was shown in the 5-node segment transitioned into the barycentre (blue area). There are no irregular regions on the field surface. Therefore, operations should be processed by reducing the high-temperature area in the 3-7-4 node segment. Fig. 5 shows the two-dimensional surface of the tested stationary field using an alternative function.

The field has a clear, transient gradient, and wave-like relief (Jacobi function). The highest temperature area is concentrated in the 4-node segment (red area), whereas the lowest temperature area was in the 2-node segment (blue area). There are vortexes (localization in the center) on the field surface. Therefore, process steps should be undertaken by reducing the high-temperature area in the 4-node segment.

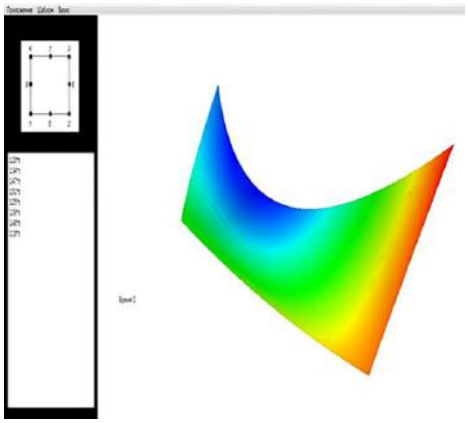

Fig.4. Standard Function

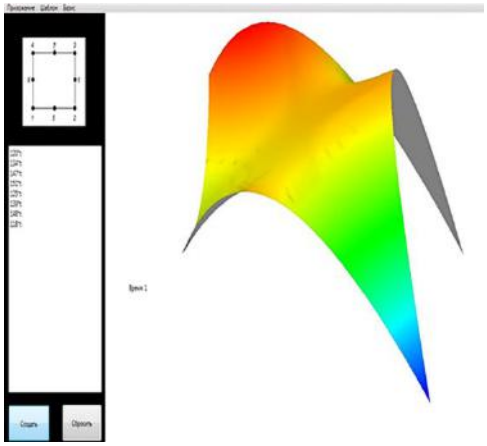

Fig.5. Alternative Function.

For the stationary field of residual stress, a square of the first order was used, and a visualization and analysis test were conducted using MATLAB software. The results showed that the highest concentration of residual stress was concentrated at the third node, and the lowest in the first. The value of the residual stress at the element barycenter was determined to be 34.5 MPa, which is confirmed by a uniform gradient. There were no anomalous areas on the field surface, and recommendations for subsequent finishing were identified from the removal of stresses in the third node area.

For the stationary temperature field, a square of the second order was used, and two-dimensional surfaces of the tested stationary field using the standard and alternative functions were analyzed. The results showed that the highest temperature area was concentrated in the 3-7-4 node segment for the standard function and in the 4-node segment for the alternative function. The lowest temperature area was shown in the 5-node segment transitioned into the barycenter for the standard function and in the 2-node segment for the alternative function. There were no irregular regions on the field surface for the standard function, but vortexes were present in the center for the alternative function.

Based on these results, the study made recommendations for subsequent finishing operations to reduce the high-temperature or residual stress areas in the identified node segments. However, it's worth noting that the results presented in the study are limited by the specific conditions and materials used in the testing. The study did not compare the results with other methods or models, and the conclusions drawn are only applicable to the specific conditions tested.

5. Conclusions

The study has used non-stationary temperature fields with dynamic thermoelements. Two different function fields were undertaken to establish an application of analysis and visualization of the physical and mechanical components of the finishing process. Through the application of simulation models and modern software systems such as MATLAB, the study successfully determined residual stress and temperature values in various control nodes, offering valuable insights into the effects of finishing on material surfaces. These findings hold significant implications for the field of material finishing, highlighting the potential for enhancing the quality and performance of finished materials. While this study provides valuable insights into

the stress and temperature patterns of material surfaces during finishing, there is still much to be learned and explored in this field. By continuing to innovate and refine our approaches to analysis and visualization, we can continue to improve the quality and performance of finished materials, and advance the field of material science as a whole. The findings of this study have important implications for the field of material finishing. The use of non-stationary temperature fields with dynamic thermoelements, in combination with the finite element method and modern software systems such as MATLAB, has demonstrated the potential for analysis and visualization of the physical and mechanical components of the finishing process. By using simulation models, the study was able to determine the values of residual stress and temperature in various control nodes, providing insights into the effects of finishing on material surfaces.

Conflict of interest statement

The author declare that they have no conflict of interest in relation to this research, whether financial, personal, authorship or otherwise, that could affect the research and its results presented in this paper.

Acknowledgments

The author is very thankful to all the associated personnel in any reference that contributed / to the purpose of this research.

References

1 Nosov N.V. (2018) Application of quasi-optimal correlation algorithm for surface quality assessment. *Journal of Physics Conference Series*, 1096, 012141–012141. DOI: 10.1088/1742-6596/1096/1/012141.

2 Snehashish Chakraverty, Deepti Moyi Sahoo, Nisha Rani Mahato. (2019) *Defuzzification.* Springer EBooks, 117–127. DOI: 10.1007/978-981-13-7430-2_7.

3 Ortwin Farle, Hill, V., Pär Ingelström, Romanus Dyczij-Edlinger. (2008) Multi-parameter polynomial order reduction of linear finite element models. *Mathematical and Computer Modelling of Dynamical Systems*, 14(5), 421–434. DOI: 10.1080/13873950701844220.

4 Nawijn M., van Tooren M.J.L., Berends J. P. T. J., Arendsen P. (2006) Automated Finite Element Analysis in a Knowledge Based Engineering Environment. *44th AIAA Aerospace Sciences Meeting and Exhibit*. DOI:10.2514/6.2006-947.

5 Guitart M. (2022) Behind Architectural Filters. DOI: 10.4324/9781003208624.

6 Pavlenko D., Kondratiuk E., Torba Y., Vyshnepolskyi Y., Stepanov D. (2022) Improving the efficiency of finishing-hardening treatment of gas turbine engine blades. *Eastern-European Journal of Enterprise Technologies*, 1(12(115)), 31–37. DOI: 10.15587/1729-4061.2022.252292.

7 Kayabekir A.E., Toklu Y.C., Bekdaş G., Nigdeli S.M., Yücel M., Geem Z.W. (2020) A Novel Hybrid Harmony Search Approach for the Analysis of Plane Stress Systems via Total Potential Optimization. *Appl. Sci.*, 10(7), 2301. DOI: 10.3390/app10072301.

8 Zobov V.A., Chernousov D.A. (2021) Analysis of the Technology of Automation of Surface Layer Quality Management during Turning. *Russian Metallurgy (Metally),* 2021(13), 1814–1820. DOI:10.1134/s003602952113036x.

9 Stern M., Soni M.L. (1976) On the computation of stress intensities at fixed-free corners. *International Journal of Solids and Structures*, 12(5), 331–337. DOI: 10.1016/0020-7683(76)90023-8.

10 Machado A., Soares C., Reis B., Bicalho A., Raposo L., Soares P. (2017) Stress-strain Analysis of Premolars With Non-carious Cervical Lesions: Influence of Restorative Material, Loading Direction and Mechanical Fatigue. *Operative Dentistry*, 42(3), 253–265. DOI: 10.2341/14-195-l.

11 Burley M., Campbell J.E., Reiff-Musgrove R., Dean J., Clyne T.W. (2021) The Effect of Residual Stresses on Stress–Strain Curves Obtained via Profilometry-Based Inverse Finite Element Method Indentation Plastometry**.** *Advanced Engineering Materials*, 23. DOI:10.1002/adem.202001478.

12 Liu C.R., Guo Y.B. (2000) Finite element analysis of the effect of sequential cuts and tool–chip friction on residual stresses in a machined layer. *International Journal of Mechanical Sciences*, 42(6), 1069–1086. DOI:10.1016/s0020-7403(99)00042-9.

13 Contreras H.(1980) The stochastic finite-element method. *Computers & Structures*, 12(3), 341–348. DOI: 10.1016/0045-7949(80)90031-0.

14 Zienkiewicz O.C., Morice P.B. (1971) *The Finite Element Method in Engineering Science*. McGraw-Hill, London. https://scholar.google.com/scholar_lookup?&title

15 David Müzel S., Bonhin E. P., Guimarães N. M., Guidi E.S. (2020) Application of the Finite Element Method in the Analysis of Composite Materials: A Review. *Polymers*, 12(4), 818. DOI: 10.3390/polym12040818.

16 Doudkin M.V., Kim A., Kim V., Mlynczak M., Kustarev G. (2018) Computer Modeling Application for Analysis of Stress-strain State of Vibroscreen Feed Elements by Finite Elements Method. *Proceeding of the Intern.*

Conf. on Computational and Information Technologies in Science, Engineering, and Education, Ust-Kamenogorsk, Kazakhstan, 82-96. DOI: 10.1007/978-3-030-12203-4_9.

17 Shukla S., Meena Murmu, Deo S.V. (2022) Study on Fracture Parameters of Basalt Fiber Reinforced Concrete Beam by Using Finite Element Method. *Lecture Notes in Civil Engineering*, 33–45. DOI:10.1007/978-981-16-8433-3_5.

18 Campaner L.M., Silveira M.P.M., de Andrade G.S., Borges A.L.S., Bottino M.A., de Oliveira Dal Piva A.M., Giudice R.L., Ausiello P., Tribst J.P.M. (2021) Influence of Polymeric Restorative Materials on the Stress Distribution in Posterior Fixed Partial Dentures: 3D Finite Element Analysis. *Polymer*, 13 (5), 758; DOI:10.3390/polym13050758.

19 Topchyi D. (2016) The theory of plafales:quadruple role of the basis functions of serendipity finite elements. Review of the results. *Scientific Works of Vinnytsia National Technical University*, 2, 1 – 7. https://hal.science/hal-01429000/document.

AUTHORS' INFORMATION

Hasan, Nazieh – PhD, Assistant Professor**,** Mechanical Engineering Department, Zarqa University, Zarqa, Jordan; SCOPUS Author ID: 57201666796; ORCID iD: 0000-0001-8017-5633; nazieh@ymail.com

SUMMARIES	ТҮСІНІКТЕМЕЛЕР	АННОТАЦИИ

Кучеренко М.Г., Кручинин Н.Ю., Неясов П.П.

Бойлық поляризацияланған алтын сфероцилиндрдің бетіндегі полиамфолиттер мен полиэлектролиттердің конформациялық құрылымы.

Жалпы бейтарап полиамфолиттің, сондай - ақ біркелкі зарядталған макротізбектердің, бойлық поляризацияланған алтын сфероцилиндр - сфералық ұштары бар цилиндрлік наноөзекшенің бетіне адсорбцияланған полипептидтердің конформациялық өзгерістері зерттелді. Байланыстар тығыздығының радиалды-бұрыштық таралуының энтропиялық және өрістік факторларын бөліп көрсететін, поляризацияланған сфероцилиндр бетіндегі адсорбцияланған макротізбектердің тепе-теңдік құрылымының аналитикалық моделі ұсынылған. Молекулалық-динамикалық модельдеу кезінде наноөзекшенің орталық цилиндрлік бөлігіндегі, сондай-ақ оның шеткі жарты шарларындағы полипептид атомдарының тығыздығының радиалды таралуы есептелген. Сонымен қатар, полипептид атомдарының сызықтық тығыздығының наноөзекше осі бойымен таралуы есептелді. Поляризацияланған наноөзекшенің бетінде ұзартылған орталық цилиндрлік бөлікте тығыз және наноөзекше ұштарында борпылдақ болатын гантель тәрізді полиамфолит жиегі пайда болды. Макромолекулалық жиектің біркелкі зарядталған полипептидтің буындарынан осы полиэлектролит жиегі ісінген наноөзекшенің қарама-қарсы зарядталған ұшына ауысуы да байқалды.

Кілт сөздері: алтын наноөзекше, поляризацияланған нанобөлшек, полиамфолит, полиэлектролит, конформациялық құрылым, молекулалық динамика.

Кучеренко М.Г., Кручинин Н.Ю., Неясов П.П.

Конформационная структура полиамфолитов и полиэлектролитов на поверхности продольно поляризованного золотого сфероцилиндра.

Исследованы конформационные изменения в целом нейтральных полиамфолитных, а также равномерно заряженных макроцепях, полипептидах, адсорбированных на поверхности продольно поляризованного золотого сфероцилиндра — цилиндрического наностержня со сферическими концами. Представлена аналитическая модель равновесной структуры адсорбированных макроцепей на поверхности поляризованного сфероцилиндра, выделяющая энтропийные и полевые факторы радиально-углового распределения плотности связей. В ходе молекулярно-динамического моделирования рассчитаны радиальные распределения плотности атомов полипептида в центральной цилиндрической части наностержня, а также на его концевых полусферах. Кроме того, были рассчитаны распределения линейной плотности атомов полипептида вдоль оси наностержня. На поверхности поляризованного наностержня образовался гантелеобразный полиамфолитный край, плотный в вытянутой центральной цилиндрической части и рыхлый на концах наностержня. Также наблюдалось смещение макромолекулярного края от звеньев равномерно заряженного полипептида к противоположно заряженному концу наностержня, на котором этот полиэлектролитный край набухал.

Ключевые слова: золотой наностержень, поляризованная наночастица, полиамфолит, полиэлектролит, конформационная структура, молекулярная динамика

Абдуллаев Ж.Ш. Сапаев И.Б.

Қоспалау пен температураның p-n және p-i-n өтпелі құрылымдардың электрфизикалық сипаттамаларына әсерін оңтайландыру.

Берілген жұмыста $p^+=n^+=2\cdot10^{17}$ және $p=n=10^{16}$ $см^{-3}$ қоспаларының концентрациясын қолдана отырып, кремний (Si) және арсенид-галлий (GaAs) p-n және p-i-n гомо-өтпелі құрылымдардың сипаттамаларына қоспалау мен температураның (300 К және 400 К температура кезінде) әсері сандық есептеу және модельдеумен зерттелді. Сонымен қатар, үш түрлі жағдай а) p-n, В) p^+-n және С) p-n^+, олардың 300 К температурада көлемдік зарядтың, потенциалдың, электр өрісінің, негізгі емес заряд тасымалдаушылардың және вольт-Ампердің (I-U) сипаттамаларының таралуына әсерін зерттеу мақсатында талданды. Алынған нәтижелерден А жағдайында рекомбинация процесі В және С жағдайларындағы асимметриялық p-n ауысуларымен салыстырғанда симметриялы p-n ауысуында төмен кернеуде байқалмайтынын көруге болады. Содан кейін 300 К температурада дайындалған үлгілердің вольт-температуралық сипаттамалары өлшенді. Кремний p-n гомоауысулардың калибрлеуі ұсынылған модельді тексеру үшін эксперименттік мәліметтерді қолдануымен жүргізілді. Бұл кешенді модельдің көмегімен келесі жұмыста радиалды p-n ауысуы сияқты әртүрлі геометриялық өзгерістердің электрфизикалық қасиеттерге әсері зерттеледі.

Кілт сөздері: көлемдік зарядтың тығыздығы, легирлеуші қоспалардың концентрациясы, модельдеу, калибрлеу, оңтайландыру.

Абдуллаев Ж.Ш. Сапаев И.Б.

Оптимизация влияния легирования и температуры на электрофизические характеристики p-n и p-i-n переходных структур.

В данной работе исследовано влияние легирования и температуры (при 300 К и 400 К) на характеристики кремниевых (Si) и арсенид-галлиевых (GaAs) p-n и p-i-n гомопереходных структур, используя концентрации легирующих примесей $p^+=n^+=2\cdot10^{17}$ и $p=n=10^{16}$ $см^{-3}$ посредством численного расчета и моделирования. Кроме того, проанализированы три различные случаи: A) p-n, B) p^+-n и C) p-n^+, чтобы исследовать их влияние на распределение объемного заряда, потенциала, электрического поля, неосновных носителей заряда и вольт-амперной (I-U) характеристики при 300 К. Из полученных результатов видно, что в случае А процесс рекомбинации не наблюдается при низком напряжении в симметричном p-n переходе по сравнению с асимметричными p-n переходами в случаях В и С. Затем были измерены вольт-температурные характеристики подготовленных образцов при температуре 300 К. Калибровка кремниевых p-n гомопереходов была выполнена с использованием экспериментальных данных для проверки предложенной модели. С помощью этой комплексной модели в нашей следующей работе будет исследовано влияние различных геометрических изменений, таких как радиальный p-n переход, на электрофизические свойства.

Ключевые слова: плотность объемного заряда, концентрация легирующих примесей, моделирование, калибровка, оптимизация.

Грешта В.Л., Наривский А.Е., Джус А.В., Вынар В.А., Яр-Мухамедова Г.Ш., Мукашев Қ., Бейсен Н.Ә., Мұсабек Г.Қ., Иманбаева А.К., Зелеле Д., Атчибаев Р.Ә., Кемельжанова А.Е.

Остеосинтез процесінің үлгі ерітіндісінде күміспен қоспаланған НЗ30К және НЗ30К магний қорытпаларының коррозиялық әрекеті.

NZ30K және 0,1 мас.% Рингер-Локк ерітіндісіндегі күміспен қоспаланған NZ30K магний қорытпаларының коррозиялық әрекеті зерттелді, себебі олардың құрамдас бөліктері адам ағзасына улы емес және сүйек сынықтарын емдеуде клиникалық асқынулар тудырмайды, ал күміс антибиотиктерге тән бактерияға қарсы қасиеттерге ие. Күміс қоспасы бар NZ30K үлгісінің E_{cor} потенциалы сынақтың алғашқы 100 секундында -1,57 В болғанымен, кейін ол 0,051 мВ/с жылдамдықпен 512 секунд ішінде -1,54 В-қа қарқынды оң жаққа өзгергені анықталды, және келесі 1000 секундтан кейін 0,014 мВ/с дейін кемиді және үлгіде E_{cor} потенциалының стационарлық мәні тіркелді. Үлгі біркелкі жалпы коррозияға ұшырады, ал оның коррозияны зерттеу кезінде E_{cor} потенциалының жақсаруы қорытпа компоненттері арасында ең теріс стандартты потенциал мәніне ие магнийдің ең қарқынды селективті еруіне және стандартты потенциалдың оң мәніне ие оның бетін Zn, Nd, Zr, Ag-мен байытуымен байланысты. Бұл үрдіс жалпы коррозия жылдамдығының төмендеуіне ықпал етті және жергілікті коррозияның дамуын мүмкін емес етті. 0,1 мас.% күміспен қоспаланған NZ30K қорытпасы остеосинтез кезінде биологиялық ыдырайтын импланттарды өндіруге арналған құрылымдық материал ретінде таңдауын негіздеу үшін одан әрі потенциодинамикалық және көлемдік коррозияны зерттеу үшін ұсынылады.

Кілт сөздері: биоимплант, күміспен қоспаланған NZ30K магний қорытпасы, жергілікті коррозия, остеосинтез.

Грешта В.Л., Наривский А.Э., Жус А.В., Вынар В.А., Яр-Мухамедова Г.Ш., Мукашев К., Бейсен Н.А., Мусабек Г.К., Иманбаева А.К., Зелеле Д., Атчибаев Р.А., Кемельжанова А.Э.

Коррозионное поведение магниевых сплавов НЗ30К и НЗ30К, легированных серебром, в модельном растворе процесса остеосинтеза.

Изучено коррозионное поведение магниевых сплавов NZ30K и легированных в растворе Рингера-Локка 0,1 мас.% серебра NZ30K, поскольку их компоненты не токсичны для организма человека и не вызывают клинических осложнений при лечении переломов костей, а серебро обладает антибактериальными свойствами, присущими антибиотикам. Установлено, что потенциал E_{cor} образца NZ30K, легированного серебром, в течение первых 100 секунд испытаний составлял -1,57 В, но затем он интенсивно смещался в положительную сторону до -1,54 В в течение 512 секунд со скоростью 0,051 мВ/с, которая уменьшалась до 0,014 мВ/с после следующих 1000 секунд, и зафиксировано стационарное значение потенциала E_{cor} на образце. Образец был подвергнут равномерной общей коррозии, а улучшение его потенциала E_{cor} при его коррозионном исследовании обусловлено наиболее интенсивным селективным растворением магния, имеющего наиболее отрицательное значение стандартного потенциала среди компонентов сплава, и обогащением его поверхности Zn, Nd, Zr, Ag, имеющими положительное значение стандартного потенциала. Эта тенденция способствовала снижению скорости общей коррозии и сделала невозможным развитие локальной коррозии. Сплав NZ30K, легированный 0,1 мас.% серебра, рекомендуется для дальнейших потенциодинамических и объемных коррозионных исследований с целью обоснования его выбора в качестве конструкционного материала для изготовления биодеградируемых имплантатов при остеосинтезе.

Ключевые слова: биоимплантат, легированный серебром магниевый сплав NZ30K, локальная коррозия, остеосинтез.

Байтелесов С.А., Тожибоев Д.Д., Садыков И.И., Кунгуров Ф.Р., Аликулов Ш.А.

«Hanford» маркалы графиттердің элементтік құрамын және жылу өткізгіштігі мен электр өткізгіштігінің өзгерістерін және жылдам нейтрондардың флюенсіне байланысты күлі аз орташа түйіршікті графитті анықтау.

Жұмыс істеп тұрған ядролық реакторлардан алынған графиттің қасиеттерін зерттеу ядролық реакторлардың одан әрі пайдаланылуын және қызмет ету мерзімін ұзартуды бағалау шеңберінде графиттің қасиеттері мен тұтастығын болжау үшін маңызды. Зерттеудің мақсаты қызмет ету мерзімін анықтау үшін реактордың қалыпты жұмыс жағдайына сәйкес келетін өлшеу температурасының диапазонында VVR-SM зерттеу реакторының жылу бағанының қалауындағы күлі аз орташа түйіршікті графит маркалы графиттің электр өткізгіштігі мен жылу өткізгіштігін анықтау болып табылады. GMZ графитінің жылу өткізгіштігі мен электр өткізгіштігінің өзгеруі, сондай-ақ жылдам нейтрондардың флюенс пен өлшеу температурасына байланысты «Hanford» маркалы графитті салыстыру үшін зерттелді. Электр өткізгіштік пен жылу өткізгіштіктің доза мен температураға тәуелділігі анықталды. Нейтрондардың ағыны неғұрлым көп болса, материалдың жылу өткізгіштігі де, электр өткізгіштігі де соғұрлым төмендейтіні көрсетілген. Жылу бағанының қызмет ету мерзімі анықталды.

Кілт сөздері: жылу өткізгіштік, электр өткізгіштік, күлі аз орташа түйіршікті графиттер, «Hanford» маркалы графит, жылдам нейтрондар, флюенс, доза.

Байтелесов С.А., Тожибоев Д.Д., Садыков И.И., Кунгуров Ф.Р., Аликулов Ш.А.

Определение элементного состава и изменения теплопроводности и электропроводности графитов марки «Hanford» и малозольного среднезернистого графита в зависимости от флюенса быстрых нейтронов.

Изучение свойств графита, извлеченного из действующих ядерных реакторов, имеет важное значение для прогнозирования свойств и целостности графита в рамках оценки дальнейшей эксплуатации и продления срока службы ядерных реакторов. Целью исследования является определение электропроводности и теплопроводности графита марки малозольного среднезернистого графита в кладке тепловой колонны исследовательского реактора VVR-SM в диапазоне температур измерений, соответствующих условиям нормальной эксплуатации реактора для определения срока службы. Исследовано изменение теплопроводности и электропроводности графита GMZ, а также для сравнения графита марки «Hanford»,в зависимости от флюенса быстрых нейтронов и температуры измерений. Установлена зависимость электропроводности и теплопроводности от дозы и температуры. Показано, что чем больше флюенс нейтронов, тем больше снижаются как теплопроводность, так и электропроводность материала. Определен срок службы тепловой колонны.

Ключевые слова: теплопроводность, электропроводность, малозольные среднезернистые графиты, графит марки «Hanford», быстрые нейтроны, флюенс, доза.

Скаков М.К., Мартыненко Е.А., Ердыбаева Н.К., Акаев А.С., Бекмулдин М.К., Прозорова И.В.

Әртүрлі жұмыс режимдері кезінде ИВГ.1М зерттеу реакторының белсенді аймағының жылутехникалық жағдайы.

Зерттеулердің өзектілігі пайдаланудың номиналды және жобалық режимдерінде төмен байытылған уран отыны бар ИВГ.1М зерттеу реакторының белсенді аймағының жылу техникалық сипаттамаларын анықтаумен байланысты. ИВГ.1М зерттеу реакторының жылу техникалық жағдайын іске қосу кезінде ақпараттық-өлшеу жүйесінің жылу жеткізгішінің температура, қысым және шығын бергіштерінің көрсеткіштері анықтайды. Белсенді аймақтың конструкциялық материалдарының температурасын анықтау және жылу таратушы құрастырудың биіктігі бойынша жылу жеткізгішінің температурасын бөлу үшін жанама әдістер, оның ішінде компьютерлік модельдеу әдістері қолданылады. Зерттеулер ANSYS Fluent бағдарламалық кешенін пайдалана отырып, шекті-элементтік талдау әдісінің көмегімен жүргізілді. Зерттеулерді жүргізудің мақсаты есептік әдістеменің сәйкестігін тексеру және реактор жұмысының қуатының номиналдан жобалыққа дейінгі диапазонында жылу бөлетін жинақта температураны бөлу туралы есептік мәліметтерді алу болды. Мақалада ИВГ.1М реакторының сипаттамасы, зерттеулер жүргізу әдістемесі, компьютерлік модель, модельдеу нәтижелері және есептік мәліметтердің эксперименттік мәліметтермен салыстыру ұсынылған. Зерттеудің ғылыми жаңалығы салқындату жағдайларына консервативті көзқарас кезінде жобалық қуаттың әртүрлі деңгейлерінде реактор жұмысы кезінде твэлдер жұмысының температуралық режимдерін айқындаудан тұрады. Зерттеу нәтижелерінің маңыздылығы компьютерлік модель реактор жұмысының әртүрлі режимдерінде ИВГ.1М реактордың белсенді аймағының сипаттамаларын анықтау үшін және жылу бөлетін құрастырудағы жылу-гидравликалық процестерді талдау үшін пайдаланылуы мүмкін.

Кілт сөздері: ИВГ.1М ЗР, твэл, температурлық өріс, компьютерлік моделдеу, ЖБҚ, жылу физикалық есептеме.

Скаков М.К., Мартыненко Е.А., Ердыбаева Н.К., Акаев А.С., Бекмулдин М.К., Прозорова И.В.

Теплотехническое состояние активной зоны исследовательского реактора ИВГ.1М при различных режимах работы.

Актуальность исследований связана с определением теплотехнических характеристик активной зоны исследовательского реактора ИВГ.1М с низкообогащенным урановым топливом при номинальных и проектных

режимах эксплуатации. Теплотехническое состояние исследовательского реактора ИВГ.1М во время проведения пусков определяют показания датчиков температуры, давления и расхода теплоносителя информационно-измерительной системы. Для определения температуры конструкционных материалов активной зоны и распределения температуры теплоносителя по высоте тепловыделяющей сборки применяются косвенные методы, в том числе методы компьютерного моделирования. Исследования проведены с помощью метода конечно-элементного анализа с использованием программного комплекса ANSYS Fluent. Цель проведения исследований состояла в проверке адекватности расчетной методики и получении расчетных данных о распределении температуры в тепловыделяющей сборке в диапазоне мощности работы реактора от номинальной до проектной. В статье представлены описание реактора ИВГ.1М, методика проведения исследований, компьютерная модель, результаты моделирования и сравнение расчетных данных с экспериментальными. Научная новизна исследования состоит в определении температурных режимов работы твэлов при работе реактора на различных уровнях проектной мощности при консервативном подходе к условиям охлаждения. Значимость результатов исследования состоит в том, что компьютерная модель может быть использована для определения характеристик активной зоны реактора ИВГ.1М при различных режимах работы реактора и для анализа теплогидравлических процессов в тепловыделяющей сборке.
Ключевые слова: ИР ИВГ.1М, твэл, температурное поле, компьютерное моделирование, ТВС, теплофизический расчет.

Мостовщиков А. В., Гребнев М. Е., Рудмин М. А., Назаренко О. Б., Дерина К. В., Гальцева О. В.,
Ультракүлгін сәулелену мен ультрадыбыстық әсері кезіндегі гидроксипатиттің синтезі және сипаттамасы.

Гидроксиапатит биомедицинада, оптика мен электроникада, сенсорларда, катализде және қоршаған ортаны залалсыздандыруда мүмкін болатын кең ауқымды қолданыстарға ие. Бұл зерттеу гидроксиапатитті дымқыл тұндыру әдісімен синтездеуге бағытталған. Кептіру уақытының синтезделген материалдың қасиеттеріне әсері зерттелді. Кептіру уақытын 24 сағаттан 96 сағатқа дейін арттырғанда бөлшектердің өлшемі 80-ден 200 мкм-ге дейін артты. Ультракүлгін сәулелену және ультрадыбыстық әсер бірлесіп және жеке әсер еткен жағдайларда алынған гидроксиапатит ұнтақтарының морфологиясы мен қасиеттері зерттелді. Алынған үлгілер рентгендік дифракция, инфрақызыл Фурье спектроскопиясы, сканерлеуші электронды микроскоп, Брунауэр-Эммет–Теллер әдістері арқылы талданды. Нәтижелер алынған гидроксиапатит ұнтақтарының қасиеттері синтез жағдайларына өте тәуелді екенін көрсетті. Синтез кезеңінде ультрадыбыстық өңдеу нәтижесінде алынған гидроксиапатит бөлшектерінің мөлшері 4 мкм-ге дейін азайды. Тұрақтандыру кезеңінде ультракүлгін сәулелендуді қолдану реакция өнімдеріндегі гидроксиапатиттің көбеюіне әкелді.
Кілт сөздері: гидроксиапатит, дымқыл тұндыру, ультрадыбыстық, ультракүлгін сәулелену.

Мостовщиков А.В., Гребнев М.Е., Рудмин М.А., Назаренко О.Б., Дерина К.В., Гальцева О.В.,
Синтез и характеристика гидроксипатита при воздействии ультрафиолетового излучения и ультразвука.

Гидроксиапатит имеет широкий спектр возможных применений в биомедицине, оптике и электронике, сенсорах, катализе и в дезактивации окружающей среды. Настоящее исследование было сосредоточено на синтезе гидроксиапатита методом мокрого осаждения. Было исследовано влияние времени сушки на свойства синтезированного материала. Размер частиц увеличивается от 80 до 200 мкм при увеличении времени сушки от 24 часов до 96 часов. Была изучена морфология и свойства порошков гидроксиапатита, полученных под действием ультрафиолетового излучения и ультразвукового воздействия, действующих совместно и по отдельности. Полученные образцы были проанализированы с использованием рентгеновской дифракции, инфракрасной Фурье-спектроскопии, сканирующего электронного микроскопа, методов Брунауэра–Эммета–Теллера. Результаты показали, что свойства полученных порошков гидроксиапатита сильно зависят от условий синтеза. Ультразвуковая обработка на этапе синтеза привела к уменьшению размера полученных частиц гидроксиапатита до 4 мкм. Использование ультрафиолетового излучения на этапе стабилизации привело к увеличению содержания гидроксиапатита в продуктах реакции.
Ключевые слова: гидроксиапатит, мокрое осаждение, ультразвук, ультрафиолетовое излучение.

Циганов В., Шейко С., Гречаный А., Васильченко Т.
Үйкеліс кезіндегі жанасу бетінің пластикалық-деформациялық күйін модельдеу.

Күрделі термодинамикалық жүктеме жағдайында үйкеліс кезінде түйіндесулердің контактілі бұзылуының механикасы қарастырылған. Жанасу кезінде беткі қабаттың қалыптасу ерекшеліктерін ескеруімен, үйкеліс түйіндерінің күрделі зақымдануын, тозу қарқындылығын математикалық сипаттау мүмкіндігі көрсетілген. Трибо-түйіндесулердің беткі беріктігі мен төзімділігін есептеу әдісі ұсынылған. Бұл нүктенің кернеу күйінің параметрлерін (үйкеліс коэффициенті, пішін факторы) процестің термомеханикалық параметрлерімен байланыстыруға мүмкіндік береді. Үйкеліс коэффициентінің, пішін параметрлерінің өзгеруін бағалау арқылы

аққыштықтың кернеуін анықтау және берілген кернеу жағдайына сәйкес құрылымдық түрлендірулерді орнату мүмкіндігі пайда болады.
Кілт сөздері: үйкеліс, жүктеме, илемділік теориясы, деформация, кернеу, триботүйіндесу.

Циганов В., Шейко С., Гречаный А., Васильченко Т.
Моделирование пластическо-деформационного состояния контактной поверхности при трении.
Рассмотрена механика контактного разрушения сопряжений при трении в условиях сложного термодинамического нагружения. Показана возможность математического описания комплексного повреждения узлов трения, интенсивности изнашивания с учетом особенностей формирования поверхностного слоя при контактировании. Представлена методика расчета поверхностной прочности и долговечности трибосопряжений. Это позволяет связать параметры напряженного состояния точки (коэффициент трения, фактор формы) с термомеханическими параметрами процесса. Оценкой изменения коэффициента трения, параметров формы появляется возможность определения напряжения текучести и установление структурных превращений, соответствующих данному напряженному состоянию.
Ключевые слова: трение, нагрузка, теория пластичности, деформация, напряжение, трибосопряжения.

Жанабаев З.Ж., Тілеу А.О., Дуйсебаев Т.С., Әлмен Д.Б.
Лазерлік газ сенсоры сигналының концентрациялық қанығуы.
Қазіргі уақытта спектроскопиялық әдістерді (оптикалық, радиотехникалық, акустикалық) қолдана отырып, газ концентрациясы 10^{-6} бөліктен аз болған кезде газдың түрін жеткілікті дәлдікпен анықтауға болады. Сонымен қатар технология мен қоршаған орта үшін жарылғыш, улы және зиянды газдардың рұқсат етілген концентрацияларының практикалық маңызы бар. Лазерлік газ датчигі реакциясының шамасы $\lesssim 10^3$ болатын белгілі физикалық эксперименттік зерттеулер тек сызықтық тәуелділікті көрсетеді. Шамасы $\gtrsim 10^3$ үшін зерттеу әдістері жану, микрожарылыс, құрылымдық және фазалық түрлендіру процестеріне негізделген және нақты практикалық жағдайларда әрқашан қолданыла бермейді. Жұмыс тек атомдық деңгейде ғана емес, сонымен қатар нанобөлшек молекулаларының кластерлерінің масштабында да әсер етуіне байланысты фотодиодтағы (сигнал қабылдағыш), газдағы лазер сәулесінің эксперименттік түрде алынған тербелістерді талдауға арналған. Газ концентрациясы флуктуация-диссипация қатынасы арқылы бағаланады. Кванттық (лазерлік фотон энергиясы) және термиялық (нанобөлшектердің температурасы) факторлары нысаналы газ концентрациясының жоғарылауымен салыстыруға болатын кезде сигнал корреляторының тұрақты мәнге қанығатыны көрсетілген. Қанығу концентрациясының критикалық мәндері осы екі фактордың теңдігімен анықталады.
Кілттік сөздер: флуктуация-диссипация, коррелятор, фотодиод, метан, тетрахлорметан, аммиак.

Жанабаев З.Ж., Тилеу А.О., Дуйсебаев Т.С., Альмен Д.Б.
Концентрационное насыщение сигнала лазерного сенсора газа.
В настоящее время с достаточной точностью можно определить вид газа при его концентрации менее 10^{-6} долей с помощью спектроскопических методов (оптических, радиотехнических, акустических). Наряду с этим практически важное значение имеет величина допустимых концентраций взрывоопасных, токсичных, вредных для техники и экологии газов. Известные физические экспериментальные исследования указывают лишь на линейную зависимость отклика лазерного газового сенсора при единицах $\lesssim 10^3$. Методы исследования для единиц $\gtrsim 10^3$основаны на процессах горения, микровзрыва, структурных и фазовых превращений и не всегда применимы в реальных практических условиях. Работа посвящена анализу экспериментально полученных флуктуаций, вызванных лазерным лучом в газе в фотодиоде (приемнике сигнала) из-за его влияния не только на атомном уровне, но и в масштабах кластеров молекул наночастиц. Концентрация газа оценивается по флуктуационно-диссипативному отношению. Показано, что коррелятор сигнала насыщается до постоянного значения, когда квантовый (энергия лазерного фотона) и тепловой (температура наночастиц) факторы сопоставимы с ростом концентрации целевого газа. Критические значения концентрации насыщения определяются равенством этих двух факторов.
Ключевые слова: флуктуация-диссипация, коррелятор, фотодиод, метан, тетрахлорметан, аммиак.

Кубич В.И., Фасоль Е.О., Чернета О.О., Ершина А.К., Сакипов Н.З.
Құрамында иттрий бар тығыздағыш жабындылардың ыстыққа төзімді кесу траекторияларын қалыптастыру кезінде механикалық бұзылуға төзімділігі.
Иттрий 0,1%, 0,3%, 0,5% қоспасымен КНА-82 қорытпасының лигатурасынан жасалған жабындыларды триботехникалық сынау нәтижелері бойынша сынақтар кезеңінде динамикалық үйкеліс коэффициентінің өзгеру сипатын және материал тозуының энергия сыйымдылығының көптеген мәндерін анықтауға мүмкіндік беретін мәліметтер алынды. Ионды-плазмалық әдіспен қалыптасқан жабындыларды бағалау жүргізілді, бұл бағалау механикалық бұзылуға максималды төзімділік динамикалық үйкеліс коэффициентінің тұрақты минималды мәнінің болуымен, төзімділік шегіне жеткенге дейін аз үйкеліс күшінің белгісі ретінде және интегралды үйкеліс жұмысының бірлігін өндіруге тура келетін бөлінген бөлшектердің санымен анықталатындығына негізделген.

Бұл бағалау параметрлері 1-ден 4-ке дейінгі баллдар саны бойынша қатарға орналастырылған. Максималды балл максималды төзімділікке сәйкес келеді, яғни материалдың тозу сыйымдылығының аз мәні және тұрақты үйкеліс коэффициентінің минималды мәні. Сынақтардың барлық дерлік кезеңдерінде (I-III) осы параметрлердің балл бойынша бірдей сәйкес келуі иттрий концентрациясы 0,3% -0,5% болатын газ жалын әдісімен қалыптасқан жабынға ие екендігі анықталды. Сынақтардың төртінші кезеңінде иттрий концентрациясы 0,1% болатын иондық-плазмалық әдіспен түзілген жабынды үшін өзгеше болды.
Кілт сөздері: тығыздау жабынды, ионды-плазмалық әдіс, газ жалыны әдісі, механикалық сынуға төзімділік, кесу іздері, жоғары температуралық жүктеме, иттрий, механикалық төзімділік, газ турбиналық қозғалтқыштар.

Кубич В.И., Фасоль Е.О., Чернета О.О., Ершина А.К., Сакипов Н.З.
Стойкость жаропрочных иттрий содержащих уплотнительных покрытий к механическому разрушению при формировании траекторий резания.
По результатам триботехнических испытаний покрытий из лигатуры сплава КНА-82 с добавкой иттрия 0,1%, 0,3%, 0,5% получены данные, позволяющие установить характер изменения динамического коэффициента трения за период испытаний и многочисленные значения энергоемкости износа материала. Проведена оценка покрытий, сформированных газопламенным и ионно-плазменным методом, которая основывалась на том, что максимальная стойкость к механическому разрушению будет определяться проявлением постоянного минимального значения динамического коэффициента трения, как признака меньшей силы трения до достижения предела выносливости, и количеством отделившихся частиц, на долю которых приходится производство единицы интегральной работы трения. Данные параметры оценки выстроены в ряд по количеству баллов от 1 до 4. Максимальному баллу соответствует максимальная стойкость, т. е. меньшее значение энергоемкости износа материала и минимальное значение стабильного коэффициента трения. Определено, что такое же совпадение этих параметров по баллам практически на всех этапах испытаний (I-III) имело покрытие, сформированное газопламенным методом с концентрацией иттрия 0,3%-0,5%. Исключение составило покрытие, сформированное ионно-плазменным методом с концентрацией иттрия 0,1% на четвертом этапе испытаний.
Ключевые слова: герметизирующее покрытие, ионно-плазменный метод, газопламенный метод, механическая стойкость к разрушению, следы резания, высокотемпературное нагружение, иттрий, механическая стойкость, газотурбинные двигатели.

Жантлесов Е.Ж., Смакова Н.С., Грузин В.В., Тогусов А.К., Жусупбеков Т.Х., Жантлесов Ж.К.
Тыйым салынған заттарды анықтауға арналған радиолокациялық құрылғының параметрлерін ғылыми-техникалық негіздеу.
Мақалада микротолқынды диапазондағы электрмагниттік сәулеленуді пайдалана отырып, тыйым салынған объектілерді анықтауға және визуализациялауға мүмкіндік беретін радиолокациялық құрылғының параметрлерінің ғылыми-техникалық негіздемесі берілген. Голографиялық әдіс негізінде объектіден шағылысқан толқындарды өлшеудің көп статикалық сұлбасының математикалық моделі жасалды. Радиолокациялық құрылғының жұмысын имитациялық модельдеуге арналған бағдарламалық кешен әзірленді, оның көмегімен радиолокациялық құрылғының сирек сенсорлық ішкі жүйелерінің әртүрлі конфигурациялары үшін объектінің кескіндерін қайта құру алынды. Сигналдың шуға ең жоғары қатынасын талдау әдісін қолдана отырып, сирек сенсорлық ішкі жүйенің оңтайлы конфигурациясы таңдалды, ол үшін көп статикалық голограмма модельденді және кілт кескінін қайта құру жасалды.
Кілт сөздер: микротолқынды визуализация, голография, мультистатикалық массив, тыйым салынған заттарды анықтау, визуализация.

Жантлесов Е.Ж., Смакова Н.С., Грузин В.В., Тогусов А.К., Жусупбеков Т.Х., Жантлесов Ж.К.
Научно-техническое обоснование параметров радиолокационного устройства для обнаружения запрещенных предметов.
В статье представлено научно-техническое обоснование параметров радиолокационного прибора, который позволяет обнаружить и визуализировать запрещенные предметы при помощи электромагнитного излучения СВЧ-диапазона. Разработана математическая модель мультистатической схемы измерения отраженных от объекта волн на основе голографического метода. Разработан программный комплекс имитационного моделирования работы радиолокационного прибора. Получены реконструкции изображений объекта для различных конфигураций разреженных сенсорных подсистем радиолокационного прибора. Методом анализа пикового соотношения сигнала к шуму выбрана оптимальная конфигурация разреженной сенсорной подсистемы, для которой смоделирована мультистатическая голограмма и сформирована реконструкция изображения гаечного ключа.
Ключевые слова: микроволновая визуализация, голография, мультистатический массив, обнаружение запрещенных предметов, визуализация.

Жанбирбаева П.А., Балтабеков А.С., Каюмова А.С., Адамбай Т.Н., Сериков Т.М.
Күйдіру ұзақтығының $LaFeO_3$ перовскитінің фотокаталитикалық қасиеттеріне әсері.
Бұл жұмыста гидротермиялық әдіспен синтезделген $LaFeO_3$ перовскиттің фотокаталитикалық қасиеттеріне күйдіру ұзақтығының әсері зерттелген. Зерттеу нысаны ретінде лантан ферриті ($LaFeO_3$) көзге көрінетін жарық әсеріндегі белсенділігі жоғары болғандықтан таңдалды. Тәжірибе барысында 2, 4 және 6 сағат ішінде күйдіру кезінде материалда болатын құрылымдық өзгерістер зерттелді. Нанобөлшектердің морфологиясын, фазалық құрамын, кристалдылығын, абсорбциялық спектрін және фотокаталитикалық белсенділігін талдауға басты назар аударылды. Нәтижелер жасыту уақытының ұлғаюы кристалдық құрылымның жақсаруына, кристаллиттер мөлшерінің ұлғаюына және оттегінің жоғары деңгейіне әкелетінін көрсетеді. Максималды фотокаталитикалық белсенділікке қол жеткізу үшін оңтайлы күйдіру уақыты 6 сағат болып анықталды. Жұмыс перовскит негізіндегі материалдардың фотокаталитикалық қасиеттерін жақсарту үшін ұзақ мерзімді күйдіруді қолдану перспективаларын растайды.
Кілт сөздер: лантан ферриті, күйдіру ұзақтығы, фотокаталитикалық белсенділік.

Жанбирбаева П.А., Балтабеков А.С., Каюмова А.С., Адамбай Т.Н., Сериков Т.М.
Влияние продолжительности отжига на фотокаталитические свойства перовскита $LaFeO_3$
В данной работе исследовано влияние продолжительности отжига на фотокаталитические свойства $LaFeO_3$ перовскита, синтезированного гидротермальным методом. Феррит лантана ($LaFeO_3$) был выбран в качестве объекта исследования из-за его высокой активности под воздействием видимого света. В ходе экспериментов были изучены структурные изменения, происходящие в материале при отжиге в течение 2, 4 и 6 часов. Основное внимание было уделено анализу морфологии наночастиц, фазового состава, кристалличности, спектров поглощения и фотокаталитической активности. Результаты показывают, что увеличение времени отжига приводит к улучшению кристаллической структуры, увеличению размера кристаллитов и более высокому уровню насыщения кислородом. Было определено, что оптимальное время отжига для достижения максимальной фотокаталитической активности составляет 6 часов. Работа подтверждает перспективность использования длительного отжига для улучшения фотокаталитических свойств материалов на основе перовскита.
Ключевые слова: феррит лантана, продолжительность отжига, фотокаталитическая активность.

Үсіпов Н., Ахметәлі А., Зайдын М., Акниязова А., Сақан А., Қаламбай М., Шүкірғалиев Б.
Жұлдыз шоғырларының фракталдық өлшемі.
Жұлдыздар шоғырының құрылымын сандық талдау олардың қалыптасуы мен эволюциясын түсіну үшін өте маңызды. Берілген мақалада жұлдыздар шоғырының эволюциясын зерттеу үшін фракталдық өлшемдік талдаудың қолданылуын, сондай-ақ фракталдық өлшемділікті, геометриялық объектілердің күрделілігі мен өзіндік ұқсастығын сандық бағалауды қамтамасыз ететін фракталдық геометриядан алынған тұжырымдаманы зерттелді. Жұлдыздар кластерлерін күрделі желілер ретінде қарастыра отырып, олардың фракталдық өлшемдерін есептеу үшін box-covering әдісін қолданылды. Бұл әдісте жақсы зерттелген minimum spanning tree (MST) және box-covering (BC) әдістерін біріктірілді және осы әдіс арқылы кластерлердің фракталдық құрылымы анықталды. Жұлдыздар шоғыры 1.3 фракталдық өлшемде ыдырап, дәрежелік заңына бағынатыны анықталды. Алынған нәтиже McLuster нәтижелерімен салыстырылғанын атап өткен жөн.
Кілт сөздер: жұлдыздар шоғыры, фракталдық өлшем, box-covering, жұлдыздардың пайда болу тиімділігі.

Усипов Н., Ахметали А., Зайдын М., Акниязова А., Сакан А., Каламбай М., Шукиргалиев Б.
Фрактальная размерность звездных скоплений.
Количественный анализ структуры звездных скоплений имеет решающее значение для понимания их формирования и эволюции. В этой статье мы исследуем применение анализа фрактальной размерности для изучения эволюции звездных скоплений, а также фрактальную размерность, концепцию из фрактальной геометрии, которая обеспечивает количественную оценку сложности и самоподобия геометрических объектов. Рассматривая звездные скопления как сложные сети, мы используем метод box-covering для вычисления их фрактальной размерности. Наша методология сочетает в себе хорошо зарекомендовавшие себя методы minimum spanning tree (MST) и box-covering (BC), и с помощью этих методов была определена фрактальная структура скоплений. Было обнаружено, что звездные скопления распадаются при фрактальной размерности 1.3 и подчиняются степенному закону. Следует отметить, что полученный результат был сопоставлен с результатами McLuster.
Ключевые слова: звездное скопление, фрактальная размерность, box-покрытие, эффективность звездообразования.

Mohammed O.A., Mohammed S.A., Ghazaly N.M.

Жел турбинасының тежегіш жүйесінің үйкеліс коэффициентіне ылғалдылық пен кварц құмының әсері.

Көлденең жел турбиналарына арналған негізгі жетек бөлшектері, соның ішінде беріліс қорабы, генератор және тежегіш жүйесінің жөндеу және ауыстыру шығындары өте жоғары және оларды аяқтауға көп уақыт жұмсалады. Берілген мақалада қоршаған ортаның ластануының жетек трибологиясының жағдайына әсері қарастырылады. Жел турбинасының жетек жүйесі модельденді және эксперименттік зерттеу жүргізілді. Жел турбиналарының механикалық тежегіш жүйесі бұл зерттеу жұмысы үшін таңдалған тақырыптық зерттеулердің бірінің тақырыбы болып табылады. Қоспалардың жел турбинасы тежегішінің үйкеліс коэффициентіне қалай әсер ететінін зерттелген. Нәтижелерге сәйкес, үйкеліс коэффициенті жел турбинасы білігінің жылдамдығының әрбір жоғарылауымен артады. Сондай-ақ, ластаушы заттардың бөлшектерінің өлшемі үйкеліс коэффициентіне айтарлықтай әсер ететіні анықталды. Сонымен қатар, нәтижелер ылғалдылық 30 мм^3-тен 90 мм^3-ке дейін жоғарылаған кезде үйкеліс коэффициентін едәуір төмендететін жетек жүйесі туралы пайдалы ақпарат бере алады.

Кілт сөздері: жел турбиналары, ылғалдылық жағдайы, кварц құмы, үйкеліс коэффициенті.

Mohammed O.A., Mohammed S.A., Ghazaly N.M.

Влияние влажности и кварцевого песка на коэффициент трения тормозной системы ветряной турбины.

Основные детали привода для горизонтальных ветряных турбин, включая коробку передач, генератор и тормозную систему, имеют очень высокие затраты на ремонт и замену и требуют много времени для завершения. В этой статье исследуется влияние загрязнения окружающей среды на поведение трибологии привода. Моделируется и исследуется экспериментальное исследование системы привода ветряной турбины. Механическая тормозная система ветряных турбин является предметом одного из тематических исследований, выбранных для этой исследовательской работы. В этом исследовании изучается, как примеси влияют на коэффициент трения тормоза ветряных турбин. Согласно результатам, коэффициент трения увеличивается с каждым увеличением скорости вала ветряной турбины. Также обнаружено, что размер частиц загрязняющих веществ значительно влияет на коэффициент трения. Кроме того, результаты могут дать полезную информацию о системе привода, которая при увеличении влажности с 30 мм^3 до 90 мм^3 значительно снижает коэффициент трения.

Ключевые слова: ветряные турбины, состояние влажности, кварцевый песок, коэффициент трения.

Sinossi M.I., Sadak T.W.

Білік диаметрінің және түсіру ойығының радиусының біртіндеп өзгергендегі кернеулер концентрациясының коэффициентін сандық зерттеу.

Бұл жұмыстың мақсаты білік диаметрінің біртіндеп өзгерісі кезіндегі кернеу концентрациясының коэффициенттеріне конустық және түсіру ойығы радиустың әсерін зерттеу болып табылады. Ақырлы элементтерді талдау сатылы біліктердегі кернеудің максималды мәнін төмендету мақсатында теориялық зерттеулер жүргізу үшін қолданылды. Түсіру ойығы жоқ түзу білікпен салыстырғанда, нәтижелер конустық бұрыштың кемуі кернеулер концентрациясы коэффициенттерінің мәндерінің төмендеуіне айтарлықтай әсер ететінін көрсетті. Екінші жағынан, біліктің сағасына түсіретін ойықтардың орналасуын ұлғайту, әсіресе конустың үлкен бұрышында, кернеу концентрациясының коэффициенттерінің мәндерін жоғарылатады.

Кілт сөздері: сатылы біліктер, білік сағасының ойығы, түсіру ойығы, кернеулер концентрациясының коэффициенттері, ақырлы элементтерді талдау.

Sinossi M.I., Sadak T.W.

Численное исследование постепенного изменения диаметра вала и радиуса разгрузочной канавки на коэффициент концентрации напряжений.

Целью данной работы является исследование влияния радиуса разгружающей канавки и конусности при постепенном изменении диаметра вала на коэффициенты концентрации напряжений. Анализ конечных элементов использовался для проведения теоретических исследований с целью снижения максимального значения напряжения в ступенчатых валах. В сравнении с прямым валом без разгружающей канавки результаты показывают, что уменьшение угла конусности оказывает значительное влияние на снижение значений коэффициентов концентрации напряжений. С другой стороны, увеличение расположения разгружающих канавок от заплечика вала имеет тенденцию к увеличению значений коэффициентов концентрации напряжений, особенно при большом угле конусности.

Ключевые слова: ступенчатые валы, галтель заплечика вала, разгрузочная канавка, коэффициенты концентрации напряжений, анализ методом конечных элементов.

Hasan N.
Беттік сынау кезіндегі кернеулер мен температуралардың қалдық өрістері: ақырлы-элементтік талдау.
Бөлшектердің бетін өңдеуде көптеген жетістіктерге қол жеткізілді, бірақ әрлеу процестерінен туындайтын беткі ақаулардың болуы олардың кернеу концентраторы ретінде қызмет ету мүмкіндігіне қатысты алаңдаушылық туғызды. Бұл мәселені шешу үшін бұл зерттеуде ақырлы элементтер әдісінің мүмкіндіктері және озық бағдарламалық қолданбалар пайдаланды. Зерттеудің негізгі мақсаты - осы бағдарламалық жүйелер ұсынатын кешенді мүмкіндіктерді пайдалана отырып, әрлеуден кейін материалдар беттерінің кернеулері мен деформацияларының күйін бағалау болып табылады. Зерттеудің маңызды құрамдас бөлігі динамикалық термоэлементтермен бақыланатын стационарлық емес температура өрістерінің материал беттеріндегі кернеулер мен деформациялар динамикасына әсеріне бағытталған. Температураның таралуындағы елеулі өзгерістерді анықтай отырып, көрсетілген өріс функцияларын бейнелеу үшін визуализациялау әдістері қолданылды. Нәтижелер стандартты функция 3-7-4 түйін сегментіндегі ең жоғары температура аймағын анықтағанын көрсетті, ал балама функция оны қызыл аймақпен белгіленген 4 түйін сегментінде анықтады. Бұл нәтижелер әрлеу процесінің механикалық және физикалық аспектілерін теңестірудегі стационарлық емес температура өрістерінің маңызды рөлін көрсетеді. Бұл зерттеу әрлеуден кейінгі материал беттерінің кернеулі деформацияланған күйін түсінуге айтарлықтай үлес қосады, бұл тереңдетілген зерттеу үшін заманауи бағдарламалық жүйелерді пайдаланудың әлеуетті артықшылықтарын көрсетеді.
Кілт сөздері: ақырлы элементтер әдісі, ақпараттық технологиялар, дәлдік, кернеулі - деформацияланған күй.

Hasan N.
Остаточные поля напряжений и температур при испытаниях поверхности: конечно-элементный анализ.
Многочисленные достижения были достигнуты в обработке поверхности деталей, однако наличие поверхностных дефектов, возникающих в результате финишных процессов, вызвало опасения относительно их потенциальной возможности служить концентраторами напряжений. Для решения этой проблемы в настоящем исследовании использовались возможности метода конечных элементов и передовые программные приложения. Основная цель исследования — оценить состояние напряжений и деформаций поверхностей материалов после финишной обработки, используя комплексные возможности, предлагаемые этими программными системами. Значительный компонент исследования был сосредоточен на влиянии нестационарных температурных полей, отслеживаемых динамическими термоэлементами, на динамику напряжений и деформаций внутри поверхностей материалов. Методы визуализации использовались для отображения указанных полевых функций, выявляя заметные изменения в распределении температур. Результаты показали, что стандартная функция определила область самой высокой температуры в сегменте узлов 3-7-4, в то время как альтернативная функция определила ее в сегменте узлов 4, обозначенном красной областью. Эти результаты подчеркивают важную роль нестационарных температурных полей в балансировке механических и физических аспектов процесса отделки. Это исследование вносит значительный вклад в понимание напряженно-деформированного состояния поверхностей материалов после отделки, подчеркивая потенциальные преимущества использования современных программных систем для углубленного исследования.
Ключевые слова: метод конечных элементов, информационные технологии, точность, напряженно-деформированное состояние.